FACHBEREICH MATHEMATIK UND NATURWISSENSCHAFTEN
FACHGRUPPE PHYSIK
BERGISCHE UNIVERSITÄT WUPPERTAL

Prospects for $t\bar{t}$ resonance searches at ATLAS

Tatjana Lenz

CERN-THESIS-2010-224
21/12/2010

November 2010

Contents

1 Introduction 1

2 Theoretical Aspects of Top Quark Physics 3
- 2.1 Basic Concepts of the Standard Model . . . 3
- 2.2 Standard Model Top Quark Pair Production and Decay . . . 10
- 2.3 Top Quark Pair Production in the BSM Models . . . 12

3 LHC and ATLAS Detector 19
- 3.1 The Large Hadron Collider . . . 19
- 3.2 The Atlas Detector . . . 21
- 3.3 Forward Detectors . . . 33
- 3.4 Data Acquisition System . . . 34
- 3.5 Performance of the LHC and the ATLAS Experiment . . . 36

4 Event Simulation 39
- 4.1 Main Aspects of Monte Carlo Event Simulation . . . 39
  - 4.1.1 Parton Level Event Generators . . . 41
  - 4.1.2 Multi-purpose Event Generators . . . 42
- 4.2 Detector Simulation . . . 43
  - 4.2.1 Full Detector Simulation . . . 43
  - 4.2.2 Fast Detector Simulation . . . 44
- 4.3 Signal and Background Event Modeling . . . 45
  - 4.3.1 Signal Event Simulation . . . 45
  - 4.3.2 Background Event Simulation . . . 48

5 Event Reconstruction 53
- 5.1 Track Reconstruction in the Inner Detector . . . 53
- 5.2 Primary Vertex Reconstruction . . . 55
- 5.3 Charged Lepton Identification . . . 56
- 5.4 Jet Reconstruction . . . 59
- 5.5 Neutrino Reconstruction . . . 67

6 Topological Vertex Finder 71
- 6.1 Properties of b-Quark Jets . . . 71
- 6.2 Association and Selection of Tracks and Jet Flavour Labelling . . . 74
- 6.3 b-Tagging Algorithms in ATLAS . . . 76
- 6.4 Topological Vertex Finder . . . 80
- 6.5 Secondary Vertex Reconstruction Performance . . . 86
- 6.6 Application to b-Tagging . . . 88

6.7 Performance in Rejecting Light Quark Jets 90

7 The $t\bar{t}$ Invariant Mass Distribution 93
7.1 Event Selection 93
7.2 Event Topology 99
7.3 Analysis Strategy 101
7.4 Selection Efficiency and Mass Resolution 106
7.5 Systematic Uncertainties 111
7.6 Resonance Width 120

8 Heavy Resonance Searches at ATLAS 123
8.1 Statistical Tools 123
8.2 Sensitivity for Heavy Resonances 125
8.3 Prospects for Heavy Resonance Searches 129

9 Summary and Conclusions 131

1 Introduction

What is the world made of? This is one of the fundamental questions scientists try to answer at the Large Hadron Collider (LHC) located at European Organisation for Nuclear Research, near Geneva. The LHC is the world's largest particle accelerator and collider. In Dezember 2009 the LHC has started its operation and since then provides collisions for the four main experiments. ATLAS is one of the general purpose experiments, it covers a broad range of topics in high energy physics. This thesis has been performed within the ATLAS collaboration.

According to our current knowledge about the constituents of matter, there are 12 fundamental particles, 6 quarks and 6 leptons. While all ordinary matter is made of the lightest two quarks, the up and down quark, and the lightest charged lepton, the electon, the other particles can be produced in collisions of high-energy particles. The mass of particles, although present in everyday's life, is theoretically not fully understood. In the Standard Model of high-energy particle physics the mass is generated through the mechanism of electroweak symmetry breaking induced by one physical Higgs field, producing one particle, the Higgs boson. Since no evidence for the Higgs boson has been found yet, alternative mechanisms of the mass generation are of interest. The top quark is the heaviest fundamental particle known so far and due to its large mass, is plays an important role in these theories. Many models predict the existence of new heavy particles which couple to top quarks. This leads to an additional production mechanism of top quarks and should be visible in the invariant mass distribution of the top quark pairs.

First searches for new heavy particles in top quark pairs events have been performed at the TEVATRON collider of the Fermi Accelerator Laboratory. So far no evidence for new particles was found. The higher centre-of-mass energy at the LHC allows one to extend these searches for the first time into the TeV-regime. In this thesis a method has been developed, which is able to reconstruct top quars in a broad range of transverse momenta, from top quarks at rest up to the range of TeV. Based on the reconstructed invariant mass distribution, a statistical analysis has been performed to estimate the sensitivity of the ATLAS experiment to detect new heavy particles in the early stage of the experiment.

Another aspect of this thesis is the implementation of a vertex reconstruction algorithm in the ATLAS software framework. Vertex reconstruction is an important tool in high energy physics. It is essential for the identification of jets originating from bottom quarks, for lifetime measurements and flavour physics. Many interesting physics proceses, for example top quark decays, contain bottom quarks in the final state, while background processes contain only up, down, strange or gluon jets. Thus, the identification of bottom jets can be used to separate signal from the background. The relatively long lifetime of b-hadrons ($\beta\gamma c\tau = \mathcal{O}(1)$ mm), produced during the hadronisation of bottom quarks, is unique and allows one to distinguish bottom jets from other jets. In this thesis a sophisticated secondary

vertex reconstruction algorithm is presented, which exploits the structure of B hadron decays inside the jets. Its application to a bottom jet identification algorithm will be discussed and compared to the algorithms available in the ATLAS software.

2 Theoretical Aspects of Top Quark Physics

The Standard Model of elementary particle physics [1–10] provides a theoretical framework to describe the fundamental particles and their interactions. Since its formulation in the 1960s and 1970s it has been tested by a large number of experiments up to energies of $\mathcal{O}(100)$ GeV and so far no significant deviations from its predictions could be observed. Nevertheless the Standard Model is not a complete theory. It includes only the description of three of the four fundamental forces in nature, the electromagnetism, the weak and the strong force. The gravitation can not be explained within the framework of the Standard Model. Another open question is the origin of the particle masses. The so-called Higgs mechanism [11] provides the particle masses in the Standard Model, but it is not experimentally confirmed yet. There are several other theoretical models trying to answer this question. One of the Standard Model particles, the top quark, often plays a special role in such theories due to its high mass. They predict the existence of new particles which couple preferably to top quarks. To discover these particles is one of the exciting prospects at the LHC.

A brief phenomenological introduction into the basic concepts of the Standard Model will be given in the first section of this chapter followed by a detailed description of top quark pair production and decay mechanisms in the Standard Model. An overview of theories beyond the Standard Model (BSM) predicting resonant top quark pair production will be given in the last section.

2.1 Basic Concepts of the Standard Model

All matter is built from quarks and leptons. The most well-known lepton is the electron. Quarks are constituents of protons and neutrons. Quarks and leptons are spin-$\frac{1}{2}$ particles, so-called fermions, and obey Fermi-Dirac statistics as well as the Pauli exclusion principle. For each kind of particle there exists a corresponding antiparticle with identical properties except for the reversal of their quantum numbers, which describes values of conserved quantities. Fermions are subdivided into three generations. Each generation is identical in their attributes except their masses. The first generation of quarks and leptons: up (u) and down (d) quarks, electron (e) and electron-neutrino (ν_e) build all known matter. The second and third generations: charm (c) and strange (s) quarks, muon (μ) and muon-neutrino (ν_μ), top (t) and bottom (b) quarks, tau (τ) and tau-neutrino (ν_τ) can only be observed in high-energy interactions since they subsequently decay into first generation particles. Charged leptons (e, μ, τ) carry one elementary charge, while the corresponding neutrinos are neutral. The quarks carry fractional electric charges, the up-type (u, c, t) quarks +2/3 and the

down-type (d, s, b) quarks -1/3 of the elementary charge. All but top quarks are bound in combinations of quarks and antiquarks, so-called hadrons, with integer charge. Hadrons built of three quarks are baryons, the quark-antiquark states are mesons. Without an additional quantum number the Pauli principle would be violated for qqq-states. Thus, quarks carry colour charge denoted as red, green and blue.

Fermions interact by four fundamental interactions: the electromagnetic force, the weak and the strong force and the gravitation. The gravitation can be neglected in high-energy physics, because its strength is about 43 orders of magnitude weaker than the strong interaction. The mediators of the interactions between fermions are gauge bosons. The gauge bosons have integer spin and obey Bose-Einstein statistics. Eight gauge bosons, so-called gluons, belong to quantum chromodynamics (QCD) that describes strong interactions. The quantum number of QCD is the already introduced colour charge. The mediators of the electromagnetic and weak interactions are photons (γ) and Z- and $W^{\pm}$-bosons. From a historical point of view, quantum electrodynamics (QED) was the first formulated gauge theory to describe electromagnetic interactions mediated by photons. Later Glashow, Weinberg and Salam [1, 4–6, 12] have succeeded to combine the description of weak and electromagnetic interactions in one gauge theory and herewith to allow a proper description of the weak interaction. The electro-weak quantum numbers are weak isospin $\vec{T}$ and hypercharge Y. The left-handed fermions have the total weak-isospin $T = 1/2$ and form weak-isospin doublets. The right-handed fermions have $T = 0$ and form singlets. The electric charge is related to the third component of the weak-isospin T_3 and the weak hypercharge by $Q = T_3 + Y/2$. The charged leptons interact electromagnetically and weakly, the neutral leptons interact only weakly. By contrast, the quarks interact via all three interactions: electromagnetic, weak and strong. All fundamental particles and some of their properties are shown in Figure 2.1.

QCD and the electro-weak theory are relativistic quantum field gauge theories, which are combined into the Standard Model. The Standard Model is a gauge theory based on the set of fields, namely three generations of fermions, one Higgs field as listed in Table 2.1 and the gauge fields of $SU(3)_C \times SU(2)_L \times U(1)_Y$ symmetry group. $SU(3)_C$ is the symmetry group of the strong interaction, $SU(2)_L$ of the weak interaction and $U(1)_Y$ of the electromagnetic interaction. The symmetry transformations can be performed both locally and globally. Each gauge symmetry is connected to the conservation of a corresponding quantum number, as stated by the Noether theorem [13]. In a gauge theory, the Lagrangian, which describes the dynamics of a physical system, is invariant under local gauge transformations. Gauge fields guarantee this invariance and the excitatitions of these fields represent the particles transmitting the forces, the gauge bosons. To obtain massive gauge bosons, the introduction of a mass term into the Lagrangian is necessary. Such a term is not invariant under local gauge transformations. A solution has been provided by Higgs [11], who introduced a new scalar field, named then Higgs field. The non-zero vacuum expectation value of the Higgs field breaks spontaneously the electro-weak symmetry. This leads to the emergence of the massive vector bosons, the W and Z bosons, and a massless photon. In the folowing, all three interactions as well as the Higgs mechanims will be explained in more details.

					colour	I	I_3	Y	Q
	$Q_L^i =$	$\begin{pmatrix} u_L \\ d_L \end{pmatrix}$	$\begin{pmatrix} c_L \\ s_L \end{pmatrix}$	$\begin{pmatrix} t_L \\ b_L \end{pmatrix}$	3	1/2	$+1/2$ $-1/2$	1/3	$+2/3$ $-1/3$
quarks	$u_R^i =$	u_R	c_R	t_R	3	0	0	4/3	$+2/3$
	$d_R^i =$	d_R	s_R	b_R	3	0	0	$-2/3$	$-1/3$
	$L_L^i =$	$\begin{pmatrix} \nu_{eL} \\ e_L \end{pmatrix}$	$\begin{pmatrix} \nu_{\mu L} \\ \mu_L \end{pmatrix}$	$\begin{pmatrix} \nu_{\tau L} \\ \tau_L \end{pmatrix}$	0	1/2	$+1/2$ $-1/2$	-1	0 -1
leptons	$e_R^i =$	e_R	μ_R	τ_R	0	0	0	-2	-1
	$\nu_R^i =$	ν_{eR}	$\nu_{\mu R}$	$\nu_{\tau R}$	0	0	0	0	0
higgs	$\phi =$	$\begin{pmatrix} \phi^+ \\ \phi^0 \end{pmatrix}$			0	1/2	$+1/2$ $-1/2$	$+1$	$+1$ 0

Table 2.1: The fields of the Standard Model and their quantum numbers. I is the total isospin and I_3 is its third component. Y is the weak hypercharge and Q is the electric charge. L and R denote left- and right-handed fermions, respectively. The left-handed states of one generation are grouped into weak-isospin doublets Q_L^i and L_L^i. The right-handed states form singlets u_R^i, d_R^i, e_R^i and ν_R^i.

Strong Interactions

The strong interactions are described by QCD [7, 8], a non-abelian gauge theory based on the gauge group $SU(3)_C$. It leads to eight massless, colour charged and thus self-interacting gauge bosons, which mediate this interaction. As already mentioned, there are three kinds of colour, denoted symbolically by red (R), green (G), and blue (B). The antiparticles are assigned to complementary colours: antired ($\bar{R}$), antigreen ($\bar{G}$) and antiblue ($\bar{B}$). Quarks carry one colour, gluons carry one colour and one different anticolour. Neither quarks nor gluons are observed as free particles. This property of the QCD dynamics is called confinement. Theoretical understanding of this phenomenon is not complete, but it explains the consistent failure of free quark searches and it can be demonstrated in lattice QCD [16]. Experimentally the number of colour charges has been shown for example by the cross section ratio measurement $R = \dfrac{\sigma(e^+e^- \to q\bar{q})}{\sigma(e^+e^- \to \mu^+\mu^-)}$ of the hadronical final states to the leptonic final states in e^+e^- annihilation.

The QCD Lagrangian describes the free propagation of quarks and gluons, the quark-gluon interaction and gluon self-interactions and can be represented by Feynman diagrams as shown in Figure 2.2. The strong coupling α_S is the fundamental parameter of QCD. In the framework of perturbative QCD predictions for observables are expressed in terms of α_S. Higher orders of perturbation theory include amongst other Feynman diagrams gluon and fermion loops. The momentum of virtual particles in such loops is not defined and it leads to ultraviolet divergences in case of large momenta. An unphysical renormalisation scale μ_R has to be chosen to remove divergences. The physical observables have to be scale-independent, therefore the scale depencence is included in the coupling constant $\alpha_S(\mu_R^2)$. When the scale μ_R is close to the scale of the momentum transfer Q in a given process, then

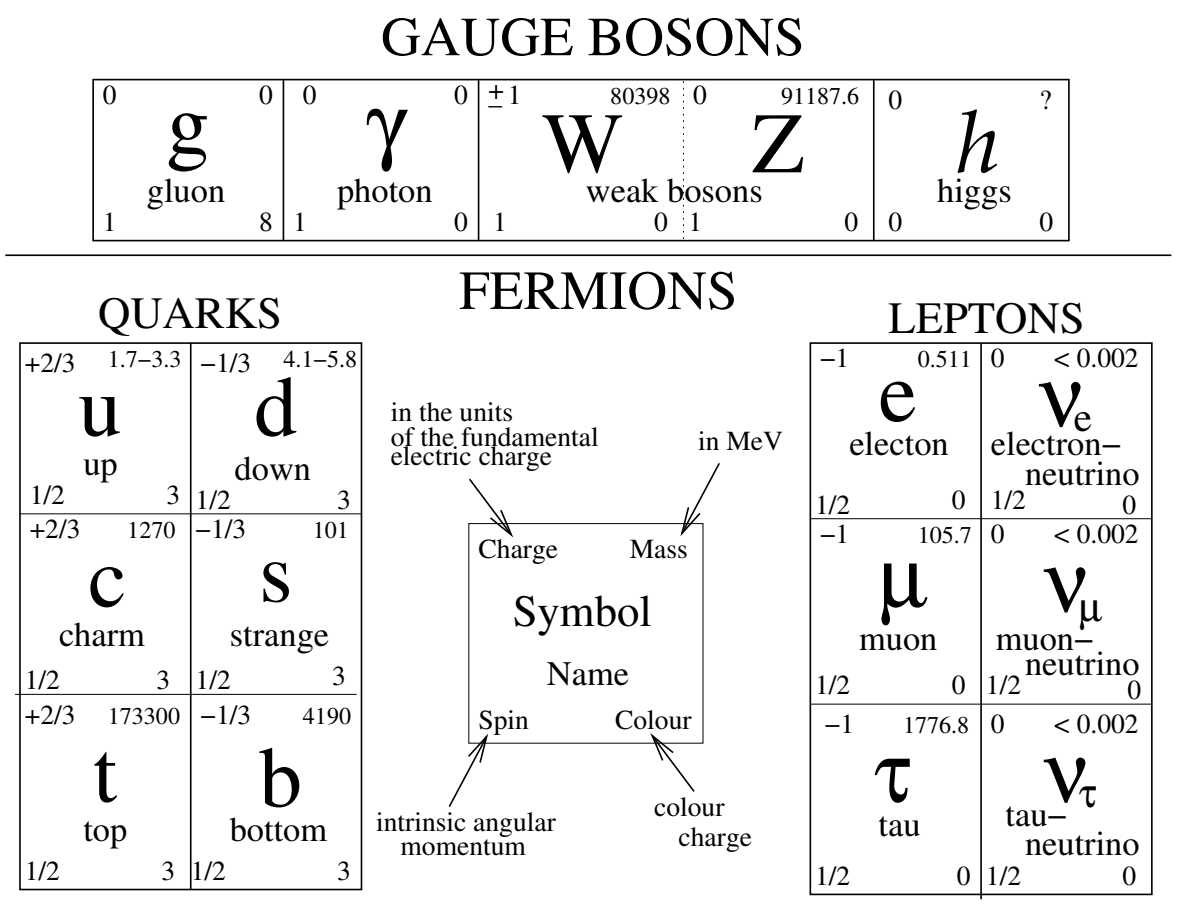

Figure 2.1: Fundamental particles of the Standard Model [14]. Top quark mass is taken from Reference [15].

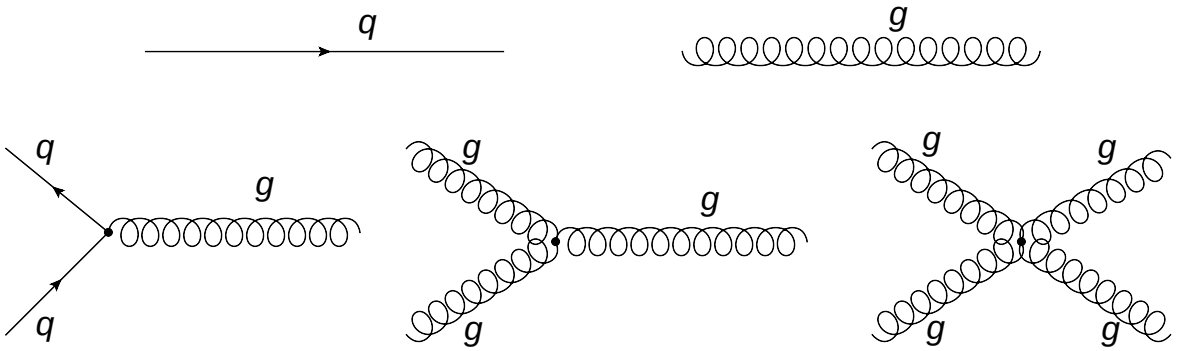

Figure 2.2: Elements of Feynman diagrams in QCD: propagators for quarks and gluons, quark-gluon vertex, three and four gluon vertex.

$\alpha_S(\mu_R^2 \approx Q^2)$ is indicative of the effective strength of the interaction in that process. The scale dependence of the renormalised coupling constant is controlled by the renormalisation group equations. In first order perturbation theory $\alpha_S(Q^2)$ has the form (corresponding

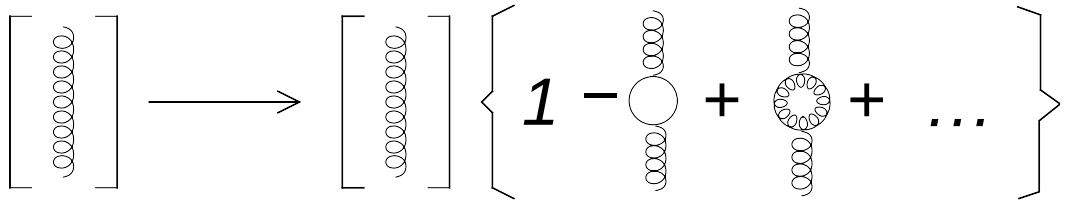

Figure 2.3: Higher order corrections to the QCD coupling α_S: gluon fluctuates into a virtual $q\bar{q}$ pair and one loop with two gluons.

Feynman diagrams are shown in Figure 2.3):

$$\alpha_S(Q^2) = \frac{12\pi}{(33 - 2n_f)\ln(Q^2/\Lambda^2)}, \tag{2.1}$$

where n_f is the number of contributing quark flavours at the considered energy and Λ is the scale at which α_S diverges, $\Lambda \sim 100 - 500$ MeV [17]. As long as the number of involved quark flavours is smaller than 16, the positive contribution of boson loops prevail the negative contribution of fermion loops and the coupling decreases with increasing energy. This leads to quasi-free quarks and gluons at high energies, the so-called asymptotic freedom. At small energy scales the strong coupling becomes large, and therefore perturbative calculations are not possible anymore. Phenomenological models are then required to describe low-energy processes, for example the process of hadronisation. The hadronisation describes the process of the formation of hadrons out of quarks and gluons. They build collimated streams of particles, called jets.

Electro-weak Interactions

QED is a abelian group theory based on the gauge group $U(1)_Y$. One massless, neutral and thus not self-interacting gauge boson, the photon γ, mediates electromagnetic interaction between electrically charged particles. The Lagrangian of the QED is postulated in the way, that applying the Euler-Lagrange equation, it results in the Dirac-equation of a free fermion. Demanding local gauge invariance, we are forced to introduce a vector field with the same properties like the photon field. Similar to the renormalisation procedure applied to the strong coupling α_S, a scale dependent electromagnetic coupling can be defined $\alpha_{QED}(Q^2)$. It describes how the effective charge depends on the separation of the two charged particles. As Q^2 increases, the photon sees more and more charge. So in contrast to the strong coupling, $\alpha_{QED}(Q^2)$ increases with increasing energy. However, the variation of α_{QED} with Q^2 is of order 10%. It increases from $1/137$ at $Q^2 = 0$ to $1/127$ at energies corresponding to the mass of the Z boson.

The weak interaction is the only interaction capable of changing lepton and quark flavours and is responsible for example for muon or charged pion decays. The observed lifetime of the muon is considerably longer than those of particles which decay either through the strong or electromagnetic interactions. The reason for it is the fact that the weak coupling is proportional to $1/{m_W}^2$ and thus several orders of magnitude smaller than the strong and electromagnetic couplings. The weak interaction distinguishes between the chirality of

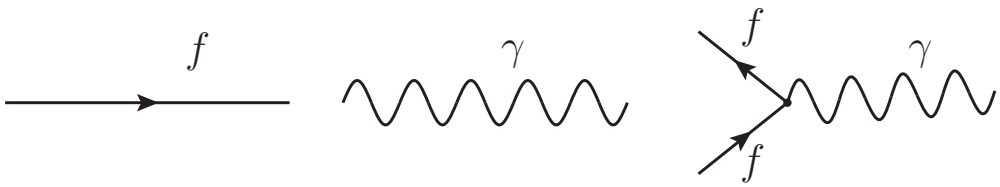

Figure 2.4: Elements of Feynman diagrams in QED: propagators for fermions and photons, fermion-photon vertex.

the particles as experimentally detected by Wu [18]. It affects only left-handed particles or right-handed antiparticles and therefore violates parity symmetry - the invariance under point reflection.

The theory of weak interaction based on $SU(2)_L$ is not a self-consistent theory. Requiring gauge invariance under the $SU(2)_L$ transformation results in two charged and one neutral gauge bosons. The latter is inconsistent with the observation, as the observed weak neutral current has a right-handed component. Only the unification of electromagnetic and weak interaction delivers a description consistent with the observation. The unified electro-weak interaction is invariant under the $SU(2)_L \times U(1)_Y$ transformation. The local gauge invariance leads to the existence of four gauge bosons: W_1, W_2, W_3 from $SU(2)_L$ and B from $U(1)_Y$. The fields of electro-weak bosons (Z^μ, $(W^\pm)^\mu$ and the photon field A^μ) are mixtures of these gauge boson fields:

$$(W^\pm)^\mu = \frac{1}{\sqrt{2}}(W_1^\mu \mp i W_2^\mu) \tag{2.2}$$

$$\begin{aligned} Z^\mu &= \frac{-g' B^\mu + g W_3^\mu}{\sqrt{g^2 + g'^2}} \\ &= -\sin\theta_W B^\mu + \cos\theta_W W_3^\mu \end{aligned} \tag{2.3}$$

$$\begin{aligned} A^\mu &= \frac{g B^\mu + g' W_3^\mu}{\sqrt{g^2 + g'^2}} \\ &= \cos\theta_W B^\mu + \sin\theta_W W_3^\mu. \end{aligned} \tag{2.4}$$

The Weinberg mixing angle θ_W and the electromagnetic coupling α_{QED} fix the gauge couplings g of $SU(2)_L$ and g' of $U(1)_Y$, namely,

$$\alpha_{\mathrm{QED}} = g \sin\theta_W = g' \cos\theta_W. \tag{2.5}$$

The unification is not completely satisfying, because we have two groups each with an independent coupling, rather than a single symmetry group.

To give the gauge bosons a mass, an additional scalar isospin doublet ϕ has to be introduced:

$$\phi = \begin{pmatrix} \phi^+ \\ \phi^0 \end{pmatrix} \quad \text{with} \quad \begin{aligned} \phi^+ &\equiv (\phi_1 + i\phi_2)/\sqrt{2}, \\ \phi^0 &\equiv (\phi_3 + i\phi_4)/\sqrt{2} \end{aligned} \tag{2.6}$$

and the field potential $V(\phi)$ of the form

$$V(\phi) = \mu^2 \phi^\dagger \phi + \lambda (\phi^\dagger \phi)^2, \tag{2.7}$$

with $\mu^2 < 0$ and $\lambda > 0$ has to be added to the Lagrangian. The potential $V(\phi)$ has its minimum at $\phi^\dagger \phi = -\frac{\mu^2}{2\lambda}$. The isospin doublet $\phi(x)$ must be expanded about a particular minimum, say

$$\phi_1 = \phi_2 = \phi_4 = 0 \quad \text{and} \quad \phi_3^2 = -\frac{\mu^2}{\lambda} \equiv v^2. \tag{2.8}$$

The effect is equivalent to the spontaneous breaking of the $SU(2)_L$ symmetry. The result is

$$\phi(x) = \sqrt{\frac{1}{2}} \begin{pmatrix} 0 \\ v + h(x) \end{pmatrix}. \tag{2.9}$$

Of the four scalar fields only one Higgs field $h(x)$ remains. The masses of the gauge bosons are acquired by their coupling to the Higgs field:

$$m_W = \frac{1}{2} v g \tag{2.10}$$

$$m_Z = \frac{1}{2} v \sqrt{g^2 + g'^2} \tag{2.11}$$

$$m_\gamma = 0. \tag{2.12}$$

The Higgs mechanism in the Standard Model predicts a neutral Higgs boson h with a zero spin and a mass of $m_h = v\sqrt{2\lambda}$. The vacuum expectation value can be calculated from the Fermi coupling constant G_F and is 246 GeV, λ is a free parameter. The Higgs boson has not been found to date. The searches at LEP set lower mass limit of $m_h > 114.4$ GeV/c^2 [19] at 95% confidence level and searches at TEVATRON exclude the Higgs masses between 162 and 166 GeV/c^2 at 95% confidence level [20]. The Feynman diagrams associated with the Higgs Lagrangian term $\mathcal{L}_{\text{Higgs}}$ are depicted in Figure 2.5.

Similar to the generation of gauge boson masses, the fermion masses can be introduced:

$$\mathcal{L}_{m_f} = -m_f f \bar{f} - \frac{m_f}{v} f \bar{f} h \quad \text{with} \quad m_f = \frac{G_f v}{\sqrt{2}}. \tag{2.13}$$

The constant G_f is not determined by the theory and the masses of the fermions have to be measured.

The electro-weak interaction changes the flavour of the fermions via charged currents. Cabbibo *et. al.* proposed, that the mass eigenstates of fermions are not identical to the weak eigenstates [21]. The transformation from one base into the other is described by a 3×3 unitary matrix, which operates on the fermion mass eigenstates, resulting in the weak eigenstates. The Cabibbo-Kobayashi-Maskawa (CKM) matrix [14,21,22] describes the mixing of the quark eigenstates:

$$V_{\text{CKM}} = \begin{pmatrix} V_{ud} & V_{us} & V_{ub} \\ V_{cd} & V_{cs} & V_{cb} \\ V_{td} & V_{ts} & V_{tb} \end{pmatrix} = \begin{pmatrix} 0.97428 & 0.2253 & 0.00347 \\ 0.2252 & 0.97345 & 0.0410 \\ 0.00862 & 0.0403 & 0.999152 \end{pmatrix}. \tag{2.14}$$

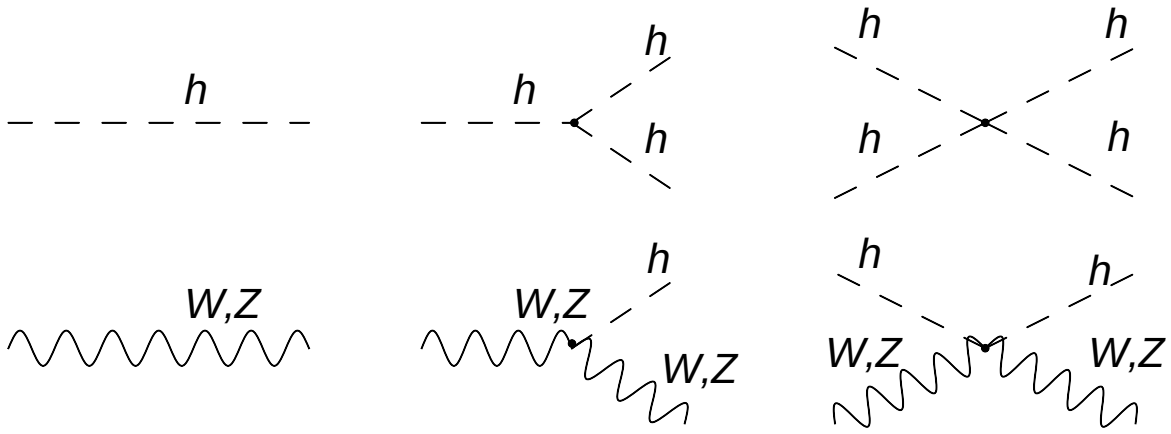

Figure 2.5: Feynman diagrams associated with the Higgs Lagrangian term $\mathcal{L}_{\text{Higgs}}$.

The probability for a quark of flavour i to be transformed to a quark of flavour j by exchange of a W boson is proportional to $|V_{ij}|^2$. The Maki-Nakagawa-Sakata (MNS) matrix [23] describes mixing in the leptonic sector. The CKM and MNS matrix elements are free parameters of the Standard Model and have to be determined by experiment.

Gravity

One of the fundamental interactions, gravity, described by the theory of general relativity cannot be incorporated in the Standard Model, because the general relativity and the quantum field theory seems to be mathematically incompatible. The quantum field theory is renormalisable and calculations give finite results, while gravity does not. This follows from the fact that the gravitational analogue of the fine structure constants of the interactions appearing in the Standard Model is dimensionful and mass dependent. The Standard Model in its present form cannot be the ultimate theory of everything. But still the effects of gravity are extremely tiny at energies accessible today at particle colliders compared to the other three interactions and therefore the gravity can be neglected.

2.2 Standard Model Top Quark Pair Production and Decay

The top quark is one of the six known quarks. Its existence as the weak-isospin partner of the bottom quark was predicted by the Standard Model. Indirect constraints on its mass have been inferred from the electro-weak precision data at LEP and other experiments. It was directly observed in 1995 by the CDF [24] and DØ [25] experiments at the FERMILAB TEVATRON collider, a $p\bar{p}$ collider at a centre-of-mass energy of $\sqrt{s}$ = 1.8 TeV in Run I and $\sqrt{s}$ = 1.96 TeV in Run II. The recent preliminary Tevatron combination of CDF and DØ results yields a top quark mass of 173.3 $\pm$ 1.1 GeV/c^2 [15]. Although the top quark decays via weak interaction, its predicted lifetime is $\tau \approx 0.5 \cdot 10^{-24}$ s. Thus the top quark decays before it can hadronise.

Top Quark Production

The dominating production mechanism for top quarks at hadron colliders is via the strong interaction in pairs [26], while the single top quark production mediated by the electroweak interaction has subleading character [27]. The underlying theoretical framework for the calculation of the production cross sections at hadron colliders is the QCD-improved parton model [28]. The colliding high-energy hadrons are considered as a composition of the quasi-free quarks and gluons, so-called partons. Each parton i carries a fraction x_i of the hadron momentum p_A. The parton distribution functions (PDFs) $f_{i/A}(x_i, \mu^2)$ describe the probability density to find a parton of a flavour i inside the hadron A carrying the momentum fraction x_i. The production cross section is calculated as a convolution of the PDFs $f_{i/A}(x_i, \mu^2)$ and $f_{j/B}(x_j, \mu^2)$ for the hadrons A and B and the parton-parton cross section $\hat{\sigma}_{ij}(ij \to t\bar{t})$:

$$\sigma(AB \to t\bar{t}) = \sum_{i,j=q,\bar{q},g} \int \mathrm{d}x_i \mathrm{d}x_j f_{i/A}(x_i, \mu^2) f_{j/B}(x_j, \mu^2) \hat{\sigma}_{ij}(ij \to t\bar{t}; \hat{s}, \mu^2), \tag{2.15}$$

where $\hat{s}$ is the square root of the centre-of-mass energy of colliding partons and μ denotes the typical energy scale of the considered interaction. The partonic $t\bar{t}$ production cross section can be calculated in perturbative QCD. The Feynman diagrams of the leading order subprocesses are depicted in Figure 2.7, contributing in α_S^2 to the perturbation series. Figure 2.6 shows exemplary the parton distribution functions for u, $\bar{u}$, d, $\bar{d}$, s quarks and gluons inside the proton in the CTEQ6.6M [29] parametrisation evaluated at $\mu = 175$ GeV. The energy of partons has to be at least large enough to produce top quark pairs at rest $\hat{s} \gtrsim 4m_t^2$. Together with the approximation $x_i \approx x_j$, this leads to a typical parton momentum value x for the $t\bar{t}$ production at the kinematic threshold $x \approx 2m_t/\sqrt{s}$, where s is the centre-of-mass energy of colliding protons. The typical value at the LHC with a centre-of-mass energy of 10 TeV is $x \approx 0.03$ and thus the dominant production mechanism at the LHC is gluon-gluon fusion with about 90% contribution. The $t\bar{t}$ production cross section at LHC is predicted to be 402^{+19}_{-26} pb at 10 TeV for $m_t = 172.5$ GeV/c^2 and CTEQ6.6 PDF parametrisation [26]. The quoted uncertainties include the uncertainty due to the choice of the scale μ and the uncertainty associated with the PDF parametrisation.

Top Quark Decay

The top quark decays via the weak interaction in a W boson and a down-type quark. The decay rates are proportional to the CKM matrix elements $|V_{tq}|^2$ with $q = d, s, b$ quarks. Under assumption of the unitarity of the three generation CKM matrix, the matrix element $|V_{tb}|$ is nearly 1, and thus the decay rate $t \to W^+ b$ is nearly 100%. The mass of the top quark is high enough to produce real W bosons and the decay width of the top quarks is large [30]:

$$\Gamma(t \to Wb) \approx 1.42\,\mathrm{GeV} \qquad \text{for} \quad m_t = 175\,\mathrm{GeV}/c^2, \tag{2.16}$$

that implies a very short lifetime of $\sim 0.5 \cdot 10^{-24}$ s. The characteristic formation time of hadrons is $\tau_{\mathrm{form}} \approx 3 \cdot 10^{-24}$ s. Therefore the top quark decays prior to hadronisation.

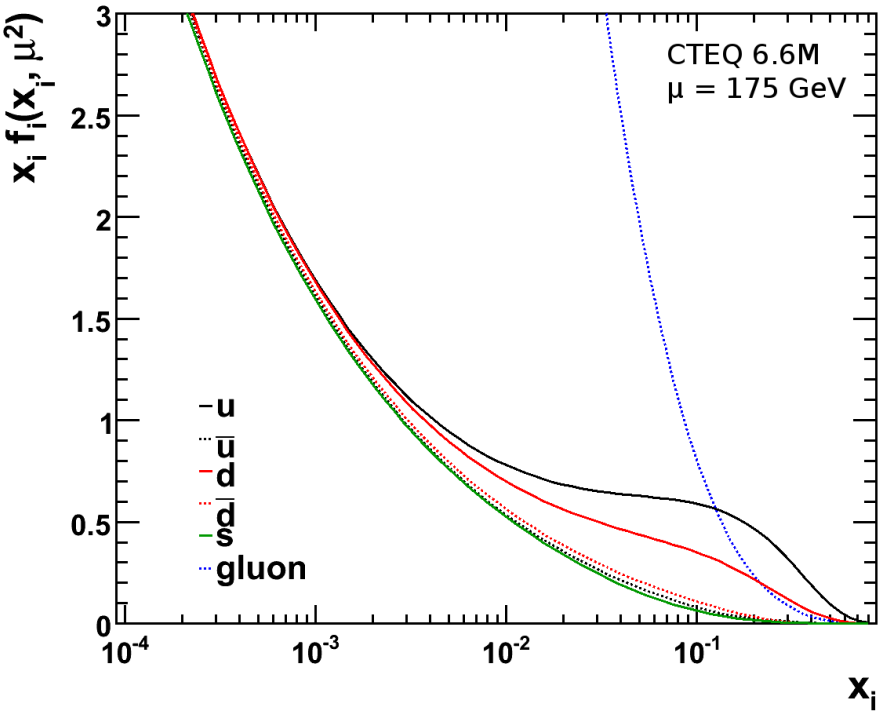

Figure 2.6: CTEQ6.6M [29] PDFs for u, $\bar{u}$, d, $\bar{d}$, s quarks and gluons evaluated at $\mu = 175$ GeV inside the proton. Parton density function $f_i(x_i, \mu^2)$ times the momentum fraction x_i is plotted versus the momentum fraction.

The typical final states for $t\bar{t}$ events are defined by the W boson decay modes: it can decay leptonically in a lepton and corresponding neutrino or hadronically in a quark-antiquark pair. The $t\bar{t}$ final states can be divided in three classes:

fully hadronic (46.2%): $t\bar{t} \to W^+bW^-\bar{b} \to q\bar{q}'bq''\bar{q}'''\bar{b}$,

semi-leptonic (43.5%): $t\bar{t} \to W^+bW^-\bar{b} \to q\bar{q}'b\ell\bar{\nu}_\ell\bar{b} + \bar{\ell}\nu_\ell bq\bar{q}'\bar{b}$,

di-leptonic (10.3%): $t\bar{t} \to W^+bW^-\bar{b} \to \ell\bar{\nu}_\ell b\ell'\bar{\nu}_{\ell'}\bar{b}$.

Disregarding phase space, the universality of the weak interaction implies that different decay channels of a W boson have the same probability. The hadronic channels $u\bar{d}$, $c\bar{s}$ are enhanced by factor three due to the three colour charges, leading to a branching ratio of $1/9$ for each of the three leptonic decay modes and branching ratios of $3/9$ for decays into a $u\bar{d}$ or $c\bar{s}$ pairs.

2.3 Top Quark Pair Production in the BSM Models

The top quark is unique among the fermions: it is the only fermion whose mass is very close to the scale of electroweak symmetry breaking (EWSB) $m_t \simeq v/\sqrt{2}$. Thus, the top quark has

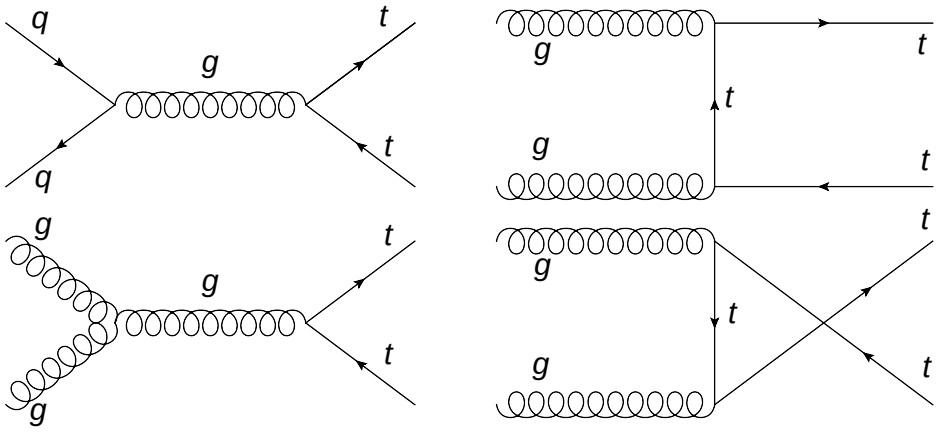

Figure 2.7: $t\bar{t}$ production channels at leading order perturbation theory.

been exploited in many scenarious of the fermion and boson mass generation beyond the Standard Model. For example it triggers the mechanism of EWSB in the supersymmetric models (SUSY) or it plays an important role in many alternative mechanisms of the mass generation. These models predict the existence of new heavy particles, which couple to the top quarks. This leads to an additional non-QCD production mechanism for the top quark pairs. In the following, an overview of the models predicting neutral s-channel resonaces will be given as well as experimantal contraints on these models. The list of the models is not complete and exemplifies only possible theories. A generic neutral colour singlet resonance will be discussed in more details.

In the Standard Model no bound states of top quark pairs are expected, since the lifetime of the top quark is shorter than the typical timescale of the strong interaction. Therefore resonant production of $t\bar{t}$ pairs is only possible through the Higgs boson decay, when the Higgs boson mass is larger than twice the top quark mass. This production mechanism is very unlikely and difficult to observe due to several reasons. Firstly, according to electro-weak precision data from LEP a light Higgs boson with mass in the range $114 \lesssim m_h \lesssim 186$ GeV/c^2 is preferred in the Standard Model [14]. Secondly the Higgs decay rate to W and Z bosons is much larger than the decay rate to the top quark pairs BR($h \rightarrow t\bar{t}$) $\approx 15\%$ and the production cross section via gluon-gluon fusion for a 400 GeV/c^2 Higgs boson at 14 TeV centre-of-mass energy is only ~ 11 pb [31,32]. Additionally the width of the scalar Higgs bosons is relatively large, about 7% of the mass, that makes its detection more difficult.

The BSM models predicting heavy $t\bar{t}$ resonances can be classified according to the spin, colour and parity of the resonance. The spin of the new particle can be 0, 1 or 2. It can be colour-neutral or coloured, scalar or pseudoscalar, vector or axialvector particle. The parameters related to each resonance are the mass, the width of the resonance and the couplings to the Standard Model particles.

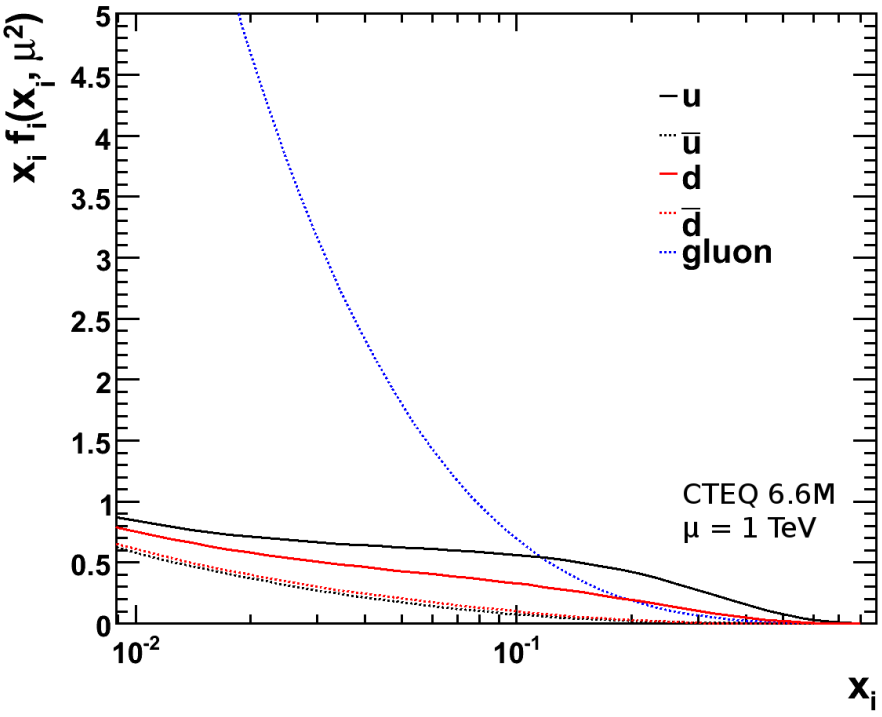

Figure 2.8: CTEQ6.6M [29] PDFs for u, $\bar{u}$, d, $\bar{d}$ quarks and gluons evaluated at μ = 1 TeV inside the proton.

Spin-0 Resonances

Several minimal supersymmetric extensions of the Standard Model (MSSM) or the two-Higgs Doublet Model (2HDM) predict heavy spin-0 scalar as well as pseudoscalar Higgs bosons, which couple primarily to top quarks [33–35]. As already explained using the example of the Standard Model Higgs boson, there is only little hope to find a spin-0 scalar resonance at the LHC, even when the coupling to the top quarks are larger than in the Standard Model. The case of a pseudoscalar or a "boson-phobic" scalar resonance is more promising and can be constructed in some SUSY models [36]. The branching ratio to the $t\bar{t}$ pairs is equal to unity and smaller resonance widths lead to a narrow resonance peak. The interference with the Standard Model $t\bar{t}$ production results in a peak-dip structure of the invariant mass spectrum.

The case of a spin-0 colour octet resonance is very similar [37, 38]. It couples only to quarks and decays mainly to the top quark pairs. The main production mechanism of the spin-0 colour singlet and octet states is through a top quark loop by gluon-gluon fusion as shown in Figure 2.9. In Figure 2.8 the parton density functions for quarks, antiquarks and gluons are compared. High momentum fractions x_i are needed to produce resonances at high masses, for example for a 1 TeV/c^2 resonance $x_i \approx 0.1$ on average is required. The gluon parton density function falls off strongly with increasing momentum fraction of partons, therefore the production cross section decrease rapidly with increasing resonance mass.

Spin-1 Resonances

Spin-1 colour singlet resonances will be produced via quark-antiquark annihilation as drawn in Figure 2.9. It can be an excitation of a Standard Model gauge boson from some extra dimensional model [39,40] or new gauge bosons which can arise in various electro-weak extensions of the Standard Model [41–44]. Additional gauge symmetries can explain the mass differences between the third family and the first two families as well as small quark CKM mixing matrix elements between the families. The family non-universal couplings generate flavour changing neutral currents, therefore these models are strongly constrained by the electro-weak precision measurements at LEP.

Technicolor models [45] provide a dynamical approach to electro-weak and flavour symmetry breaking. The new interactions are asymptotically free at very high energies and become strong and confining at lower energies. The masses of fermions and bosons are generated through dynamics of new interactions similar to the mass generation in QCD. Each Standard Model particle gets its corresponding techniparticle. Massive colour octet gauge bosons, colorons, mediate the interaction between fermions and technifermions and generate the fermion masses.

The Topcolor model [46] explains the large top quark mass through the formation of a dynamical $t\bar{t}$ condensate, generated by a new strong force, which couples preferentially to the third generation. The mediator of the new strong force is a neutral gauge boson, Z', with an attractive interaction between $t\bar{t}$ and a repulsive interaction between $b\bar{b}$ to block the formation of a $b\bar{b}$ condensate. Combination of these two theoretical models, the so-called "topcolor assisted technicolor" model [47] provides a dynamical mechanism for electro-weak symmetry breaking and explains the large top quark mass.

The Z' boson decaying into top quark pairs produces a simple narrow peak in the invariant mass spectrum. The width and the height of the peak depends on the strength of the couplings to the fermions. For massive colorons a coupling strength equal to the strong coupling α_S can be assumed for their coupling to quarks. Therefore the resonance peak will be more pronounced than for a colour singlet Z' boson.

Spin-2 Resonances

The interactions between gravitons and Standard Model particles are suppressed at TeV energies, but there are some models with extra dimensions where the contributions from gravitons could be visible at the LHC. The Randall-Sundrum model [48,49] postulates one extra dimension that is compactified to a orbifold. Two branes exist on the orbifold, a "Plank" brane and a "TeV" brane where the Standard Model fields are confined. It predicts a limited number of Kaluza Klein modes but the couplings are enhanced by a large "warp" factor. The $t\bar{t}$ invariant mass spectrum is disturbed by a series of narrow width peaks.

A few benchmark models and corresponding parameters are listed in Table 2.2.

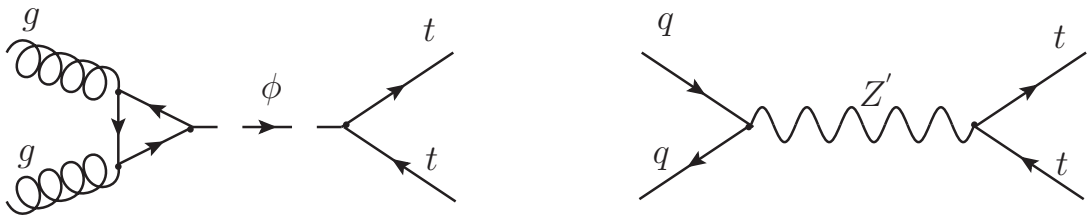

Figure 2.9: Feynman diagrams for resonant $t\bar{t}$ production: spin-0 colour singlet or octet particle ϕ and spin-1 Z' boson resonance.

resonance	spin	colour	mass, GeV/c^2	$\sigma_X \times \mathrm{BR}(X \to t\bar{t})$, pb	Γ/m_X
SM Higgs	0	0	400	1.65	7%
sequential Z'	1	0	1000	1.6	2.7%
topcolor Z'	1	0	1000	6.6	3.3%
graviton (k/M_{Pl} = 0.1)	2	0	1000	2.0	1.4%
KK gluon	1	8	1000	27.8	15.3%

Table 2.2: Overview of some $t\bar{t}$ resonance benchmark models.

Experimental Constraints

New heavy particles in the BSM theories are indirectly constrained by electro-weak data from LEP and directly by the searches at the TEVATRON. None of the searches at LEP or the TEVATRON have led to an observation of a significant deviation from the Standard Model expectation. The results have been used to contrain the models. Di-lepton searches exclude sequential Z' boson with masses lower 1 TeV/c^2 at 95% confidence level [50–52]. Di-jet searches lead to severe constraints on Z' bosons, but constrain models involving coloured objects like excited quarks, axigluons, colorons stronger. The upper mass limit varies from 600 GeV/c^2 to 1250 GeV/c^2 depending on the model [53]. The $t\bar{t}$ searches have been primarily used to constrain models, where the top quark acquires a special role. TEVATRON's lower mass limit is around 820 GeV/c^2 at 95% confidence level for a leptophobic Z' boson in the Topcolor model [54,55]. Limits on couplings to fermions have been obtained for models predicting Kaluza-Klein gluons, which do not couple to leptons and quarks of the third family are favoured over light quarks [56–58].

Neutral Spin-1 Colour Singlet Z' Boson

Additional $U(1)'$ gauge symmetries lead to the existence of the neutral spin-1 colour singlet Z' gauge bosons. The interaction of the Z' boson to the Standard Model fermions f can be written as [59]:

$$\mathcal{L} = \frac{g}{4\cos\theta_W}\bar{f}\gamma^\mu(C_V - C_A\gamma^5)fZ'_\mu, \tag{2.17}$$

where $g = 0.626$ is the $SU(2)_L$ gauge coupling, θ_W is the Weinberg angle and γ^μ, γ^5 are the chiral operators. The axial C_A and vector C_V couplings to fermions can be expressed as:

$$C_A = 2\cos\theta_W(z_{f_L} - z_{f_R})g_{Z'}/g, \tag{2.18}$$

$$C_V = 2\cos\theta_W(z_{f_L} + z_{f_R})g_{Z'}/g, \tag{2.19}$$

with the $U(1)_{Z'}$ gauge coupling $g_{Z'}$ and the left and right handed fermion charges z_{f_L} and z_{f_R}. The couplings to fermions are free parameters and can be set for example the same as the Standard Model Z boson couplings. This so-called "sequential" Standard Model (SSM) is not gauge invariant, but is often used for purpose of comparison and is representative for a large range of models. The narrow width Z' boson exclusion limits from pp and $p\bar{p}$ collisions show only a weak model dependence [60]. The Z' boson production cross section depends on the fourth power of the model dependent couplings to fermions, but the properties of the parton density functions leads only to an effective logarithmic dependence on the couplings as investigated in [61]. Thus, the SSM serves as a useful reference case.

At pp colliders only a direct production of Z' boson via Drell-Yan process is allowed. The Drell-Yan production cross section is proportional to:

$$\sigma(q\bar{q} \to Z' \to f\bar{f}) \propto \frac{\hat{s}}{(\hat{s} - m_{Z'}^2)^2 + \hat{s}\Gamma_{Z'}^2}, \tag{2.20}$$

where $\sqrt{\hat{s}}$ is the partonic centre-of-mass energy of the process. In the limit of infinite centre-of-mass energy the Drell-Yan production is preferred and the differential cross section $\frac{\mathrm{d}\sigma_{Z'}}{\mathrm{d}m_{Z'}}$ peaks at the Z' boson mass with the width of $\Gamma_{Z'}$. In the limit of infinite Z' boson mass the shape will correspond to the $f\bar{f}$ continuum shape with the highest cross section at the $f\bar{f}$ mass threshold. At finite $m_{Z'}$ and centre-of-mass energy, at the LHC $\langle\sqrt{\hat{s}}\rangle \sim 600$ GeV, we have a mixture of both cases [62]. Figure 2.10 demonstrates how the tails to lower masses become more pronounced with increasing $m_{Z'}$.

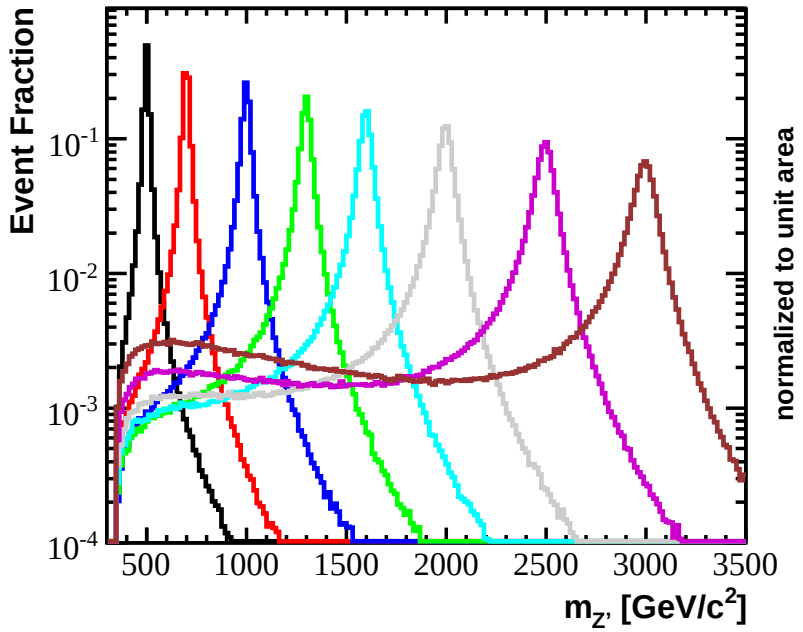

Figure 2.10: Z' boson mass distributions for $Z' \to t\bar{t}$ in the mass range 500-3000 GeV/c^2.

3 LHC and ATLAS Detector

The Large Hadron Collider (LHC) is a two-ring-superconducting hadron collider installed in a 26.7 km tunnel, that has been constructed between 1984 and 1989 for the Large Electron Positron machine, LEP. It is designed to collide proton beams with a centre-of-mass energy of 14 TeV and a peak luminosity of 10^{34} cm^{-2}s^{-1} as well as lead ions with an energy of 2.8 TeV per nucleon and a peak luminosity of 10^{27} cm^{-2}s^{-1}. There are five main experiments acquiring LHC collision data. ATLAS [63] and CMS [64] are two general purpose experiments aiming at the highest luminosity for proton operation. The low luminosity experiments are LHCb [65] for B-physics and TOTEM [66] for the detection of protons from elastic scattering at small angles. ALICE [67] is a dedicated ion experiment for the lead-lead ion operation. A brief summary of the accelerator and collider complex as well as of the ATLAS detectors will be provided in this chapter. More detailed information can be found in the overviews about the LHC machine [68] and the ATLAS experiment [63].

3.1 The Large Hadron Collider

The injector chain Linac2 – Proton Synchrotron Booster (PSB) – Proton Synchrotron (PS) – Super Proton Synchrotron (SPS) supply the LHC rings with protons as illustrated in Figure 3.1. The linear accelerator Linac2 with a length of 30 m (first run in 1978) provides pulsed 1 Hz beams of up to 175 mA at 50 MeV, with pulse lengths varying between 20 and 150 μs depending on the required number of protons. The beams are injected into the PSB, the first and smallest circular proton accelerator. It was built in 1972 and contains four superimposed rings with a radius of 25 meters. The protons are accelerated up to 1.4 GeV and are fed to the PS, a circular accelerator with a circumference of 628.3 m. It was built in the late 1950s and has been upgraded several times to improve the performance. The PS accelerates the beams to 26 GeV and can produce bunch trains with the LHC bunch spacing of 25 ns, which are then sent to SPS. It is a 6.9 km long circular accelerator and took its operation in 1976. It accelerates protons up to 450 GeV and injects protons in the LHC in a clockwise and anticlockwise direction. Finally the protons are accelerated in the LHC rings to the nominal energy.

The LHC tunnel was designed for the electron-positron machine LEP. It has eight straight sections and eight arcs and lies between 45 m and 170 m below the surface on a plane inclined at 1.4% sloping towards the Léman lake. The long straight sections were nessesary for the LEP to reduce energy lost though the synchroton radiation. The LHC machine does not have the same synchrotron radiation problem like LEP, because protons are 10^4 times heavier than electrons and the synchrotron radiation is proportional to $1/m^4$ of the particle mass m. Longer arcs and shorter straight sections would be ideal, but accepting the tunnel "as built" was the cost-effective solution.

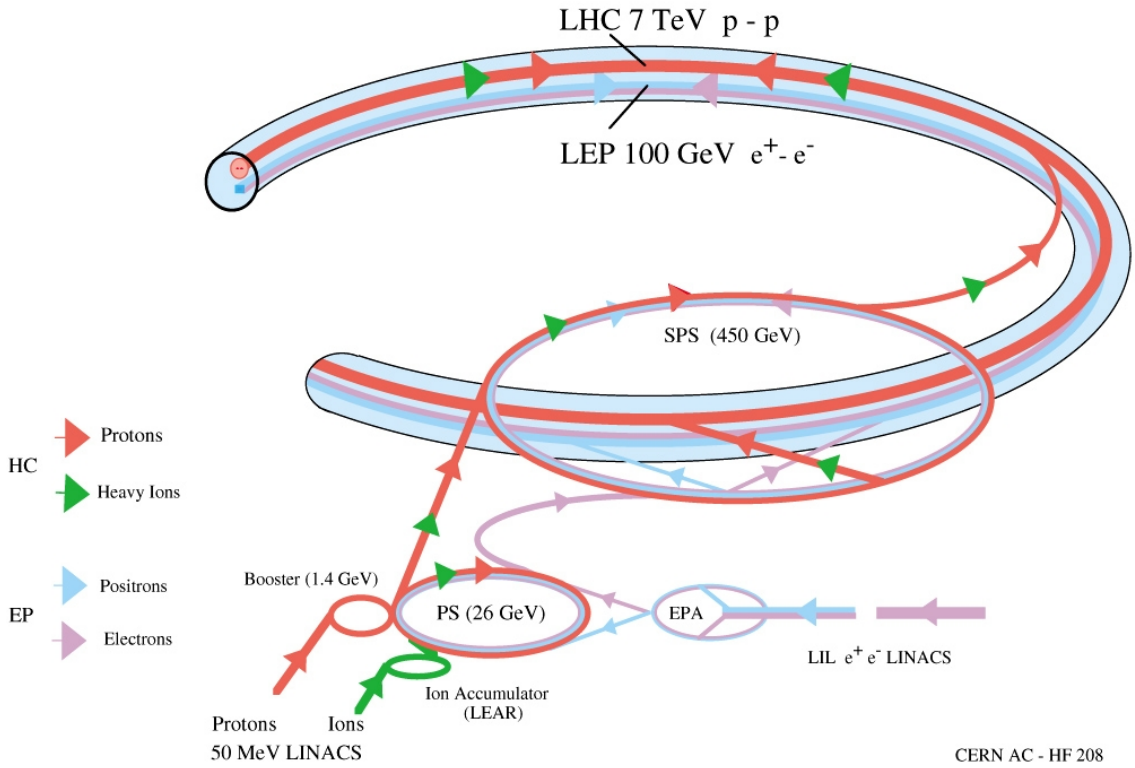

Figure 3.1: The LHC injector complex [69].

The tunnel in the arcs has a diameter of 3.7 m, therefore only one proton ring could be installed. But for a particle-particle accelerator opposite magnetic dipole fields are required. The twin-bore magnet design has been adopted to solve the space and the cost problem. The main arcs have separate magnet fields and vacuum chambers, the common sections are only at the insertion regions where the experiments are located. The nominal magnetic field is 8.33 T, corresponding to an energy of 7 TeV. The LHC superconducting magnet system uses the well-proven technology based on NbTi Rutherford cables and cools the magnets to a temperature below 2 K with superfluid helium.

The machine luminosity depends on the beam parameters and can be written as:

$$L = \frac{N_b^2 n_b f_{rel} \gamma_r}{4\pi\varepsilon_n \beta^*} F, \tag{3.1}$$

where N_b is the number of particles per bunch, n_b the number of bunches per beam, f_{rel} the revolution frequency, γ_r the relativistic gamma factor, ε_n the normalised transverse beam emittance, β^* beta function and F the geometric luminosity reduction factor due to the crossing angle at the interaction point. The number of protons per bunch is limited to $1.15 \cdot 10^{11}$ by the non-linear beam-beam interactions and the mechanical aperture of the LHC. A maximum acceptable transverse beam emittance is $\varepsilon_n = 3.75$ μm. The nominal number of bunches is 2808 per ring. The gaps between the bunches are 7 m long corresponding to the bunch spacing of 25 ns and collision frequency of 40 MHz. The mechanical aperture of the triplet magnets limits the minimum attainable β^* value and the maximum

detector component	required resolution	η coverage measurement	η coverage trigger
tracking	$\sigma_{p_T}/p_T = 0.05\%\ p_T \oplus 1\%$	$\pm$ 2.5	–
electromagnetic calorimetry	$\sigma_E/E = 10\%\ /\ \sqrt{E} \oplus 0.7\%$	$\pm$ 3.2	$\pm$ 2.5
hadronic calorimetry barrel and end-cap forward	 $\sigma_E/E = 50\%\ /\ \sqrt{E} \oplus 3\%$ $\sigma_E/E = 100\%\ /\ \sqrt{E} \oplus 10\%$	 $\pm$ 3.2 $3.1 < \lvert\eta\rvert < 4.9$	 $\pm$ 3.2 $3.1 < \lvert\eta\rvert < 4.9$
muon spectrometer	$\sigma_{p_T}/p_T = 10\%$ at $p_T = 1$ TeV/c	$\pm$ 2.7	$\pm$ 2.4

Table 3.1: General performance goals of the ATLAS detector [63].

attainable crossing angle at the interaction point. The nominal crossing angle is of the order of 150-200 μrad to avoid unwanted collisions near the interaction point. The limit of beta function β^* is 0.55 m for the high-luminosity proton-proton collisions at ATLAS and CMS. The resulting nominal peak luminosity is 10^{34} cm^{-2}s^{-1}.

3.2 The Atlas Detector

ATLAS (A Toroidal LHC ApparatuS) is one of two general purpose experiments at the LHC. The high luminosity provided by the LHC and high cross sections due to the high energy enable further precision tests of the Standard Model as well as searches for physics beyond the Standard Model. Several benchmark searches have been used to establish the performance of the ATLAS detector. The search for the Standard Model Higgs boson is particularly important, since a broad range of production and decay mechanisms is covered by ATLAS. Many theories beyond Standard Model predict new particles with masses in TeV-range and small production cross sections. These rare processes have to be distinguished from the dominating inelastic proton-proton interactions and QCD jet production.

The basis criteria when constructing the detector were a very good electromagnetic calorimetry for electron and photon identification, full-coverage hadronic calorimetry for jet and missing energy measurements, high-precision muon momentum measurements and efficient tracking at high luminosity. The layout of the ATLAS detector is depicted in Figure 3.2 and its main performance goals are listed in Table 3.1. The following coordinate system and nomenclature is used: the interaction point is defined as the origin of the coordinate system. For a righthanded system the beam direction defines the z-axis, the positive x-axis points from the interaction point to the centre of the LHC ring and the positive y-axis points upwards. The azimuthal angle, ϕ, is measured around the beam axis and the polar angle, θ, is the angle with respect to the beam axis. Instead of θ the pseudorapidity η is widely used, defined as $\eta = -\ln\tan(\frac{\theta}{2})$. The transverse momentum p_T, the transverse energy E_T and the missing transverse energy E_T^{miss} are defined in the x-y plane. The distance ΔR in the pseudorapidity-azimuthal angle space is defined as $\Delta R = \sqrt{\Delta\phi^2 + \Delta\eta^2}$.

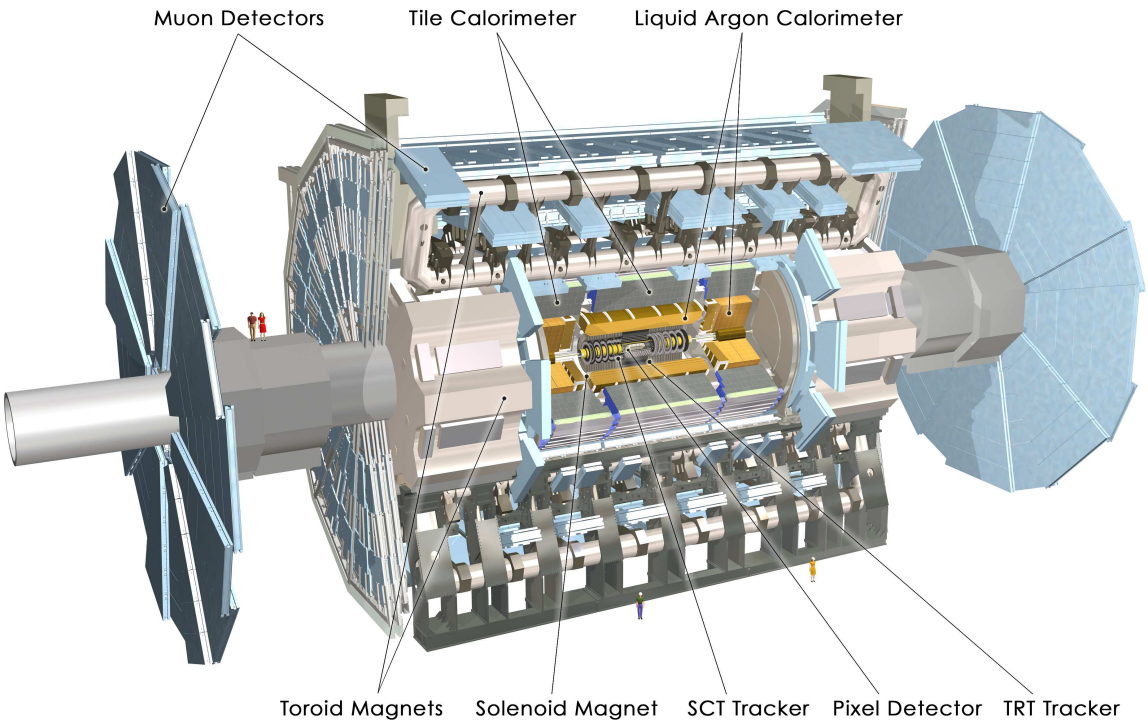

Figure 3.2: View of the ATLAS detector [70]. It measures 44m in length, has a diameter of 25m and weighs about 7000 tons.

The detector is built forward-backward symmetric around the interaction point. The innermost part is a tracking detector. Measurements in the high-resolution semiconductor pixel and strips detectors are combined with the measurements in the straw-tube tracking detector, that allow one to distinguish particle types by the transition radiation. The tracking detector is immersed in a 2 T solenoidal magnetic field. The high granularity liquid-argon (LAr) electromagnetic sampling calorimeters cover the pseudorapidity range $|\eta| < 3.2$. The hadronic calorimeter in the range $|\eta| < 1.7$ is a scintillator-tile calorimeter, in the end-caps $1.5 < |\eta| < 3.2$ the LAr technology has been used. The LAr forward electromagnetic and hadronic calorimeters extend the pseudorapidity coverage to $|\eta| = 4.9$. The calorimeter is surrounded by the muon spectrometer consisting of three layers of high precision tracking chambers. One barrel and two end-caps of the large superconducting air-core toroid generate the magnetic field in the spectrometer.

A short summary of most important properties of the ATLAS detector components will be presented in the following sections.

Inner Detector

The inner detector is designed to measure tracks of charged particles above a given transverse momentum threshold (100 MeV/c in the initial measurements of minimum bias events and 500 GeV/c at high luminosities because of the increasing track multiplicity) and within

the pseudorapidity range of $|\eta| < 2.5$. Precise measurements in the innermost pixel layer is one of the important requirements for a good b-jet identification and allows one to reconstruct secondary vertices a few millimetre distant from the interaction point. The detector is contained within a cylindrical envelope of 3512 mm length and 1150 mm radius and is composed of three sub-elements. Figure 3.3 shows drawings of the sensors and structures of the inner detector as well as the exact positions of the elements.

At innermost radii the pixel detector is placed containing three silicon pixel layers in the barrel region and three silicon pixel discs in each of the end-caps. The layers are composed of 112 staves and the discs of 48 sectors, assembled on the supporting carbon-fibre structure. All staves and sectors are identical in the construction. 13 modules are mounted on each stave and 6 modules on each sector. The barrel modules are located in the way to have no gaps in the detector, this requires an overlap of the modules in z and ϕ. The disk modules are mounted on both sides of the disk, which are slightly twisted to achieve the complete coverage.

The barrel and disk modules are identical. The main components of a pixel module are a silicon sensor, 16 electronic readout chips (FEs) 18x160 pixels each, a module controller chip (MCC), and the interconnection foil (flex) as shown in Figure 3.4. The sensitive silicon detector area is connected via bump bonds with the front-end chips. The nominal pixel size is 50×400 μm^2 (about 90% of pixels) and is defined by the read-out pitch of the front-end chips. The size of the remaining pixels is 50×600 μm^2 in the regions between two front-end chips on a module to avoid dead space. The barrel pixels are assembled in the way that 400 (600) μm are positioned along the z-axis and the disk pixels have 400 (600) μm in r, defined as $\sqrt{x^2+y^2}$. The detector typically provides three space points per track with a resolution of about 10 μm in $r\phi$ and about 115 μm in z (or r in end-caps).

The pixel detector is surrounded by the SemiConductor Tracker (SCT), which consists of four concentric barrel layers in the radial range between 299 and 514 mm and nine disks in the forward and backward region in the longitudinal range between 853.8 and 2720.2 mm. The SCT detector consists of 4088 modules, 2112 modules are installed in the barrel and 1976 modules in the end-caps. The modules use 80 μm pitch micro-strip sensors, two each on the top and bottom side rotated by $\pm$ 20 mrad around the geometrical centre of the sensors. The active length of the barrel modules is 126.09 mm. In the inner end-caps the active length is 59.1 mm, in the middle 115.61 mm (in the short-middle end-caps 52.48 mm) and in the outer end-caps 119.14 mm, see Figure 3.4. The dead space between sensors is 2.09 mm. The SCT provides a space point resolution of about 17 μm in $r\phi$ and about 580 μm in z (or r in the end-caps).

The Transition Radiation Tracker (TRT) combines the concept of a straw tracker with the transition radiation detection for the particle identification. It consists of 52 544 straws of 144 cm in length in the barrel region and 319 488 straws of 37 cm in length arranged in wheels in both end-cap regions. Figure 3.5 presents the TRT barrel and end-caps structures and modules. The straws have a diameter of 4 mm. The barrel consists of three cylindrical rings, each containing 32 modules. Each module contains axially positioned straws. The end-caps consist of three wheels with radial positioned straws. All straws are embedded in stacks of polypropylene/polyethylene fibres, which produce transition-radiation X-rays used for the particle identification. The straw anodes are 31 μm in diameter gold-plated

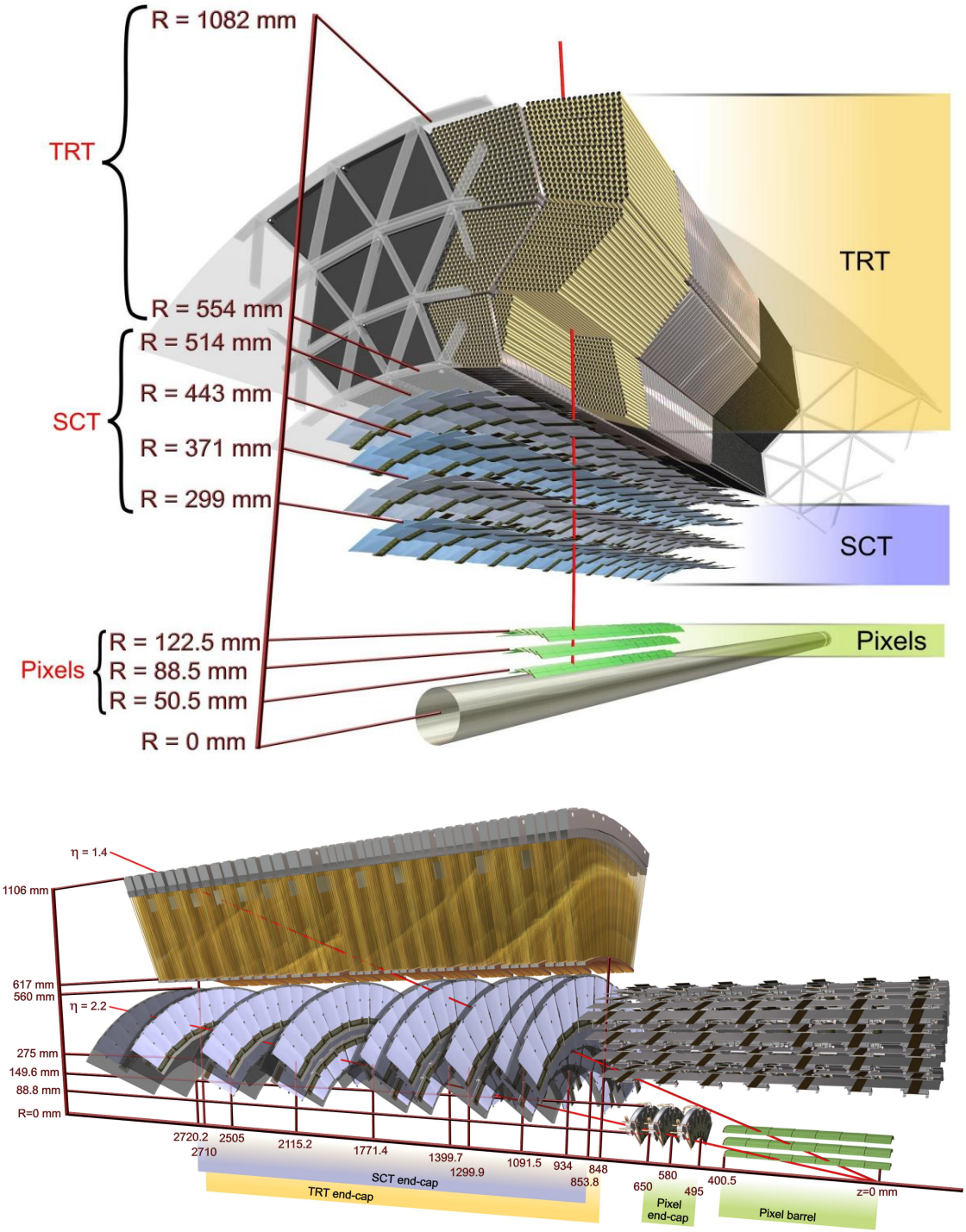

Figure 3.3: Sensors and structural elements of the ATLAS inner detector [70]. Drawing on top shows a charged track traversing in the barrel at $\eta = 0.3$. Drawing at the bottom shows two charged tracks traverse in the end-caps at $\eta = 1.4$ and 2.2.

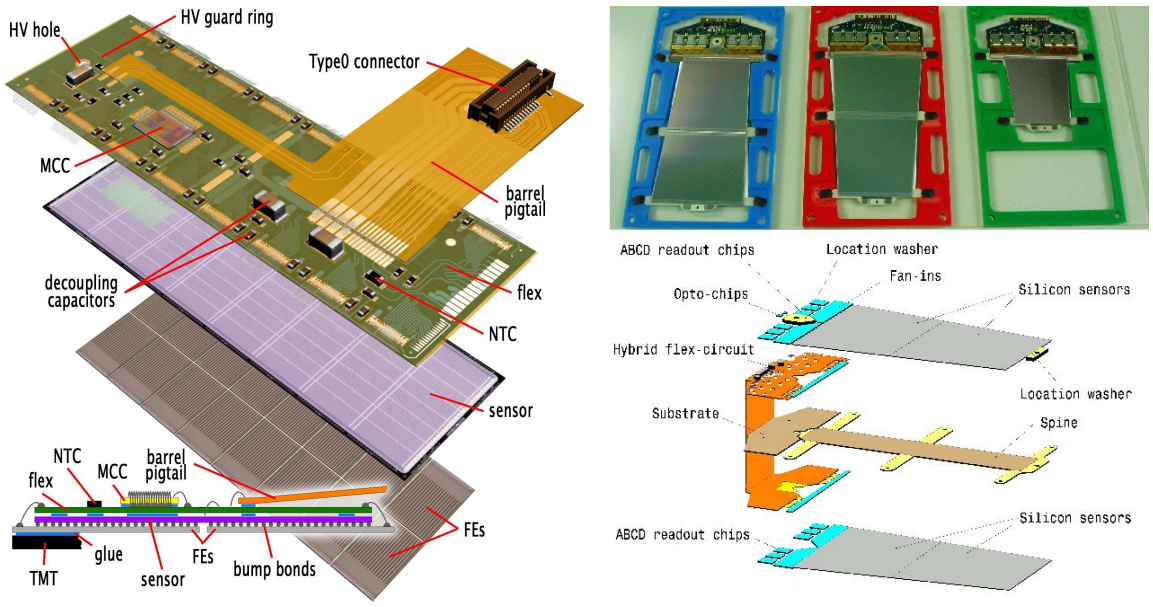

(a) pixel barrel module (b) SCT end-cap modules

Figure 3.4: (a) Schematic view of a barrel pixel module and the SCT end-cap modules. (b) The upper photograph on the right shows the outer, middle and inner modules (from left to right). The lower schematic shows the components of the middle module [63].

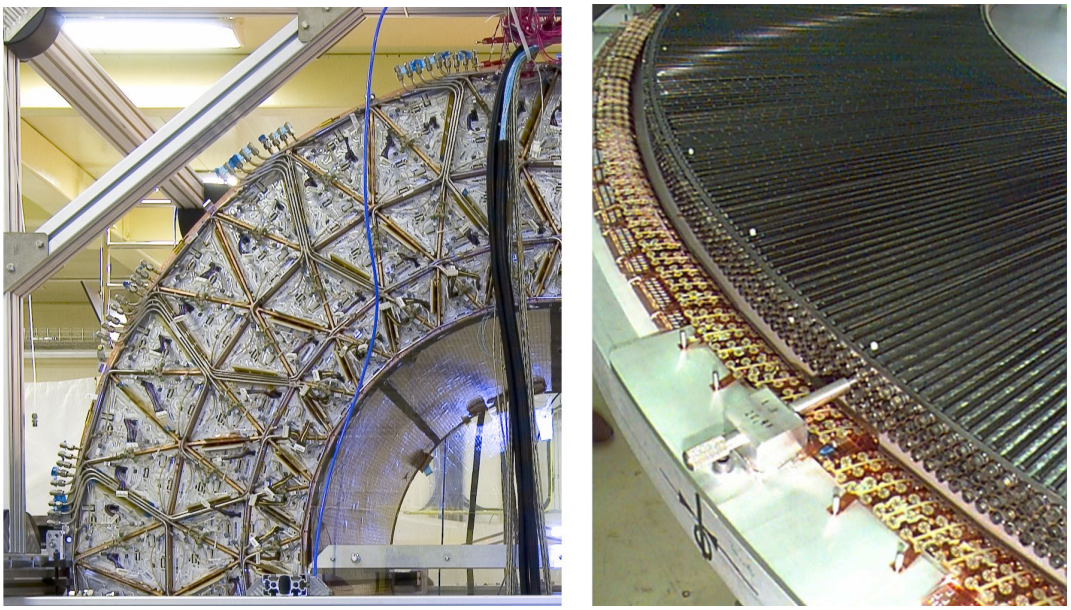

Figure 3.5: (a) Photograph of one quarter of the barrel TRT. (b) The triangular design of the support structure and the shapes of the inner, middle and outer TRT modules can be seen. Photograph of a TRT end-cap wheel (right) with 4 planes of straws [63].

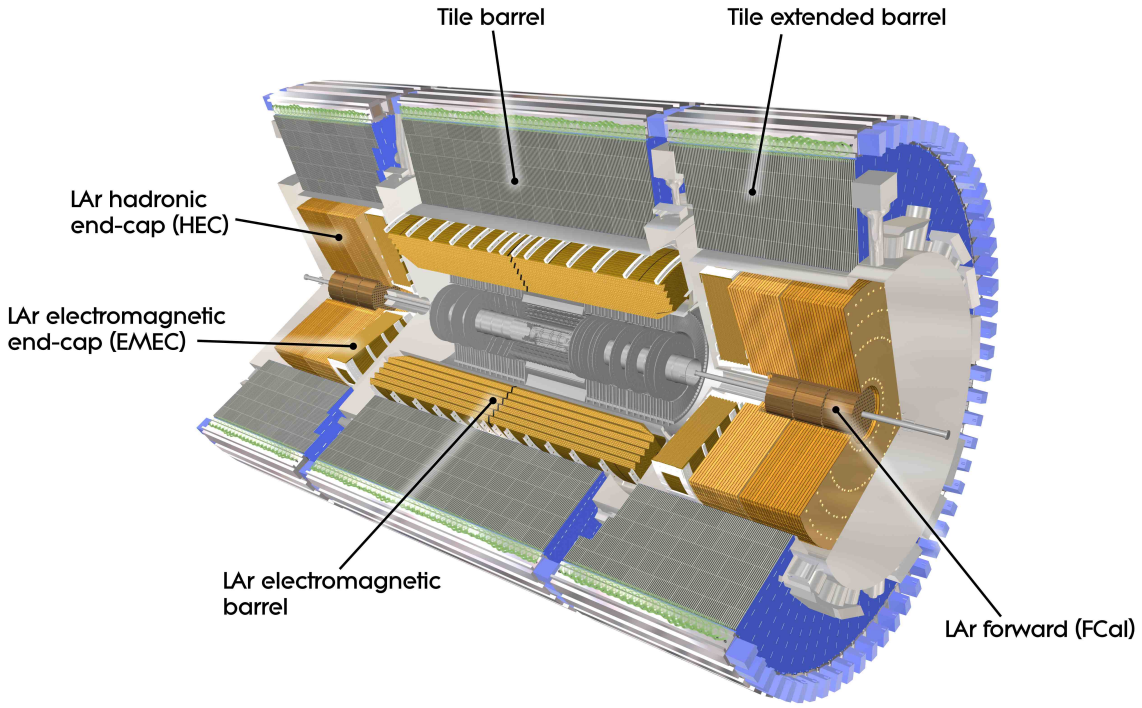

Figure 3.6: Cut-away view of the calorimeter system [70].

tungsten wires. The ionisation gas is a xenon-base gas mixture (70% Xe, 23% CO_2 and 3% O_2). All charged tracks with $p_T > 500$ MeV/c and $|\eta| < 2$ will traverse at least 36 straws, except in the barrel-end-caps transition region ($0.8 < |\eta| < 1.0$), where only 22 measurements are possible. Typically seven to ten high threshold hits from transition radiation are expected for electrons above 2 GeV/c. The intrinsic straw $r\phi$ resolution is 130 μm, implying that each wire position is constrained within $\pm$ 50 μm.

The high-radiation environment imposes stringent conditions on the inner-detector sensors, on-detector electronics, mechanical structure and services. To maintain an adequate noise performance after radiation damage, the silicon sensors must be kept at low temperature of approximately -15 °C. The TRT can be operated at room temperature.

Calorimeters

The ATLAS calorimeters consist of a number of sampling detectors with full ϕ-symmetry and coverage in η. The signal readout is separated from the particle absorption. The schematic view of the components is shown in Figure 3.6 and its main parameters are listed in Table 3.2. The calorimeters closest to the beampipe are housed in cryostats. The barrel cryostat contains the electromagnetic calorimeter. The end-cap cryostats contain electromagnetic (EMEC) and hadronic (HEC) end-cap calorimeters and a forward hadronic calorime-

	barrel		end-cap	
electromagnetic calorimeter granularity $\Delta\phi \times \Delta\eta$ versus η				
presampler	0.025×0.1	$\lvert\eta\rvert < 1.52$	0.025×0.1	$1.5 < \lvert\eta\rvert < 1.8$
calorimeter 1st layer	$0.025/8 \times 0.1$	$\lvert\eta\rvert < 1.40$	0.050×0.1	$1.375 < \lvert\eta\rvert < 1.425$
	0.025×0.025	$1.40 < \lvert\eta\rvert < 1.475$	0.025×0.1	$1.425 < \lvert\eta\rvert < 1.5$
			$0.025/8 \times 0.1$	$1.5 < \lvert\eta\rvert < 1.8$
			$0.025/6 \times 0.1$	$1.8 < \lvert\eta\rvert < 2.0$
			$0.025/4 \times 0.1$	$2.0 < \lvert\eta\rvert < 2.4$
			0.025×0.1	$2.4 < \lvert\eta\rvert < 2.5$
			0.1×0.1	$2.5 < \lvert\eta\rvert < 3.2$
calorimeter 2nd layer	0.025×0.025	$\lvert\eta\rvert < 1.40$	0.050×0.025	$1.375 < \lvert\eta\rvert < 1.425$
	0.075×0.025	$1.40 < \lvert\eta\rvert < 1.475$	0.025×0.025	$1.425 < \lvert\eta\rvert < 2.5$
			0.1×0.1	$2.5 < \lvert\eta\rvert < 3.2$
calorimeter 3rd layer	0.050×0.025	$\lvert\eta\rvert < 1.35$	0.050×0.025	$1.5 < \lvert\eta\rvert < 2.5$
Number of readout channels				
presampler	7808		1536 (both sides)	
calorimeter	101760		62208 (both sides)	
LAr hadronic end-cap calorimeter granularity $\Delta\phi \times \Delta\eta$ versus η				
			0.1×0.1	$1.5 < \lvert\eta\rvert < 2.5$
			0.2×0.2	$2.5 < \lvert\eta\rvert < 3.2$
LAr hadronic forward calorimeter granularity $\Delta x \times \Delta y$ (cm) versus η				
			FCal1: 3.0×2.6	$3.15 < \lvert\eta\rvert < 4.30$
			FCal1:	$3.10 < \lvert\eta\rvert < 3.15$
			$\sim$ four times finer	$4.30 < \lvert\eta\rvert < 4.83$
			FCal2: 3.3×4.2	$3.24 < \lvert\eta\rvert < 4.50$
			FCal2:	$3.20 < \lvert\eta\rvert < 3.24$
			$\sim$four times finer	$4.50 < \lvert\eta\rvert < 4.81$
			FCal3: 5.4×4.7	$3.32 < \lvert\eta\rvert < 4.60$
			FCal3:	$3.29 < \lvert\eta\rvert < 3.32$
			$\sim$ four times finer	$4.60 < \lvert\eta\rvert < 4.75$
Scintillator tile calorimeter granularity $\Delta\phi \times \Delta\eta$				
1st, 2nd layer	0.1×0.1		0.1×0.1 (extended barrel)	
3rd layer	0.2×0.1		0.2×0.1 (extended barrel)	
Number of readout channels				
LAr end-cap			5632 (both sides)	
LAr forward			3524 (both sides)	
scintillator tile	5760		4092 (both sides, extended barrel)	

Table 3.2: Granularity and number of readout channels of the ATLAS calorimeters [63].

ter (FCal). Liquid argon has been chosen as the sampling medium for these calorimeters because of its intrinsic linear behaviour, its stability of response over time and its intrinsic radiation-hardness. Lead is used as absorber for the electromagnetic calorimeter, copper for the hadronic end-cap calorimeters and copper-tungsten for the forward calorimeter. The

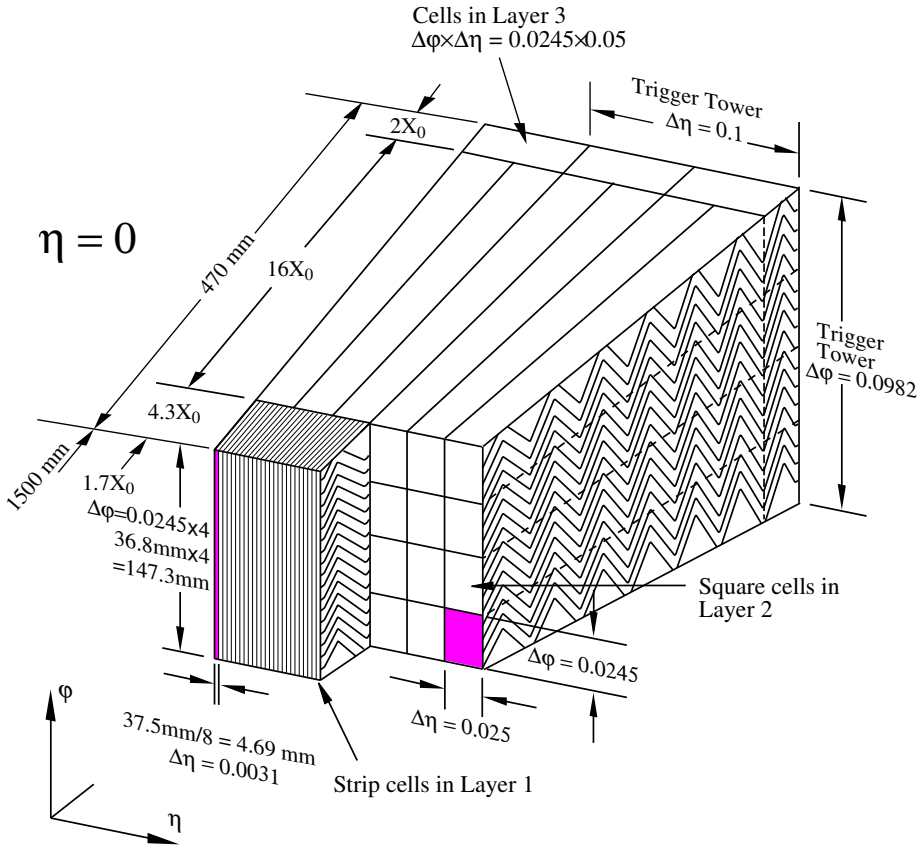

Figure 3.7: Sketch of the barrel module of electromagnetic calorimeter [63].

outer hadronic calorimeter use scintillator tiles as the sampling medium and steel as the absorber medium.

An accordion geometry for the absorbers and the electrodes allows the liquid argon calorimeters to have several active layers in depth, three in the central region $0 < |\eta| < 2.5$ and two in the forward region $2.5 < |\eta| < 3.2$ and in the overlap region $1.35 < |\eta| < 1.475$ between the barrel and the end-caps. It provides naturally a full coverage in ϕ without any cracks, and a fast extraction of the signal at the electrodes.

The tile calorimeter realises a well proven technology, its design is simple and cost effective. A module forms an almost-periodic steel-scintillator structure with a ratio by volume of approximately 4.7:1. It allows one to construct a large detector by assembling smaller sub-modules together.

The electromagnetic calorimeter in the region $|\eta| < 1.475$ consists of two identical half-barrels, separated by a small gap of 4 mm at $z = 0$. The length of each half-barrel is 3.2 m, their inner and outer diameters are 2.8 m and 4 m respectively. The first layer is finely segmented in strips along η to measure the direction of particles, the second layer collects the largest fraction of the energy of the shower, and the third layer collects only the tail of the shower and is therefore less segmented in η. The third layer is additionally used to trigger on energy deposits in the calorimeter. A detailed sketch of all layers and the

granularity in η and ϕ is presented in Figure 3.7. To measure the energy lost by electrons and photons before reaching the calorimeter, a presampler detector is placed in front of the barrel. It is a thin liquid argon layer with 11 mm in depth. The electromagnetic end-cap calorimeters consist of two wheels covering the range $1.375 < |\eta| < 3.2$. Each wheel is 63 cm thick, the external and internal radii are 2098 mm and 330 mm, respectively. In the overlap region between the barrel and the end-cap calorimeters, where the material in front of the calorimeter amounts to several interaction lengths, again a LAr presampler is installed, covering the range $1.5 < |\eta| < 1.8$. The resolution of the electromagnetic calorimeter is expected to be $\sigma_E/E = 10\%/\sqrt{E} \oplus 0.7\%$.

The hadronic tile calorimeter is located in the region, $|\eta| < 1.7$, behind the electromagnetic calorimeter. It is comprised of a central barrel, 5.8 m in length, and two extended barrels, 2.6 m in length and each having an inner radius of 2.28 m and an outer radius of 4.25 m. The barrels are divided azimuthally into 64 modules and are segmented in depth in three layers. The hadronic end-cap calorimeter covers the range $1.5 < |\eta| < 3.2$, overlapping with the tile and forward calorimeters to reduce the drop in material density in the transition region. The hadronic end-cap calorimeter consists of two wheels per end-cap and 32 identical modules per wheel. Each wheel is divided into two segments in depth, for a total of four layers per end-cap. The wheels closest to the interaction point are built from 25 mm parallel copper plates, while those further away use 50 mm copper plates. The copper plates are interleaved with 8.5 mm LAr gaps. The outer radius of the copper plates is 2.03 m, while the inner radius is 0.475 m. Except in the overlap region with the forward calorimeter where this radius becomes 0.372 m. The forward calorimeter located in the region $3.1 < |\eta| < 4.9$ consists of three modules in each end-cap. The first module is made of copper and optimised for electromagnetic measurements. The other two layers are made of tungsten and measure predominantly the energy of hadronic interactions. The resolution of the hadronic calorimeters is expected to be $\sigma_E/E = 50\% \ / \ \sqrt{E} \oplus 3\%$ in the barrel and end-caps and $\sigma_E/E = 100\%/\sqrt{E} \oplus 10\%$ in the forward calorimeter.

The total thickness of the electromagnetic calorimeter is more than 24 radiation lengths in the barrel and above 26 radiation lengths in the end-caps. The total thickness of the hadronic calorimeter is approximately 9.7 interaction lengths in the barrel and 10 interaction lengths in the end-caps. The cumulative amounts of material in front of the electromagnetic calorimeters, in the electromagnetic and hadronic calorimeters and in front of the first active layer of the muon spectrometer in units of interaction length is visible in Figure 3.8. It provides a good containment for electromagnetic and hadronic showers and limits punch-through of particles into the muon system.

On the inner face of the endcap calorimeter cryostats at $z = \pm 3560$ mm and perpendicular to the beam direction the Minimum Bias Trigger Scintillators (MBTS) are mounted. They will be used to trigger on minimum collision activity for the initial running period at luminocities below 10^{33} cm^{-2}s^{-1}. The MBTS detector consists of 32 scintillator paddles, 2 cm thick, organized into 2 disks, one on each side of the interaction point of ATLAS. The light emitted by each scintillator segment is collected by wavelength-shifting optical fibers and guided to a photomultiplier tube. The signals are read out by the tile calorimeter electronics.

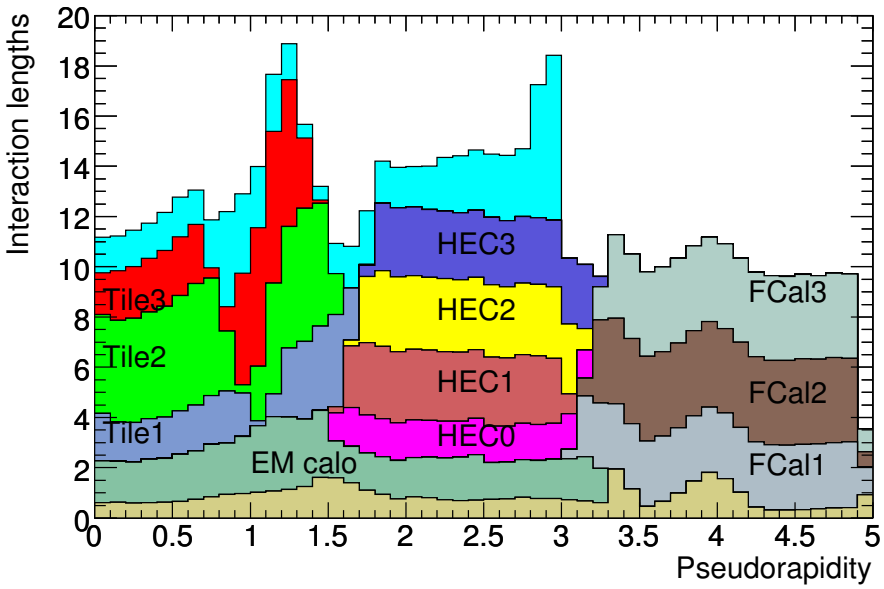

Figure 3.8: The cumulative amounts of material in front of the electromagnetic calorimeters, in the electromagnetic and hadronic calorimeters and in front of the first active layer of the muon spectrometer in units of interaction length versus pseudorapidity [63].

Muon Spectrometer

The outermost part of the ATLAS detector is the muon spectrometer. All particles except muons and neutrinos should be stopped by the calorimeters and therefore only muons are assumed to reach the spectrometer, neutrinos will escape the detector anyway. The overall view of the muon chambers and of the magnet system is depicted in Figure 3.9. The main parameters of the muon spectrometer are listed in Table 3.3.

The spectrometer measurement is based on the deflection of charged particles in the magnetic field of the superconducting air-core toroid magnets. A large toroid is installed in the barrel, $|\eta| < 1.4$, and two smaller toroids are placed in the end-caps, $1.6 < |\eta| < 2.7$. In the transition region, $1.4 < |\eta| < 1.6$, the magnetic field is induced by two toroids. The barrel toroid consists of eight coils encased in individual stainless-steel vacuum vessels and supported by rings of struts. The overall size is 25.3 m in length, with inner and outer diameters of 9.4 m and 20.1 m, respectively. Each end-cap toroid is made of a single cold mass built from eight flat, square coil units and eight keystone wedges. The length of end-cap toroids is 5.0 m, the inner diameter is 1.65 m and the outer diameter is 10.7 m. The toroids are arranged in a way that the magnetic field is mostly orthogonal to the particle trajectory. The magnetic field in the barrel is approximately 0.5 T, in the end-caps it is around 1 T and is measured by approximately 1800 Hall sensors distributed throughout the spectrometer volume.

The barrel tracking chambers are monitored drift tubes (MDT), which are installed be-

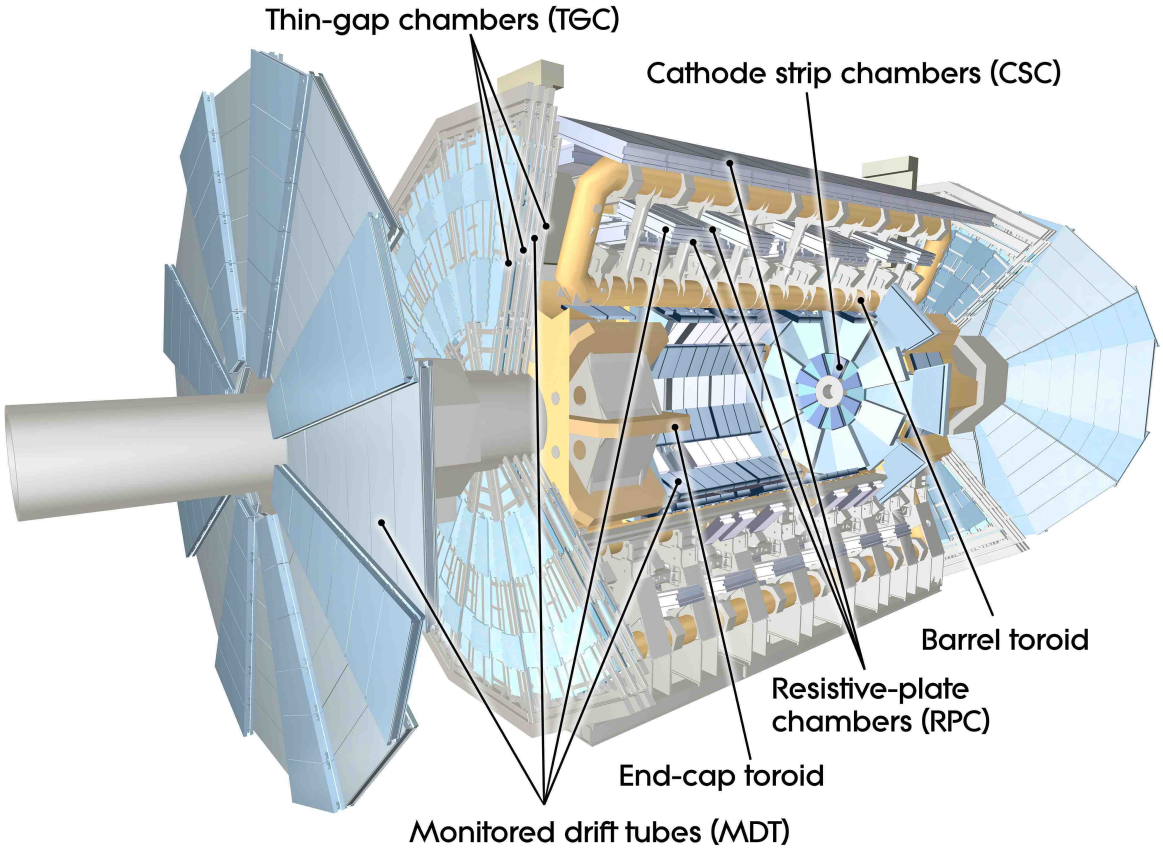

Figure 3.9: Schematic view of the muon spectrometer [70].

tween and on the eight coils of the barrel magnet. They are arranged in three concentric cylindrical shells at radii of approximately 5 m, 7.5 m and 10 m from the beam axis. Due to a high particle flux in the transition region and in the end-caps the cathode strip chambers (CSC) have been installed in the innermost ring additionally to the three layers of MDTs. The CSCs have a higher rate capability and time resolution than MDTs. The end-cap chambers are mounted in front and behind the end-cap toroids. They form large wheels, perpendicular to the z-axis and located at distances of $|z| \sim 7.4$ m, 10.8 m, 14 m and 21.5 m from the interaction point.

The MDTs are built of aluminium tubes of 30 mm diameter filled with argon-gas-mixture at an absolute pressure of 3 bar and contain a 50 μm diameter tungsten-rhenium wire in the centre. The typical single wire resolution is 80 μm, the resolution per chamber is 35 μm in the bending plane. The CSCs are multi-wire proportional chambers filled with argon (30%) - carbonic acid (50%) - tetrafluormethane (20%) gas mixture with cathode planes segmented into strips in orthogonal directions. The diameter of one single wire made of tungsten-rhenium is 30 μm, its spatial resolution is about 60 μm. The resolution of a chamber is 40 μm in the bending plane and about 5 mm in the transverse plane.

An essential design criterion of the muon system was the capability to trigger on muon

MDT: monitored drift tubes	
coverage	$\|\eta\| < 2.7$ (innermost layer: $\|\eta\| < 2.0$)
number of chambers	1150
number of channels	354 000
function	tracking
resolution	35 μm (z)
CSC: cathode strip chambers	
coverage	$2.0 < \|\eta\| < 2.7$
number of chambers	32
number of channels	31 000
function	tracking
resolution	40 μm (R), 5 mm (ϕ)
RPC: resistive plate chambers	
coverage	$\|\eta\| < 1.05$
number of chambers	606
number of channels	373 000
function	triggering, second coordinate
resolution	10 mm (z), 10 mm (ϕ)
RPC: resistive plate chambers	
coverage	$1.05 < \|\eta\| < 2.7$ (2.4 for triggering)
number of chambers	3588
number of channels	318 000
function	triggering, second coordinate
resolution	2-6 mm (R), 3-7 mm (ϕ)

Table 3.3: Main parameters of the muon spectrometer [63].

tracks. The muon trigger chambers cover the pseudorapidity range $|\eta| < 2.4$ and provide a bunch crossing identification, well-defined p_{T}-thresholds and a measurement of the second coordinate orthogonal to the coordinate measured in the tracking chambers. Resistive plate chambers (RPC) are used in the barrel and thin gap chambers (TGC) in the end-cap regions. The RPCs are gaseous detectors with 2 mm thick Bakelite plates separated by polycarbonate spacers whereas the TGCs are multi-wire proportional chambers. Both chamber types deliver signals with a spread of 15-25 ns, thus providing the ability to tag the beam-crossing. The MDT tracking chambers determine the coordinate of the particle track only in the bending plane. After matching the MDT and trigger chambers measurements in the bending plane, the trigger chamber's coordinate in the non-bending plane is adopted as the second coordinate of the MDT measurement.

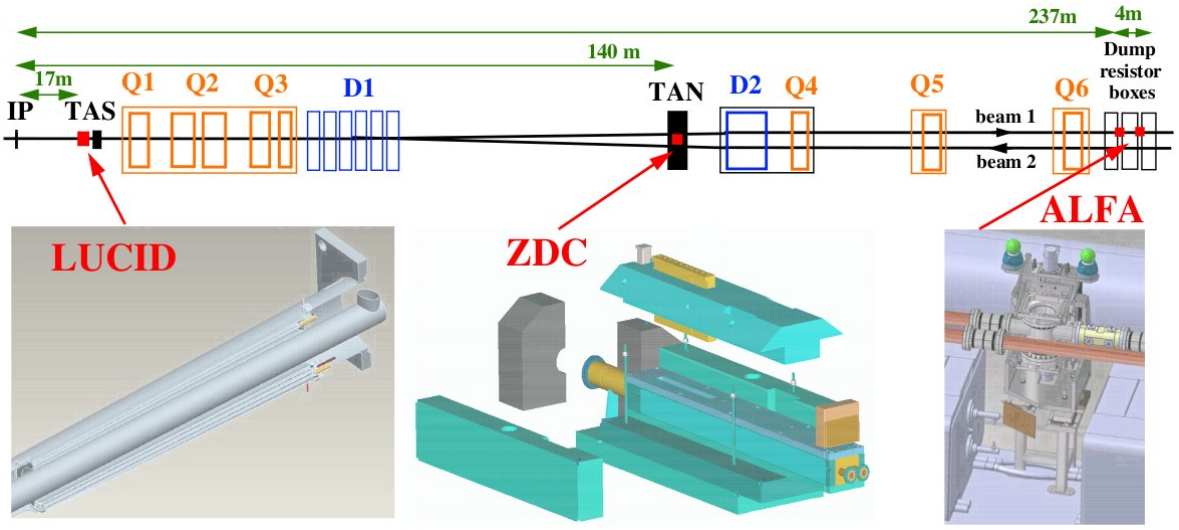

Figure 3.10: Placement of the forward detectors LUCID, ZDC and ALFA along the beamline around the interaction point (IP) [63]. LUCID is located near the Target Absorber Secondaries (TAS) collimator. The ZDC is embedded in the Target Absorber Neutral (TAN).

3.3 Forward Detectors

Three small detectors are being built to provide a good coverage in the very forward region. The main function of the first two systems is to determine the luminosity delivered to ATLAS. Closest to the ATLAS detector, at the distance of $\pm$ 17 m from the interaction point, a Cherenkov detector called LUCID (LUminosity measurement using Cherenkov Integrating Detector) is placed. The second detector is ALFA (Absolute Luminosity For ATLAS) will be located at $\pm$ 240 m and is still under construction. The third system is the Zero-Degree Calorimeter (ZDC) to determine the centrality of heavy-ion collisions and is located at $\pm$ 140 m away from the interaction point. The placement of the three detectors and their schematic view are shown in Figure 3.10.

LUCID is a relative luminosity detector. Detecting inelastic pp scattering in the forward direction, it measures the integrated luminosity and monitors on-line the instantaneous luminosity and beam conditions. LUCID can determine the luminosity to a precision of 20-30% using calculations based on the LHC machine parameters. It is built of an array of twenty Cherenkov tubes filled with C_4F_{10} at a pressure of 1.2-1.4 bar. The Cherenkov light emitted by a particle traversing the tube is measured by photomultiplier tubes, the signal amplitude is used to distinguish the number of particles per tube. Counting the number of tubes with a signal above a certain threshold provides a luminosity measurement for on-line monitoring.

The ALFA detector will measure the absolute luminosity via elastic scattering at small angles. The optical theorem connects the elastic-scattering amplitude in the forward direction to the total cross-section and can be used to extract the luminosity. Extremely small scattering angles of order 3 μrad are needed to make these measurements, therefore the de-

tectors have to be placed far away from the interaction point and as close as possible to the beam. The Roman pots technique will be used to move the scintillating-fibre tracker as close as 1 mm to the beam. The goal is to measure the luminosity with an uncertainty of better than 5%.

The primary purpose of ZDC is to detect forward neutrons in heavy-ion collisions and to measure the centrality of such collisions. During the start-up phase of the LHC it will enhance the acceptance of the ATLAS detector for diffractive processes and can also provide an additional minimum-bias trigger for ATLAS.

3.4 Data Acquisition System

At the LHC the collision rate is 40 MHz for a bunch spacing of 25 ns. The LHC has started its operation with a peak luminosity of 10^{29} $cm^{-2}s^{-1}$ and the luminosity will be increased up to the design luminosity of 10^{34} $cm^{-2}s^{-1}$ step by step. The incoming interaction rate at the design luminosity is about 1 GHz. On the one hand recording all data with such a high frequency exceeds our technical possibilities and on the other hand we do not need to record all physics processes with the same rate. Events with a lower production rate should be recorded more often than events with a higher production rate. The trigger system classifies the events by the specified properties and decides if a specific event will be written to mass storage or not.

The ATLAS trigger system is based on three levels of event selection, which reduces the output event storage from 40 MHz rate to about 200 Hz rate. The first step is a hardware based Level 1 trigger [71]. The next two steps are software based Level 2 and Event Filter triggers, collectively named as the High Level Trigger [72]. From Figure 3.11 we can see the reduction rates after each trigger level and production rates for different physics processes. The aim is to reduce the amount of low energy QCD processes and to achieve an efficient selection of rare processes.

The Level 1 trigger receives all collision data and has to take its decision within 2.5 μs to reduce the output rate to 75 kHz. The decision is based on the multiplicities and energy thresholds for the following objects reconstructed by the Level 1 trigger algorithms: electromagnetic clusters, taus, jets, missing transverse energy, scalar sum of transverse energy in the calorimeter, total transverse energy of observed jets and trajectories of muons measured in the muon spectrometer. The total number of allowed Level 1 configurations is 256. Using a prescale factor N (where only 1 of N events is selected), each configuration can be weighted also depending on the current peak luminosity during the run.

The Level 2 trigger uses the regions-of-interest identified by the Level 1 trigger and analyses locally but using fine-grained data from the detector. Depending on the type of selected object the size of the region-of-interest is defined and the Level 1 object is re-reconstructed with improved precision. The Level 2 trigger uses information from the inner detector, which is not available for the Level 1 trigger and combines information from different subdetectors to provide additional purity of the selected events. The average processing time is 40 ms, including the time for data transfers. The output rate is reduced to 2 kHz.

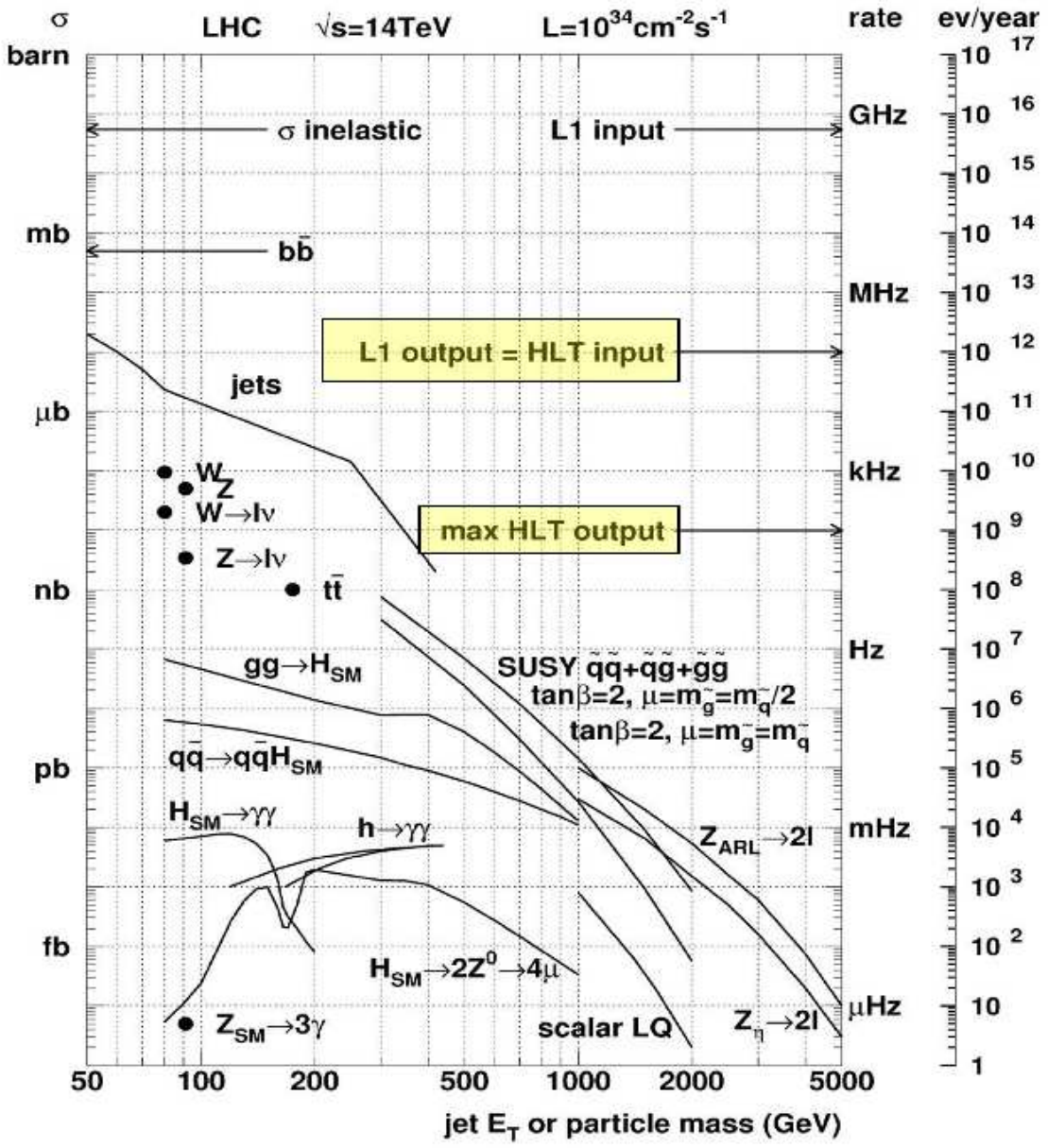

Figure 3.11: Expected event rates and cross section for several physics processes as a function of energy at a luminosity of 10^{34} cm^{-2}s^{-1} and 14 TeV centre-of-mass energy [73].

The last step in the on-line selection is the Event Filter. It uses objects reconstructed by the Level 2 trigger, but it has direct access to the complete data for a given event as the Event Filter runs after the event building process. The Event Filter uses typically the same algorithms as the offline reconstruction, hence a more complex pattern recognition procedure and calibration. The average processing time is 4 s per event and it provides an

additional rejection to 200 Hz.

The raw data events are written in one or more inclusive streams depending on the trigger decision. The initial streams are “egamma”, “jetTauEtmiss”, “muons”, and “minbias”. Each stream contains events that pass at least one of the trigger signatures. For example, events passing the electron or photon triggers will be written to the egamma stream. The streams have approximately the same proportion of events and the event duplication across streams is less than 10%.

At the LHC start-up the strategy is to commission the trigger and the detector with well-measured Standard Model processes. Many triggers will operate in pass-through mode to validate the trigger selection and trigger reconstruction algorithms. With increasing luminosity a higher thresholds and tighter selections will be applied to select the most interesting physics processes.

3.5 Performance of the LHC and the ATLAS Experiment

In Dezember 2009 the ATLAS detector has started to record data from collisions. The beam energy and the corresponding dipole field is reduced to 3.5 TeV per beam to allow a safe operation. All main components of the detector are fully operational and all levels of the trigger and data aquisition system performed as expected. The approximate operational fraction of ATLAS detector components is listed in Table 3.4. The commissioning and calibration of the ATLAS detector was started during the cosmic ray data taking in 2008 and 2009. Performance close to design goals has been obtained for different detector components: inner detector [74], LAr calorimeter [75] and muon spectrometer [76]. Currently collision data at 7 TeV centre-of-mass energy is used to calibrate the detector as well for the first physics studies.

The instantaneous luminosity given by Equation 3.1 characterises the performance of the LHC machine. It is determined in real time approximately one per second using a number of detectors and algorithms. The highest peak luminosity obtained to date is of order 10^{32} cm^{-2}s^{-1}. The full history is displayed in Figure 3.12(a).

Integrating the instantaneous luminosity over time gives the integrated luminosity $\mathcal{L}_{\text{int}}$, which corresponds to the amount of collected data. Figure 3.12(b) shows the delivered luminosity by the LHC machine and the recorded luminosity by the ATLAS experiment. The uncertainty on the measured luminosity is 11% and has been obtained using an absolute calibration via beam separation scans [77]. To calculate the number of events N of a certain physics process, the total luminosity has to be multiplied with the probability of the process occurring, the cross section σ:

$$N = \sigma \cdot \mathcal{L}_{\text{int}} \tag{3.2}$$

The cross section σ given in cm ^{2} is preferably quoted in picobarn (pb), where 1 pb = 10^{-36} cm^2.

component	num. of channels	operational fraction
pixels	$80 \cdot 10^6$	97.4%
silicon strips	$6.3 \cdot 10^6$	99.2%
transition radiation tracker	$350 \cdot 10^3$	98.0%
LAr EM calorimeter	$170 \cdot 10^3$	98.5%
tile calorimeter	9800	97.3%
hadronic endcap LAr calorimeter	5600	99.9%
forward LAr calorimeter	3500	100%
level 1 calo trigger	7160	99.9%
level 1 muon RPC trigger	$370 \cdot 10^3$	99.5%
level 1 muon TGC trigger	$320 \cdot 10^3$	100%
muon drift tubes	$350 \cdot 10^3$	99.7%
cathode strip chambers	$31 \cdot 10^3$	98.5%
RPC barrel muon chambers	$370 \cdot 10^3$	97.0%
TGC endcap muon chambers	$320 \cdot 10^3$	98.6%

Table 3.4: Operational fraction of ATLAS detector components (May, 2010).

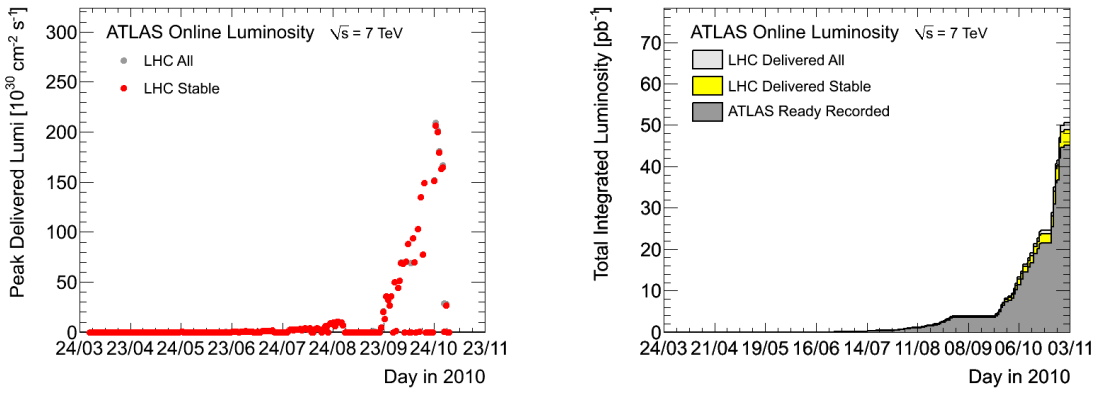

Figure 3.12: (a) The delivered instantaneous luminosity measured online and taken at $\sqrt{s} = 7$ TeV. (b) The delivered and recorded by ATLAS total integrated luminosity at $\sqrt{s} = 7$ TeV.

4 Event Simulation

The simulation of physics processes with the according detector response is an essential tool in high energy physics. During the preparation stage of an experiment it allows one to predict sensitivity to various physics processes, to develop and to validate readout and reconstruction algorithms. At the running stage of a experiment it is used to test predictions of theoretical models against the real detector response. The simulation is divided into three steps: generation of events and immediate decays, simulation of interactions in the detector and digitalisation of energy deposited in the detector into voltages and currents for readout electronics. The output format of the simulation is identical to the true detector output format and can be run through the same trigger and reconstruction algorithms.

The first part of this chapter deals with simulation of physics processes. The main aspects of the event generation techniques and the event generators used in this thesis will be discussed. The second part summarise the simulation of detector response, the full detector simulation based on GEANT4 [78] and the fast detector simulation ATLFAST-II [79]. Afterwards the simulated signal and background processes will the described in more details.

4.1 Main Aspects of Monte Carlo Event Simulation

The Monte Carlo event simulation enables the description of the final states resulting from high-energy collisions. The state-of-the-art knowledge about quantum chromodynamics is implemented using numerical Monte Carlo techniques. The aim is to produce events imitating Nature's behaviour in a real experiment. The ability to isolate independent phases of the overall collision, the concept of "factorisation", makes possible to simulate complex final states with hundreds of particles.

In particular, factorisation allows one to separate parts that describe the structure of the proton and the final-state hadron formation from the hard interaction part. The time scale at that the hard scattering takes place is so short, that the details of the parton distributions and their interactions in proton or what will happen to it after the hard collision, are irrelevant. Figure 4.1 illustrates the general structure of a hard proton-proton collision. The hard interaction among the partons can be calculated perturbatively. The parton density functions depend only on the energy scale of the hard scatterers and not on the nature of the probe and are determined by global fits to data from deep inelastic scattering, Drell-Yan and jet production. After the hard process, created partons emit themselves partons. The parton shower process, governed by perturbative QCD, continue until a low virtuality scale is reached (the region labelled with the dotted line in the figure). At this point the hadronisation process starts. The hadronisation is assumed to be independent of the initial hard process, therefore its parametrisation, tuned in some reference process, can be used in

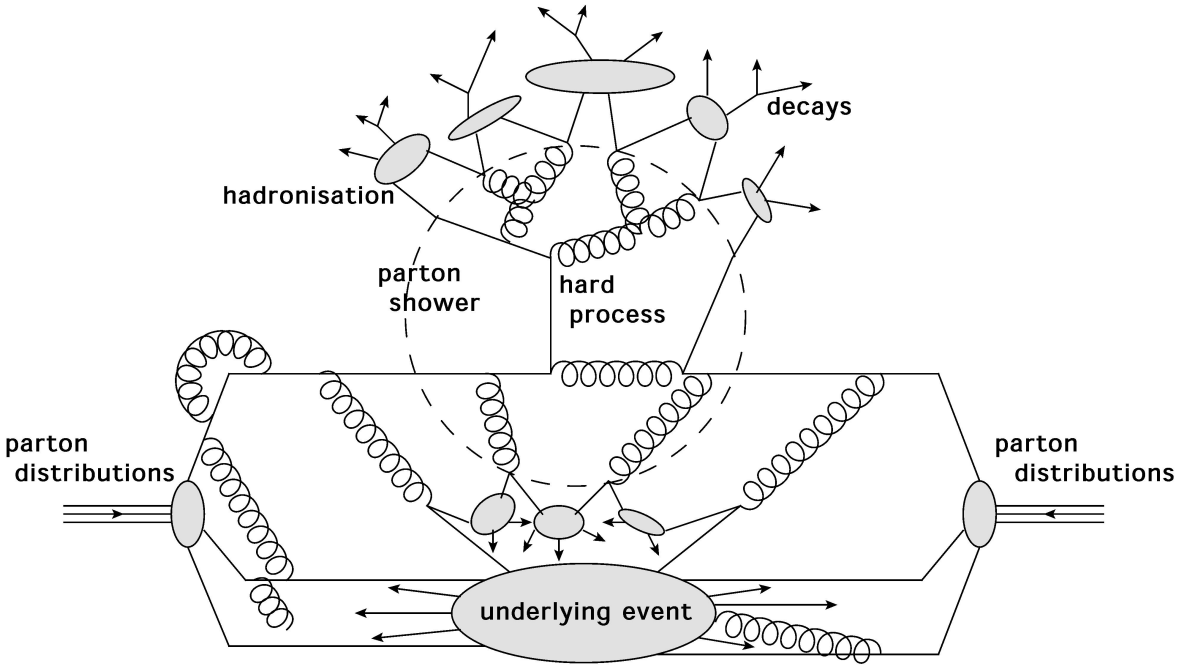

Figure 4.1: General structure of a hard proton-proton collision [80].

other hard interactions. Nearby partons combine into colour-singlet clusters (the grey small blobs in figure), which build hadrons. The remnants of colliding protons undergo similar shower and hadronisation processes. The evolution of the underlying event (the labelled large grey blob) depends on the hard event, because at least colour quantum numbers must be exchanged to guarantee overall neutralisation. In our picture, the initial partons emit further partons, which split into $q\bar{q}$ pairs shared with underlying event. Finally the decays of unstable hadrons are handled. Multi-parton interactions, wherein more than one pair of partons from protons interact as well as pile-up from other proton-proton collisions in the same bunch crossing are accounted for.

Additional partons in the final states can be handled in two ways: by the matrix element or by the partron shower methods. In the matrix element method additional Feynman diagrams are calculated, taking into account exact kinematics, interferences and helicity structure. This approach is correct, but calculations becomes extensive with increasing number of final states. The parton shower method allows one to add an arbitrary number of branchings of one parton into two (or more) partons. It is possible by simplifying the kinematics, and the interference and helicity structure of the process. Both approaches have strong and weak points. The parton shower method yields good descriptions of relatively soft gluon emission, while at higher energy scale the matrix element method provides more reasonable results. The ultimate goal is to combine the best aspects of the both methods.

There are multi-purpose Monte Carlo generators, which handle all phases of event simulation, as well the specialised generators, which cover only single steps. The most accurate theoretical predictions are often obtained by combining components of different simulation programs - one program to produce a hard process, another to evolve the final states of the

hard process through the parton shower, a third to hadronise the products of parton shower and so forth. Depending on the problem of interest, best suitable tools should be chosen.

In the following the used Monte Carlo programs and some simulation components will be discussed in more details in context of their implementation in event generators.

4.1.1 Parton Level Event Generators

The parton level Monte Carlo event generators simulate final states consisting of leptons, bare quarks and gluons. The colliding partons can be considered as free at smallest scale in time and distance and the perturbative expansion provides reliable predictions. The code is often based on the direct computation of the relevant Feynman diagrams, but also programs for automatic generation of parton-level processes exist. At the tree level the limiting factor for the automatic generation is the CPU power. The computation of higher order corrections in particular of virtual emissions is technically more complex.

The parton-level computation has to be combined with the partonic evolution given by the shower Monte Carlo programs in a consistent way. A final state with n partons can be obtained from $n-k$ partons generated by the matrix event generator plus k additional partons from the shower Monte Carlo simulations. This implies that the same final state can be generated starting from different $(n-k)$-parton configurations. To avoid double counting the parton configuration generated by the parton shower should be matched to the parton configuration generated by the matrix element generators.

ALPGEN

ALPGEN [81] allows exact computation of tree level matrix elements with a fixed number of partons in the final state for a large list of pre-defined Standard Model processes in hadronic collisions. Emphasis has been placed on final states with a large parton multiplicity. The b-quark and top quark masses are included, the c-quark mass is taken into account in some special cases and the top-quark and gauge-boson decays are implemented with helicity correlations. Full information on the colour and flavour structure of parton level events is provided to enable the evolution of the partonic final states into fully hadronised final states. A strategy [82, 83] has been developed to match the multiparton final states with the shower development. The phase space is separated in the matrix element and parton shower domains by definition of a cut value. The matrix elements are reweighted with Sudakov form factors [84] and the parton showers are subjected to a veto procedure to cancel dependence on the cut value to next-to-leading logarithmic accuracy.

MC@NLO

MC@NLO [85] is a method for matching next-to-leading order QCD calculations of hard processes and parton shower Monte Carlo simulations. The total rates are accurate to the next-to-leading order, the distributions are recovered upon expansion in the strong coupling constant α_S. The next-to-leading order calculations include virtual and real emission of partons. The real emissions are also included in the parton shower simulation and should not

be double-counted. The matching is based on the subtraction method widely used for the next-to-leading order calculations. The result is a set of leading order and next-to-leading order parton configurations that are fed into a parton shower generator. In order to reproduce the next-to-leading order corrections fully, some of the configurations have negative weights. The MC@NLO formalism is general, but in the current version only the showering and hadronisation code of HERWIG is supported.

4.1.2 Multi-purpose Event Generators

Multi-purpose event generators are able to simulate a wide variety of the initial and final states with the frequency as predicted by theory. The hard subprocess is often the only process dependent part and everything else is almost completely generic. Therefore such generators have a modular structure and the parton level event generators can be interfaced to the shower and hadronisation modules. The multi-purpose simulation programs provide an exclusive description of events. For example, a Z boson produced in the hard subprocess has zero transverse momentum. Through the parton shower the transverse momentum can be produced, since the final state particles from the hard subprocess must recoil against those produced by the shower. Thus, the general purpose generators are ideal to describe the full event necessary for a more realistic description of collision events.

PYTHIA

PYTHIA [86] is a general-purpose Monte Carlo program for hadronic event simulation in pp, $e^+e^-$and ep colliders. Around 300 different $2 \to n$ (maximal 3) subprocesses are implemented. Not all contributing Feynman graphs are always included, but the more important ones. Also various approximations in the matrix element calculations are used. To the partonic processes the initial and final state parton shower are added. The final state shower is based on forward evolution in terms of decreasing time-like virtuality $m^2 = E^2 - \vec{p}^2$ with angular ordering imposed by veto. The framework is a leading-log approximation, but includes energy-momentum conservation and other next-to-leading-log aspects. The initial state radiation is based on the backwards evolution, starting at the hard scattering scale and moving backwards in time. The Lund string model [87] is used to simulate the hadronisation process. The assumption of linear confinement provides a starting point for the model. The energy stored in a colour dipole field between a charge and an anticharge increases linearly with the separation between the charges. The string breaks by the production of new $q\bar{q}$ pairs and the quark and antiquark from two adjacent string breaks can combine to form a meson. The simulation of underlying event is approximated by a set of $2 \to 2$ scatterings taking into account energy conservation and colour connections.

HERWIG

HERWIG [88, 89] is a general-purpose event generator for the simulation of lepton-lepton, lepton-hadron and hadron-hadron collisions. A large list of $2 \to n$ processes for the Standard Model and its supersymmetric extensions are implemented. The full spin correlations

are included for the most processes to take into account the correlations between the production and decay of the particles as well between all decays in an event in a correct way. An interface is provided to include further hard subprocesses. The initial and final state radiation is generated using a coherent branching algorithm. The full available phase space is restricted to an angular-ordered region for correct treatment of the leading soft and collinear singularities. In case of the final state radiation, at each branching, the angle between two emitted partons is smaller than that of the previous branching. The initial-state branching algorithm is based on the backward evolution. Azimuthal correlations due to spin effects are also taken into account. HERWIG is using the cluster hadronisation model based on the colour pre-confinement property of the angular-ordered parton shower. After the parton showering, all outgoing gluons are split into light quark-antiquark pairs. In the limit of a large number of colours, all quarks and antiquarks can form colour-singlet clusters. The high mass clusters split into low mass clusters using string-like mechanism. Cluster splitting continues till all hadrons are build. The underlying event model is based on the minimum-bias event generator [90] of the UA5 collaboration, but also an external package JIMMY [91] can be used.

4.2 Detector Simulation

Detector simulation allows one to study the detector response for a wide range of physics processes and scenarios. Taking events generated with a Monte Carlo program as input, it provides an output as expected to that of the real detector. The GEANT4 simulation toolkit contains models for physics and infrastructure for particle transport through the detector material. These models as well as the description of detector components has to be validated with data. Combined test beam studies, cosmic ray data and collision data have been used to validate and to improve the detector description. The ATLAS detector is divided in approximately 4.8 million volumes to match the as-build detector as close as possible. Large computing resources are required to accurately model the detector geometry and physics descriptions. Therefore also fast simulations have been developed to allow a faster but still precise simulation of data.

4.2.1 Full Detector Simulation

The ATLAS detector geometry is built from databases containing the information describing the physical construction and conditions data. The detector structure can be viewed in terms of solids and basic shapes. Out of it logical volumes are build. Repeating structures are combined in physical volumes and finally out of nested physical volumes total volumes are created. The most complex structure has the smallest detector - the inner detector with 1.8 million volumes. The calorimeter consists of 1.6 million volumes and the muon system counts 1.4 million volumes. It is a challenging task to create such a dense geometry, to remove volume overlaps and touching surfaces. A review of the status of the software and the detector geometry can be found in Reference [79].

Despite a careful weighting and accounting of detector components, data-driven methods are crucial to evaluate the material in the inner detector. Several complementary meth-

ods have been used to map out the detector with first 900 GeV and 7 TeV data taken last and this year. Measurements of the track length in the outer SCT layers, the SCT-extension efficiency and hit patterns, track residuals in different silicon layers, K^0_S mass and so on have been used to estimate the material budget of the inner detector. It has been found that the nominal Monte Carlo simulation describes accurately the material of the real detector [92, 93].

Alignment of the inner detector is the next crucial point. After assembly of the detector, the position of the individual modules is known with much worse accuracy than their intrinsic resolution. A track-based alignment has been applied to determine the absolute position of modules. A position precision of $\sim$10 μm is required for physics measurements. The estimated size of the misalignments in the pixel barrel is $\sim$17 μm and in the SCT $\sim$25 μm. The distributions in the TRT barrel agree perfectly with expectations, the distributions in the TRT end-caps require further improvements [94]. A good performance has been achieved so far and further improvements are expected with more collision data.

Test beam data are used to validate the calorimeter response for single pions and protons and to determine parameter settings for the hadronic interaction model used by GEANT4 [95]. The simulation compared to collision data at 7 TeV agrees within 5% [96]. The description of the electromagnetic shower profiles has been tested with cosmic muon data. A good agreement between data and Monte Carlo simulations has been found as well [75].

The simulation of the muon reconstruction in the muon spectrometer and in the inner detector has been tested with the first collision data, too. The key properties like the identification efficiencies, rates of secondary muons from pions, momentum resolution are well described by the simulation [97].

To summarise, the detector description is in a good shape and comparisons with data taken 2010 confirm that the full detector simulation describes the real detector with the required precision.

4.2.2 Fast Detector Simulation

Because of the complicated detector geometry and detailed physics description, it is impossible to provide the needed simulated statistics for many physics studies due to the limited computer resources. Therefore several fast simulation programs have been developed. The most time consuming part, approximately 80%, is the simulation of particles traversing the calorimetry, especially of low energetic electromagnetic particles. These particles are removed from the simulation and replaced with pre-simulated showers. This simplification is used by default for all processes that donot require an extremely accurate modeling of the calorimeter response and agrees within 1-2% with the full calorimeter simulation.

The ATLFAST-II [79] detector simulation uses a full simulation of the inner detector and muon system and a fast simulation of the calorimeter. ATLFAST-II is about factor 20-40 faster than the full detector simulation. The single particle shower in the calorimeter is parametrised in the longitudinal and lateral energy profiles. Fine binning of the parametrisation in energy and pseudo-rapidity as well in the longitudinal depth of the shower centre is provided. The electron and photon showers are approximated by the photon parametrisation and all hadronic showers by the charged pion parametrisation. The ATLFAST-II sim-

ulation differs at 5% level from the full simulation, especially in properties sensitive to the shape of hadronic showers and in the electron identification efficiency.

4.3 Signal and Background Event Modeling

To evaluate ATLAS potential to discover $t\bar{t}$ resonances, the signal and most relevant background samples have been generated at the centre-of-mass energy of 10 TeV. A generic narrow width Z' boson sample generated with PYTHIA is representative for the electroweak Z' bosons in a large range of models. The Z' boson masses have been chosen in the region 500 - 3000 GeV/c^2 to have an overlap with the current searches at the TEVATRON on the one hand and to extend the mass reach into the TeV regime on the other hand. The main irreducible background is the Standard Model $t\bar{t}$ production. The predicted cross section involving at least one lepton from the W boson decay is 216 pb and 186 pb for fully hadronic decays. Other sources of irreducible backgrounds are W boson plus jets production and the single top production. The QCD multi-jet and Z boson plus jets event contribute to background, too. The signal process has been generated using the full and ATLFAST-II detector simulation, all background samples are processed with the full detector simulation. The detector geometry and material description corresponds to a perfectly aligned detector. The consistency between the full and fast simulation has been checked on a sample with smaller statistics. In the following, a detailed description of used Monte Carlo signal and background samples will be given.

4.3.1 Signal Event Simulation

PYTHIA 6.418 generator with the CTEQ6.6 leading order PDF set has been used to produce a neutral spin-1 colour singlet Z' boson. The axial C_A and vector C_V couplings to fermions for each generation of leptons and quarks and the mass of the Z' boson are the only free parameters of the PYTHIA Z' boson model. The couplings have been defined in Section 2.3. Two scenarios have been simulated: Z' boson with the Standard Model Z-boson-like couplings (sequential Standard Model, SSM) and Z' boson with the non-Standard Model couplings (nSM). In both cases the couplings are equal for all three fermion generations. The vector and axial couplings to quarks and leptons are listed in Table 4.1. The width of the Z' boson is given by its couplings and increases to a good approximation linearly with the mass. The width of the Z' boson with Standard Model couplings is about 3.2% of the Z' boson mass and the non Standard Model couplings lead to the smaller width of about 1.23%. The Z' boson cross section σ and its width Γ are tabulated as a function of Z' boson mass for SSM, nSM and Topcolor models in Table 4.2.

Figure 4.2 compares the invariant mass $m_{t\bar{t}}$, rapidity y and p_{T} distributions of the top and antitop quarks for the SSM and nSM scenarios at generator level. The shape of the invariant mass distributions differs significantly, but in both cases the width is still smaller than the expected detector resolution. Nevertheless the effect of the width on the analysis after detector simulation will be investigated in Section 7.6. The rapidity and p_{T} distributions are more similar for both scenarios. It means, that the model dependent couplings have only a small

model	d-type quark		u-type quark		lepton		ν_{lepton}	
	C_V	C_A	C_V	C_A	C_V	C_A	C_V	C_A
SSM	-0.639	-1	0.387	1	-0.08	-1	1	1
nSM	-0.410	-0.592	0.299	0.592	-0.047	-0.592	0.592	0.592

Table 4.1: PYTHIA parameter settings for Z' boson couplings to fermions.

$m_{Z'}$, GeV/c^2	SSM / PYTHIA		nSM / PYTHIA		topcolor / [98]	
	σ, pb	Γ, GeV/c^2	σ, pb	Γ, GeV/c^2	σ, pb	Γ, GeV/c^2
500	5.465	15.2		–		–
700	3.325	21.9		–		–
750		–		–	13.17	15.0
1000	0.634	31.8	0.239	12.3	3.28	20.0
1250		–		–	1.53	25.0
1300	0.204	41.9		–		–
1500		–		–	0.56	30.0
1600	0.0723	51.8	0.0269	20.0		–
2000	0.0214	65.1	0.0076	25.1	0.13	40.0
2500	0.005	81.6		–		–
3000	0.001	98.2		–		–

Table 4.2: Cross section σ and width Γ are tabulated as a function of the Z' boson mass for SSM, nSM and Topcolor models. Top quark mass was set to 172.5 GeV/c^2.

influence on the distributions of final decay products and with it on the signal acceptance in the detector.

The difference in the rapidity distribution of top and antitop quarks is significant. The top quarks are produced at higher rapidities than the antitop quarks. One quark and one antiquark are needed to produce a Z' boson. At pp colliders and at high energies, the quark will be a valence quark with a larger fraction of protons momentum and the antiquark will be a sea-quark with less momentum. The top quark follows mostly the direction of the incoming quark and the antitop quark follows the direction of the incoming antiquark. Thus, the top quark can be produced at higher rapidity than the antitop quark. The p_{T} distribitions show a typical Jacobian peak at $m_{Z'}/2$ as expected.

To keep the statistics as high as possible, 1 million $Z' \to t\bar{t}$ events per mass point have been produced at the generator level. All possible $t\bar{t}$ decay modes are allowed: semi-leptonic, full hadronic and di-leptonic. For all events fast detector simulation ATLFAST-II has been performed. To check the consistency with the full detector simulation also full detector simulation have been prepared for 3 mass points, 1000 GeV/c^2, 2000 GeV/c^2 and 3000 GeV/c^2. Comparison between both simulations will be discussed in Section 7.1.

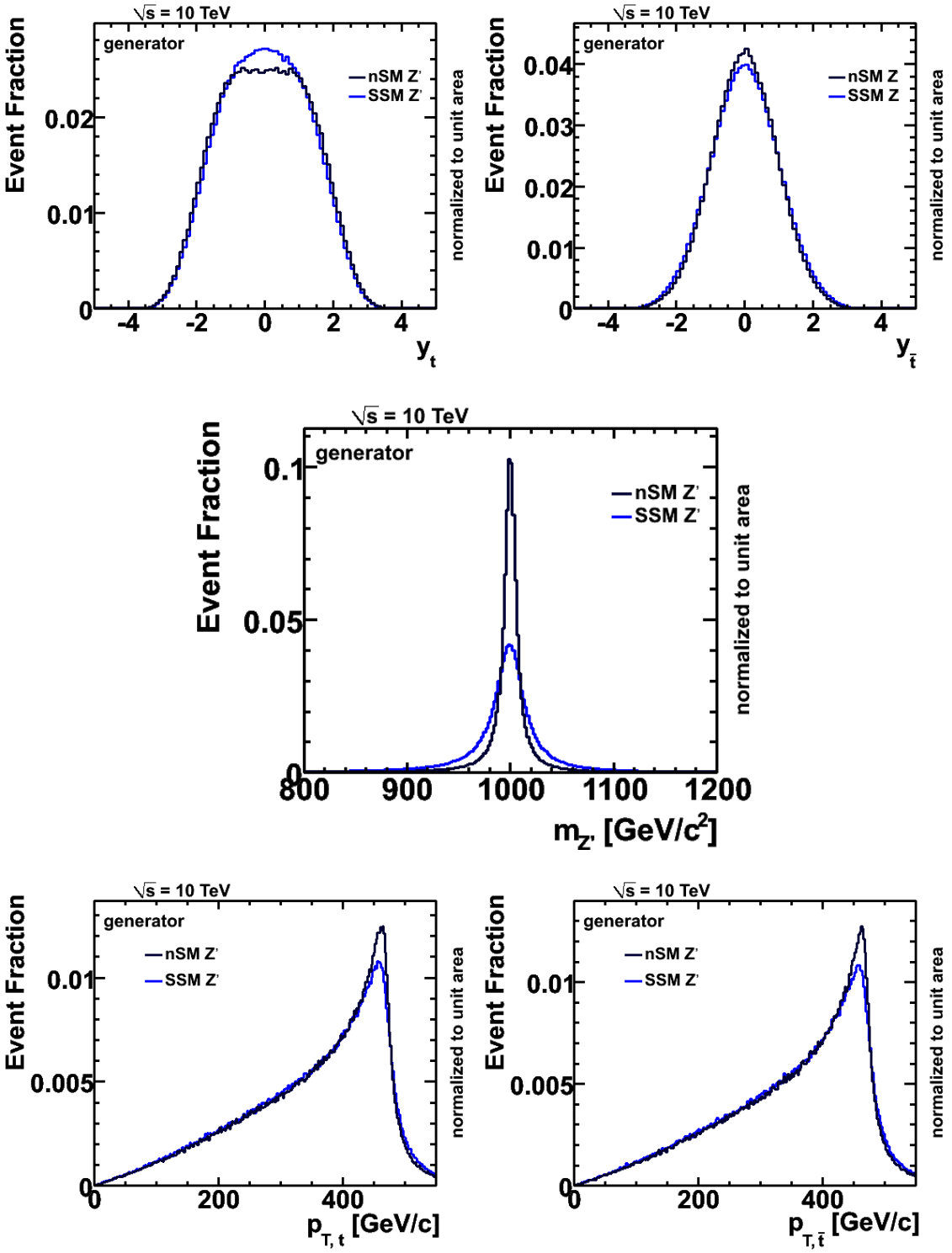

Figure 4.2: The invariant mass $m_{Z'}$, rapidity y and p_T distributions of top and antitop quarks for SSM and nSSM modelsand Z' boson mass of 1000 GeV/c^2.

dataset	physics process	m_t, GeV/c^2	generator	σ, pb	k-factor	$\mathcal{L}_{\text{tot}}$, pb^{-1}
105200	$t\bar{t}$ no hadronic	172.5	MC@NLO	202.86	1.07	2843
105204	$t\bar{t}$ fully hadronic	172.5	MC@NLO	170.74	1.07	121
106202	$t\bar{t}$ no hadronic	160.0	MC@NLO	295.96	1.06	300
106203	$t\bar{t}$ no hadronic	180.0	MC@NLO	166.82	1.06	300
105503	Wt di-lepton	172.5	AcerMc	2.79	0.99	17918
108340	t-channel $e\nu$	172.5	MC@NLO	14.46	1	454
108341	t-channel $\mu\nu$	172.5	MC@NLO	14.46	1	459
108342	t-channel $\tau\nu$	172.5	MC@NLO	14.46	1	448

Table 4.3: Generated single top quark and top quark pairs samples. ATLAS specific dataset number, the name of physics process, the used top quark mass, the Monte Carlo generator name, the theoretical cross section with the according k-factor and the produced total luminosity are tabled.

4.3.2 Background Event Simulation

The non-resonant $t\bar{t}$ production is the main source of background for our searches. The default generator for the official $t\bar{t}$ Monte Carlo production in 2008-2009 in ATLAS is MC@NLO 3.31 with the CTEQ6.6 next-to-leading order PDF set. The final states are passed to Herwig parton shower generator. Similar to the Z' boson sample, all possible top quark decay modes are allowed and the default top quark mass is set to 172.5 GeV/c^2. MC@NLO is also used for the t - channel single top quark production. The Wt-channel is generated with AcerMc 3.6. It is a leading order matrix element generator interfaced to the Pythia parton shower generator. Used single top quark and top quark pair samples are tabulated in Table 4.3. A "k-factor " normalises the generator cross section to the theoretically calculated cross section.

The W + jets process mimics the signal event signature of one leptonically decaying W boson and several additional jets. The Z + jets events contribute if one of the two leptons is lost or a τ-lepton decays hadronically. The QCD multijet events can mimic the signal signature if a lepton from a semileptonic b quark decay or a jet is errorneously identified as an isolated lepton. The Alpgen 2.13 generator is used to simulate multijet final states for QCD events and for the associated production of vector bosons (W/Z). The parton shower is modeled by the Herwig generator, the CTEQ6L1 is the default PDF set. The $W(Z)$ boson mass is set to 80.403 (91.1876) GeV/c^2 and the width is 2.141 (2.4952) GeV/c^2. For the W + jets process, Alpgen includes all processes with u, d, s and c quarks, which are treated as massless. The W + $b\bar{b}$ + jets process is neglected, because of the low production cross section, $\sigma(W + b\bar{b} + \text{jets}) = 17.86$ pb, and because the b-jet identification has not been used in this analysis. The Z + jets process includes both Z boson and γ^* propagator terms as well as their interference terms. A lower and upper cut is applied on $m_{\ell^+\ell^-}$, 60 GeV/c^2< $m_{\ell^+\ell^-}$ < 200 GeV/c^2, that limits the phase space to the region dominated by the Z boson propagator. The generated W + jets and Z + jets samples are listed in Table 4.4 and 4.5, respectively.

The Alpgen QCD multijet cross section with leading jet p_{T} > 10 GeV/c is about 6 billion pb. Thus, the QCD multijet samples cannot be produced inclusively in useful amounts of

dataset	physics process	σ, pb	k-factor	$\mathcal{L}_{\text{tot}}$, pb^{-1}
107680	$W \to e\nu$ + 0 partons	10184.7	1.22	299.4
107681	$W \to e\nu$ + 1 partons	2112.3	1.22	301.8
107682	$W \to e\nu$ + 2 partons	676.0	1.22	3004.4
107683	$W \to e\nu$ + 3 partons	203.3	1.22	2990.4
107684	$W \to e\nu$ + 4 partons	56.1	1.22	2975.9
107685	$W \to e\nu$ + 5 partons	16.6	1.22	3018.4
107690	$W \to \mu\nu$ + 0 partons	10125.7	1.22	301.1
107691	$W \to \mu\nu$ + 1 partons	2155.5	1.22	295.9
107692	$W \to \mu\nu$ + 2 partons	682.3	1.22	2976.9
107693	$W \to \mu\nu$ + 3 partons	202.0	1.22	3009.5
107694	$W \to \mu\nu$ + 4 partons	55.5	1.22	3008.6
107695	$W \to \mu\nu$ + 5 partons	16.3	1.22	3065.0
107700	$W \to \tau\nu$ + 0 partons	10178.3	1.22	299.6
107701	$W \to \tau\nu$ + 1 partons	2106.9	1.22	302.7
107702	$W \to \tau\nu$ + 2 partons	672.8	1.22	3018.7
107703	$W \to \tau\nu$ + 3 partons	202.7	1.22	3000.1
107704	$W \to \tau\nu$ + 4 partons	55.3	1.22	3017.8
107705	$W \to \tau\nu$ + 5 partons	17.0	1.22	2942.8

Table 4.4: Generated W + jets samples. ATLAS specific dataset number, the name of physics process, the theoretical cross section with the according k-factor and the produced total luminosity are tabled.

the integrated luminosity. For this reason the QCD multijet process has been divided in multiple samples according to the leading jet p_{T} in the event. The definition of slices and corresponding cross sections are summarised in Table 4.6. No events are generated with the leading jet p_{T} below 35 GeV/c due to practical limitations. The flavour content of multijet events is similar to that of W + jets events. The light quarks are produced through the matrix element calculations and treated as massless, pairs of b quarks are produced only through the $g \to b\bar{b}$ parton showering process. A detailed description of all generator settings can be found in [99].

dataset	physics process	σ, pb	k-factor	$\mathcal{L}_{\text{tot}}$, pb^{-1}
107650	$Z \to ee$ + 0 partons	898.18	1.22	300.1
107651	$Z \to ee$ + 1 partons	206.57	1.22	300.1
107652	$Z \to ee$ + 2 partons	72.50	1.22	3000.1
107653	$Z \to ee$ + 3 partons	21.08	1.22	3012.2
107654	$Z \to ee$ + 4 partons	6.00	1.22	3082.3
107655	$Z \to ee$ + 5 partons	1.73	1.22	3186.2
107660	$Z \to \mu\mu$ + 0 partons	900.21	1.22	300.5
107661	$Z \to \mu\mu$ + 1 partons	205.21	1.22	302.1
107662	$Z \to \mu\mu$ + 2 partons	69.35	1.22	3006.3
107663	$Z \to \mu\mu$ + 3 partons	21.63	1.22	3004.8
107664	$Z \to \mu\mu$ + 4 partons	6.08	1.22	3041.5
107665	$Z \to \mu\mu$ + 5 partons	1.70	1.22	3239.2
107670	$Z \to \tau\tau$ + 0 partons	902.71	1.22	300.2
107671	$Z \to \tau\tau$ + 1 partons	209.26	1.22	301.1
107672	$Z \to \tau\tau$ + 2 partons	70.16	1.22	3000.1
107673	$Z \to \tau\tau$ + 3 partons	21.07	1.22	3013.7
107674	$Z \to \tau\tau$ + 4 partons	6.04	1.22	3062.5
107675	$Z \to \tau\tau$ + 5 partons	1.71	1.22	3218.3

Table 4.5: Generated Z + jets samples. ATLAS specific dataset number, the name of physics process, the theoretical cross section with the according k-factor and the produced total luminosity are tabled.

dataset	physics process	σ, pb	k-factor	$\mathcal{L}_{\text{tot}}$, pb^{-1}
J5plus slice: p_{T}(min) = 280 GeV/c p_{T}(max) = ∞				
108371	QCD 6 partons	972.6	1	300
108370	QCD 5 partons	1392.8	1	300
108369	QCD 4 partons	2149.9	1	300
108368	QCD 3 partons	1944.8	1	300
108367	QCD 2 partons	750.2	1	300
J4 slice: p_{T}(min) = 140 GeV/c p_{T}(max) = 280 GeV/c				
108366	QCD 6 partons	11571.7	1	10
108365	QCD 5 partons	24249.3	1	10
108364	QCD 4 partons	49028.2	1	10
108363	QCD 3 partons	65508.9	1	10
108362	QCD 2 partons	31872	1	10
J3 slice: p_{T}(min) = 70 GeV/c p_{T}(max) = 140 GeV/c				
108360	QCD 5 partons	189793.0	1	1
108359	QCD 4 partons	552311.1	1	1
108358	QCD 3 partons	1486726.3	1	1
108357	QCD 2 partons	1116548.7	1	1
J2 slice: p_{T}(min) = 35 GeV/c p_{T}(max) = 70 GeV/c				
108355	QCD 5 partons	249184.8	1	0.1
108354	QCD 4 partons	1494832.2	1	0.1
108353	QCD 3 partons	9835389.5	1	0.1
108352	QCD 2 partons	30114236.6	1	0.1

Table 4.6: Generated QCD multijet samples. ATLAS specific dataset number, the name of physics process, the theoretical cross section with the according k-factor and the produced total luminosity are tabled.

5 Event Reconstruction

Particles produced in proton-proton collisions go through the detector material and leave signals in form of electrical charges, which are collected, digitalised and read out by the detector electronics. Event reconstruction starts with electronic signals in the detector and builds physics objects out of it. The aim is to identify the type of objects and to measure their momentum and energy with the best possible precision. This chapter describes the signature of different object types in the detector, the algorithms to identify and to reconstruct individual signatures and the corresponding performance. The reconstruction of electons, muons, jets, neutrinos and particle tracks will be discussed, because these objects have been used for this analysis.

5.1 Track Reconstruction in the Inner Detector

At the design luminosity of 10^{34} $cm^{-2}s^{-1}$ about 1000 charged particles will go through the ATLAS detector every 25 ns. Such a dense track environment requires high-precision measurements as well as a powerful track reconstruction to meet the momentum and vertex resolution requirements of physics processes. As already discussed in Chapter 3.2, the ATLAS inner detector consists of three sub-detectors: the pixel detector, the semiconductor tracker and the transition radiation tracker. The pixel detector delivers directly three-dimensional measurements, measurements in the SCT are transformed into three-dimensional space points combining the information from the opposite sides of a module. The transition radiation tracker provides only two-dimensional measurements, but allows an additional discrimination between electrons and pions utilising transition radiation in foils and fibres.

Reconstruction of tracks starts with a pattern recognition procedure, which associates detector measurements to track candidates. Global methods like histogramming and HOUGH-transform [100] are used to identify all tracks simultaneously. The measurement positions are transformed from measurement space (measurement coordinates) into track parameter space (parameters to describe trajectory of a particle). Each measurement corresponds to one curve. The point where all curves belonging to one track cross corresponds to the parameter of that track. To find these points, the transformed measurements are histogramised. For example for straight-line tracks the angle between the track and one of the axes is histogramised. Measurements which belong to one track will peak in the histogram. The pattern recognition procedure starts with measurements in the three pixel layer and the first SCT layer to search for tracks originating from the interaction region. Found seeds are then extended through the SCT to form track candidates.

After the pattern recognition procedure, many tracks not belonging to any particle, the so-called "ghost" tracks, will be produced. Such tracks will be identified in the track fitting

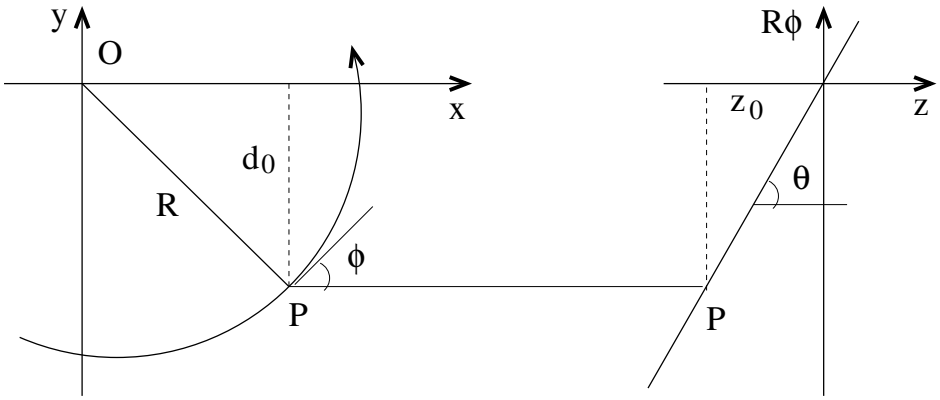

Figure 5.1: Track helix in the transverse and in the longitudinal plane.

procedure and removed. There are two categories of track fitters: global-χ^2 fitters and recursive track filters. In general the performance is equal, but for the recursive track filters it is easier to include material effects like multiple scattering or energy loss. The global-χ^2 fitters define a measure for the distance between the fitted track and measurements and minimise this measure. The recursive track filters like Kalman-filter [101] add measurements successively to the track. After the track fitting procedure track quality cuts are applied to remove "ghost" tracks. The selected tracks are then extended into the TRT and re-fitted again.

To improve the reconstruction efficiency for secondary tracks from decays of long-lived particles or conversions, a complementary track finding strategy, so-called "back-tracking" is applied. The track finding starts with unused track segments in the TRT and extends these segments into the SCT and pixel detector.

A detailed description of the inner detector track reconstruction algorithms and those implementation in the ATLAS software framework can be found in Reference [102].

The tracks are parametrised using the so-called "perigee" representation. The trajectory is defined at the point of closest approach P to a reference point O according to the reference plane defined in Section 3.2. Track helix in the transverse and in the longitudinal plane is shown in Figure 5.1. Five parameters are used in ATLAS: signed transverse impact parameter d_0, longitudinal impact parameter z_0, azimuthal ϕ and polar θ angle of the track tangent at P and charge signed inverse transverse momentum $\frac{q}{p_{\mathrm{T}}}$. The sign of d_0 is positive if the origin is to the right side of the track, otherwise negative.

The resolution σ_X of a track parameter X is a function of the particle p_{T}:

$$\sigma_X(p_{\mathrm{T}}) = \sigma_X(\infty)(1 \oplus p_X/p_{\mathrm{T}}). \tag{5.1}$$

At high transverse momenta the parameter resolution is given by the intrinsic detector resolution, thus $\sigma_X(\infty)$ denote the asymptotic resolution expected at infinite momentum. At low transverse momenta the resolution is dominated by multiple scattering. The constant p_X represent the transverse momentum value for which the intrinsic and multiple-scattering terms are equal and $\oplus$ denotes addition in quadrature. The expected track parameter resolutions for single muons are presented in Table 5.1. The distributions for pions are slightly

track parameter	0.25<$\|\eta\|$<0.5		1.5<$\|\eta\|$<1.75	
	$\sigma_X(\infty)$	p_X, GeV/c	$\sigma_X(\infty)$	p_X, GeV/c
inverse transverse momentum, q/p_T	0.34 TeV^{-1}	44	0.41 TeV^{-1}	80
azimuthal angle, ϕ	70 μrad	39	92 μrad	49
polar angle, $\cot\theta$	0.7 $\times 10^{-3}$	5.0	1.2 $\times 10^{-3}$	10
transverse impact parameter, d_0	10 μm	14	12 μm	20
longitudinal impact parameter, $z_0 \times \sin\theta$	91 μm	2.3	71 μm	3.7

Table 5.1: Expected track parameter resolutions for isolated, single muons. The values are given for two η-ranges, in the barrel with minimal amount of material and in the end-cap region with maximal amount of material [73].

broader and have small tails. The tails for electrons are even larger due to bremstrahlung. The specialised track reconstruction algorithms estimate the energy loss in detector and take it into account during the track fitting procedure [102].

5.2 Primary Vertex Reconstruction

On average 4.6 proton-proton interactions per bunch crossing are expected at luminosity of 10^{33} cm^{-2}s^{-1}. The number of collisions rises up to 23 per bunch at the nominal luminosity. In general one triggered and reconstructed high-energy signal interaction superimposed with several low-energy interactions is expected. The interaction region is described by a Gaussian with the width of about 5.6 cm in the beam direction and about 15 μm in the transverse plane. The task of the primary vertex reconstruction is an efficient and precise reconstruction of all primary interaction vertices per bunch crossing and definition of the signal collision.

The primary vertex reconstruction can be subdivided in two steps similar to the track reconstruction procedure:

- **pattern recognition procedure**: association of reconstructed tracks to a particular vertex candidate
- **fitting procedure**: reconstruction of the vertex position and determination of its error matrix, estimation of the fit quality and re-fit of track parameters at vertex

Two approaches are implemented in the ATLAS software framework [103]. The "fitting-after-finding" approach selects tracks compatible with the bunch crossing region and clusters the tracks according to the longitudinal impact parameter position. The track clusters are fitted and cleaned iteratively from outliers. The number of vertices is fixed and the rejected tracks are not used in any other cluster.

Outlier treatment can be improved with the "finding-through-fitting" procedure. The signal vertex is expected to have a higher track multiplicity, thus all tracks are fitted to one single vertex candidate at first. After the first fit, the incompatible tracks are used to create a new vertex candidate. At the next iteration a simultaneous fit of both vertices is performed. The number of vertex candidates is growing after each iteration and vertices are competing

with each other to obtain more tracks. The vertex with the largest sum of squared transverse momenta of all associated tracks $\sum p_{\mathrm{T}}^2$ is defined as the signal vertex.

The performance of the primary vertex reconstruction is physics process dependent. The reconstruction efficiency for $t\bar{t}$ events is 100% and the selection efficiency of the signal vertex is around 99%. The position resolution in the transverse plane to the beam axis is 11 μm and along the beam axis 40 μm [73].

5.3 Charged Lepton Identification

As the expected Z' boson production cross section is small, an excellent lepton identification especially at high transverse momenta is crucial. In the next two sections the electron and muon reconstruction and identification relevant for this analysis will be described.

Reconstruction and Identification of Electrons

Electrons are charged particles which leave tracks in the inner detector and induce shower in the electromagnetic calorimeter. Electrons going through matter primarily emit photons in the bremstrahlung process. Photons convert into an electron-positron pair, the produced electrons and positrons emit photons again. The pair production and the bremstrahlung continue in turn, until produced particles are absorbed by atoms. Therefore, the electromagnetic showers induced by electrons and photons are very similar. Photons are neutral particles and do not produce tracks as long as they do not convert in the material of the inner detector. To distinguish between electrons and photons we require a track not associated to a photon conversion.

Reconstruction of electrons starts from clusters reconstructed in the electromagnetic calorimeter. Electron identification variables are built from track properties and measurements in the calorimeters. An electromagnetic tower seed with transverse energy above ~ 3 GeV and a matching track which donot belong to a photon conversion in the material of the inner detector are required for an electron candidate. A track extrapolated to the electromagnetic calorimeter must match the cluster in the middle layer in a $\Delta\eta \times \Delta\phi$ window of 0.05×0.10. The ratio of energy of the cluster to the momentum of the track is required to be lower than 10. The selection efficiency of true isolated electrons with E_{T}> 20 GeV and $|\eta| < 2.5$ is about 93%. The inefficiency is caused mainly by the large amount of material in the inner detector.

The signal in the electromagnetic calorimeter induced by electrons has to be distinguished from the shower induced by hadrons like pions or protons. Due to the design of the ATLAS detector, hadrons go first through the electromagnetic calorimeter and deposit a small amount of their energy in the electromagnetic calorimeter. In general the width of an electron shower is narrower than for hadrons. Electrons leave a core with a high activity surrounded by a small area with low activity in the calorimeter. Additionally hadron showers are often produced by several particles which belong to one jet and thus their shower is broader. It is more difficult to discriminate between single pions decaying into two photons and isolated electons. The granularity of the electromagnetic calorimeter is high enough to

resolve both photons. Counting the number of energy maxima found in the electromagnetic shower allows one to identify single electrons. As the main part of the energy deposit of hadrons is in the hadronic calorimeter, a good discriminant is the ratio of the energy stored in the hadronic calorimeter to the energy stored in the electromagnetic calorimeter, the so-called hadronic leakage. Also the ratio of energy deposit in electromagnetic calorimeter to the track momentum for charged hadrons is much lower than for electrons.

To identify true high-p_T electrons, three sets of selection criteria, loose, medium and tight, have been defined, depending on the electron identification efficiency and the corresponding background rejection rate. This provides some flexibility in the choice of an optimal electron selection depending on the process we are interested in. The standard electron identification is based on cuts, optimised in up to seven bins in η and up to six bins in p_T. Briefly summarised, the selection criteria are:

- **loose electron selection criteria**
  - detector acceptance within $|\eta| < 2.47$
  - hadronic leakage
  - ratio in η of cell energies in 3×7 versus 7×7 cells from the middle layer of electromagnetic calorimeter
  - ratio in ϕ of cell energies in 3×3 versus 3×7 cells from the middle layer of electromagnetic calorimeter
  - lateral width of shower
- **medium electron selection criteria**
  - includes loose cuts
  - difference between the second largest energy deposit in a window $\Delta\eta \times \Delta\phi = 0.125 \times 0.2$ around the cell with the highest E_T and the minimal energy between the first and the second maxima
  - second largest energy deposit normalised to the cluster energy
  - total shower width
  - shower width over three strips in the first layer of electromagnetic calorimeter around the one with the maximal energy deposit
  - fraction of energy deposited outside the shower core of three central strips but within seven strips
  - track quality cuts: at least one pixel hit, at least nine pixel and SCT hits and transverse impact parameter < 1 mm
- **tight electron selection criteria**
  - includes medium cuts
  - at least one hit in the first pixel layer
  - total number of hits in the TRT
  - ratio of high-threshold hits in the TRT to the total number of hits in the TRT

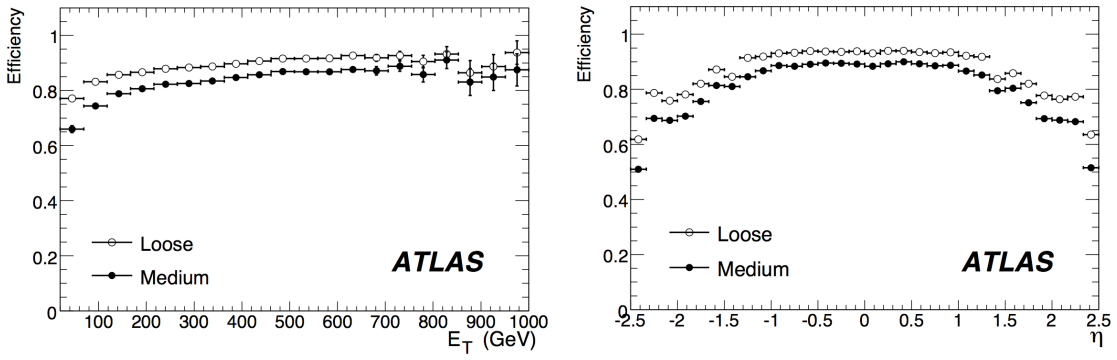

Figure 5.2: Electron identification efficiency as a function of E_T (left) and η (rigth) for electrons from $Z' \to e^+e^-$ events [73].

- $\Delta\eta < 0.005$ and $\Delta\phi < 0.02$ between the cluster and the matched track
- ratio of the cluster energy to the track momentum
- two different cuts optimised for the isolated and non-isolated electrons in jets: in case of isolated electrons additional cut on the ratio of transverse energy in a cone $\Delta R < 0.2$ to the total cluster transverse energy is applied. In case of non-isolated electrons tighter TRT cuts are required

The medium and loose electron reconstruction efficiency for $Z' \to e^+e^-$ process in E_T and η bins is presented in Figure 5.2. The loose electron selection provides the best efficiency, but a low jet rejection rate. For example the loose reconstruction efficiency in $Z \to e^+e^-$ process is about 88% and the jet rejection rate $1/\epsilon_{\text{jet}}$ is ~ 570 [73]. The medium selection improves the background rejection by a factor of 3-4 and leads to a moderate efficiency loss of $\sim 10\%$. For a tight selection the electron identification efficiency drops down to 61 - 65%, but the jet rejection rate is of order 10^5. For this analysis electrons with medium quality cuts will be used. This provides a good selection efficiency and a reasonable jet rejection rate.

Reconstruction and Identification of Muons

The primary system to detect muons is the muon spectrometer. It has been designed to identify muons with p_T above 3 GeV/c and covers the pseudorapidity range $|\eta| < 2.7$. The muon spectrometer provides a precise measurement of muon momentum up to 1 TeV/c. At low momentum, the resolution is mainly limited by the energy loss in the material in front of spectrometer. In the intermediate range the multiple scattering in the spectrometer plays a decisive role. At very high transverse momenta above 300 GeV/c, prevails the single hit resolution.

Other parts of the ATLAS detector have an impact on the muon reconstruction, too. The calorimeter absorbs hadrons, electrons and photons, thus the rate of particles except muons is reduced significantly before entering the spectrometer. The characteristic minimum ionising signature of muons in the calorimeter can aid in the muon identification. Direct measure-

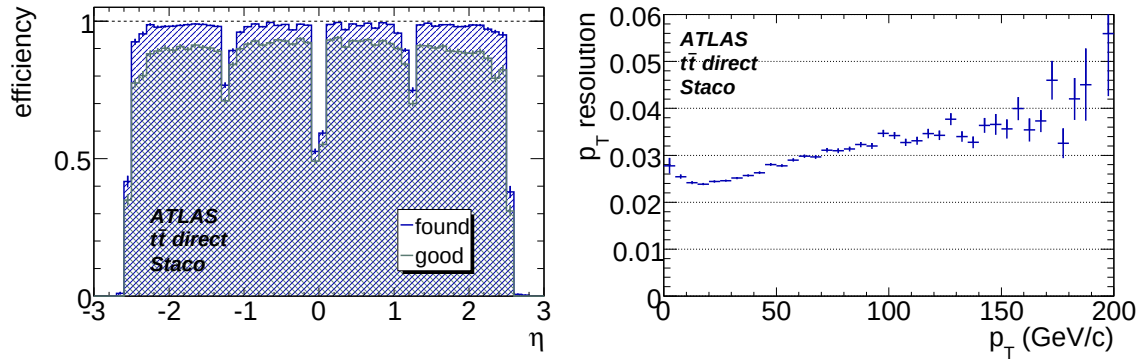

Figure 5.3: Combined muon reconstruction efficiency in $t\bar{t}$ events for "Staco" algorithm and muon momentum resolution as function of η [73]. For "good"muons a good distance match ($\chi^2 < 4.5$) between reconstructed and truth track is required.

ment of the muon energy lost in the calorimeter improves the energy resolution. The inner detector provides an independent and very precise momentum measurement for muons as well a confirmation of the spectrometer measurement, but in a reduced $|\eta| < 2.5$ range.

The muon momentum resolution is improved by a combination of measurements in the inner detector and in the spectrometer for muons with transverse momenta between 30 GeV/c and 200 GeV/c. At transverse momenta below 30 GeV/c the resolution achieved in the inner detector is better than in the spectrometer. At very high momenta above 200 GeV/c, the spectrometer has better performance due to the longer lever arm.

As shown in Figure 5.3, the muon reconstruction efficiency is close to 100% except in regions where the detector coverage is poor, that is for $|\eta|$ around 0.0 and 1.2. On average the reconstruction efficiency in $t\bar{t}$ events is 94.3% and for high p_{T} muons from the Z' boson decay is 91.0%. The transverse momentum resolution $\sigma_{p_{\mathrm{T}}}/p_{\mathrm{T}}$ is around 3-4% for muon p_{T} below 200 GeV/c and increases up to 10% at 1 TeV/c. Misreconstruction and charge misidentification rates are around 0.01%.

5.4 Jet Reconstruction

Jet algorithms define the jets. They provide a set of rules that indicate how close two particles must be to belong to one jet and how the momentum of the combination is calculated. A jet algorithm should fulfil several requirements, which become apparent in different application of jets in the experiments and in theory. The jet definition should be mostly independent of the non-perturbative effects like hadronisation and underlying event. The measured observables should be comparable to the theoretical calculations. Addition of an infinite soft parton (infrared safety, illustrated in Figure 5.4(a)) or a parton radiated by an infinite small angle (collinear safety, illustrated in Figure 5.4(b)) should not change properties and number of resulting jets and they should be independent of the detector details.

At the LHC a new energy regime will be explored, heavy particles like W and Z bosons or top quarks will be produced relatively often at high transverse momenta. Their hadronic

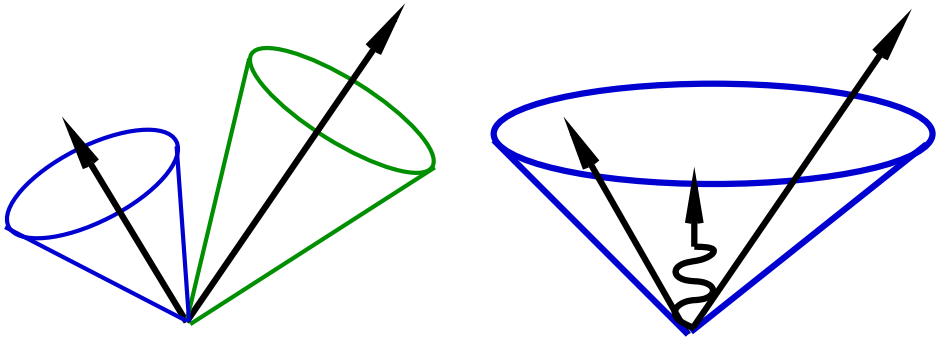

(a) infrared safety

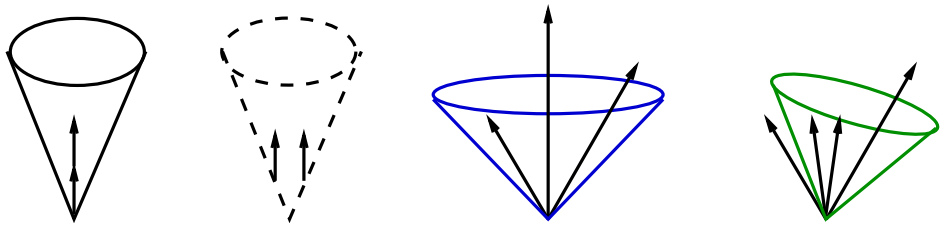

(b) collinear safety

Figure 5.4: (a) Illustration of infrared sensitivity: the arrows represent seed particles, a soft radiated parton causes a merging of the seeds in one jet. (b) Illustration of the collinear sensitivity: the splitting into two particles changes the number of jets or jet properties.

decay products may form single jets with a complex substructure. To study such substructures, we need a suitable jet finder. In the ATLAS reconstruction framework the same jet finder can be run on miscellaneous objects like calorimeter signal towers, topological cell clusters in the calorimeters, reconstructed tracks, generator particles and partons. A well-maintained open-source software package FastJet [104] is used for all jet finder implementations, except for the ATLAS Cone algorithm.

A common feature of all jet finder implementations in ATLAS is the full four-momentum recombination scheme. This scheme conserves energy and momentum and provides a meaningful single-jet mass. The algorithms can be divided in two broad categories. The first category is based on the energy flow into a geometric cone (cone algorithms) and the second one on the recombination of the closest pairs of the particles (cluster algorithms).

ATLAS Cone Algorithm

There is a wide range of "cone algorithms" based on the maximisation of the energy in a geometric cone. The key parameter of the cone algorithms is the radius of the cone in the $(\eta - \phi)$-plane, R_{cone}. The ATLAS cone algorithm uses seeds in order to initiate the first cone candidates. The seed is a calorimeter tower or cluster, parton or particle with E_{T} or p_{T} above the seed threshold. All objects with a distance R smaller than the fixed cone size R_{cone} will be

combined with the seed. The direction of the seed is updated from the four-momenta of the constituents inside the initial cone and a new cone is centred around it. The recombination continues untill a seed with a stable direction is found. This procedure is repeated for all found seeds. The seeds can share the constituents, the ambiguities are solved in the last so-called "split and merge" step. The jets which share constituents with 50% of E_{T} or p_{T} of the lowest energy jet will be merged.

The seeded cone algorithms are not infrared safe. An additional soft particle, acting as a new seed, can cause the iterative process to find a new stable cone. This can lead in the split-merge step to the modification of the final jets. The ATLAS cone algorithm is still used in many physics analysis for more or less historical reasons. The ATLAS performance group responsible for the jet and missing transverse energy calibration has established now the Anti-k_{T} jet algorithm, which belongs to the second category of the jet reconstruction algorithms.

Cluster Algorithms

The cluster algorithms are based on the pair-wise clustering of initial constituents. The key parameters are a distance measure between the objects and some condition upon which clustering should not be carried out. The distance measures d_{ij} between two objects i and j and d_{iB} between the object i and the beam, are defined as:

$$d_{ij} = \min\left(p_{\mathrm{T}i}^{2m}, p_{\mathrm{T}j}^{2m}\right)\frac{(\Delta\mathrm{R})_{ij}^{2}}{R^{2}}, \tag{5.2}$$

$$d_{iB} = p_{\mathrm{T}i}^{2m}, \tag{5.3}$$

where $(\Delta\mathrm{R})_{ij}^{2}$ is the distance between two objects in the $(\eta-\phi)$-plane. The d values are computed for all possible combinations. If d_{ij} is the smallest value, objects i and j are combined using four-momentum combination and the remaining combinations are recalculated. If the smallest value is d_{iB}, this object is considered as a jet and is removed from the initial objects. The variable R defines the resolution at which jets are resolved from each other compared to the beam.

There are three different cluster algorithms, depending on the value of variable m:

- k_{T} algorithm [105, 106] with $m = 1$,
- Anti-k_{T} algorithm [107] with $m = -1$,
- Cambridge/Aachen algorithm [108, 109] with $m = 0$.

If $m = 1$, the objects with low relative p_{T} are merged first and the final merge is the hardest one. In some sense this procedure is inverse to the splitting within a parton shower and provides a tool to analyse the substructure of jets. Not merged soft partons will be rejected by a final p_{T} cut and associated with the beam.

If $m = -1$, the soft objects will tend to cluster with the hard ones, long before they cluster among themselves. The hard objects will accumulate all soft ones within a cone of radius R, if no hard neighbours are within $2R$. The result will be a perfectly conical jet. Two comparably hard objects within $R < \Delta\mathrm{R} < 2R$ will share the energy between them

depending on the relative p_T and the distance. The hard objects within $\Delta R < R$ will be merged in one single jet.

For $m = 0$ the p_T of the objects is irrelevant and the clustering will be carry out according to the angular distance R between two objects, starting with the closest one. This algorithm can improve the single-jet mass resolution, removing small and peripheral subjets.

All three cluster algorithms are infrared and collinear safe. The Anti-k_T algorithm is the most preferred one at ATLAS. Studies in Reference [110] demonstrate that the Anti-k_T jets are less affected by underlying event and pileup effects and show best performance for all jet flavours, fragmentation and showering models in terms of reconstruction efficiency. The jet area is the most stable and should be the easiest to calibrate.

Calorimeter Jets

The jets are reconstructed with the jet algorithms described above using calorimeter signals. The ATLAS calorimeter is a complex system with about 200 000 cells. The cells are combined into a larger signal objects, which are the input for the jet finder. There are two concepts for the combination: signal towers and topological cell cluster.

- **signal towers**: The calorimeter cells are projected onto a grid in the (η, ϕ)-plane as illustrated in Figure 5.5(a). The towers have a fixed size of $\Delta\eta \times \Delta\phi = 0.1 \times 0.1$. The whole acceptance region is divided uniform in 6 400 towers in total. The signal cells contribute their total raw signal as measured in the calorimeter to the tower signal, weighted by the overlap fraction of the cell area with the towers. The energy scale of the raw signal is called electromagnetic (EM) energy scale. No further corrections or calibrations are applied at this stage.
- **topological cell cluster**: The signal cells are clustered to three-dimensional "energy blobs", representing the particle showering in the calorimeter. The clustering starts with the seed cells, whose signal significance defined as the cell energy E_{cell} devided by the cell noise σ_{noise}, $\Gamma = E_{\text{cell}}/\sigma_{\text{noise}}$, is above a certain threshold, $|\Gamma| > 4$. All direct neighbours are collected first. Neighbours of neighbours are added to the cluster if their signal is above a secondary threshold, $|\Gamma| > 2$. Finally, the ring of guard cells with the significance $|\Gamma| > 0$ are added. Afterwards the initial clusters are analysed for the local signal maxima and splitted if any are found. An example of reconstructed clusters is illustrated in Figure 5.5(b).

In the pseudorapidity range $1.5 \lesssim |\eta| \lesssim 2.5$ single particles can be resolved by the clustering algorithm. In the central region $|\eta| \lesssim 1.5$ the cell size is larger and the shower of single particles may overlap. On average 1.6 particles are reconstructed in one cluster. In the forward region $|\eta| \gtrsim 2.5$ the linear distance between the particles is smaller and the calorimeter cells are larger. Either leads to a worse resolution.

Similar to the tower signals, the topological cell clusters are build from the cell signals at the EM scale. Additionally the energy can be calibrated to a local hadronic energy scale. The clusters are classified as electromagnetic, hadronic and noise. The energy of hadronic clusters is corrected according to their location and the signal shape. The energy lost in the

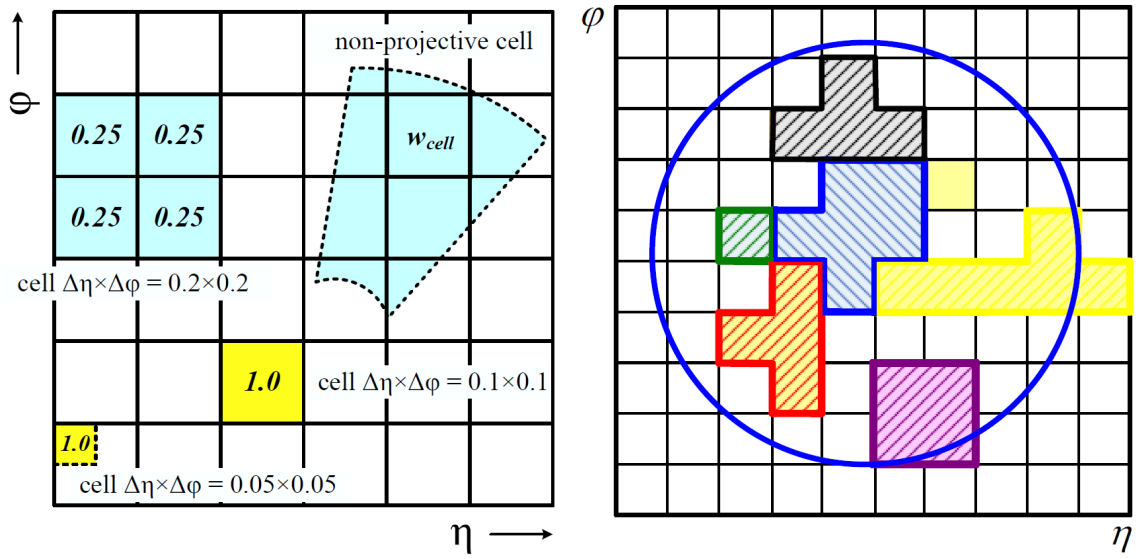

(a) signal towers (b) signal clusters

Figure 5.5: (a) Building of signal towers, cells contribute with their total signal weighted by the overlap fraction w_{cell}. (b) Building of signal clusters, cells contribute only when their signal significance is above a certain threshold. Thus clusters have noise suppression build in.

dead material is corrected for all clusters. The correction functions are based on the single particle simulations.

Jet Reconstruction Flow

The jet reconstruction flow is sketched in Figure 5.6. It starts from calorimeter towers or topological clusters measured at the EM scale. The charge output for hadrons in the calorimeter is smaller than for electrons and has to be corrected to the hadronic energy scale. The way how to calibrate hadronic signals will be discussed later. The tower signals are only on the EM scale. The topological clusters are either on this scale or are calibrated on a local hadronic energy scale. Signal fluctuations from noise can lead to a negative tower signal. Combination of negative signal towers with nearby positive signal towers cancels most of the fluctuations. Only negative signal towers without nearby positive towers are droped. The topological clusters have noise suppression build in.

Towers or clusters are input to the jet finding algorithms. The output are calorimeter jets on the electromagnetic energy scale or already fully calibrated calorimeter jets on the hadronic energy scale. On the non-calibrated calorimeter jets cell weighting technique is applied [111]. The signal in each calorimeter cell i is weighted depending on the cell location and the cell signal density $\rho_i = E_i/V_i$, where E_i is the energy in the cell on the electromagnetic scale and V_i is its volume. For the high signal densities more likely generated by electrons the weighting factor is around 1. It rises up to 1.5, the typical electron/pion signal

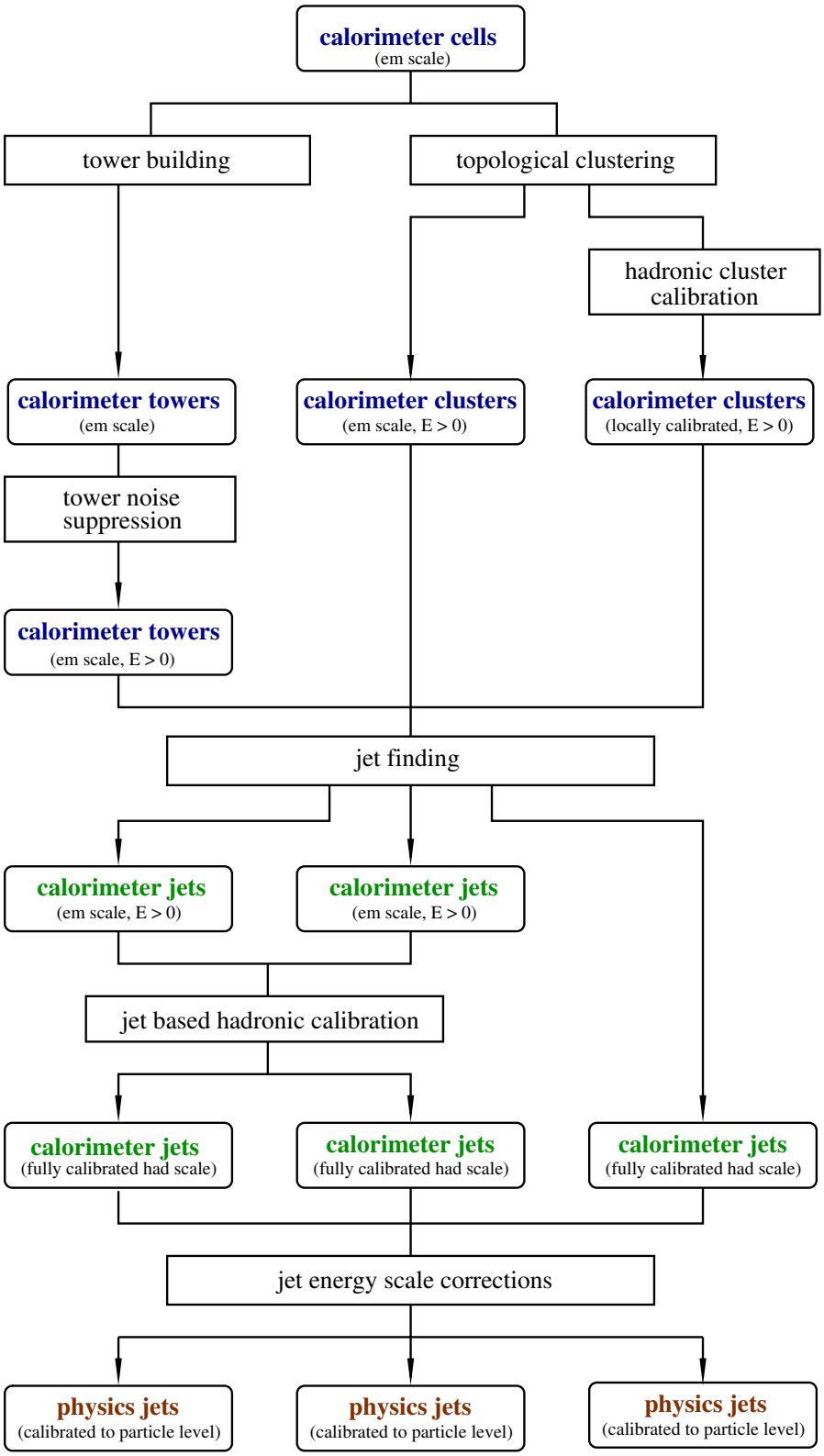

Figure 5.6: Jet reconstruction flow in ATLAS.

ratio for the ATLAS calorimeter for decreasing cell signal densities more likely generated by hadrons. The weighting functions are determined using the cone R_{cone}= 0.7 jets in fully simulated QCD di-jet events by fitting the reconstructed calorimeter tower jet energies to the matched Monte Carlo truth particle jet energies.

The calibrated calorimeter jets with energy below 7 GeV are discarded. More refined corrections are needed to calibrate the calorimeter jets to the particle level. Those corrections depend on the jet reconstruction algorithm and include noise, pile-up and algorithm effects. Again this calibration step relies on the Monte Carlo simulations.

For this analysis calibrated calorimeter jets reconstructed with the default ATLAS cone R_{cone}= 0.4 jet algorithm have been used. One outstanding issue has to be studied before we can decide which type of calorimeter objects to use in the analysis, towers or topological cell clusters. Because of the expected production of heavy particles, the invariant jet mass has gained interest and will be investigated in more details in the next section.

Jet Mass

The invariant jet mass is expected to be a useful property in the selection of events with highly boosted top quarks and electroweak bosons [112–114]. Partons are massless, except for the heavy quarks, but the jets are not. The mass of QCD gluon or light-quark jets is generated by the gluon emission. A heavy quark jet has additionally an intrinsic mass from the heavy quark. The expected average jet mass arising from perturbative QCD interactions has been calculated to the first non-trivial order in the hadron collider context [115]:

$$\left\langle M_{\text{J}}^2 \right\rangle \simeq \overline{C}\left(\frac{p_{\text{T}}}{\sqrt{s}}\right) \cdot \alpha_{\text{S}}\left(\frac{p_{\text{T}}}{2}\right) \cdot p_{\text{T}}^2 R^2, \tag{5.4}$$

where the prefunction $\overline{C}$ depends on the relative fraction of quarks and gluons and decreases slowly with increasing momentum fraction of jets $\frac{p_{\text{T}}}{\sqrt{s}}$. R is the cone size of the used jet algorithm and $\sqrt{s}$ is the centre-of-mass energy. Alone from perturbative QCD the jet mass growing nearly linearly with the jet size is expected. The authors claim, within 25% accuracy, the numerical value for the prefactor is roughly 0.2:

$$\sqrt{\left\langle M_{\text{J}}^2 \right\rangle} \simeq \left(0.2 + \frac{1}{6}\left(0.3 - \frac{p_{\text{T}}}{\sqrt{s}}\right)\right) \cdot p_{\text{T}} R, \tag{5.5}$$

including the dependence on α_{S}, the colour charges and the parton density functions.

Jet mass distribution of the jet with the highest p_{T} for four dijet p_{T} slices [1)] can be found in Figure 5.7(a). The peak shifts to higher jet masses for rising dijet p_{T}, above the peak the distribution falls slowly. The dependence of the average jet mass with respect to the jet p_{T} is presented in Figure 5.7(b) for PYTHIA dijet and ALPGEN + HERWIG multijet events. The cluster jets are reconstructed with the cone R_{cone}= 0.4 algorithm and a jet with the highest p_{T}

[1)] The dijet p_{T} slicing strategy is similar to the strategy used for ALPGEN QCD multijet samples defined in Section 4.3.2. The QCD dijet process is divided in multiple samples that correspond to bins of dijet p_{T} in the event [99].

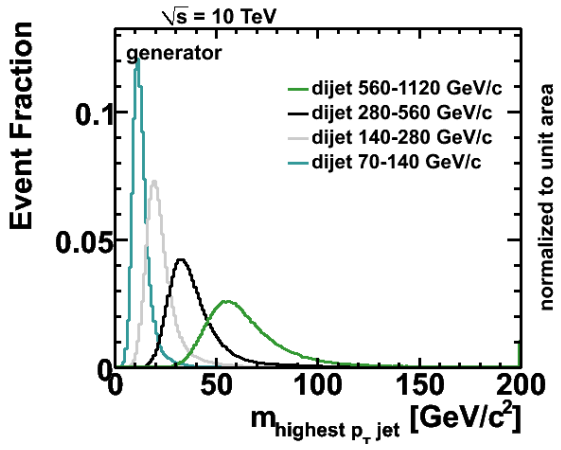

(a) jet mass distributions

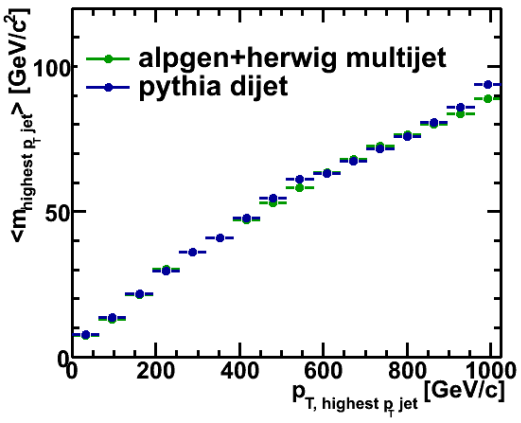

(b) average jet mass

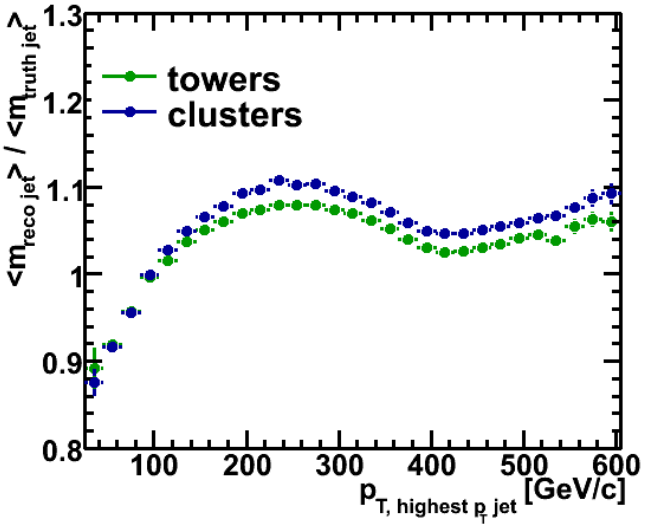

(c) jet mass ratio

Figure 5.7: (a) PYTHIA QCD jet mass distributions of the highest p_T jet for several jet p_T slices. (b) Average jet mass distribution of highest p_T jet in QCD events generated with PYTHIA and ALPGEN. (c) Ratio of the reconstructed jet mass for tower and cluster jets to truth jet mass at generator level as a function of jet p_T in $Z' \to t\bar{t}$ events. Reconstructed jets are matched to truth jets requiring $\Delta R < 0.2$

is selected. According to Equation 5.5, for a jet with p_T = 500 GeV/c we expect a jet mass of around 50 GeV/c^2 and this fits quite well to this simple rule. We observe a good agreement between both generators too, though different hadronisation models have been used. A jet p_T above 800 GeV/c is needed to produce QCD jets with a mass comparable to the W boson mass. The production cross section for high-energy QCD jets is only a few pb and for the first resonance searches in the semi-leptonic channel negligible, but one should keep in mind that the QCD jets are not massless.

From the experimental point of view, the jet mass reconstruction is a challenging task. To get a perfect jet mass resolution, all hadrons in jet have to be reconstructed as precisely as possible. Due to the showering and resulting overlap of signals in the calorimeter, the jet mass will be smeared. In the pseudorapidity range $1.5 \lesssim |\eta| \lesssim 2.5$ single particles can be resolved, but in the central and in the forward region the calorimeter cells are too large to resolve single particles. Low-energy particles with $p_{\mathrm{T}} < 500$ MeV/c will be bent by the magnetic field in the inner detector and get lost for the jet reconstruction. Dead material in the detector will absorb the low-energy photons. The reconstructed jet mass agrees with the true jet mass within 10% as presented in Figure 5.7(c). At jet transverse momenta below 100 GeV/c, the jet mass is underestimated, at higher p_{T} overestimated. The ratio $\frac{m_{\text{reco jet}}}{m_{\text{truth jet}}}$ is closer to 1 for tower jets, because tower truth jets have been used to calibrate the jet energy scale. Thus, for this analysis the tower jets will be used.

5.5 Neutrino Reconstruction

The interaction probability for neutrinos with the material of the detector is close to zero. Therefore they can be reconstructed only indirectly from the total energy balance of the event. The longitudinal component of the energy in hadron-hadron collisions is unknown, since the colliding partons carry only a fraction of the energy of the hadrons. But the initial transverse component is zero and the transverse energy balance can be used to reconstruct at least the transverse energy of neutrino, so-called $\vec{E}_{\mathrm{T}}^{\mathrm{miss}}$.

A precise measurement of the missing transverse energy is essential for the QCD multijet background suppression. The main challenge is to minimise the impact of the limited detector coverage, finite detector resolution, presence of dead regions and noise in the detector that can produce fake $\vec{E}_{\mathrm{T}}^{\mathrm{miss}}$. The transverse missing energy is primarily reconstructed from the energy deposits in the calorimeter and reconstructed muon tracks. The calorimeter extends to a large pseudorapidity range and detects particles even in the very forward region. There are several inactive transition regions between different parts of the calorimeter, which have to be taken into account. Also dead and noisy readout channels contribute to fake $\vec{E}_{\mathrm{T}}^{\mathrm{miss}}$.

Two algorithms are available to reconstruct missing transverse energy. One uses the calorimeter cells as input and the other uses the reconstructed objects. The object-based $\vec{E}_{\mathrm{T}}^{\mathrm{miss}}$ reconstruction is used for analyses that are sensitive to low-p_{T} deposits coming from pions, soft jets, the underlying event and from pile-up. A detailed description for the object-based algorithm can be found in [73], for this analysis only the cell-based method is used. The cell-based missing energy reconstruction starts with cells that survive the noise suppression procedure and sums up the transverse energy deposits in the calorimeter, corrected by the energy lost in the cryostat and energy of measured muons.

The calorimeter cells are calibrated depending on the nature of the shower - electromagnetic or hadronic one. Muons reconstructed in the muon spectrometer and with a matched track in the inner detector are considered. But only the energy measurement in the spectrometer is taken, hence the energy lost in the calorimeter is already included. The energy of jets is corrected by the energy lost in the cryostat between electromagnetic and hadronic calorime-

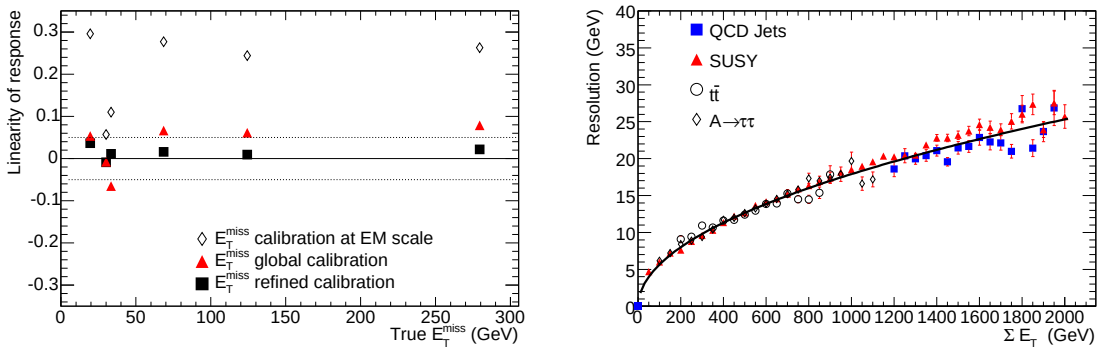

(a) linearity (b) resolution

Figure 5.8: (a) Linearity of reconstructed missing transverse energy for different physics processes as a function of true missing transverse energy at different calibration stages. (b) Missing transverse energy resolution as a function of the total transverse energy. The curve corresponds to $\sigma = 0.57\sqrt{\sum E_{\mathrm{T}}}$ fit [73].

ter. Already at this point a good linearity $\frac{|\vec{E}_{\mathrm{T}}^{\mathrm{miss}}|(\mathrm{true}) - |\vec{E}_{\mathrm{T}}^{\mathrm{miss}}|(\mathrm{reco})}{|\vec{E}_{\mathrm{T}}^{\mathrm{miss}}|(\mathrm{true})}$ and a good energy resolution is achieved. Finally the calorimeter cells are associated with the reconstructed and identified high-p_{T} objects, in a chosen order: electrons, photons, muons, hadronically decaying τ-leptons, b-jets and light jets. Refined calibration of the objects is used to improve the global calibration of calorimeter cells. For calorimeter cells not associated with any reconstructed high-p_{T} objects only the global calibration can be used. The linearity of response for reconstructed $\vec{E}_{\mathrm{T}}^{\mathrm{miss}}$ at different calibration stages as well as the $E_{\mathrm{T}}^{\mathrm{miss}} = |\vec{E}_{\mathrm{T}}^{\mathrm{miss}}|$ resolution is presented in Figure 5.8. Refined $E_{\mathrm{T}}^{\mathrm{miss}}$ calibration shows the best results compared to the calibration at the earlier stages. For $E_{\mathrm{T}}^{\mathrm{miss}}$ above 40 GeV, the linearity is within 2%, at lower missing transverse energies the measurement is biased due to the finite resolution. The $E_{\mathrm{T}}^{\mathrm{miss}}$ resolution behaves close to $\sigma = 0.57\sqrt{\sum E_{\mathrm{T}}}$. Only at very low $E_{\mathrm{T}}^{\mathrm{miss}}$ values, where the contribution of noise is more important, and at very high $E_{\mathrm{T}}^{\mathrm{miss}}$ values, where the constant term in the resolution dominates, we observe a stronger deviation from the $\sqrt{\sum E_{\mathrm{T}}}$ behaviour.

Reconstruction of the longitudinal component of the neutrino momentum $p_{z,\nu}$ is only possible when some additional information is taken into account. In our case the neutrino is coming from the W boson decay. Thus, assuming the W boson is produced on-shell, we can use its pole mass m_W= 80.4 GeV/c^2 as constraint to obtain an equation for the missing longitudinal component of the neutrino momentum. The sum of the four-vectors of the lepton p_ℓ and the neutrino p_ν is equal to the four-vector of the W boson p_W:

$$p_W = p_\ell + p_\nu. \tag{5.6}$$

After squaring the equation, rearranging its terms and neglecting the invariant masses of

the lepton and the neutrino, a quadratic equation in $p_{z,\nu}$ is obtained:

$$p_{z,\nu}^2 - 2 \cdot \frac{\mu p_{z,\ell}}{E_\ell^2 - p_{z,\ell}^2} \cdot p_{z,\nu} + \frac{E_\ell^2 p_{T,\nu}^2 - \mu^2}{E_\ell^2 - p_{z,\ell}^2} = 0, \tag{5.7}$$

$$\text{with} \quad \mu = \frac{1}{2} m_W^2 + p_{T,\ell} p_{T,\nu} \cos\Delta\phi, \tag{5.8}$$

where the azimuthal angle difference between the missing transverse energy and the lepton is given by $\Delta\phi$. E_ℓ is the energy and $p_{z,\ell}$ is the longitudinal component of the lepton momentum and $p_{T,\nu}$ is the transverse component of the neutrino momentum. Equation 5.7 is solved by

$$p_{z,\nu}^{\pm} = \frac{\mu p_{z,\ell}}{p_{T,\ell}} \pm \sqrt{\frac{\mu^2 p_{z,\ell}^2}{p_{T,\ell}^4} - \frac{E_\ell^2 p_{T,\nu}^2 - \mu^2}{p_{T,\ell}^2}}. \tag{5.9}$$

If the radicand is positive, two real solutions will be retrieved. The solution with the smaller absolute value is taken, because in about 70% of $t\bar{t}$ events the smaller solution leads to values close to the true values. But if the reconstructed transverse mass of the W boson $m_{T,W}$

$$m_{T,W}^2 = E_{T,W}^2 - \vec{p}_{T,W} = 2 p_{T,\ell} p_{T,\nu} (1 - \cos\Delta\phi) \tag{5.10}$$

exceeds the pole mass and the radicand becomes negative, the solutions become complex. The width of the W boson is too narrow to explain the large values of $m_{T,W}$ and the main reason is the imperfect reconstruction of the missing transverse energy. An approach has been developed in [116] to handle complex solutions. The idea is to modify the E_x^{miss} and E_y^{miss} components, so that the resulting solution for the longitudinal component becomes real. It has been shown that the modified values for the transverse missing energy are closer to the true values and improve the missing energy reconstruction.

6 Topological Vertex Finder

Vertex finding implies the finding and reconstruction of the common intersection points between sets of tracks. It can be the proton-proton interaction point as well as the decay point of an unstable particle. Most of the tracks in an event originate from the collision point, indicating the primary vertex of that event. Some tracks originate from long-lived particles, which decay at a measurable distance from the primary vertex, at the so-called secondary vertex. Unstable particles produced at secondary vertices decay again and build tertiary vertices. A primary vertex in $t\bar{t}$ events often contains 50 or more tracks while secondary or tertiary vertices are built of just 2 or 3 tracks.

Requirements on a vertex finder depend on the type of vertices. A primary vertex finder is designed to identify and to reconstruct the location of the hard parton collision with a high precision in the environment of high track multiplicities. A well identified primary vertex is an important ingredient for the reconstruction of secondary vertices. A secondary vertex finder is designed to identify vertices with a low track multiplicity, also in case of mis-measured tracks which can fake secondary tracks or vertices very close to the primary interaction.

One of the important applications of the secondary vertex reconstruction is the identification of jets originating from b-quarks, so called b-tagging. Many interesting physics processes, for example top quark decays, contain bottom quarks in the final state, while the background processes contain only light (up, down, strange) quark jets, gluon jets or charm quark jets. Thus b-tagging can be used to separate signal from background.

This chapter starts with a description of the b-jet properties used in b-tagging as well the selection and association of tracks to jets. An overview of b-tagging algorithms available in ATLAS will be also given. In the second part of this chapter a new vertex finder algorithm, topological vertex finder, will be introduced. Finally, its application to b-tagging and its performance will be discussed using $t\bar{t}$ Monte Carlo events.

6.1 Properties of b-Quark Jets

Several properties of the hadronisation of b-quarks are unique and allow one to identify jets originating from b-quarks. A b-quark fragments into a b-flavoured hadron, since the strong interaction is flavour blind. In about 86% of cases an excited B hadron B^* or B^{**} is produced, otherwise a ground state B hadron is produced directly. The excited B hadron decays immediately into a ground state B hadron and produces one or more additional particles. The produced B hadron decays weakly, its lifetime is of order 1.6×10^{-12} s.

The B hadron keeps on average a significant fraction of b-quark energy as described by the fragmentation function shown in Figure 6.1. The combination of the long lifetime and

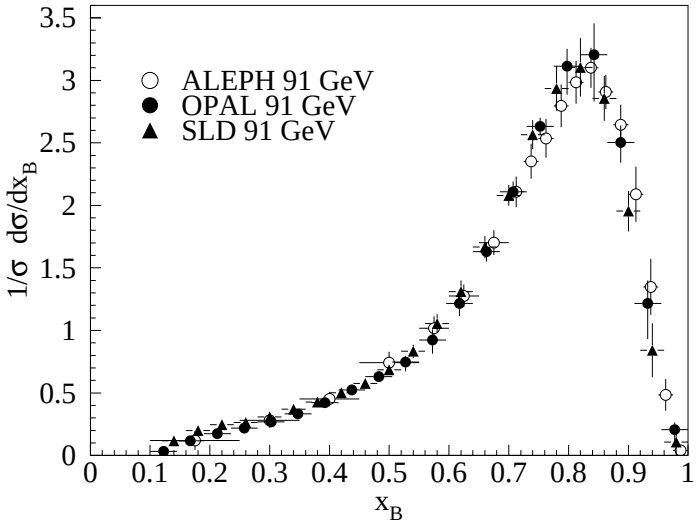

Figure 6.1: Measured e^+e^- fragmentation function of b-quarks into B hadrons at $\sqrt{s} \approx 91$ GeV [14].

the high kinetic energy leads to a secondary vertex significantly displaced with respect to the primary vertex position. On average, a B hadron in jet with $p_T = 50$ GeV/c travels circa 3 mm, before it decays. The heavy mass of the B hadron leads to the relatively wide angles between the flight direction of the B hadron and its decay products. This effect simplifies the reconstruction of the secondary vertex position. The presence of a displaced secondary vertex with a large energy fraction of the original b-quark retained by the B hadron, form a typical signature used to identify b-quark jets.

Since the CKM matrix element $|V_{cb}|$ is larger than $|V_{ub}|$, the B hadron decays preferably into a D hadron. A D hadron has a shorter lifetime and its momentum is lower than the B hadron momentum, thus the travelled distance is on average smaller, but still a tertiary vertex can be separated from the secondary vertex. Reconstruction of a D hadron decay vertex improves the performance of the b-jet identification.

About 42% of B hadron decays, direct or via D hadron, contain an electron or a muon. On average the lepton transverse momentum is of order of the B or D hadron mass. The identification of a lepton with a high transverse momentum with respect to the jet axis is used to tag b-jets, since leptons in light jets are produced from in-flight decays of charged kaons, neutral or charged pions and γ-conversions.

The main properties of B and D hadrons are listed in Table 6.1. A $B \rightarrow D$ hadron decay chain in b-jets is depicted in Figure 6.2. Few tracks from the primary vertex as well secondary tracks from B and D hadrons are shown. The flight direction of hadrons is close to the jet axis, defined by the jet momentum.

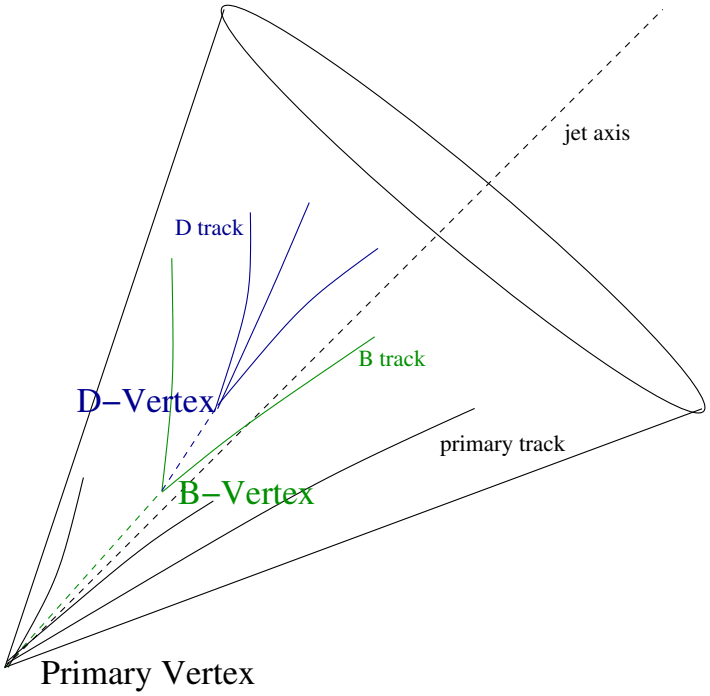

Figure 6.2: Schematic view of a $B \rightarrow D$ hadron decay chain in b-jets.

hadron		branching fraction, %	mass, MeV/c^2	lifetime $\times 10^{-12}$, s
B hadron: $\bar{b} \rightarrow B$ hadron				
B^+		40.1 ± 1.3	5279.17 ± 0.29	1.638 ± 0.011
B^0		40.1 ± 1.3	5279.50 ± 0.30	1.525 ± 0.009
B_s^0		11.3 ± 1.3	5366.3 ± 0.6	$1.472^{+0.024}_{-0.026}$
B baryon	Λ_b^0	8.5 ± 2.2	5620.2 ± 1.6	$1.391^{+0.038}_{-0.037}$
	Σ_b^+		5807.8 ± 2.7	–
	Σ_b^-		5815.2 ± 2.0	–
	Ξ_b^0		5790.5 ± 2.7	$1.49^{+0.19}_{-0.18}$
	Ξ_b^-		5790.5 ± 2.7	1.56 ± 0.26
	Ω_b^-		6071 ± 40	$1.1^{+0.5}_{-0.4}$
D hadron: B meson $\rightarrow D$ hadron + anything				
$D^\pm$		23.1 ± 1.5	1869.60 ± 0.16	$(1040 \pm 7) \times 10^{-3}$
$D^0/\bar{D}^0$		62.5 ± 2.9	1864.83 ± 0.14	$(410 \pm 1.7) \times 10^{-3}$
$D_S^\pm$		8.3 ± 0.8	1968.47 ± 0.33	$(500 \pm 7) \times 10^{-3}$

Table 6.1: Main decay modes and some properties of B and D hadrons [14].

6.2 Association and Selection of Tracks and Jet Flavour Labelling

The main ingredient for the identification of b-jets are tracks of charged particles. Since jets are reconstructed in the calorimeter and tracks are reconstructed in the inner detector, they have to be associated to each other. This is done using the angular distance of track momenta $\vec{p}_{\text{trk}}$ to the jet momentum $\vec{p}_{\text{jet}}$ at the point of closest approach to the interaction point:

$$\Delta\text{R}(\vec{p}_{\text{jet}}, \vec{p}_{\text{trk}}) < R_{\text{cut}}. \tag{6.1}$$

The default R_{cut} value is 0.4, independently from the parameters of jet finding algorithms. The performance of b-tagging algorithms can be improved using a cut value, that depends on the jet p_{T} as investigated in Reference [73], but typically only in case of significant environmental contamination like additional tracks from underlying event, pile-up or from close lying light quark jets. For these studies it is sufficient to use the default cut value of $R_{\text{cut}} = 0.4$.

In this analysis, jets are reconstructed with the ATLAS cone $\Delta\text{R} = 0.4$ algorithm using calorimeter towers. Selected jets have transverse momentum $p_{\text{T}} > 15$ GeV/c and $|\eta| < 2.5$. At least one reconstructed track has to be associated with jets. After association of tracks to jets, the tracks are filtered to remove mis-measured tracks as well as secondary tracks coming not from B hadron decays. The aim is to reduce the number of fake vertices due to the mis-measured tracks, which can randomly cross primary tracks and to remove secondary vertices of long lived particles like K^0_{S}, Λ and electromagnetic (γ conversions) or hadronic interactions with the detector material. The selection cuts are summarised in Table 6.2.

To reduce the number of tracks from long lived particles or from material interactions in the detector, at least one hit in the first layer of the pixel detector is required. The measurement in the first layer is also crucial for the resolution of the vertex position. To fit requirements on track quality, a minimum number of hits in the pixel and SCT detectors are required. Track fit quality divided by the number of degrees of freedom should be $\chi^2/n.d.f. < 5$. As already mentioned in the previous section B hadrons keep about 70% of the original b-quark energy. In b-jets the transverse momentum of B hadron decay products is on average higher than for tracks originating from the b-quark fragmentation as shown in Figure 6.3. B hadrons decay on average to five charged particles. The transverse momentum of tracks from D hadrons is on average slightly higher than for B hadron tracks because of the smaller charged decay multiplicity of approximately 3 tracks for D hadrons. The tracks in light jets have lower p_{T}, than the B hadron tracks. But their p_{T} is still higher, than p_{T} of the fragmentation tracks in b-jets. The track p_{T} cut is set to 800 MeV/c to reject low p_{T} tracks from fragmentation.

Secondary tracks are expected to have high transverse $IP_{r\phi}$ and longitudinal IP_z impact parameters. They are calculated at the point of the closest approach with respect to the primary vertex:

$$IP_{r\phi} = d_0 \qquad \text{and} \qquad IP_z = z_0 \cdot \sin\theta, \tag{6.2}$$

where d_0, z_0 and θ are perigee parameters. Figure 6.3 shows that tracks originating from B and D hadrons have significantly higher impact parameters than prompt tracks from fragmentation but still lower than the impact parameters of tracks from K^0_{S}, Λ or γ decays. Since

selection criteria	cut value
jet selection criteria	
transverse momentum	$p_T > 15$ GeV/c
pseudo-rapidity	$\|\eta\| < 2.5$
number associated tracks	$n_{tracks} >= 1$
track selection criteria	
transverse momentum	$p_T > 800$ MeV/c
track fit quality	$\chi^2/n.d.f. < 5$
number of b-layer hits	$n_{b\text{-}layer} \geq 1$
number of pixel detector hits	$n_{pixel} \geq 2$
number of SCT hits	$n_{SCT} \geq 4$
number of pixel + SCT hits	$n_{pixel+SCT} \geq 7$
transverse impact parameter	$\|IP_{r\phi}\| < 4$ mm
longitudinal impact parameter	$\|IP_z\| < 6$ mm
transverse impact parameter error	$\sigma(IP_{r\phi}) < 0.35$ mm
longitudinal impact parameter error	$\sigma(IP_z) < 2.5$ mm

Table 6.2: Jet and track selection criteria for b-tagging.

vertices of long lived particles and from material interactions will be reconstructed and rejected, a looser selection cut on impact parameters can be chosen. Impact parameter errors $\sigma(IP_{r\phi})$ and $\sigma(IP_z)$ are required to be below 0.35 mm and 2.5 mm, respectively.

The relative contribution of tracks in b- and light jets is presented in Table 6.3. About 95% of selected tracks in light jets are prompt tracks. b-jets contain 38% tracks from fragmentation, 30% of tracks are from B hadron and 28% of tracks are from D hadron decays. On average 62% of B hadron tracks and 63% of D hadron tracks survive the selection in b-jets.

To study the performance of b-tagging algorithms, we have to associate reconstructed jets to the initial partons or τ leptons. As already discussed in Section 5.4, this association is ambiguous in some cases. To label jets, a default ATLAS reconstruction procedure based on the geometrical closeness of a particle to a jet have been applied. Firstly all closest b, c quarks or τ leptons with p_T above 5 GeV/c and inside the cone $\Delta R < 0.3$ around the jet axis are found. If there is a b-quark found, the jet is labelled as a b-jet. If there is a c quark found, the jet is labelled as a c-jet and otherwise if a τ lepton is found, the jet is a τ-jet. If no b, c quarks or τ leptons could be found, the jet is considered as a light jet. The disadvantage of this method is that jets, which cannot be correctly labelled as b-, c- or τ-jets, are automatically labelled as light jets. Jets from gluon splitting into b- or c-quarks are labelled as b- or c-quark jets, respectively.

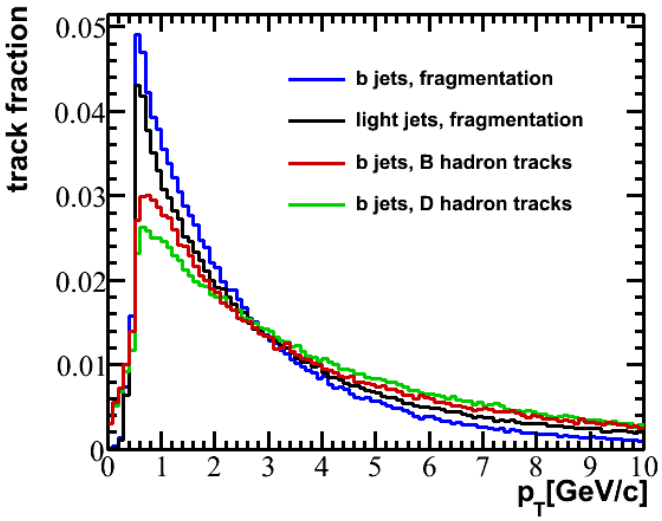

(a) track transverse momentum

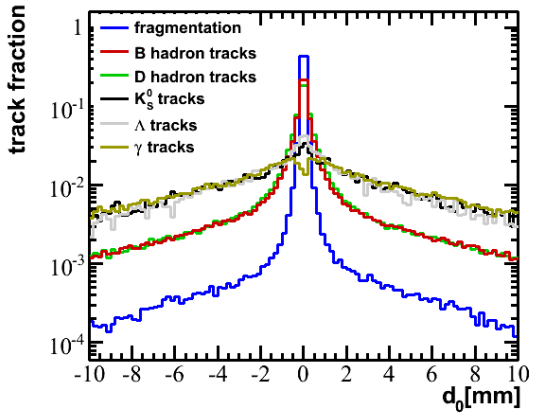

(b) track transverse impact parameter

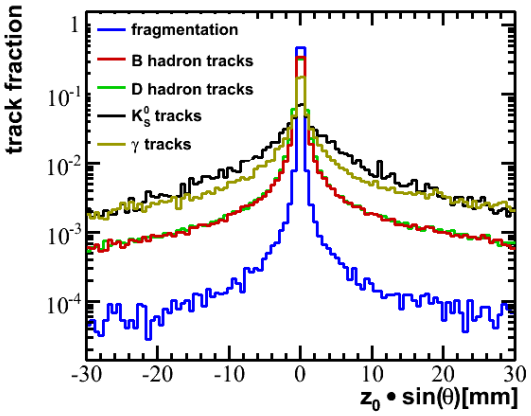

(c) track longitudinal impact parameter

Figure 6.3: Transverse momentum distributions of tracks associated to light and *b*-jets (a). Transverse (b) and longitudinal (c) impact parameter distributions of tracks associated to *b*-jets. Tracks are subdivided into categories according to their physical origin.

6.3 *b*-Tagging Algorithms in ATLAS

Two types of *b*-tagging algorithms are available in ATLAS: impact parameter based and secondary vertex based. Both types will be discussed in more details in this section.

	b-jet		light jet	
	associated	selected	associated	selected
average track multiplicity	11.04	6.353	7.560	3.954
track origin				
from fragmentation	27.30%	38.09%	59.73%	95.13%
from B hadron	28.15%	30.49%	–	–
from D hadron	26.05%	28.67%	–	–
from K^0_S	1.713%	0.518%	2.893%	0.833%
from Λ	1.139%	0.295%	3.007%	0.614%
from γ	6.074%	0.439%	17.94%	1.745%
other	9.574%	1.498%	16.43%	1.678%

Table 6.3: Average track multiplicity in b- and light jets with relative contribution of tracks obtained from $pp \rightarrow t\bar{t}$ (where one or both W bosons decay leptonically) Monte Carlo sample.

Impact Parameter Based b-Tagging Algorithms

Impact parameter based algorithms use the signed longitudinal and transverse impact parameter significance to discriminate between prompt tracks in light jets and displaced tracks from B or D hadron decays. The significance is defined as impact parameter divided by its error: $IP/\sigma(IP)$. The sign is positive if the track intersects the jet axis in front of the primary vertex, like in case of tracks from B and D hadron decays, or negative for tracks from secondary vertices opposite to the jet direction as depicted in Figure 6.4. The computation of the sign assumes that the jet direction reproduces the B hadron flight direction. This assumption is valid up to a good approximation.

Distributions of the signed impact parameter significances are presented in Figure 6.5 for different track categories in light and b-jets. Since no correlations with the jet direction are expected for prompt tracks, the distributions are fairly symmetric. The width of the distribution is given by the track parameters resolution. Secondary track distributions from B and D hadron decays are asymmetric with significant tails to positive values due to a real hadron lifetime. Negative tails are mostly caused by resolution effects on prompt tracks or by the approximation of the B hadron flight direction through the jet axis. Signed impact parameter significance distributions of tracks from K^0_S, Λ or from γ conversion decays in light jets have tails to positive and negative values, because their decay vertices are uncorrelated with the jet direction.

The impact parameter significances of all selected tracks N are combined into a single discriminating variable as a product of probability density functions based on the single track distributions: $\prod_{i=1}^{N} \mathrm{PDF}_{\text{jet flavour}}(IP_i)$. The discrimination variable used for b-tagging is

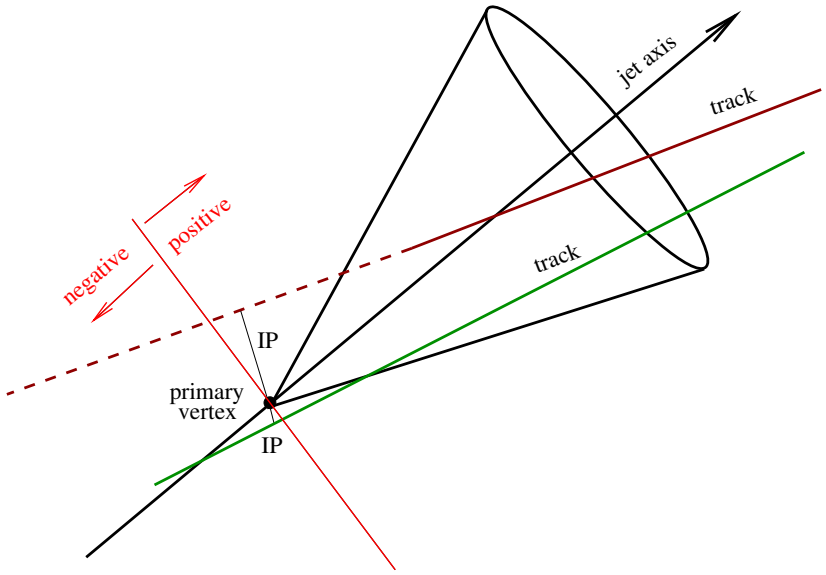

Figure 6.4: Definition of the signed track impact parameter IP in jets. The sign is positive if the track intersects the jet axis in front of the primary vertex or negative for tracks from secondary vertices opposite to the jet direction.

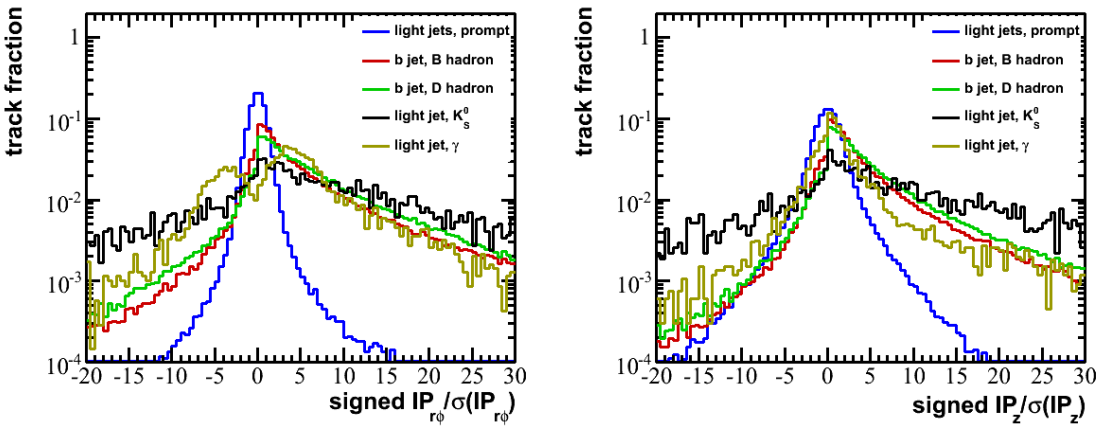

(a) transverse signed impact parameter significance (b) longitudinal signed impact parameter significance

Figure 6.5: Transverse (a) and longitudinal (b) signed impact parameter significance distributions for tracks from B and D hadrons as well as primary and secondary tracks in light jets.

defined as:

$$\text{weight} = \log\left(\frac{\prod_{i=1}^{N}\text{PDF}_{b-\text{jet}}(IP_i)}{\prod_{i=1}^{N}\text{PDF}_{\text{light jet}}(IP_i)}\right). \tag{6.3}$$

Single track based PDFs have to be calibrated for each quark flavour. This method is fairly

simple and requires only reconstruction of tracks. Separation of PDFs in jet p_T and η bins improves the performance at the cost of a more difficult calibration on data [73].

Secondary Vertex Based *b*-Tagging Algorithms

Secondary vertex based b-tagging algorithms attempt to reconstruct B and D hadron decay vertices in a inclusive way. An exclusive reconstruction cannot be performed at high efficiency due to a huge number of different decay modes, missing tracks of neutral particles and limited detector resolution.

Even the inclusive secondary vertex reconstruction is a challenging task: the average number of reconstructed and selected secondary tracks from B/D hadrons is below 2, as evaluated in Table 6.3. Decays of hadrons close to the primary vertex are difficult to separate from the primary interaction and they cannot be considered for the secondary vertex reconstruction. The probability to distinguish between B and D hadron vertices depends strongly on the distance between the vertices and on the track parameters resolution. Especially at low track momenta, the resolution is not sufficient to separate both vertices.

The VKalVrt [117] reconstruction package implemented in the ATLAS software framework attempts to reconstruct a single secondary vertex. It starts with the selected tracks associated to a jet and forms a "two-track" vertex from all possible combinations of two tracks, which satisfy following selection criteria:

- the impact parameter significance of each track is larger than 2 and the sum of these two significances is larger than 6
- the probability of the vertex fit, based on χ^2 of the fit, is > 3.5%
- "two-track" vertices $\vec{r}_{2\text{tr}}$ are required to be produced in the b-jet direction, $\vec{p}_{\text{jet}}$, by requiring the scalar product $(\vec{r}_{2\text{tr}} - \vec{r}_{\text{primary}}) \cdot \vec{p}_{\text{jet}}$ to be positive, where $\vec{r}_{\text{primary}}$ is the position of the primary vertex
- "two-track" vertices compatible with K^0_S Λ, γ decays or with material interactions are rejected

All tracks from the accepted two-track vertices are used to fit a single secondary vertex. If the resulting vertex has a χ^2 above χ^2_{max}, the track with the highest contribution is removed and the vertex fit is redone. This procedure is repeated until a $\chi^2 < \chi^2_{max}$ is obtained.

Properties of the reconstructed secondary vertex are used in the b-tagging algorithm BTagVrtSec [118] to separate light and b-jets. The presence of a reconstructed vertex in the jet itself is the first variable, because the probability to find a secondary vertex in b-jets is significantly higher for b-jets than for light jets. The mass of the reconstructed vertex M, the ratio of the energy of charged particle tracks at vertex to the total energy of all charged particles R and the number of accepted "two-track" vertices N are also used. The distance between primary and secondary vertices is only used if the tagger is not combined with a impact parameter based tagger. These variables are transformed to facilitate the calibration of the b-tagging algorithm on data and to reduce the necessary amount of data:

- transformed invariant mass: $M' = \frac{M}{M+1}$
- transformed energy ratio: $R' = R^{0.7}$

- transformed number of accepted "two-track" secondary vertices: $N' = \log N$

The probability density function is defined as:

$$\text{PDF} = (1 - \epsilon) \cdot \delta(M', R', N') + \epsilon \cdot \text{ASH}(M', R', N'), \tag{6.4}$$

where ϵ is the secondary vertex reconstruction efficiency and $\delta(M', R', N')$ is a δ-function to account for a less than 100% efficient reconstruction. A continuous probability density function $\text{ASH}(M', R', N')$ of the vertex variables is constructed using the ASH smoothing method [119]. Additionally, the correlations between all three variables as used in the "SV2" tagger or the correlations between M' and R' as used in the "SV1" tagger can be taken into account [73].

A new inclusive secondary vertex reconstruction algorithm, JetFitter [120], has been recently developed. It assumes that B and D hadron decay vertices lie on the same line defined by the B hadron flight path. Tracks of all charged particles originating from either B or D hadron decay will intersect this flight path. This method allows one to reconstruct incomplete decay topologies, even the topology with a single track from the B hadron and a single track from the D hadron decay is accessible. Reconstruction of the $B \rightarrow D$ hadron decay topology increases the discrimination power against light quark jets.

6.4 Topological Vertex Finder

The topological vertex finder, ZVTOP, is an inclusive multi-vertex finder optimised to reconstruct the $B \rightarrow D$ hadron decay topology in b-jets. This method has been developed by the SLD collaboration and successfully applied to reconstruct hadronic Z-boson decays [121]. The main concept is to search for vertices in the three dimensional space rather than by forming vertices from all track combinations. Vertex seeds are found using a vertex probability function which is defined by the trajectories and position resolution of tracks. Compatible vertex seeds are combined into vertex clusters and fitted to retrieve the vertex position. Tracks can be associated to several vertex seeds. In the final step the track ambiguities are solved taking into account the decay topology. This method can be used to reconstruct all vertices in one event, but due to a high charged tracks multiplicity at ATLAS, it will be a very CPU time consuming task. Thus, we will concentrate on reconstruction of vertices in jets.

In the following, the single reconstruction steps:

- construction of track probability tubes
- construction of vertex probability function
- vertex seed finding
- clustering of vertex seeds
- vertex fit
- ambiguity solving

will be introduced in all details.

construction of track probability tubes

Vertex finding starts with a construction of Gaussian probability tubes for all selected tracks, associated to a jet. Tracks are parametrised using the perigee parametrisation: $\vec{q} = (d_0, z_0, \phi, \theta, \frac{q}{p_T})$. Track parameter errors are defined by the covariance matrix $\text{cov}_{\vec{q}}$ calculated during the track fitting procedure. A Gaussian track probability tube for a track trajectory is given by:

$$f(\vec{r}) = \exp\left(-\frac{1}{2}\Delta\vec{q}^T(\vec{r})\text{cov}_{\vec{q}}^{-1}(\vec{r})\Delta\vec{q}(\vec{r})\right), \tag{6.5}$$

where $\Delta\vec{q}(\vec{r})$ is the residual to the track trajectory at the position $\vec{r}$. Additionally a further function $f_0(\vec{r})$ is introduced, which describes the location of the interaction point and its uncertainty. The interaction point is described by a Gaussian with the width of $\mathcal{O}(1)$ cm in the beam direction and of $\mathcal{O}(10)$ μm in the transverse plane corresponding to the beam spot size. The residual is defined to the interaction point at $\vec{r}$ and the covariance matrix is given by its uncertainty. This function allows one to constrain the reconstructed primary vertex to be consistent with the interaction point position.

The interaction point function $f_0(\vec{r})$ is weighted by a constant $K_{IP} = 1.1$. Large values of K_{IP} enhance the probability function at the interaction point and more tracks can be absorbed into the primary vertex. It reduces the probability to find secondary vertices near the interaction point. Trajectories of individual tracks around the primary vertex can be seen in Figure 6.6(a). A pronounced peak at the interaction point as well as few outgoing tracks are shown. The Gaussian tubes of two tracks in the x-y plane are well visible.

vertex probability function

Vertex probability at the position $\vec{r}$ is defined in such a way that at least the probability functions of two tracks or of one track and the interaction point should be nonzero at this position. It should be a smooth and continuous function to ensure finding of its maxima. These requirements results in the form:

$$V(\vec{r}) = \sum_{i=0}^{N} f_i(\vec{r}) - \frac{\sum_{i=0}^{N} f_i^2(\vec{r})}{\sum_{i=0}^{N} f_i(\vec{r})}, \tag{6.6}$$

where N is the number of tracks. The sum over track probability functions $\sum_{i=0}^{N} f_i(\vec{r})$ is a measure of the multiplicity and degree of overlap of tracks. The second term ensures that the vertex probability is $V(\vec{r}) = 0$, if only one track or only the interaction point contribute to $V(\vec{r})$.

Known physics information can be included in the vertex probability function. The flight direction of a hadron is well approximated by the jet direction and we expect small angles between the jet axis and the reconstructed flight direction. To take it into account, $V(\vec{r})$ is modified by a factor dependent on the angular location of the position $\vec{r}$:

$$V(\vec{r}) \to V(\vec{r}) \exp(-K_\alpha \alpha^2), \tag{6.7}$$

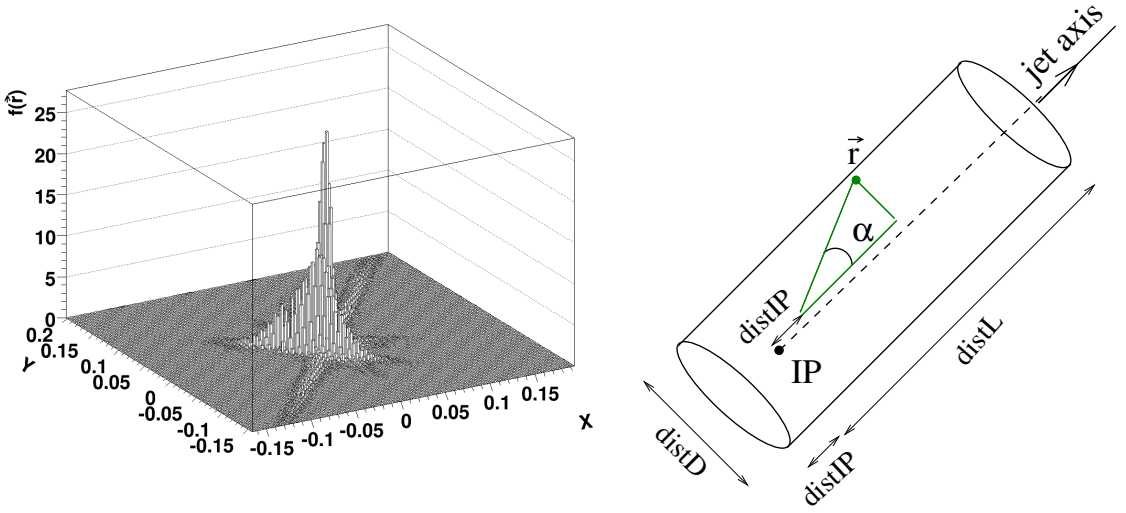

(a) track probability tubes (b) angular displacement

Figure 6.6: (a) Trajectories of individual tracks around a primary vertex. (b) Construction of α, the angular displacement.

where α is the angle between the position $\vec{r}$ and the jet axis as shown in Figure 6.6(b). A cylinder centred on the jet axis is constructed in order to avoid, that the vertex probability is reduced in the area close to the interaction point. In regions outside the cylinder, $V(\vec{r})$ is set to zero. These locations are unlikely to contain useful vertices. The factor K_α is proportional to the jet momentum. With the increasing jet momentum, the angle between the jet axis and the hadron flight axis will decrease and a harder cut on the angular displacement can be performed.

vertex seed finding

After the construction of the track probability tubes $f_i(\vec{r})$ and the vertex probability function $V(\vec{r})$, the maxima of $V(\vec{r})$ have to be found. To simplify the search, the maxima of $f_i(\vec{r})f_j(\vec{r})$ are found first by a direct calculation. In the proximity of the found maxima of $f_i(\vec{r})f_j(\vec{r})$, a three dimensional scan with a step size of $ScanStep = 30$ μm is performed to find maxima of the vertex probability function as depicted in Figure 6.7(a). This procedure reduces the effective three dimensional search area.

clustering of vertex seeds

Found vertex seeds have to be clustered together to form vertex candidates. Two vertex seeds are resolved, if a minimum of $V(\vec{r})$ could be found between these two locations as shown in Figure 6.7(b). The absolute value of the minimum should depend on the value of the vertex probability function of both seeds and this leads to the following resolution

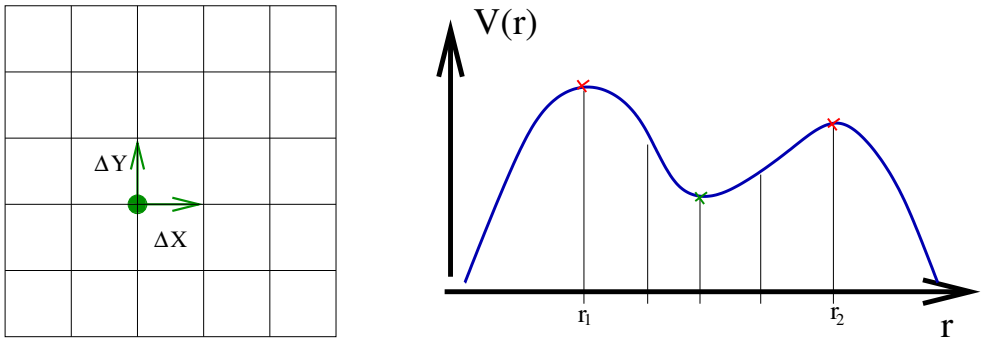

(a) vertex seed finding (b) clustering of vertex seeds

Figure 6.7: (a) A scan (shown only in 2 dimensions) with a step size of $(\Delta X, \Delta Y)$ to find maxima of the vertex probability function. The maximal size of the scanned area is $480 \times 480 \times 480\ \mu\text{m}^3$. (b) Two locations $\vec{r}_1$ and $\vec{r}_2$ are resolved if a minimum of $V(\vec{r})$ with $R < R_0$ on a straight line joining $\vec{r}_1$ and $\vec{r}_2$ could be found.

criterion. Two locations $\vec{r}_1$ and $\vec{r}_2$ are resolved if:

$$\frac{\min\{V(\vec{r}) : \vec{r} \in \vec{r}_1 + \alpha(\vec{r}_2 - \vec{r}_1), \quad 0 \leq \alpha \leq 1\}}{\min\{V(\vec{r}_1), V(\vec{r}_2)\}} < R_0, \tag{6.8}$$

where the numerator is the minimum of $V(\vec{r})$ on a straight line joining $\vec{r}_1$ and $\vec{r}_2$ and the denominator is the lower of the two vertex probabilities. $V(\vec{r})$ is determined for a finite number of points $N_{step} = 16$ on this line. The number of steps can be smaller, if the step size is below a certain minimal length, $\min L_{step} = 15\mu\text{m}$. The number of found vertices depends on the cut value R_0, the default value is set to $R_0 = 0.6$.

vertex fit

The clustered vertex candidates are fitted in order to calculate vertex positions and their errors. Used vertex fitter is based on the Billoir vertex fitting technique [122]. Vertex clusters with the two dimensional distance significance $\text{dist}_{2D}/\sigma(\text{dist}_{2D})$ below $signif2D = 2$ are compatible with the interaction point position. This cluster is labeled as "primary" and fitted using the interaction point constraint. Tracks with a large contribution to the χ^2 of the vertex fit are iteratively removed. The fitting and track removal procedure continue, till at least two tracks remain. If χ^2 of the vertex candidate is still above a threshold $\chi^2_{\text{max}} = 7$, this vertex candidate will be dropped. The vertex candidate is rejected if the number of tracks is less than two, except for the primary vertex, which can have only one associated track because of the interaction point constraint.

Vertex candidates with two associated tracks may be produced through hadronic interactions in the inner detector, K^0_S and Λ decays or γ conversions. If tracks have opposite charges, the invariant mass at vertex is calculated using (p,π), (π,π) and (e,e) mass hypotheses for the tracks. The invariant mass distributions $m(\pi,\pi)$ and $m(p,\pi)$ are presented in Figure 6.8(a) and 6.8(b), respectively. Sharp peaks at $m_{K^0_S} \approx 500$ MeV/c^2 and at $m_\Lambda \approx$

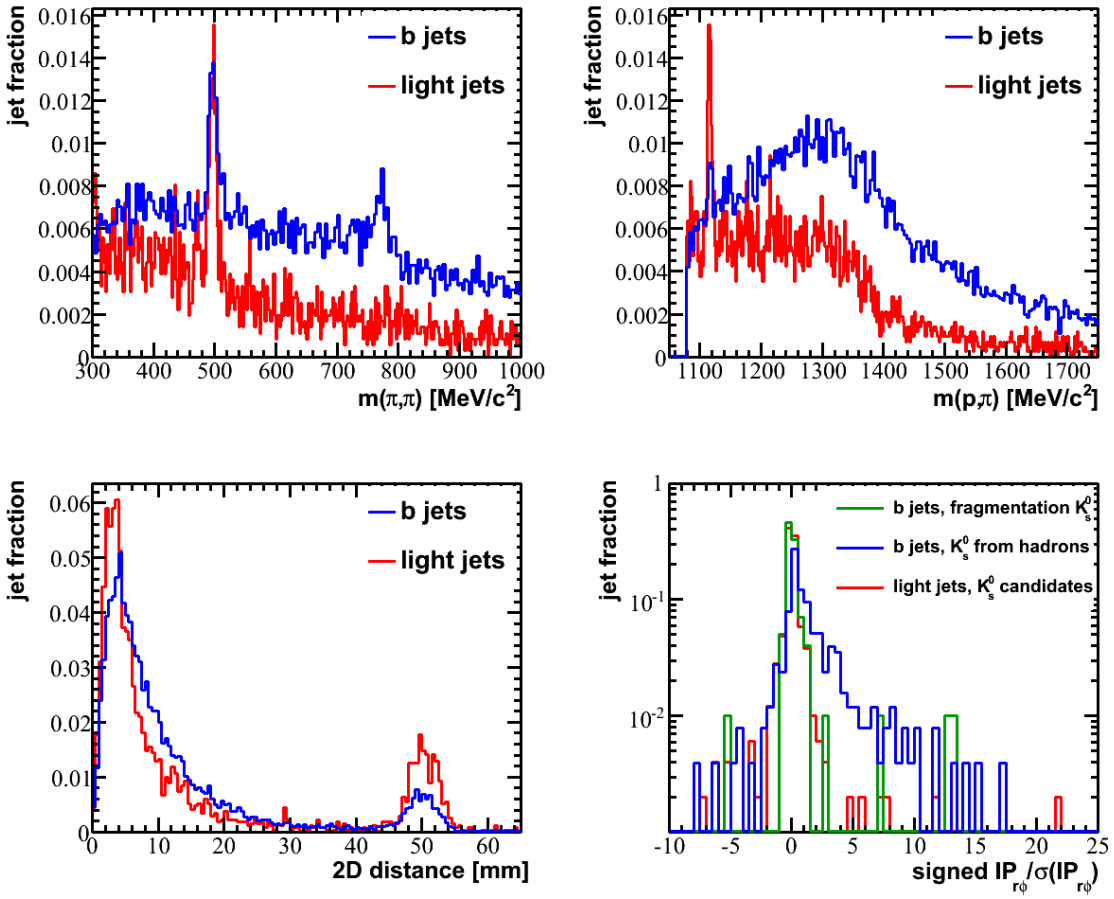

Figure 6.8: Reconstructed "two-track" vertices from K^0_S (a), Λ (b) decays and material interactions (c) in light and b-jets. The proton mass is assigned to the track with the largest momentum. (d) Signed impact parameter significance of K^0_S candidates selected in the K^0_S mass window.

1116 MeV/c^2 are visible in particular for light jets. The fraction of Λ baryons in b-jets is negligible.

A neutral particle is reconstructed out of both charged tracks and its signed three dimensional impact parameter significance is calculated with respect to the primary vertex. The distributions of the signed impact parameter significances are shown in 6.8(d). K^0_S and Λ particle candidates in light jets are expected to be produced at primary vertex, thus they will have small impact parameters significances, $signifNeutral < 2$. All two track vertices within the K^0_S or Λ particle mass window and compatible with the primary vertex as well as vertices within the γ mass window are rejected.

In Figure 6.8(c) secondary vertices produced through material interactions in the detector are clearly visible around 50 mm at the position of the first layer. A small peak can be seen around 30 mm, at the position of the beam pipe. Such vertices are rejected, if the distance difference to the beam pipe walls is $\Delta R_{BP} < 1$ mm or to the layers of the inner detector

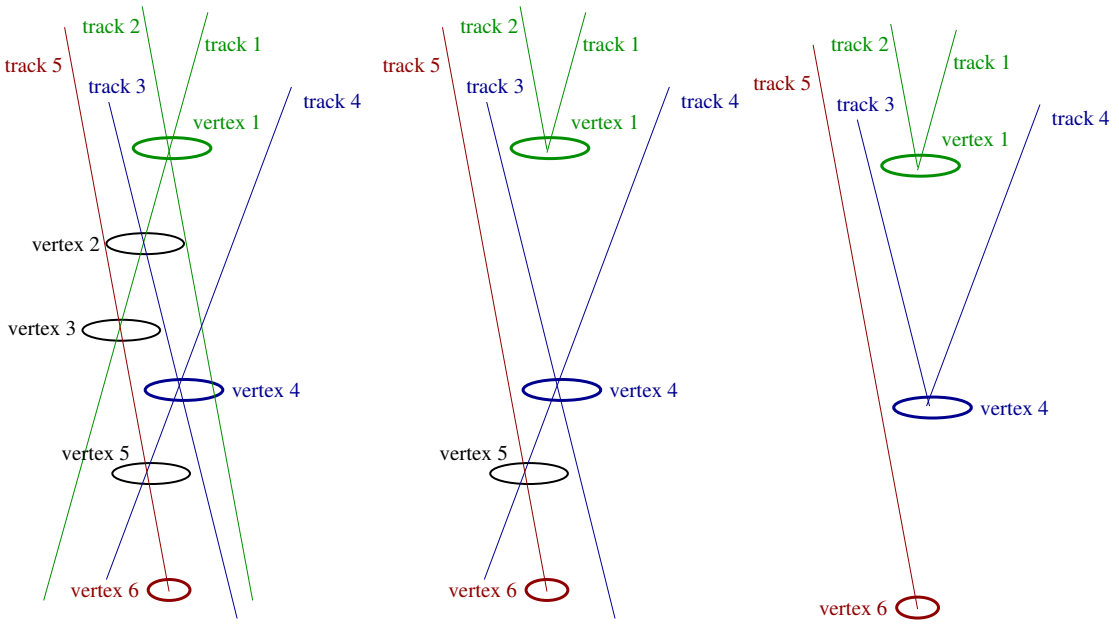

(a) step 1 (b) step 2 (c) step 3

Figure 6.9: Ambiguity solving procedure: (a) association of tracks 1 and 2 to vertex 1, removal of these tracks from vertex 2 and 3, vertices 2 and 3 are rejected; (b) association of tracks 3 and 4 to the vertex 4, removal from vertex 5; vertex 5 is rejected; (c) final association.

$\Delta R_{\text{Blay}} < 3.5$ mm.

ambiguity solving

In general each track can be associated with more than one vertex candidate. It enhances the vertex finding efficiency, but these ambiguities will be resolved in the last step. The following procedure, presented in Figure 6.9, is applied to solve the ambiguities. All selected vertex candidates are sorted according to their three dimensional distance from the interaction point. The tracks associated to the furtherst vertex are fixed in that vertex and removed from any others. Vertices with removed tracks are refitted and the distance to the interaction point is recalculated again. The remaining vertices are considered in order of decreasing distances and the procedure is repeated again till all ambiguities are solved.

This procedure allows one to associate compatible tracks with the D hadron vertex at first, in the second step with the B hadron vertex and in the final step with the primary vertex. If the opening angle between decaying particles is very small, the tracks of decay products can be associated to the decay vertex as well to the production vertex of the decaying particle. The "outside-inside" ambiguity solving procedure provides an optimal solution in such cases.

ZVTOP parameter		default value
impact parameter factor	K_{IP}	1.1
angular distance factor	K_α	300[GeV/c]/p_{Tjet}[GeV/c]
	distD	0.1 mm
angular distance cylinder	distIP	0.1 mm
	distL	65 mm
vertex seed finder scan step	$ScanStep$	30 μm
vertex clustering number steps	N_{step}	16
vertex clustering minimum step length	min L_{step}	5 μm
vertex clustering cut value	R_0	0.6
vertex significance	$signif2D$	2
vertex fit maximal χ^2 value	χ^2_{max}	7
K^0_S mass window	$\Delta m_{K^0_S}$	18 MeV/c^2
Λ mass window	Δm_Λ	7 MeV/c^2
γ mass windows	Δm_γ	30 MeV/c^2
beam pipe interaction	ΔR_{BP}	1 mm
first pixel layer interaction	ΔR_{Blay}	3.5 mm
neutral particle vertex significance	$signifNeutral$	2

Table 6.4: The list of tunable parameter of topological vertex finder and corresponding default values.

All discussed tunable parameter of topological vertex finder and corresponding default values optimised to reconstruct secondary vertices in $t\bar{t}$ events are listed in Table 6.4.

6.5 Secondary Vertex Reconstruction Performance

The performance of the topological vertex finder will be discussed in this section. The main point of interest is the secondary vertex reconstruction efficiency and purity in light and b-jets. The performance of ZVTOP vertex finder will be compared with the performance of the inclusive secondary vertex finder VKalVrt using jets reconstructed in $t\bar{t}$ Monte Carlo events.

Reconstructed vertices are labeled as secondary vertices, if their three dimensional flight length significance $\mathrm{dist}_{3D}/\sigma(\mathrm{dist}_{3D})$ is above 3.5. Secondary vertex reconstruction efficiency in b-jets is defined as a number of b-jets with at least one reconstructed secondary vertex divided by the number of all b-jets. This definition makes a comparison with a single vertex finder possible. Secondary vertex reconstruction purity is defined as a number of b-jets with at least one reconstructed secondary vertex divided by the number of light and b-jets with at least one reconstructed secondary vertex. Efficiency times purity is a measure of the reconstruction performance.

The secondary vertex reconstruction efficiency and purity have been calculated in bins of jet p_{T} and η and plotted in Figure 6.10(a) and 6.10(b). With the increasing jet momentum, the transverse momentum of tracks in jets increases. At higher transverse momenta

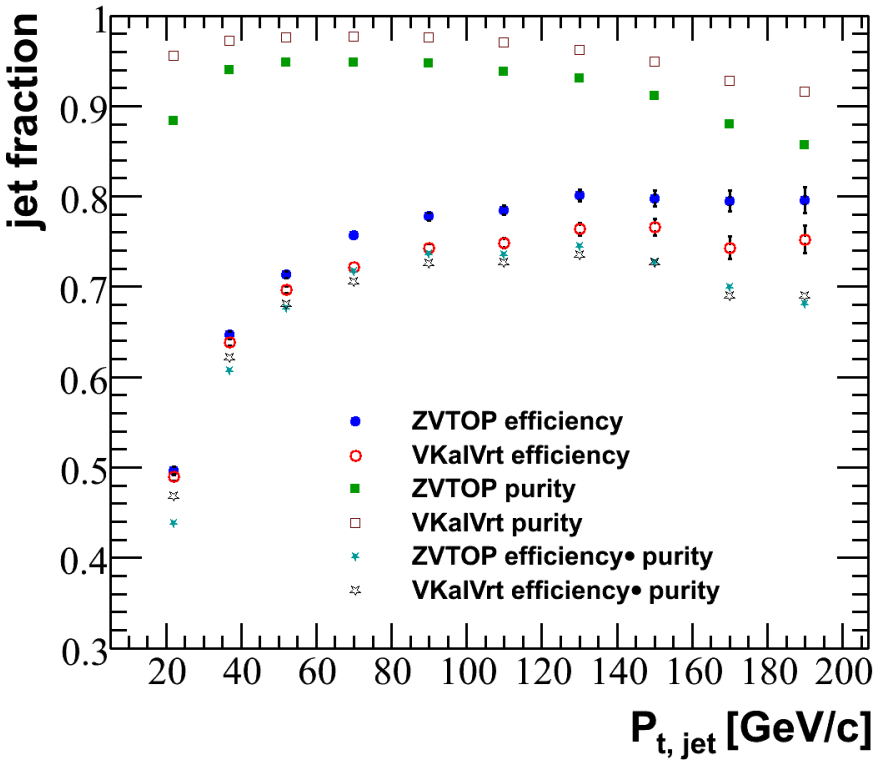

(a) reconstruction performance versus jet p_T

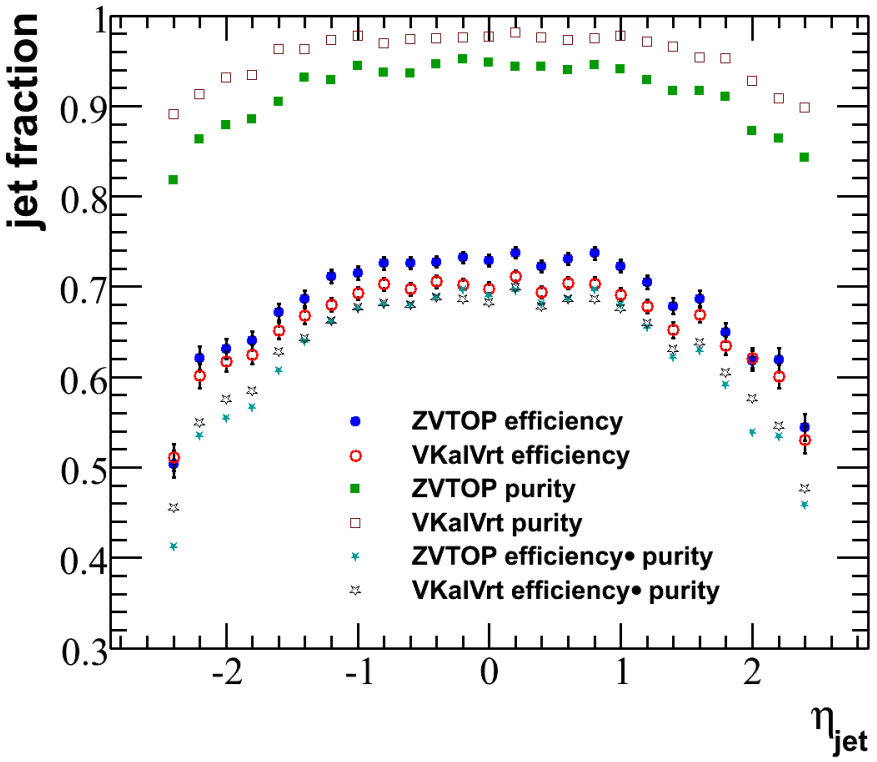

(b) reconstruction performance versus jet η

Figure 6.10: Secondary vertex reconstruction performance versus jet p_T (a) and η (b).

the track reconstruction becomes more efficient and the track resolution improves as well. This leads to an improvement in the vertex reconstruction efficiency. Both vertex finders show the expected behaviour. Above a certain p_T, the reconstruction efficiency approaches approximately a value around 75-80% for ZVTOP and 70-75% for VKalVrt. The amount of reconstructed vertices in light jets is rising with the increasing jet p_T, too. One of the sources of secondary tracks are real secondary decays from K^0_S, Λ particles or material interactions in the detector. Another source is the increased number of tracks in jets due to the fragmentation process, which produces more tracks at higher jet p_Ts. Thus, the number of tracks which can fake secondary tracks rises in light jets. The ZVTOP algorithm reconstructs more fake vertices in light jets, but the efficiency times purity of both vertex finders is comparable.

Different resolutions can be achieved in different parts of the inner detector, thus the vertex reconstruction efficiency depends on the jet pseudo-rapidity. At jet $|\eta| > 1.5$ the track resolutions get worse and the track reconstruction efficiency drops. The consequence is a decrease in the vertex reconstruction efficiency and an increase of fake vertices.

6.6 Application to *b*-Tagging

The number of reconstructed secondary vertices and their properties are used to tag b-quark jets. The b-tagging algorithm is based on a likelihood function built of the following variables:

- number of secondary vertices
- total number of tracks at these vertices
- invariant mass of all charged particle tracks associated to the secondary vertices with a correction for neutral particles
- the sum over the energies of charged particles at vertex divided by the sum of the energies of all charged particles associated to the jet
- three dimensional flight length significance of the furthest displaced vertex

All variables will be introduced and discussed below. Distributions of these variables are presented in Figure 6.11 for b-quark and light quark jets in $t\bar{t}$ events. They are compared to the distributions retrieved with the VKalVrt reconstruction algorithm as well.

Both secondary vertex finder require secondary vertices with the flight length significance above 3.5. ZVTOP has a higher secondary vertex reconstruction efficiency of $\sim 70\%$ but also a higher fake rate of $\sim 4\%$ in light jets compared to VKalVrt algorithm ($\sim 67\%$ and $\sim 2\%$, respectively).

Secondary vertices in light quark jets contain mostly only two associated tracks. The average number of tracks at secondary vertices in b-quark jets is 3.42 and 3.14 for ZVTOP and VKalVrt, respectively. ZVTOP associates 8% more tracks to secondary vertices in b-quark jets and around 5% more tracks in light quark jets. In Table 6.3 it has been shown that on average 3.76 tracks from B and D hadrons are expected in the b-quark jets. This number agrees quite well with the number of tracks associated to the secondary vertices.

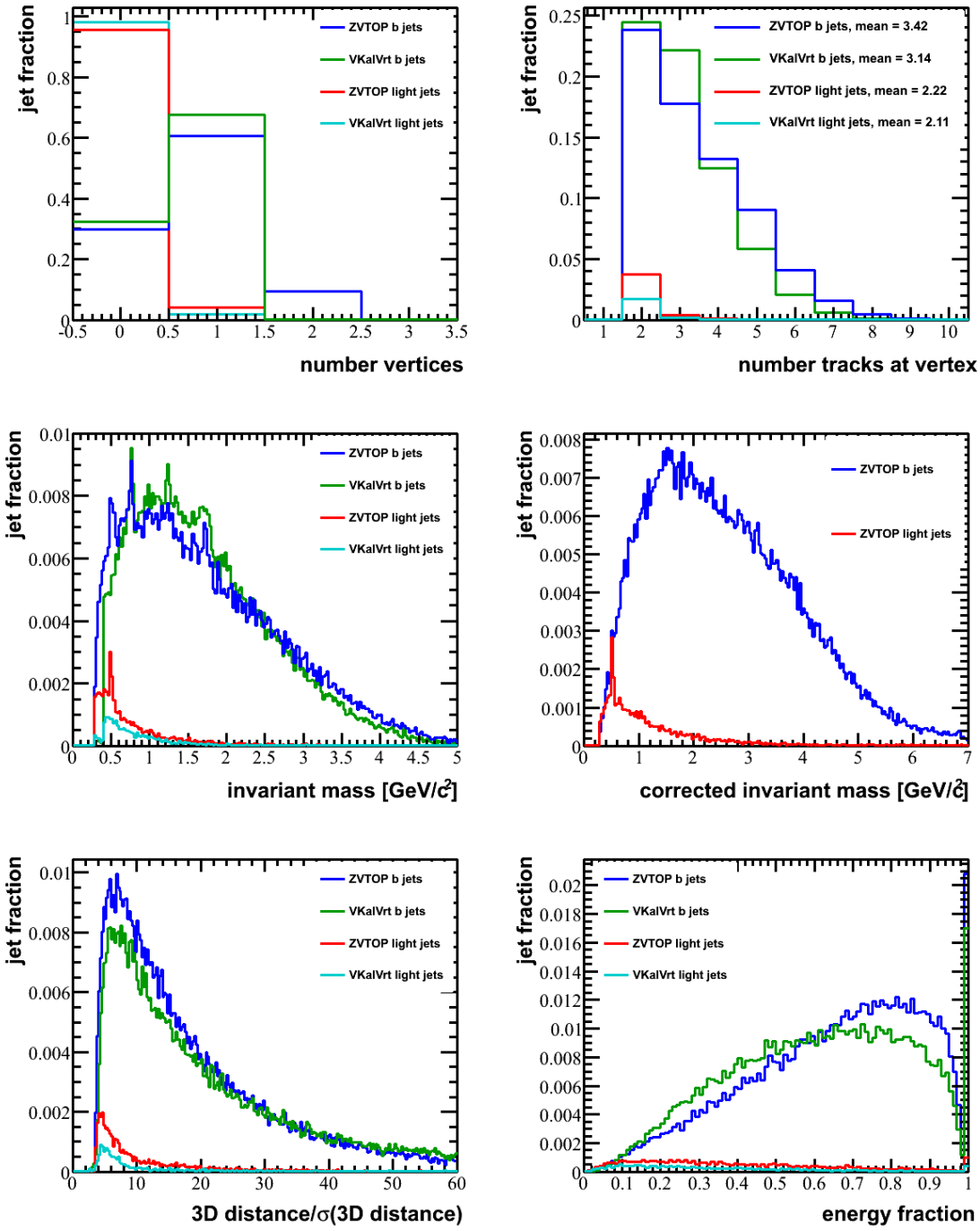

Figure 6.11: Distributions of variables used to tag *b*-jets: number of reconstucted vertices, number of tracks associated to a vertex, corrected invariant mass at vertex, flight length significance and energy fraction at vertex for light and *b*-jets. They are compared to distributions retrieved with the VKalVrt reconstruction algorithm. The invariant mass without a correction for the neutral tracks is shown for a better comparison between both vertex finder.

The invariant mass at vertex is calculated assuming that each track has the mass of a pion. For the topological vertex finder the mass is partially corrected for the presence of neutral particles at the B/D hadron decay vertex. If all decay products of hadrons could be detected and reconstucted, the sum of all momenta at decay vertex $\vec{p}_{\text{vertex}}$ would point into the B-flight direction. This property can be used to correct for the missing transverse component of the momentum $p_{T,\text{vertex}}$ with respect to the flight direction, since the longitudinal component is not accessible [123]:

$$m_{B,\text{corrected}} = \sqrt{m^2_{\text{charged}} + p^2_{T,\text{vertex}}} + |p_{T,\text{vertex}}|. \tag{6.9}$$

The invariant mass calculated using only charged track particles distributions is comparable for both vertex finder apart from the very low and very high mass tails. The K^0_S and Λ invariant mass peaks are still visible and can be removed increasing the mass window cut. The corrected invariant mass distribution is shifted to higher mass values and shows a good separation between b- and light quark jets.

ZVTOP reconstructs more secondary vertices with a lower flight length significance, but the shapes are still well comparable for both vertex finder. The energy fraction at vertex is lower for VKalVrt, because VKalVrt associates on average less charged track particles to vertex than ZVTOP.

As already mentioned, a likelihood function is built out of these variables. The likelihood function is defined as a product of the single probability density functions:

$$\text{L}_{\text{jet flavour}} = \prod_{i=1}^{5} \text{PDF}_{\text{jet flavour}}(\text{variable}_i), \tag{6.10}$$

and the discrimination variable used for b-tagging is the logarithm of the ratio of PDFs:

$$\text{weight} = \log\left(\frac{\text{L}_{b-\text{jet}}}{\text{L}_{\text{light jet}}}\right). \tag{6.11}$$

Additionally a multilayer perceptron (MLP) neural network (NN) [124] implemented in TMVA [125] have been used. The input layer contains as many neurons as input variables and one additional neuron, the so-called "bias node". The output layer contains only a single neuron for the signal weight used as a discrimination variable for b-tagging. Only one hidden layer has been used. All neuron inputs to a layer are linear combinations of the neuron output of the previous layer. The transfer from input to output is performed via a sigmoid activation function. A detailed information on the NN implementation can be found in Reference [125].

6.7 Performance in Rejecting Light Quark Jets

The performance of the topological vertex finder developed in this thesis will be analysed and compared to the performance of another inclusive secondary vertex based algorithm available in ATLAS, BtagSecVtx. Before starting the discussion about the performance of

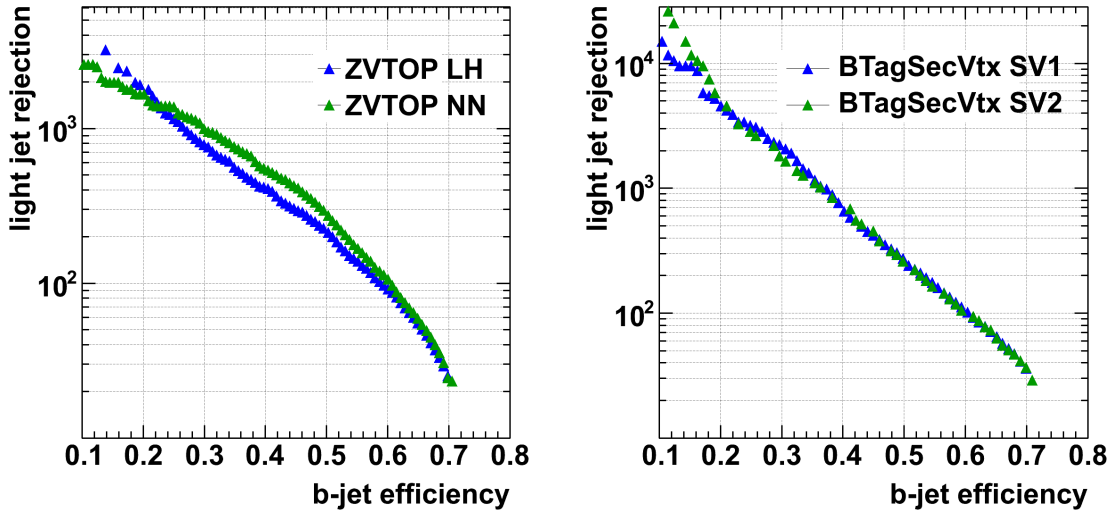

Figure 6.12: B-tagging efficiency versus light quark jet rejection for $t\bar{t}$ events. The ZVTOP performance is shown for the likelihood (LH) and neural network (NN) methods. For the BTagSecVtx tagger SV1 and SV2 methods have been used.

b-tagging algorithms, two definitions will be introduced: tagging efficiency and rejection. The efficiency to tag a jet of flavour q as b-quark jet, ϵ_q is defined as:

$$\epsilon_q = \frac{\text{number of jets of real flavour } q \text{ tagged as } b}{\text{number of jets of real flavour } q}. \tag{6.12}$$

ϵ_b is called b-tagging efficiency and ϵ_{uds} is mis-tagging rate. The inverse of the mis-tagging rate $r_{uds} = 1/\epsilon_{uds}$ is called light quark jet rejection.

The b-tagging efficiency versus the light quark jet rejection rate is ploted in Figure 6.12 and the rejection rates for the fixed b-tagging efficiencies of 50%, 60% and 70% are listed in Table 6.5 for different tagging algorithms. The maximum achievable b-tagging efficiency of secondary vertex based algorithms is limited by the efficiency to reconstruct a displaced vertex.

The performance of ZVTOP tagger based on the use of a likelihood discriminator is worse than the performance of the SV1 and SV2 taggers, because these tagger consider the correlations between the b-tagging variables, while in the likelihood approach of ZVTOP they are not considered. The correlations are taken into account in the neural network based approach. It shows best rejection power compared to the likelihood based methods. Nevertheless its performance drops at efficiencies below 40%, because of the low statistics for the NN training. The performance of the SV1 and SV2 taggers is very similar, the SV1 tagger has a slighly better rejection power and is the default algorithm in ATLAS.

There is still a lot of room for performance improvement of the topological vertex finder. The calibration and tuning of the ZVTOP tagger will be done using collision data. The b-tagging group in ATLAS has started with the calibration of the simple b-tagging algorithms

b-tagging efficiency	light quark jet rejection rate			
	ZVTOP		BTagSecVtx	
	LH	NN	SV1	SV2
50%	217 ± 13	280 ± 14	265 ± 13	260 ± 13
60%	92 ± 3	108 ± 3	102 ± 3	94 ± 3
70%	24 ± 1	25 ± 1	36 ± 1	37 ± 1

Table 6.5: Light quark jet rejection for the fixed b-tagging efficiencies of 50%, 60% and 70% for $t\bar{t}$ events. The ZVTOP performance is shown for the likelihood (LH) and neural network (NN) methods. For the BTagSecVtx tagger SV1 and SV2 methods have been used.

based on one or two variables like the flight length significance based SV0 tagger. Next step will be more complex but also more powerful tagger: BTagSecVtx, JetFitter, ZVTOP or also impact parameter based tagger.

7 The $t\bar{t}$ Invariant Mass Distribution

This analysis is based on a model independent search of a narrow width resonance in the semi-leptonic decay channel of the top quark pairs. First direct searches for resonant $t\bar{t}$ production have been done at the TEVATRON [54, 55]. So far no significant deviation from the Standard Model predictions could be observed. A higher centre-of-mass energy at the LHC allows one to extend these searches for the first time into the TeV-regime.

The production cross-section of the new heavy particles is very low compared to the Standard Model $t\bar{t}$ pair production. We will focus on the efficient selection and identification of signal events in the whole accessible $m_{t\bar{t}}$-range. The topology of events produced at the $t\bar{t}$ mass threshold differs strongly from the event topology at a few TeV. A new reconstruction scheme has been developed to deal with the different topologies. In this chapter we start with the discussion of the semi-leptonic event selection and identification of the event topology at different resonance masses. Based on it, an analysis strategy will be developed and the performance of the reconstruction algorithm will be discussed. Finally the expected systematic uncertainties will be given.

7.1 Event Selection

The $t\bar{t}$ final state is quite complex. The top quarks decay to nearly 100% in a W boson and a bottom quark. The W boson decays into a lepton and neutrino pair or in a quark anti-quark pair. Requiring semi-leptonic $t\bar{t}$ decays, we expect exactly one lepton, missing transverse energy due to the escaping neutrino and jets. The decay products should have high transverse momenta, because the mass of the resonance particles is of the order of several top quark masses. We consider only reconstructed electrons and muons. The tau leptons decaying leptonically are difficult to distinguish from the direct electron or muon decays and therefore contribute to the signal. The hadronical tau decays may be misidentified as electrons, since the tau jets are also narrow and have low track multiplicities.

To select the reconstructed objects - jets, lepton and $\vec{E}_{\mathrm{T}}^{\mathrm{miss}}$, following criteria have been applied. We are using the inclusive isolated electron and muon triggers with 15 GeV thresholds. The trigger efficiency well above the threshold is nearly 100% for electrons and about 95% for muons in $t\bar{t}$ events [73]. Selected events must have at least one lepton with transverse momentum larger than 25 GeV/c. Depending on the flavour of the selected lepton, the corresponding trigger has to fire.

Electrons of "medium" quality[1)] within the volume of the inner detector $|\eta| < 2.47$ are selected. In the transition region between barrel and end-caps of the electromagnetic calorimeter $1.37 \leq |\eta| \leq 1.52$ the reconstruction efficiency and the jet rejection rate are very

[1)] defined in Section 5.3

low. Therefore electrons reconstructed in the so-called "crack" region of the calorimeter are rejected. Electrons are required to be isolated - the transverse energy in a cone of opening 0.2 around the electromagnetic cluster's centroid minus the cluster energy E_{T} has to be below 4 GeV+ 0.023·E_{T} [126]. The constant of 4 GeV accounts for the noise and the energy dependent term accounts for the increased bremsstrahlung with a higher electron energy.

Muons have to be reconstructed in the tracker and the muon-spectrometer within $|\eta| < 2.5$. To reject non-isolated muons, for example from B hadrons, track and calorimeter based isolation criteria have been applied. The relative transverse energy in a cone of 0.2 around a muon, $E_{\mathrm{T\,cone\,0.2}}/{p_{\mathrm{T}}}^{\mathrm{muon}}$, has to be below 0.1. The sum of transverse momenta of tracks reconstructed around the muon within ΔR< 0.3 has to be less than 4 GeV/c. Muons close to jets with ΔR(muon,jet) < 0.3 are rejected. Muons from prompt W boson decays may give rise to jets of small p_{T} very close to the muons. Therefore only jets with p_{T} larger 20 GeV/c and ${p_{\mathrm{T}}}^{\mathrm{jet}} > \frac{1}{2}{p_{\mathrm{T}}}^{\mathrm{muon}}$ are taken into account for this isolation requirement. It additionally improves the performance of track based and calorimeter based isolation cuts [126].

Jets are reconstructed with the standard ATLAS cone $\Delta\mathrm{R} = 0.4$ algorithm using calorimeter towers. Selected events must have at least three jets with $p_{\mathrm{T}} > 40$ GeV/c and be inside $|\eta| < 2.5$. In semi-leptonic $t\bar{t}$ decays we could expect at least four jets, but with the increasing transverse momentum of the top quarks the partons may merge in one jet, therefore we require less jets. The event topology will be discussed in more details in the next section. Any reconstructed electron is also reconstructed as a jet by the ATLAS software. To remove electron-jets, jets within $\Delta\mathrm{R} < 0.2$ of a selected electron are removed.

A neutrino from a W boson decay is expected to carry similar transverse momentum as the charged lepton. Therefore we require the missing transverse energy to be larger than 25 GeV. The correlation between missing transverse energy and the transverse W boson mass $m_{T,W} = m_T(\mathrm{lep}, \mathrm{raw}E_{\mathrm{T}}^{\mathrm{miss}})$ are presented in Figure 7.1 for different signal and background sources. The "raw" $E_{\mathrm{T}}^{\mathrm{miss}}$ denotes the measured missing transverse energy without modifications as described in Section 5.5. Events with fake leptons like QCD multijet events or $t\bar{t}$ fully hadronic events have lower transverse energies and lower transverse W boson masses in comparison to the semi-leptonic and di-leptonic $t\bar{t}$ events. Thus, additionally a combined $E_{\mathrm{T}}^{\mathrm{miss}}$ and a transverse W boson mass cut is applied, $E_{\mathrm{T}}^{\mathrm{miss}} > 50$ GeV and $m_{T,W} > 40$ GeV/c^2. All selection cuts are summarised in Table 7.1.

At present, ATLFAST-II does not contain a simulation of the High Level trigger. Thus, the selection efficiency for signal samples simulated with ATLFAST-II has to be corrected for the trigger efficiency. Three full simulated samples, with $m_{Z'}$ = 1000 GeV/c^2, 2000 GeV/c^2 and 3000 GeV/c^2, have been used to estimate the trigger efficiency after selection cuts. Figure 7.2 shows the fraction of events that have passed the selection cuts and are also required to pass the lepton trigger cuts as a function of lepton p_{T} for the electron and muon channel separately. The efficiency is roughly flat in p_{T} and nearly 98% for electrons and 82% for muons. The detector acceptance is well modelled in the fast simulation. Kinematic distributions of the leptons or jets like p_{T}, η and missing transverse energy are in good agreement within 5% with the full detector simulation as shown in Figure 7.3. Only the jet mass distribution shows larger deviations of order 20%, especially at low values, due to a simplified simulation of calorimeter signals. But this variable is not used in the event selection. Therefore, the ATLFAST-II events need only to be scaled by these factors to correct for the overall efficiency.

Object	Selection
Trigger	Electron channel: medium, $E_T > 15$ GeV Muon channel: $E_T > 15$ GeV
Electrons	medium $p_T > 25\text{GeV}/c$ $\lvert\eta\rvert < 1.37$ or $1.52 < \lvert\eta\rvert < 2.47$ $E_{\text{Tcone }0.2} < 4$ GeV+ $0.023 \cdot E_T$
Muons	"Staco" algorithm combined reconstruction $p_T > 25\text{GeV}/c$ $\lvert\eta\rvert < 2.5$ $E_{\text{Tcone }0.2}/p_T \leq 0.1$ mm and $p_{\text{Tcone }0.2} < 4$ GeV/c ΔR(muon,jet) > 0.3 if $p_T^{\text{jet}} > \frac{1}{2} p_T^{\text{muon}}$
Jets	cone ΔR = 0.4, tower jets $p_T > 40\text{GeV}/c$ $\lvert\eta\rvert < 2.5$ jets within $\Delta R < 0.2$ of a selected electron are removed
E_T^{miss}	refined calibration $E_T^{\text{miss}} > 25\text{GeV}$
QCD cut	$E_T^{\text{miss}} > 60\text{GeV}$ and $m_{T,W} > 40\text{GeV}$

Table 7.1: Summary of the semi-leptonic event selection cuts.

cut	$t\bar{t}$	single top	W + jets	Z + jets	QCD ALPGEN
total	79950	9228	9691534	883570	9045692520
triggered	26166	4394	3144797	441510	10370206
isolated lepton	16970	3146	2324786	195091	1345721
at least 3 jets	8112	146.2	6819	1368	7803
E_T^{miss}	6806	124.1	5517	388.8	1125
QCD rejection	6327	116.9	5163	325.1	510.4
efficiency, %	7.91	1.27	0.0533	0.0368	5.64×10^{-6}

cut	Z' 500	Z' 700	Z' 1000	Z' 1300	Z' 1600	Z' 2000	Z' 2500	Z' 3000
total	1093	665.0	126.8	40.8	14.5	4.28	1.00	0.20
triggered	904.4	555.9	106.5	34.3	12.2	3.60	0.84	0.17
isolated lepton	230.8	151.1	30.6	10.0	3.60	1.01	0.22	0.041
at least 3 jets	105.9	92.2	20.8	6.77	2.37	0.67	0.15	0.027
E_T^{miss}	87.8	80.1	18.7	6.23	2.21	0.63	0.14	0.026
QCD rejection	81.1	75.0	17.8	5.96	2.13	0.61	0.13	0.025
efficiency, %	7.42	11.3	14.0	14.6	14.7	14.2	13.5	12.6

Table 7.2: Number of expected signal and background events after the semi-leptonic selection cuts normalised to the integrated luminosity of 200 pb^{-1}. The assumed signal cross section (SSM model) is listed in Table 4.2.

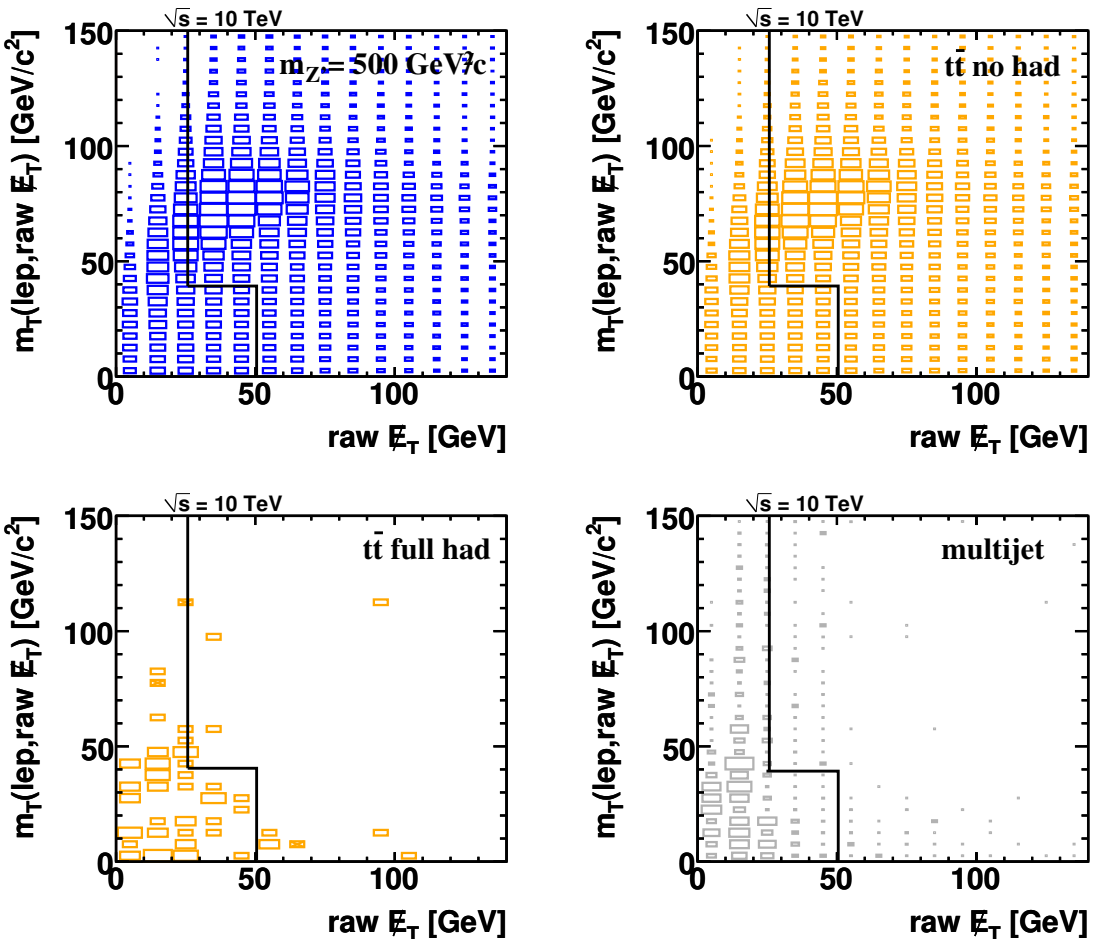

Figure 7.1: Missing transverse energy versus transverse W boson mass $m_{T,W} = m_T(\text{lep}, \text{raw}E_{\text{T}}^{\text{miss}})$ for events with the high-p_{T} leptons like in the semi-leptonic and di-leptonic $t\bar{t}$ events or fake leptons in the QCD multijet and in the $t\bar{t}$ fully hadronic events. The Z' boson sample contains all possible $t\bar{t}$ decay modes, also fake leptons from the fully hadronic $t\bar{t}$ decays.

The number of expected events for signal and the main sources of background after the semi-leptonic selection cuts are listed in Table 7.2. They are given for the whole $m_{t\bar{t}}$-range and for an expected luminosity of 200 pb^{-1}. The fraction of expected signal and background events under the Z' boson mass peak, relevant for the sensitivity of the signal will be discussed in Section 7.4. Now, we will discuss the overall selection efficiency for the signal and background.

The signal selection efficiency is rising with increasing Z' boson mass up to 14.7%. For Z' boson mass of 500 GeV/c^2, the efficiency is comparable to the selection efficiency of $t\bar{t}$ background as expected. In the most interesting mass range between 1000 and 2000 GeV/c^2 the signal selection efficiency is nearly constant and at its highest value for the chosen cuts. At Z' boson masses larger than 2000 GeV/c^2 the lepton isolation criterion leads to a decrease

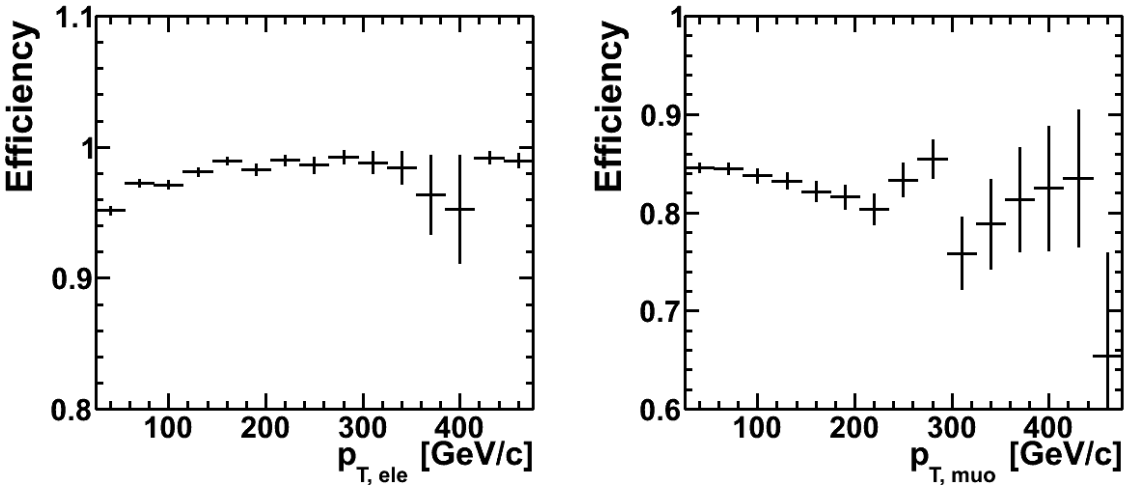

Figure 7.2: Lepton trigger efficiency versus lepton p_T for signal events after semi-leptonic selection cuts.

in the efficiency, because the lepton can merge with jets.

$t\bar{t}$ events have the highest contribution to the background, followed by W + jets events. About 7.9 % of all $t\bar{t}$ events are selected. The probability to select a W + jets event is of order 0.05 %, but the production cross section is two magnitudes higher than for the $t\bar{t}$ events. The QCD background is reduced by a factor 10^{-6}. Z + jets events can pass the selection if one of the leptons is not reconstructed and not selected. The selection probability is 0.037 %, but the production cross section is a factor 10 lower compared to W + jets. The single top quark background is the smallest one because of the small production rate and a low selection efficiency. Additional jets are required to mimic the second top quark, therefore the selection efficiency is lower than for the $t\bar{t}$ events.

To check the purity of the selected signal events, they have been categorised as di-leptonic, semi-leptonic and fully hadronic events using the Monte Carlo truth information. Tau leptons are counted as leptons only if taus decay leptonically, otherwise they are counted as jets. The categories are:

- **di-leptonic signature**

  ee, $\mu\mu$ + jets and $e\tau$, $\mu\tau$, $\tau\tau$ + jets with $\tau \rightarrow$ leptons (branching ratio $\sim$ 6.5%)

- **semi-leptonic signature**

  I. e, μ + jets and τ + jets with $\tau \rightarrow$ leptons (branching ratio $\sim$ 34.6%)

  II. $e\tau$, $\mu\tau$ + jets with $\tau \rightarrow$ hadrons and $\tau\tau$ + jets with one $\tau \rightarrow$ leptons and one $\tau \rightarrow$ hadrons (branching ratio $\sim$ 3.5%)

- **fully hadronic signature**

  jets and τ, $\tau\tau$ + jets with $\tau \rightarrow$ hadrons (branching ratio $\sim$ 55.3%)

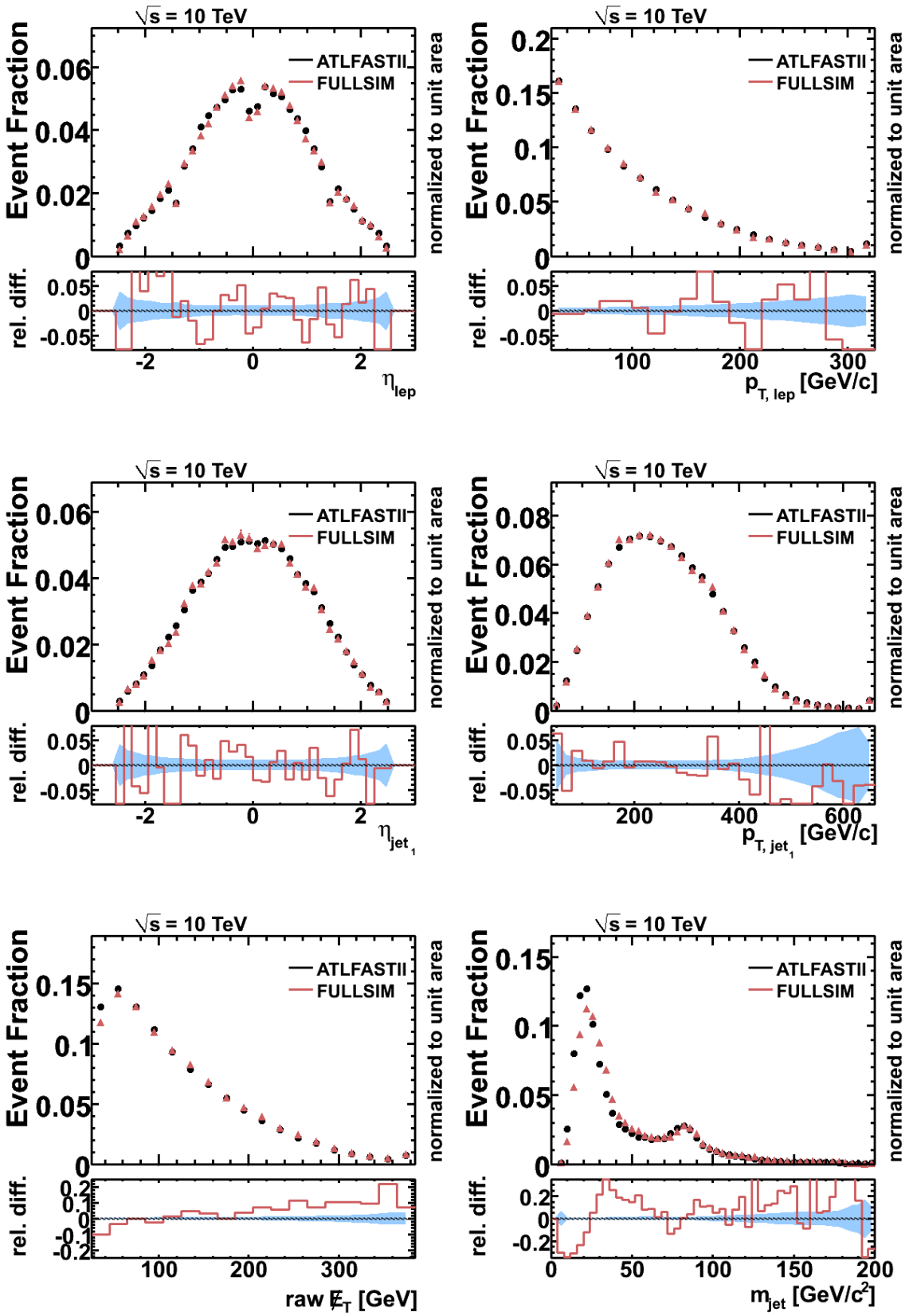

Figure 7.3: Comparison between the ATLFAST-II and full simulation for a Z' boson with $m_{Z'}$ = 1000 GeV/c^2. p_T and η of selected lepton and of selected jet with the highest transverse momentum, missing transverse energy and the highest invariant jet mass are plotted.

$m_{Z'}$, GeV/c^2	di-leptonic	semi-leptonic cat. I	semi-leptonic cat. II	fully hadronic
500	6.18%	88.29%	5.00%	0.53%
700	6.49%	86.93%	5.79%	0.79%
1000	7.49%	83.98%	6.79%	1.73%
1300	8.45%	81.44%	7.24%	2.87%
1600	9.33%	81.36%	7.43%	3.58%
2000	10.42%	77.81%	7.62%	4.15%
2500	11.71%	76.28%	7.64%	4.36%
3000	12.52%	75.67%	7.51%	4.31%

Table 7.3: Categorisation of selected signal events in the di-leptonic, semi-leptonic and fully hadronic channels using Monte Carlo truth information.

The purity of the selected signal events is reasonable, see Table 7.3. At low Z' boson masses more than 90% of events have semi-leptonic signature. The fraction of events with the di-leptonic and fully hadronic signature increases with the increasing Z' boson mass.

7.2 Event Topology

The high centre-of-mass energy at the LHC allows top quark production in a broad range of momenta. The top quarks can be produced at rest as well as at very high momenta of order of 1 TeV/c. To achieve a good reconstruction efficiency, we have to optimise the reconstruction algorithm in the whole p_{T} range. Previous Monte Carlo studies [73] have shown that the efficiency of the "standard" top quark reconstruction algorithms degrade rapidly with rising resonance mass or rather rising momenta. Our aim is to analyse this loss in efficiency and to develop a new method to reconstruct top quarks at various p_{T}s.

The "standard" top reconstruction algorithms assume well separated decay products. One isolated lepton, two jets coming from b-quarks, two jets coming from light quarks plus additional jets from gluon radiation are expected for the semi-leptonic $t\bar{t}$ decays. This topology is dominant at low transverse momenta of the top quarks. With the increasing energy the decay products of the individual top quarks will be more collimated. The partons, coming from W bosons most probably, may merge in one jet. At transverse momenta much higher than the top quark mass, all decay products of a single top quark may be collimated in one jet. At such high momenta, the isolation criterion for leptons may be not fulfilled any more.

To understand qualitatively the dependence of the event topology on the transverse momenta of the top quarks, the probability for various topologies at different Z' boson masses has been investigated. The event topology is defined by the jet with the highest number of partons in a cone $\Delta\mathrm{R} < 0.4$ around the jet. Events containing only jets with one matched parton, will be tagged as events with the "resolved" topology. Events with two matched par-

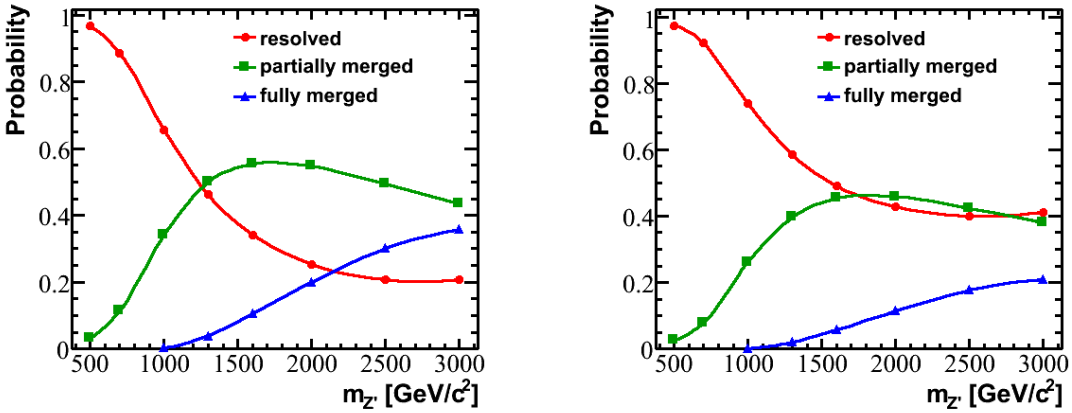

(a) generator level (b) detector level

Figure 7.4: Probability that partons from hadronic decaying top quarks will not be merged (red circles), that two partons will be merged in one jet (green squares) and all three partons will be merged (blue triangles) at generator level 7.4(a) and after the detector simulation 7.4(b). Jets are reconstructed with the ATLAS Cone 0.4 jet algorithm.

tons are named "partially merged" events and such with three merged partons are so-called "fully merged" events.

The fraction of resolved, partially merged and fully merged events is presented in Figure 7.4. The plot on the left is obtained using truth jets reconstructed from generator particles without detector simulation. Only $t\bar{t} \rightarrow e$ + jets and $t\bar{t} \rightarrow \mu$ + jets decay modes are considered here. At low $m_{t\bar{t}}$ dominates the resolved event topology. The fraction of partially merged events increases with the rising Z' boson mass and achieves its maximum at about 1600 GeV/c^2. At the same time the amount of fully merged events is increasing and leads to a decrease of partially merged events. A similar behaviour is observed for the reconstructed jets after detector simulation. But the reconstruction efficiency for the partially and fully merged topology is in general lower.

To identify the event topology in collision data, the invariant jet mass can be used. As discussed in Section 5.4 the invariant mass of jets originating from W bosons or top quarks is related to the mass of the parent particle. In case of partially merged events we expect that quarks from the W boson decay will be merged into one jet and the jet mass will be distributed around 80.4 GeV/c^2. In case of fully merged events, all quarks from the top quark decay will be merged in one jet and the mass of the jet will be around 172.5 GeV/c^2. The mass of gluon or light quark jets is generated by gluon emission. Thus, the masses of single parton jets will be well below 50 GeV/c^2 as shown in Section 5.4. The invariant jet mass distributions for all three event topologies are presented in Figure 7.5.

For the resolved event topology the standard top quark pair reconstruction can be applied. At least four jets, one isolated lepton and missing transverse energy are characteristic for this channel. In case of partially merged events prevalently the light quarks coming from

W boson will be reconstructed in one jet. Thus only three or more jets are required as defined in Section 7.1. A pronounced peak at the W boson mass is visible in Figure 7.5(b). With the increasing Z' boson mass, leading to an increasing jet p_{T}, the jet mass peak is shifted to higher values. The angle between the lepton and the b-quark of the leptonically decaying top quarks is decreasing with the increasing Z' boson mass as shown in Figure 7.6. Thus not all leptons can fulfil the lepton isolation criteria. At least three jets, one lepton and missing transverse energy is the signature of the partially merged topology. For the fully merged topology a peak at the top quark mass is visible in Figure 7.5(c). At least two jets, one lepton and missing transverse energy are expected for the fully merged topology. In the mass region below 2000 GeV/c^2, this event topology is less probable. Thus, we will neglect these events and deal exclusively with the resolved and the partially merged topologies in this analysis.

7.3 Analysis Strategy

This reconstruction approach is designed for the $t\bar{t}$ resonance searches in the early stage of the experiment. The strategy is to keep the signal efficiency as high as possible and to use as few observables as possible. The goal is to reduce the systematic uncertainty and to test a wide range of $m_{t\bar{t}}$ also increasing the sensitivity in a mass range which is currently tested by DØ and CDF.

No attempt is made to fully reconstruct the individual top quarks to calculate $m_{t\bar{t}}$. The invariant mass is reconstructed by summing up the four momenta of the selected jets, the lepton and the reconstructed neutrino. The number of required jets depends on the event topology, which is defined using the highest invariant jet mass in the event. The events are separated into sub-samples with different jet multiplicities and jet masses. That allows one to prepare a topology-dependent reconstruction of signal events. The composition and the size of background varies for different sub-samples. The events can be separated in a very signal pure and in a background enriched sub-samples to optimise the sensitivity for the signal in a wide $m_{t\bar{t}}$ range.

The selected events are classified in the following way:

- **4 jets sub-sample**

  events containing four jets are supposed to be fully resolved events. The four jets, the lepton and reconstructed neutrino are used to compute the $t\bar{t}$ invariant mass.

- **5 or more jets sub-sample**

  events containing more than four jets are supposed to be fully resolved events with additional jets from gluon radiation. The four jets with highest transverse momenta, the lepton and reconstructed neutrino are used to compute the $t\bar{t}$ invariant mass.

- **3 jets low and high jet mass sub-samples**

  events containing three jets are supposed to have merged jets. These events are split into two sub-samples according to the highest jet mass m_{jet} found in the event. The cut value is chosen in the way to separate events in background dom-

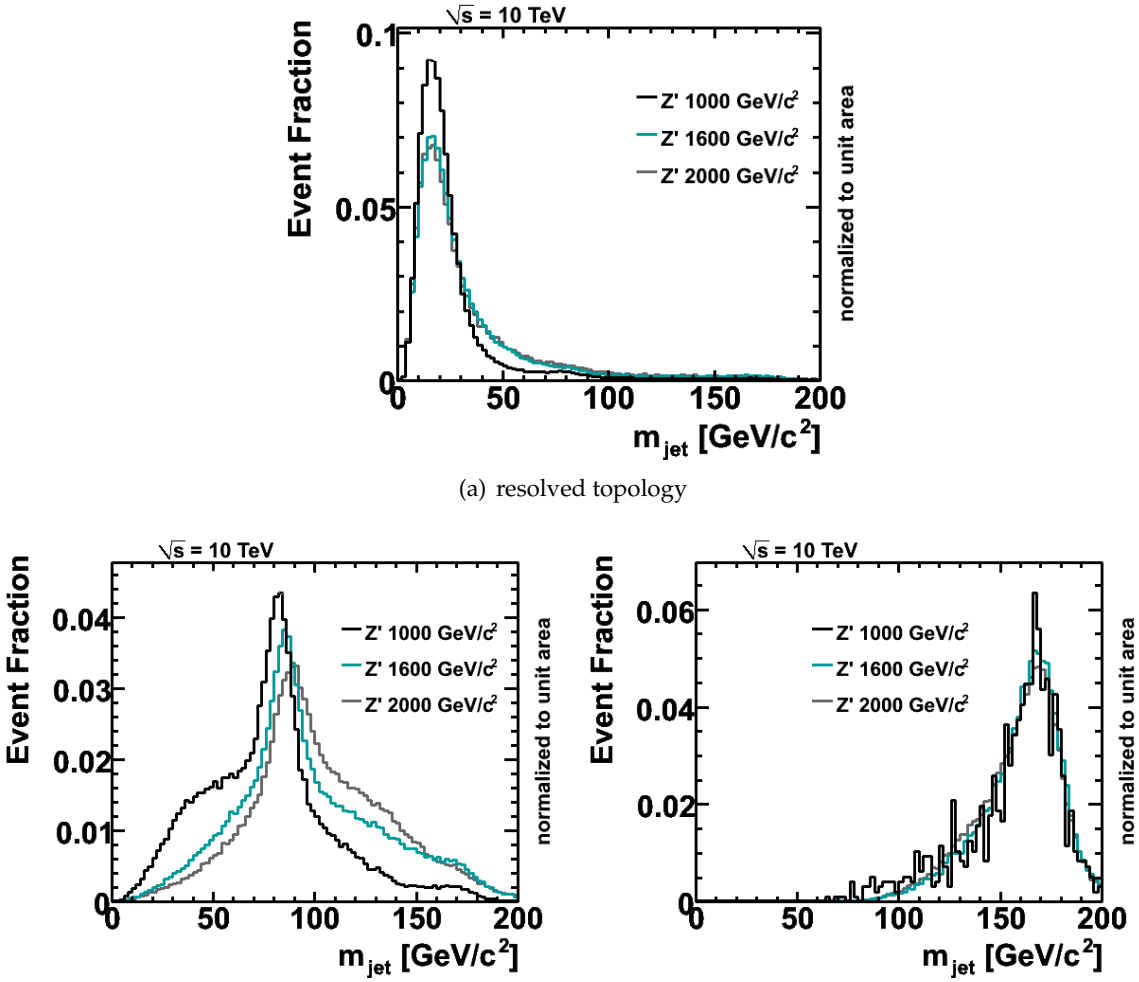

(a) resolved topology

(b) partially merged topology

(c) fully merged topology

Figure 7.5: Invariant jet mass distributions for the resolved (a), partially merged (b) and fully merged (c) event topologies evaluated for signal events with $m_{Z'}$ = 1000, 1600 and 2000 [GeV/c^2].

inated and signal dominated regions. The first sub-sample consists of three jet events with m_{jet} below 65 GeV/c^2, three jet events with m_{jet} above 65 GeV/c^2 forming the second sub-sample. The three jets, the lepton and reconstructed neutrino are used to compute the $t\bar{t}$ invariant mass.

The contribution of different background sources differs for electron and muon channels. Therefore the single sub-classes are separated additionally into electron and muon subsamples.

The number of selected jets and the highest jet mass for the main background processes and Z' boson with $m_{Z'}$ = 1000 GeV/c^2 are plotted in Figure 7.7. About 82% of W + jets and single top events and about 76% of Z + jets and QCD multi-jets events are in the 3 jet bin. 63% of $t\bar{t}$ events are in the 3 jet bin, about 29% of $t\bar{t}$ are in the 4 jet bin and 8% of events have

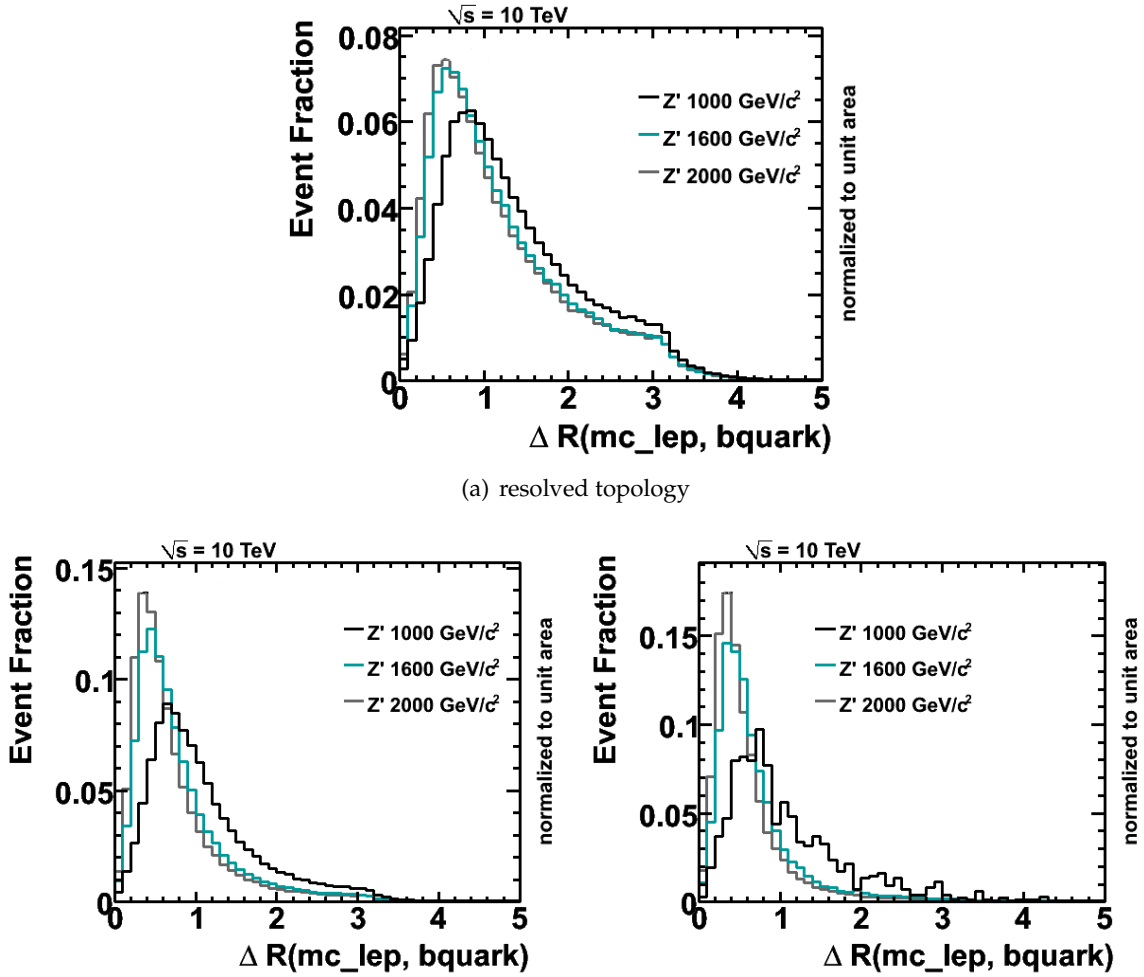

(a) resolved topology

(b) partially merged topology

(c) fully merged topology

Figure 7.6: The angle between the true lepton and the b-quark ΔR(mc_lep,bquark) for the resolved (a), partially merged (b) and fully merged (c) event topologies evaluated for signal events with $m_{Z'}$ = 1000, 1600 and 2000 [GeV/c^2].

5 or more jets. Signal events have a higher jet multiplicity, about 51% of events are in the 3 jet bin, 31% in the 4 jet bin and 11% are in the 5 jet bin. The jet mass distributions are similar for all background processes, because most of events do not contain partially or fully merged topology like this is the case for the signal events.

The amount of expected signal and background events in the different sub-samples, normalised to $\mathcal{L}$ = 200 pb^{-1}, is listed in Table 7.4. The number of events has been calculated over the whole $m_{t\bar{t}}$ range. The main source of background in the "3 jet low m_{jet}" sub-sample are W + jets events, $t\bar{t}$ events are the second important background. With the increasing jet multiplicity the $t\bar{t}$ background dominates over the W + jets events. Contributions of other sources of background are small compared to the main backgrounds. With the increasing Z' boson mass, the "3 jet high m_{jet}" sub-sample contains more and more signal events, because

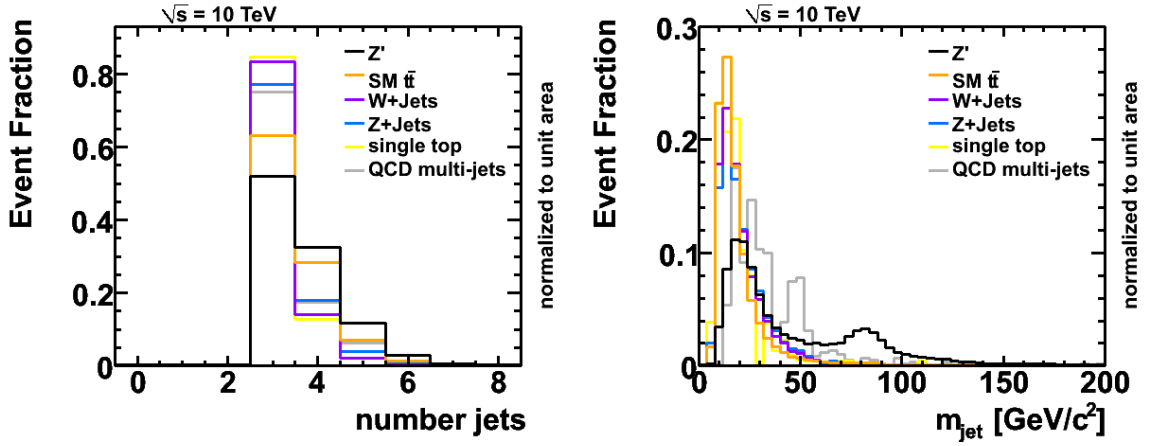

(a) number jets (b) highest jet mass

Figure 7.7: Number of reconstructed jets (a) and the highest invariant jet mass in the 3 jet bin (b) after selection cuts for the main background processes and a signal process with $m_{Z'}$=1000 GeV/c^2.

	3 jet low m_{jet}		3 jet high m_{jet}		4 jet		5 or more jets	
	e	μ	e	μ	e	μ	e	μ
$t\bar{t}$	1920	1973	54.5	44.9	890	901	269	275
W + jets	2071	2183	37.1	24.4	350	384	58.5	66.2
Z + jets	120	109	2.19	1.17	32.4	21.7	9.43	4.52
single top	47.6	54.8	1.41	0.47	7.48	8.27	2.01	1.10
QCD (ALPGEN)	268.6	87.8	17.4	9.37	79.1	10.7	12.0	25.4
all background	4427.2	4407.6	112.6	80.31	1361	1325.7	350.9	371.2
Z' boson (SSM model) with $m_{Z'}$ [GeV/c^2]								
$m_{Z'}$ = 500	28.2	32.7	0.25	0.23	10.6	12.2	3.00	3.40
$m_{Z'}$ = 700	14.6	17.3	1.06	0.96	8.44	9.92	2.94	3.45
$m_{Z'}$ = 1000	3.30	4.06	1.46	1.52	2.91	3.55	1.40	1.69
$m_{Z'}$ = 1300	0.75	0.99	0.76	0.86	0.93	1.17	0.53	0.69
$m_{Z'}$ = 1600	0.19	0.26	0.32	0.38	0.33	0.42	0.20	0.28
$m_{Z'}$ = 2000	0.041	0.056	0.10	0.12	0.091	0.12	0.063	0.088
$m_{Z'}$ = 2500	0.0083	0.011	0.025	0.03	0.021	0.028	0.015	0.022
$m_{Z'}$ = 3000	0.0022	0.0029	0.0063	0.0074	0.0054	0.0072	0.0041	0.0058

Table 7.4: Number of expected signal and background events subdivided in sub-samples according to the number of jets, the highest jet mass and the lepton types normalised to 200 pb^{-1}. The "3 jet low m_{jet}" sub-sample consists of three jet events with the highest jet mass below 65 GeV/$c^2$and the "3 jet high m_{jet}" sub-sample of three jet events with the highest mass above 65 GeV/c^2.

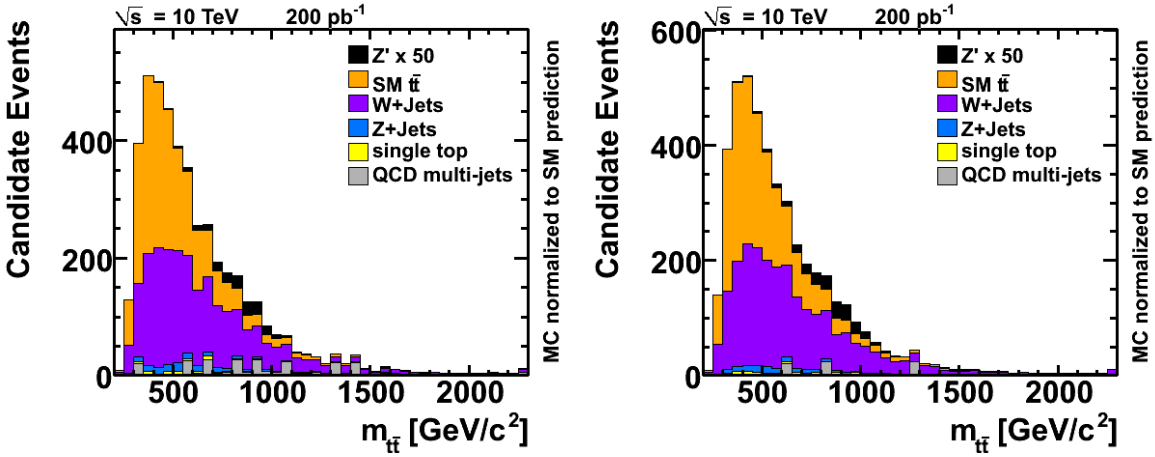

(a) electron + 3 jets, low m_{jet}

(b) muon + 3 jets, low m_{jet}

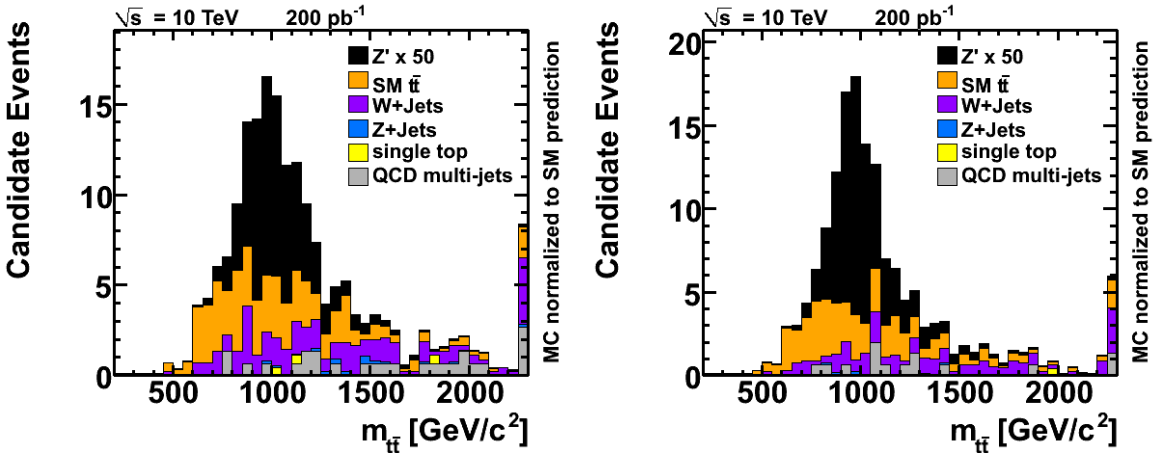

(c) electron + 3 jets, high m_{jet}

(d) muon + 3 jets, high m_{jet}

Figure 7.8: The $t\bar{t}$ invariant mass distributions in 3 jet channel for electron + 3 jets, low m_{jet} (a), muon + 3 jets, low m_{jet} (b), electron + 3 jets, high m_{jet} (c) and muon + 3 jets, high m_{jet} (d) sub-samples. The Z' boson cross section (SSM model) has been multiplied by a factor of 50.

the amount of merged jets increases.

The reconstructed $t\bar{t}$ mass distributions are shown in Figure 7.8 and 7.9 for all sub-samples. The signal events are scaled by a factor of 50 for a better visibility. Not only the amount of events, but also the $m_{t\bar{t}}$ shape differs for individual sub-samples for the signal and as well as for the background.

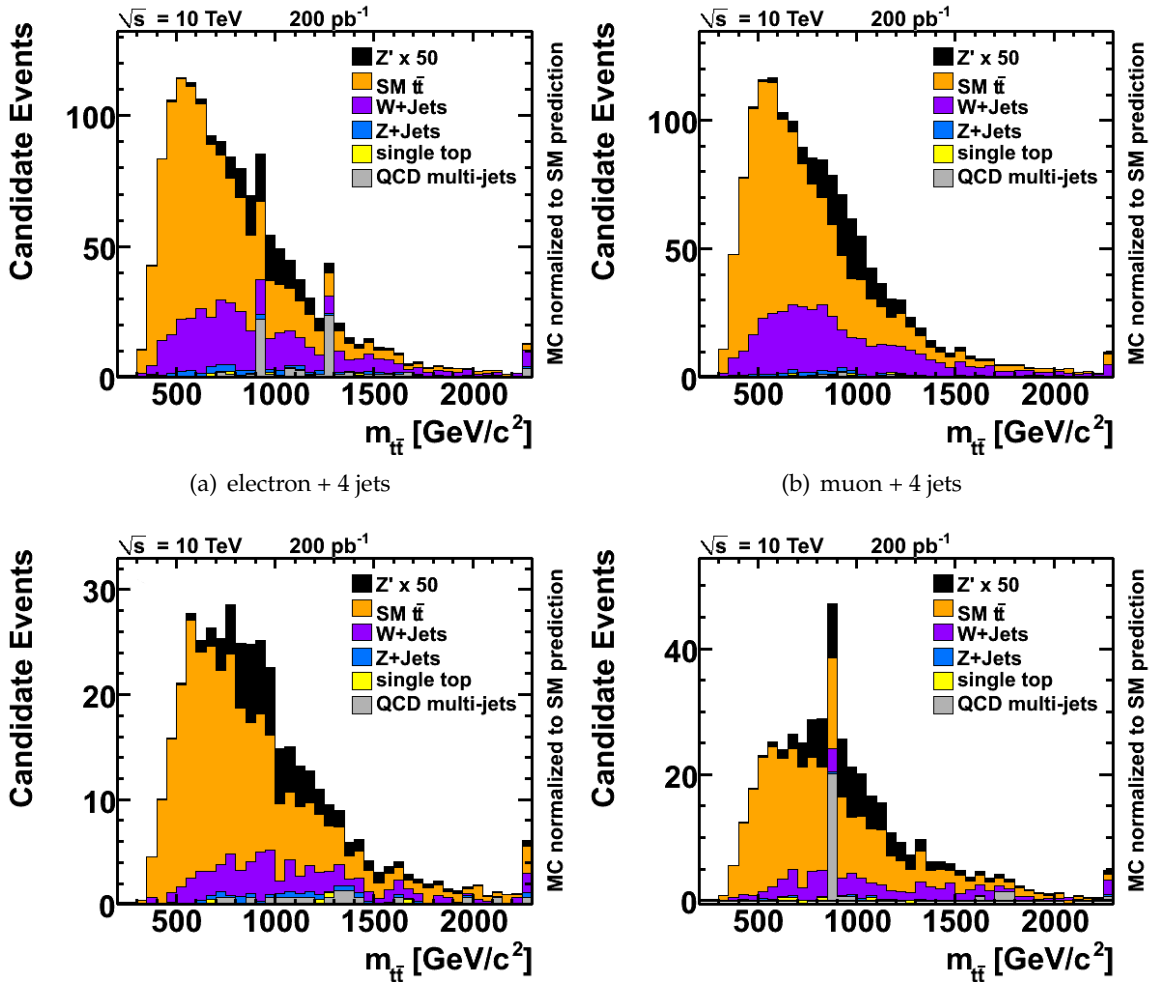

(a) electron + 4 jets

(b) muon + 4 jets

(c) electron + 5 or more jets

(d) muon + 5 or more jets

Figure 7.9: The $t\bar{t}$ invariant mass distributions in 4 and 5 or more jets channel for electron + 4 jets (a), muon + 4 jets (b), electron + 5 or more jets (c) and muon + 5 or more jets (d) sub-samples. The Z' boson cross section (SSM model) has been multiplied by a factor of 50.

7.4 Selection Efficiency and Mass Resolution

In this section an estimate for the sensitivity of this analysis for $t\bar{t}$ resonances in different sub-samples will be given. The focus will be put on two aspects: the event selection efficiency in a mass window around the reconstructed resonance peak and the mass resolution. The ratio of signal events to the square root of background events $S/\sqrt{B}$ determines the sensitivity of the individual sub-samples. In addition to the total rates, the width of the reconstructed $m_{t\bar{t}}$ distribution influences the sensitivity to the signal. A good mass resolution allows an easier separation of the resonance peak and $t\bar{t}$ continuum.

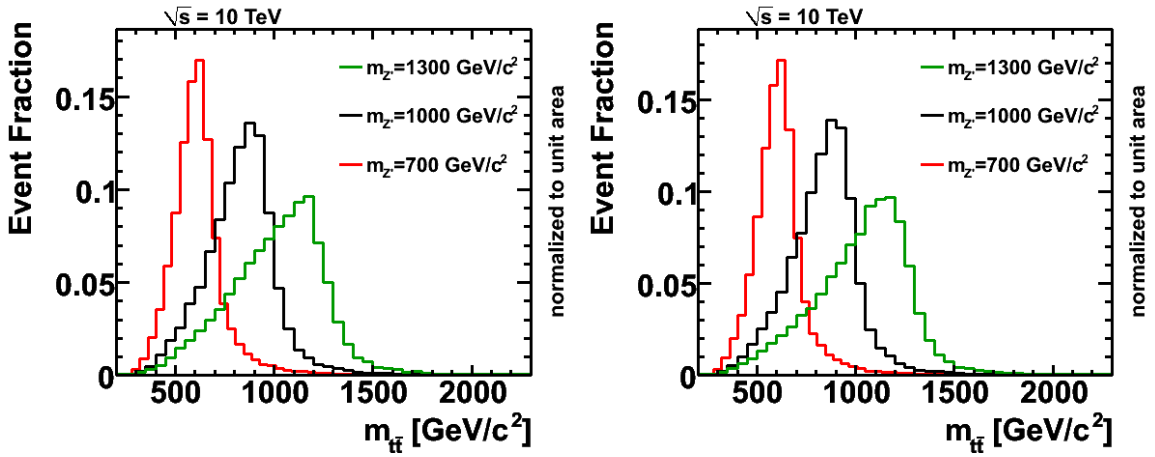

(a) electron + 3 jets, low m_{jet}

(b) muon + 3 jets, low m_{jet}

(c) electron + 3 jets, high m_{jet}

(d) muon + 3 jets, high m_{jet}

Figure 7.10: Z' boson mass distribution in electron + 3 jets, low m_{jet} (a), muon + 3 jets, low m_{jet} (b), electron + 3 jets, high m_{jet} (c) and muon + 3 jets, high m_{jet} (d) sub-samples for Z' boson masses of $m_{Z'}$ = 700, 1000, 1300 GeV/c^2.

Selection Efficiency

To take into account signal events with the partially merged topology, defined in Section 7.2, events with only three jets are considered as well. That increases the amount of background events by a factor of 2.6. But for the sensitivity to the resonant signal not the total number of background events is of interest, but rather the amount of background events under the signal bump. Therefore, the number of expected events in the ± 1 root mean square (RMS) range around the reconstructed signal mass peak has been determined. The RMS and the maximal value have been taken from the Z' boson $m_{t\bar{t}}$ distributions shown in Figure 7.10 and 7.11. The results are summarised in Table 7.5.

The "3 jet low m_{jet}" sub-sample has the highest background rate especially from the

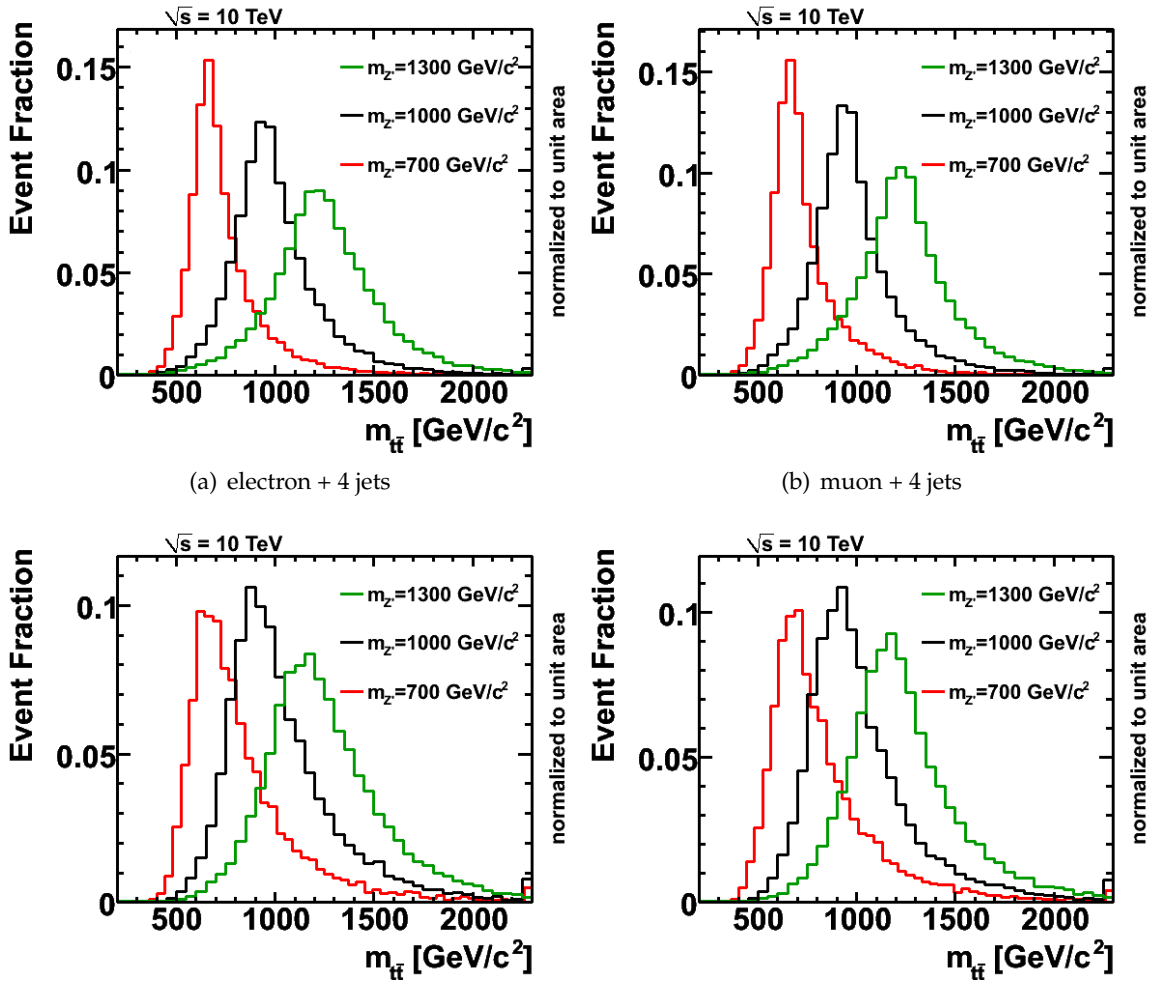

(a) electron + 4 jets

(b) muon + 4 jets

(c) electron + 5 or more jets

(d) muon + 5 or more jets

Figure 7.11: Z' boson mass distribution in electron + 4 jets (a), muon + 4 jets (b), electron + 5 or more jets (c) and muon + 5 or more jets (d) sub-samples for Z' boson masses of $m_{Z'}$ = 700, 1000, 1300 GeV/c^2.

W + jets events, but it still has a high amount of the signal events. Thus its sensitivity is comparable to the "4 jets" and "5 or more jets" category particularly at lower Z' boson masses. But this sub-sample looses its importance for the higher Z' boson masses, because the number of the expected signal events decreases.

As shown in Figure 7.4(b), the fraction of events with the merged topology rises with the increasing Z' boson mass. More and more signal events populate the "3 jet high m_{jet}" category. Due to a low background rate in this category, it has the best $S/\sqrt{B}$ ratio especially at high Z' boson masses.

The $S/\sqrt{B}$ ratio of the "4 jet" and "5 or more jets" sub-samples is of the same size. The muon channel is slightly more sensitive for all event topologies, because a higher signal selection efficiency prevails a partly higher background selection efficiency. Finally the combi-

	3 jet low m_{jet}		3 jet high m_{jet}		4 jet		5 or more jets	
	ele	muo	ele	muo	ele	muo	ele	muo
Z' boson with $m_{Z'}$ = 1000 GeV/c^2								
max [GeV/c^2]	874.3	874.3	974.6	974.6	946.3	946.3	923.2	923.2
RMS [GeV/c^2]	184.3	183.9	193.2	194.1	234.9	230.5	276.5	271.3
$t\bar{t}$	232	243	25.2	20.3	296	301	117	123
W + jets	516	548	13.4	8.36	159	172	29.2	29.4
Z + jets	33.1	31.3	0.40	0.48	16.1	9.87	4.83	2.15
single top	7.26	12.8	0.88	0.0	3.45	4.09	0.07	0.52
QCD (ALPGEN)	99.1	33.4	2.68	4.68	36.1	7.36	5.34	21.4
Z'	2.64	3.02	1.19	1.26	2.28	2.84	1.02	1.26
$S/\sqrt{B}$	0.089	0.10	0.18	0.22	0.10	0.13	0.082	0.095
Z' boson with $m_{Z'}$ = 2000 GeV/c^2								
max [GeV/c^2]	1627	1627	1936	1936	1933	1933	1813	1813
RMS [GeV/c^2]	423	429	328	291	422	397	400	380
$t\bar{t}$	27.3	29.1	2.81	3.03	20.3	41.3	13.6	17.6
W + jets	101	115	5.44	4.04	29.6	32.4	7.44	14.4
Z + jets	8.01	6.43	0.24	0.16	3.38	1.96	1.77	0.54
single top	0.97	0.0	0.45	0.45	0.44	0.45	0.44	0.0
QCD (ALPGEN)	67.5	26.3	5.35	0.67	8.02	2.67	2.67	3.34
Z'	0.024	0.034	0.068	0.083	0.064	0.088	0.043	0.063
$S/\sqrt{B}$	0.0017	0.0026	0.018	0.029	0.0081	0.0099	0.0084	0.011

Table 7.5: Number of expected signal and background events in the ± 1 RMS range around the reconstructed signal mass peak normalised to the integrated luminosity of 200 pb^{-1}. The RMS and the maximal value have been taken from the Z' boson $m_{t\bar{t}}$ distributions shown in Figure 7.10 and 7.11.

nation of all sub-samples provides the sensitivity in a broad mass range from twice the top quark mass into the TeV-regime.

Mass Resolution

The Z' boson mass resolution is determined from the residual distribution of the reconstructed $t\bar{t}$ mass minus the generated Z' boson mass. The distributions for $m_{Z'}$ = 700, 1000 and 1300 GeV/c^2 are presented in Figure 7.12 and 7.13 for each sub-sample. The full width at half maximum (FWHM) and the position of maximum (max) are listed in Table 7.6.

The mass peak is shifted to the negative values for nearly all sub-samples and Z' boson masses. In the "3 jet low m_{jet}" sub-sample the incomplete reconstruction of the $t\bar{t}$ system leads to the shift to smaller $m_{t\bar{t}}$. The shift in the "3 jet high m_{jet}" and "4 jets" sub-samples is of the same size and increases with the increasing Z' boson mass.

$m_{Z'}$	3 jet low m_{jet}		3 jet high m_{jet}		4 jet		5 or more jets	
	FWHM	max	FWHM	max	FWHM	max	FWHM	max
electron + jets								
500	133	-60	363	56	147	-20	312	19
700	178	-100	171	-25	164	-22	308	-22
1000	269	-77	247	-25	267	-49	352	-90
1300	365	-125	305	-47	344	-78	438	-125
1600	524	-189	289	-64	442	-65	523	-163
2000	854	-125	505	-65	506	-60	614	-159
2500	553	-65	598	-85	638	-65	754	-186
3000	248	-67	534	-67	530	-67	638	-170
muon + jets								
500	128	-60	442	15	150	-20	322	19
700	188	-83	109	-25	153	-22	294	-22
1000	267	-77	162	-25	249	-32	318	-90
1300	322	-125	234	-47	295	-54	363	-125
1600	489	-155	259	-64	356	-65	467	-163
2000	682	-125	313	-65	368	-65	489	-167
2500	437	-90	362	-85	403	-70	522	-186
3000	247	-67	420	-90	393	-67	593	-188

Table 7.6: The full width at half maximum and the position of the maximum for different resonance masses. All values are given in GeV/c^2.

The shift in the "5 or more jets" sub-sample is twice as high as in the "4 jets" sub-sample. The main reason for the shift is gluon radiation off the partons from the top quark decay. If the radiation is hard enough, the radiated parton can be reconstructed as an additional jet. This jet is not taken into account in the $m_{t\bar{t}}$ calculation and the reconstructed invariant mass is underestimated. The probability to radiate gluons rises with the increasing quark energy, thus the shift is larger for higher Z' boson masses.

The mass is overestimated for Z' boson with $m_{Z'}$ = 500 GeV/c^2 in the "3 jet high m_{jet}" and "5 or more jets" sub-samples. Only one per cent of events with the partially merged topology are expected at low Z' boson masses. So it is less probable to find correctly reconstructed signal events in this category and the required high jet mass leads to a higher $m_{t\bar{t}}$. Four jets with the highest p_{T} are taken to calculate the invariant mass in the "5 or more jets" sub-sample, that shifts the mass peak to the higher values.

The residual distributions are asymmetric, in particular for the Z' boson masses below 1300 GeV/c^2. The $m_{t\bar{t}}$ distribution in the 3 jet bin channel shows longer tails to smaller masses for low m_{jet} and vice versa for higher m_{jet}. With the increasing Z' boson mass the distributions become more symmetric. The full width at half maximum varies on average from 20 to 30% of the Z' boson mass depending on the sub-sample.

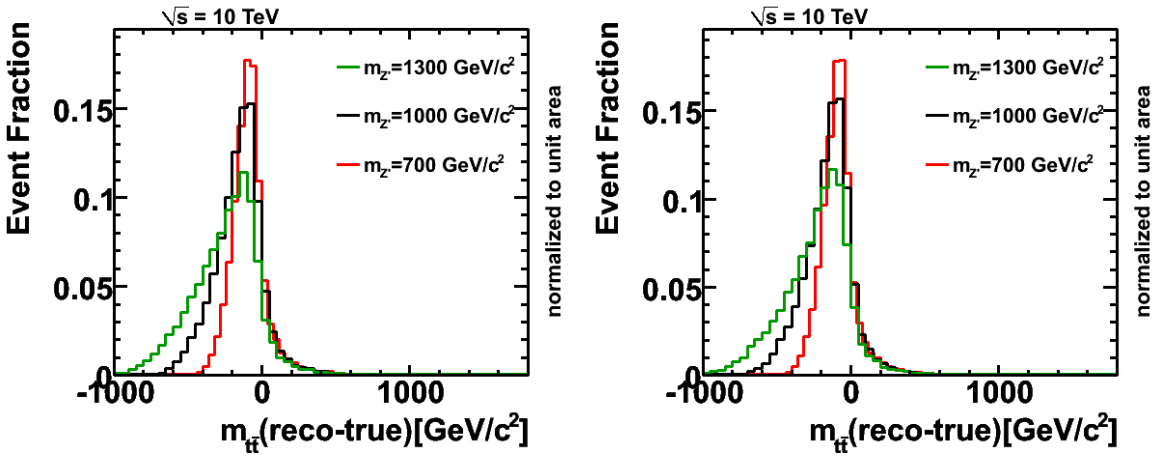

(a) electron + 3 jets, low m_{jet}

(b) muon + 3 jets, low m_{jet}

(c) electron + 3 jets, high m_{jet}

(d) muon + 3 jets, high m_{jet}

Figure 7.12: Z' boson mass resolution in electron + 3 jets, low m_{jet} (a), muon + 3 jets, low m_{jet} (b), electron + 3 jets, high m_{jet} (c) and muon + 3 jets, high m_{jet} (d) sub-samples for Z' boson masses of $m_{Z'}$ = 700, 1000, 1300 GeV/c^2.

7.5 Systematic Uncertainties

The discovery sensitivity of this analysis to narrow width $t\bar{t}$ resonances is affected by several sources of systematic uncertainties. The estimated ratio of signal and background events as well the shape of the $m_{t\bar{t}}$ distribution or both can be affected. Following sources of systematic uncertainties have been considered:

- luminosity
- jet energy scale and resolution
- parton distribution function
- initial and final state radiation

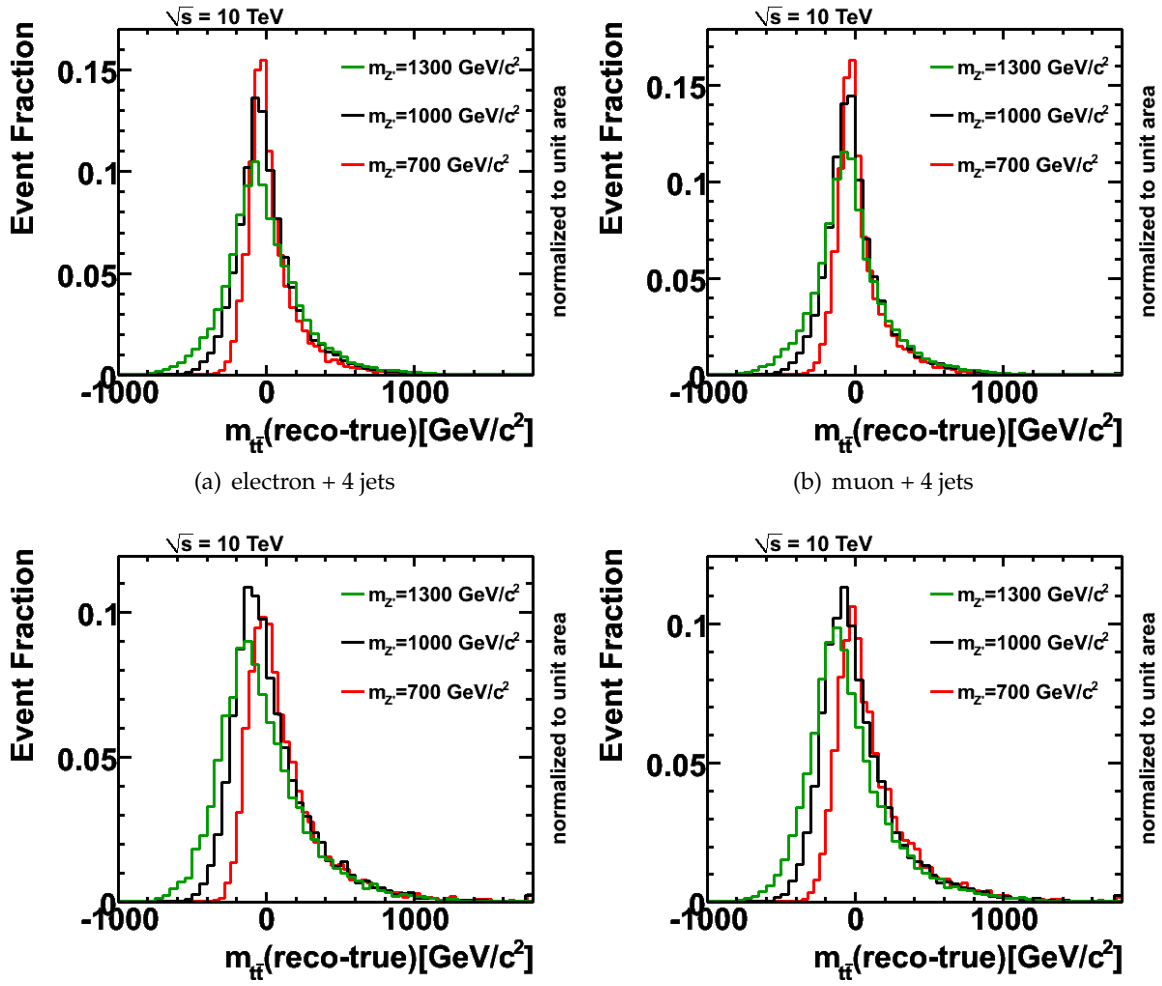

(a) electron + 4 jets (b) muon + 4 jets

(c) electron + 5 or more jets (d) muon + 5 or more jets

Figure 7.13: Z' boson mass distribution in electron + 4 jets (a), muon + 4 jets (b), electron + 5 or more jets (c) and muon + 5 or more jets (d) sub-samples for Z' boson masses of $m_{Z'}$ = 700, 1000, 1300 GeV/c^2.

- QCD background estimation
- top quark mass

and will be discussed here.

Luminosity

The uncertainty on the measured integrated luminosity is expected to be 10%. At the time of writing, the uncertainty of 11% could be achieved in collision data using an absolute calibration via beam separation scans [77]. This uncertainty effects all processes for which the expected rate is determined using Monte Carlo efficiencies.

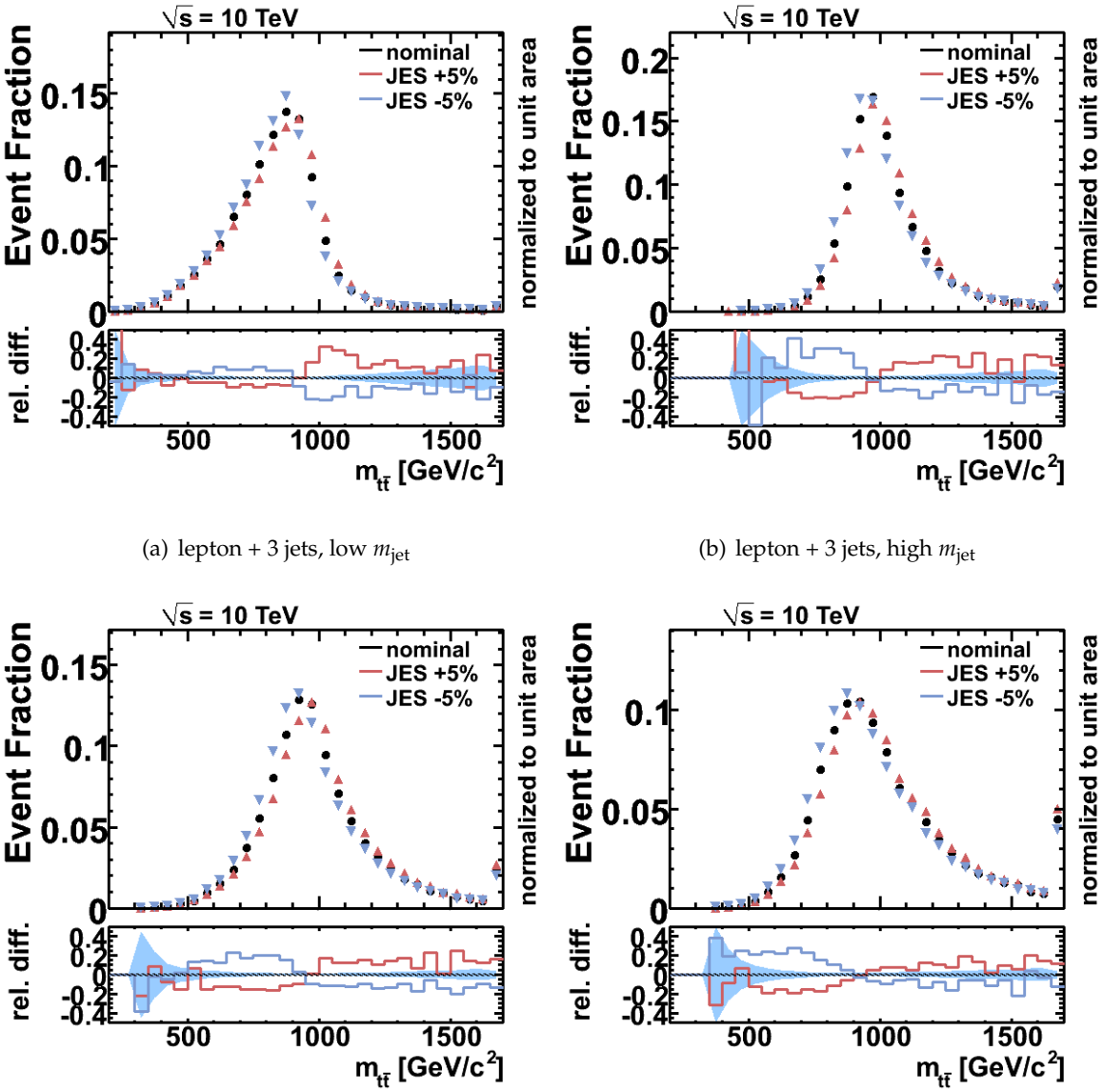

(a) lepton + 3 jets, low m_{jet}

(b) lepton + 3 jets, high m_{jet}

(c) lepton + 4 jets

(d) lepton + 5 or more jets

Figure 7.14: Jet energy scale systematics for Z' boson events with $m_{Z'} = 1000$ GeV/c^2 subdivided in "lepton + 3 jets, low m_{jet}" (a), "lepton + 3 jets, high m_{jet}" (b), "lepton + 4 jets" (c), "lepton + 5 or more jets" (d) samples. The blue band is the statistical uncertainty of the nominal distribution.

Jet Energy Scale and Resolution

The uncertainty on the jet energy scale (JES) and the jet energy resolution (JER) has a strong impact on this analysis, because jets are used to calculate the invariant $t\bar{t}$ mass. As mentioned in Section 5.4, the jet energy measured in the calorimeter has to be calibrated to the

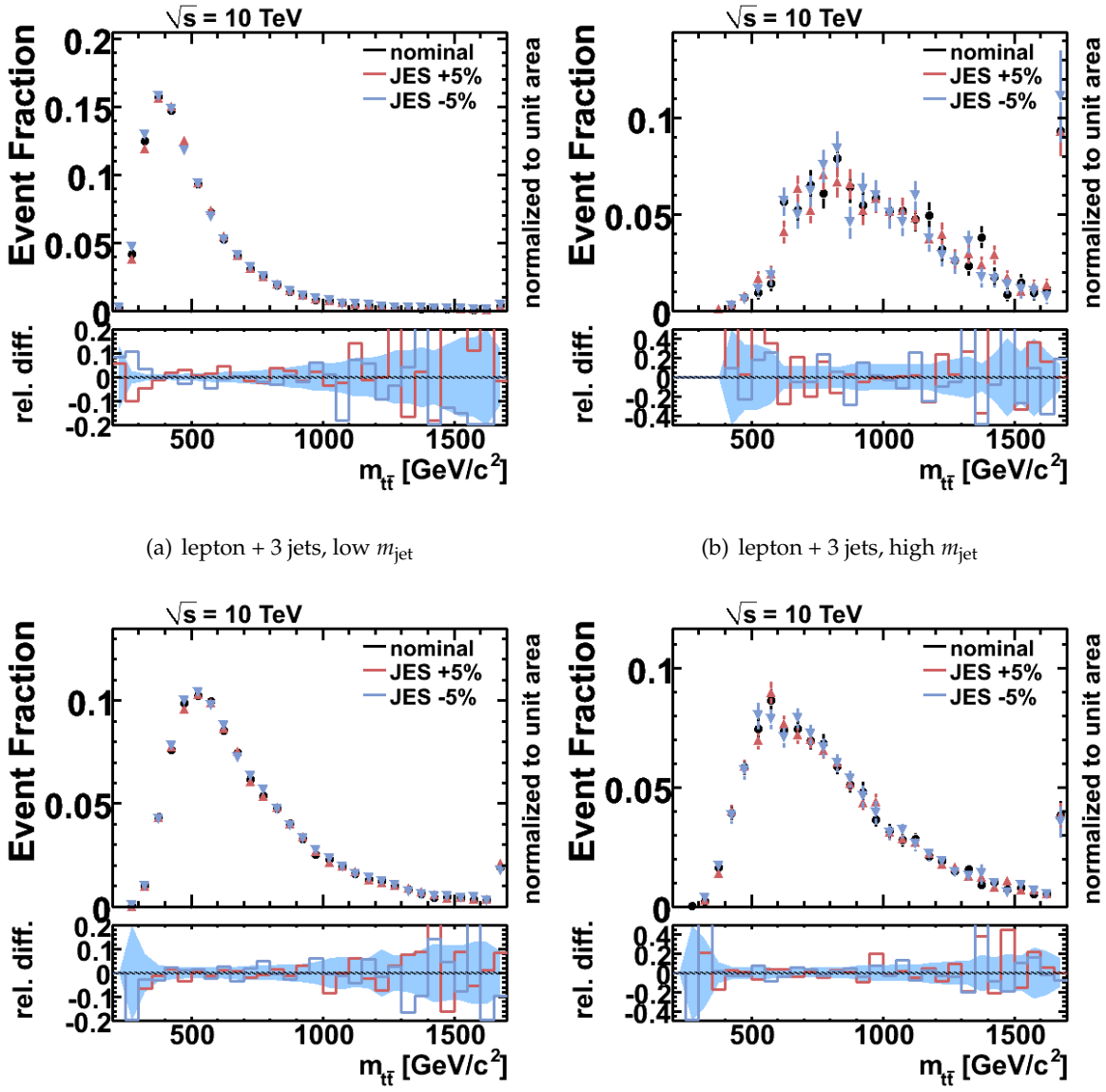

(a) lepton + 3 jets, low m_{jet}

(b) lepton + 3 jets, high m_{jet}

(c) lepton + 4 jets

(d) lepton + 5 or more jets

Figure 7.15: Jet energy scale systematics for $t\bar{t}$ events sub-divided in "lepton + 3 jets, low m_{jet}" (a), "lepton + 3 jets, high m_{jet}" (b), "lepton + 4 jets" (c), "lepton + 5 or more jets" (d) samples. The blue band is the statistical uncertainty of the nominal distribution.

hadronic energy scale using a detailed simulation of hadronic showers in the detector. This calibration can systematically shift the jet energy to higher or lower values. Additionally the jet energy resolution could be underestimated in the Monte Carlo simulations compared to the measured resolution in collision data. Both affect the sensitivity to the signal. To estimate the impact of these uncertainties on the analysis, the energy of all selected jets have

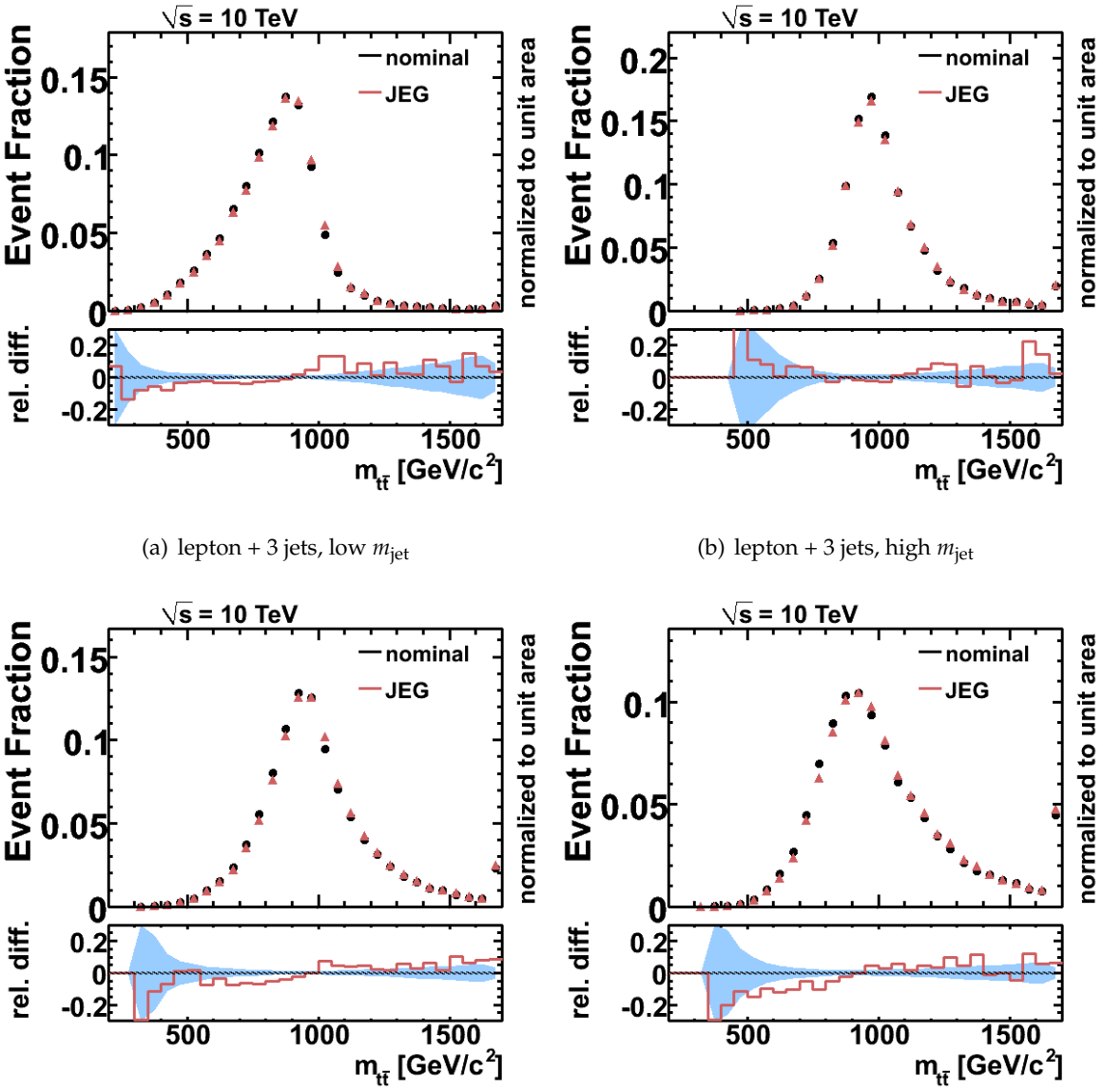

(a) lepton + 3 jets, low m_{jet}

(b) lepton + 3 jets, high m_{jet}

(c) lepton + 4 jets

(d) lepton + 5 or more jets

Figure 7.16: Jet energy resolution systematics for Z' boson events with $m_{Z'} = 1000$ GeV/c^2 sub-divided in "lepton + 3 jets, low m_{jet}" (a), "lepton + 3 jets, high m_{jet}" (b), "lepton + 4 jets" (c), "lepton + 5 or more jets" (d) samples. The blue band is the statistical uncertainty of the nominal distribution.

been scaled up and down by 5% and have been smeared by a Gaussian function with the width of $\frac{25\%}{\sqrt{E_{\text{jet}}}} + 5\%$. For each jet a random number is generated from this Gaussian function and the jet energy is scaled by this number. Missing transverse energy is calculated from the total energy balance of the event. Thus, the difference between the unscaled and scaled jet energy is vectorially added to $E_{\text{T}}^{\text{miss}}$.

The influence of the jet energy scale variation on the reconstructed $m_{t\bar{t}}$ shape for the signal events can be seen in Figure 7.14 and for the $t\bar{t}$ background events in Figure 7.15. The electron and muon channels are combined in these plots, because this systematic uncertainty affects the $m_{t\bar{t}}$ shapes of both channels in the same way. The shift of the jet energy scale leads to the shift of the Z' boson mass peak, the relative difference of the nominal and shifted distributions is of order 20-25%. The background shapes are not affected, the relative difference of the nominal and shifted distributions is of the same order as the statistical uncertainty.

Figure 7.16 presents the jet energy resolution uncertainty for the signal events. An additional smearing of the jet energy has a small effect on the $m_{t\bar{t}}$ distributions. The maximal relative difference between the nominal and smeared distributions is about 10%.

Not only the shapes, but also the number of expected signal and background events are affected. The relative uncertainty on the number of events is listed in Table 7.7. The negative shift of JES leads to an overall loss of events or to a migration of events to the lower jet bins and for the positive shift vice versa. The jet energy smearing leads to an increase of the background and a decrease of signal events in the 3 jet bin.

Parton Distribution Function

The systematic uncertainty due to the choice of the parametrisation of the parton distribution functions (PDF) used for the signal event simulation is examined by a re-weighting scheme. It uses Monte Carlo truth information about the hard partons that participated in the hard process. The probability of an event with a particular kinematic characteristic to be produced is evaluated and re-weighted according to the new values of the PDFs. The CTEQ6LL [29] is default PDF set used to simulate signal events and the MRST2001LO [127] as an alternative PDF set.

Reconstructed $m_{t\bar{t}}$ distribution for signal events is shown in Figure 7.17. The shapes of distributions in the peak region are not affected at all. The relative change in the number of expected signal events can be found in Table 7.7 and is around 3%.

Initial and Final State Radiation

To estimate the uncertainty due to the modelling of initial (ISR) and final (FSR) state radiation for signal events, two samples have been produced for which the simulation is altered to produce either less or more gluon radiation compared to the nominal settings. The Λ_{QCD} value in the strong coupling α_S controlling the parton shower has been varied to enhance the initial state radiation and at the same time to suppress the final state radiation and vice versa.

Figure 7.18 presents the $m_{t\bar{t}}$ shapes of the nominal and altered distributions. The relative change is of order of 5-10%, in the tails prevails the statistical uncertainty. The suppressed final state radiation results in a higher energy jets, which can more easily pass the selection cuts and the number of selected events rises in the higher jet bins as shown in Table 7.7.

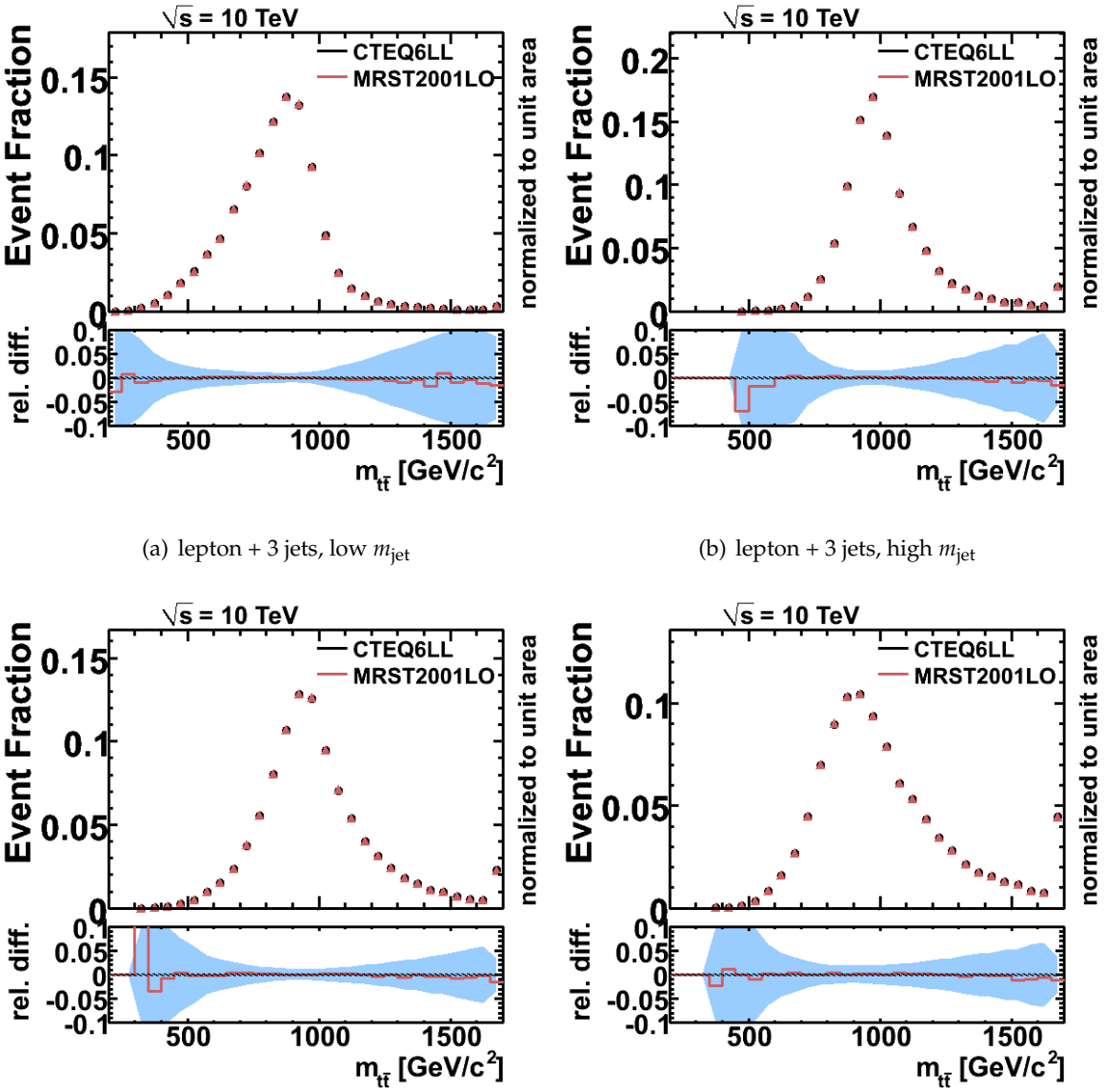

(a) lepton + 3 jets, low m_{jet}

(b) lepton + 3 jets, high m_{jet}

(c) lepton + 4 jets

(d) lepton + 5 or more jets

Figure 7.17: Parton distribution function systematics for Z' boson events with $m_{Z'} = 1000$ GeV/c^2 sub-divided in "lepton + 3 jets, low m_{jet}" (a), "lepton + 3 jets, high m_{jet}" (b), "lepton + 4 jets" (c), "lepton + 5 or more jets" (d) samples. The blue band is the statistical uncertainty of the nominal distribution.

QCD background estimation

A correct estimate of the QCD background contribution is difficult due to a high cross section but also a low selection efficiency of order 10^{-6} and thus limited statistics available in particular at low energies. The number of selected events is too low to get smooth distribu-

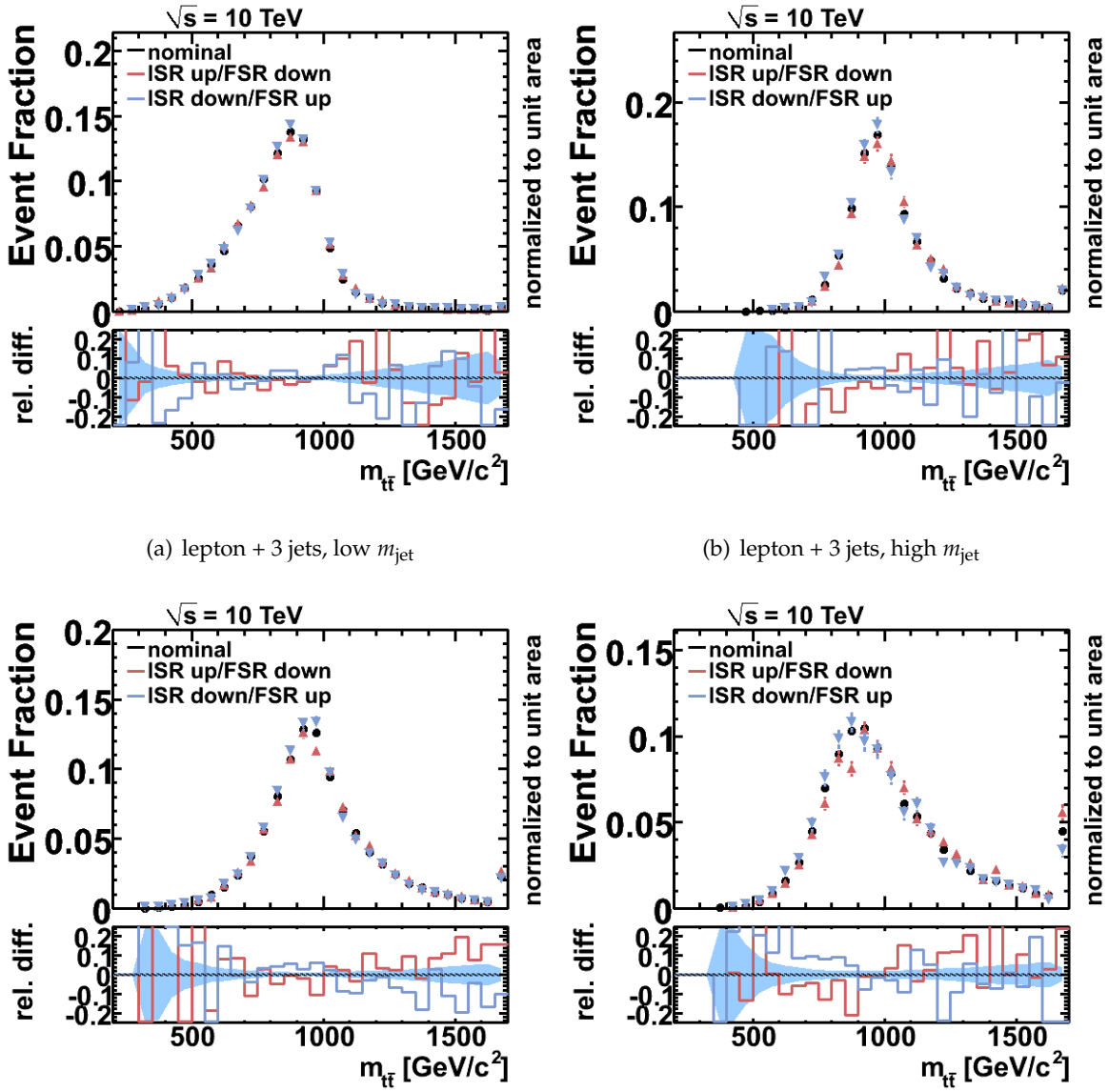

(a) lepton + 3 jets, low m_{jet}

(b) lepton + 3 jets, high m_{jet}

(c) lepton + 4 jets

(d) lepton + 5 or more jets

Figure 7.18: Initial and final state radiation systematics for Z' boson events with $m_{Z'} = 1000$ GeV/c^2 sub-divided in "lepton + 3 jets, low m_{jet}" (a), "lepton + 3 jets, high m_{jet}" (b), "lepton + 4 jets" (c), "lepton + 5 or more jets" (d) samples. The blue band is the statistical uncertainty of the nominal distribution.

tions. The amount of QCD background events has to be measured in data. To evaluate the effect of an over- or underestimation of the QCD background, the number of QCD events has scaled up and down by 30%.

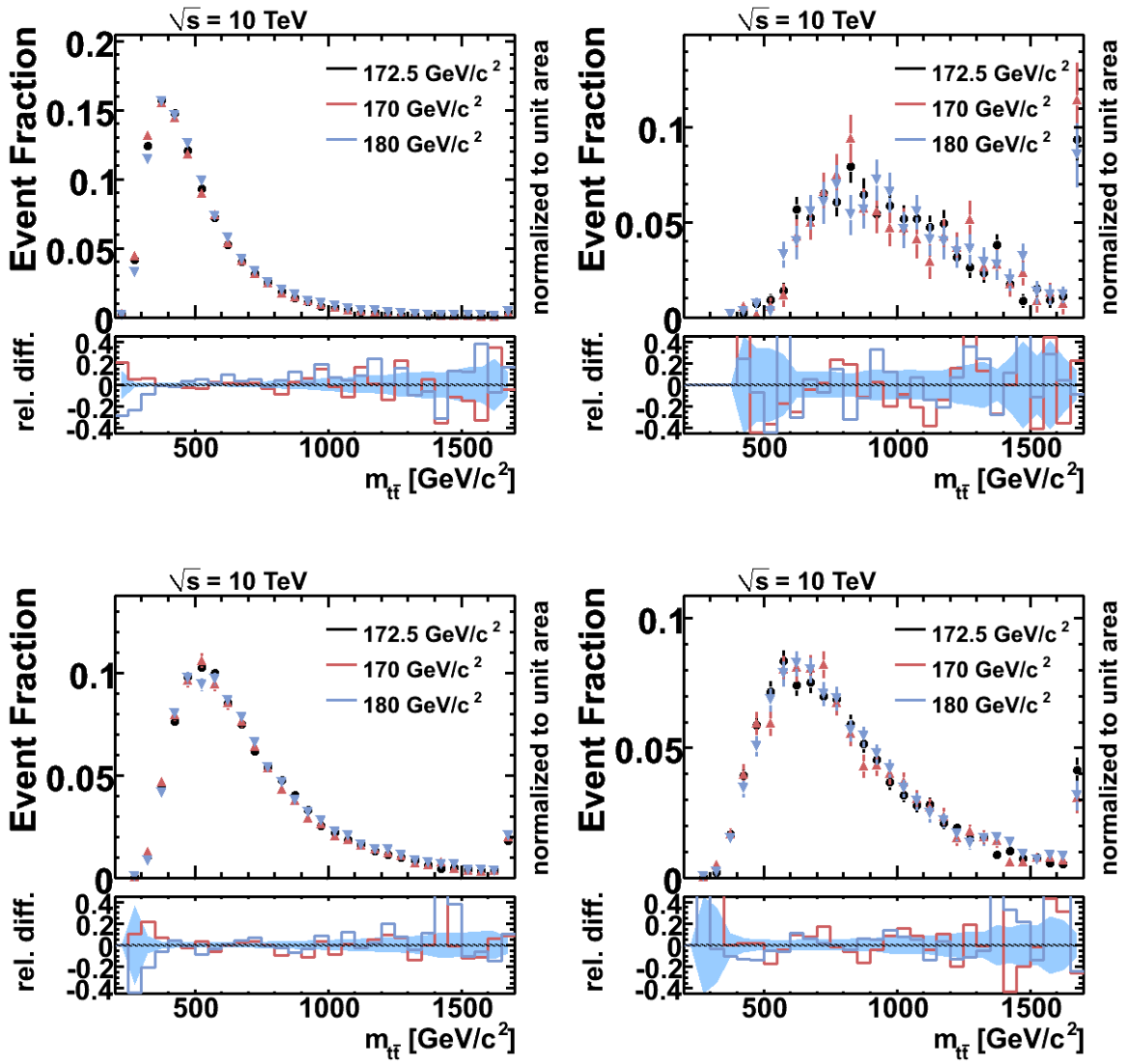

Figure 7.19: The reconstructed $t\bar{t}$ mass distribution for $t\bar{t}$ sample with different top quark masses. The events are sub-divided in "lepton + 3 jets, low m_{jet}" (a), "lepton + 3 jets, high m_{jet}" (b), "lepton + 4 jets" (c), "lepton + 5 or more jets" (d) samples. The blue band is the statistical uncertainty of the $m_{\text{top}} = 172.5$ GeV/c^2 distribution.

Top Quark Mass

The mass of the top quark influences the kinematic properties of its decay products. Thus, it can affect the shape of the $m_{t\bar{t}}$ distribution. Figure 7.19 demonstrates that the changes due to the top quark mass uncertainty are negligible. The uncertainty on the top quark mass will have also a small effect on the $m_{t\bar{t}}$ distribution of the signal events, because the resonance mass is much larger than $2 \cdot m_{top}$.

source		relative systematic uncertainty (%)							
		3 jet low m_{jet}		3 jet high m_{jet}		4 jet		5 or more jets	
		up	down	up	dowm	up	down	up	down
electron + jets									
JES	sig	-4.5	+4.6	+3.8	-9.0	+2.2	-5.2	+9.7	-18
	bgd	+19	+3.2	+22	-17	+22	-8.8	+27	-21
JEG	sig	-10		-1.0		+8.0		+0.44	
	bgd	+12		+11		+28		+8.6	
ISR/FSR	sig	-0.93	+2.9	+1.2	-3.8	+3.4	-6.4	+7.7	-12
PDF	sig	+3.2		+3.2		+3.3		+3.4	
muon + jets									
JES	sig	-4.1	+4.5	+4.6	-9.6	+2.6	-5.9	+10	-18
	bgd	+24	-1.5	+22	-12	+25	-12	+31	-23
JEG	sig	-3.6		+3.6		-6.1		+13	
	bgd	+13		+26		+11		+33	
ISR/FSR	sig	-0.84	+3.0	-4.6	+2.5	+2.2	-4.8	+15	-21
PDF	sig	+3.2		+3.0		+3.2		+3.3	

Table 7.7: Summary of the relative uncertainty on the number of expected signal and background events for shape and selection efficiency changing systematics. "ISR/FSR down" means ISR down, FSR up and "ISR/FSR up" means ISR up, FSR down.

7.6 Resonance Width

In Section 4.3.1 the effect of the Z' boson width on the kinematic distributions of top and anti-top quarks and on the $t\bar{t}$ invariant mass distribution has been studied at generator level. In this section the shape of the $m_{t\bar{t}}$ distribution after the detector simulation will be compared for two Z' boson widths. The width of Z' boson is given by its couplings to the fermions. The default Z' boson sample is generated with the Standard Model Z boson couplings which correspond to a width of 3.2% of $m_{Z'}$. One sample with a narrower resonance has been generated with $\Gamma/m_{Z'} = 1.23\%$.

In Figure 7.20 the shapes of both $m_{t\bar{t}}$ distributions are plotted. The relative difference in the peak region and in the tails to higher masses is below 10%. Only the tails to lower masses show larger deviations in particular for 1600 and 2000 GeV/c^2 Z' boson masses. Thus, at high masses the effect of the Z boson width should be taken into account. For this analysis, we are interested in the mass range around 1000 GeV/c^2 and can neglect this effect.

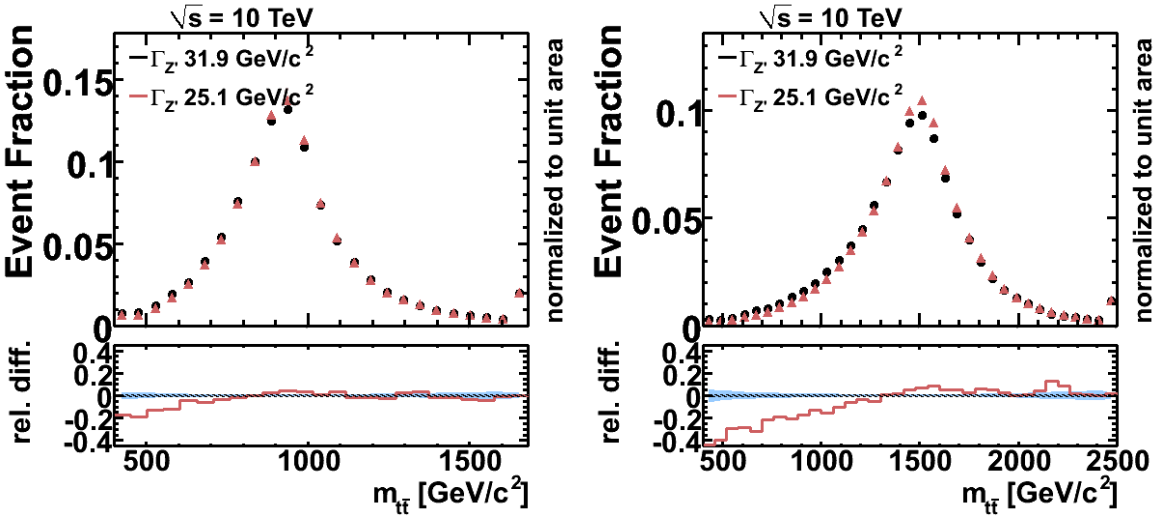

(a) lepton+jets, $m_{Z'}$ = 1000 GeV/c^2

(b) lepton+jets, $m_{Z'}$ = 1600 GeV/c^2

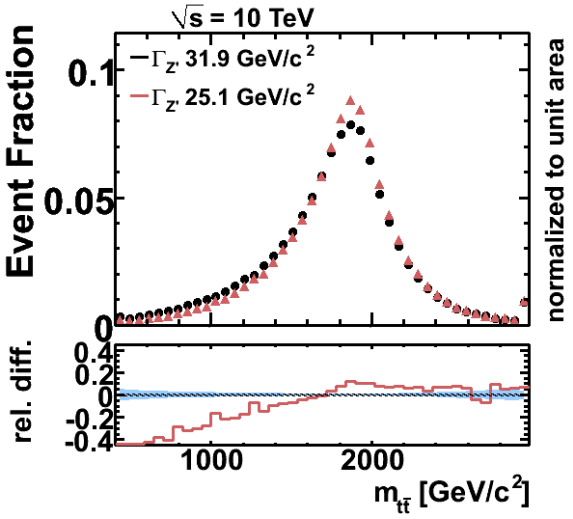

(c) lepton+jets, $m_{Z'}$ = 2000 GeV/c^2

Figure 7.20: Dependence of the invariant $t\bar{t}$ mass distribution on the width of Z' boson with $m_{Z'}$ = 1000 (a), 1600 (b) and 2000 GeV/c^2 (c). The blue band is the statistical uncertainty of the nominal distribution.

8 Heavy Resonance Searches at ATLAS

In the previous chapter the reconstruction method of heavy top quark resonances has been discussed and its performance in terms of signal selection efficiency and mass resolution as well as systematic uncertainties has been investigated. In this chapter a Bayesian approach will be presented, which has been used to extract the Z' boson cross section from the reconstructed $t\bar{t}$ invariant mass spectrum. If no significant excess of signal events in data can be found, a upper limit on the signal cross section times branching ratio $\sigma_{Z'} \times \mathrm{BR}(Z' \to t\bar{t})$ can be set. Combination of theoretical predictions of BSM models with the experimental limits allows to constrain these models. In the following the main ideas of the Bayesian method will be introduced in the context of the cross section measurement using binned signal and background distributions [128, 129]. Detailed information concerning Bayesian techniques can be found in [130]. In the second part of this chapter the sensitivity of the ATLAS experiment for the $t\bar{t}$ resonance searches will be investigated. This study has been performed assuming an integrated luminosity of 200 pb^{-1} and including expected systematic uncertainties. An estimate of the ATLAS sensitivity at 7 TeV centre-of-mass energy will be given.

8.1 Statistical Tools

In high energy physics one is often interested in making statistical inferences about a certain theoretical model using a given sample of data. The aim is to determine parameters of the model or to exclude the model. To quantify the random aspects of experiments, two main approaches can be used, frequentist or Bayesian. Frequentist interpret the probability as the frequency of the outcome of a repeatable experiment. In Bayesian statistics, the interpretation of the probability is more general and includes degree of belief. The probability density function for a hypothesis or for a parameter expresses the state of knowledge about its true value. The prior degree of belief is then updated by data from the experiment.

Suppose the outcome of the experiment is given by a vector of data $\vec{D}$, whose probability density function (p.d.f.) depends on an unknown parameter σ, the signal cross section which we would like to determine. For a given bin, the probability to observe a count D, if the mean count is d, is given by the Poisson distribution:

$$p(D|d) = \frac{e^{-d} d^D}{D!}. \tag{8.1}$$

The mean count d is a sum of the predicted contributions from signal and background. The signal yield is the product of the signal cross section σ and the effective luminosity a, defined as the signal acceptance times the integrated luminosity. The background yield b is the sum over all background sources. The probability to observe a count in a given bin i is

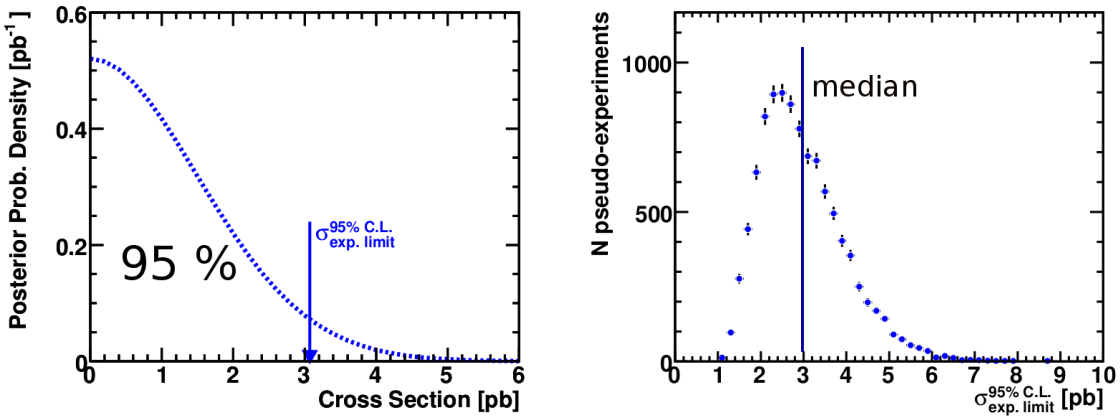

(a) posterior p.d.f. (b) pseudo-experiments

Figure 8.1: (a) An example of the posterior probability density function is shown. The upper limit on the signal cross section is calculated at 95% confidence level. (b) A distribution of the upper limits for 10000 pseudo-datasets is shown. The expected cross section is defined as a median of the distribution.

independent of the counts in the other bins, therefore the probability for the distribution of counts is the product of all single-bin counts, $1 \ldots N$:

$$L(\vec{D}|d) \equiv L(\vec{D}|\sigma, a, b) = \prod_{i=1}^{N} p(D_i|\sigma, a_i, b_i). \tag{8.2}$$

To combine several independent channels for example the e + jets and μ + jets channel, the single channel probabilities are replaced by the product of the channel probabilities.

Using Bayes' theorem, the posterior probability density function $p(\sigma|\vec{D})$ for the parameter σ is obtained, which gives the degree of belief for σ to take on values given the observed data $\vec{D}$:

$$p(\sigma|\vec{D}) = \frac{1}{\mathcal{N}} \iint L(\vec{D}|\sigma, a, b)\pi(\sigma, a, b)\ da\ db, \tag{8.3}$$

where $\pi(\sigma, a, b)$ is the prior knowledge of effective luminosity a and background yields b. The overall normalisation $\mathcal{N}$ is calculated from the requirement $\int_0^{\sigma_{\max}} p(\sigma|\vec{D})d\sigma = 1$. The upper bound $\sigma_{\max}$ is defined at the value of the posterior sufficiently close to zero. The lower bound is given by the assumption that the signal cross section is non-negative. The prior knowledge $\pi(\sigma, a, b)$ is independent of the signal cross section:

$$\pi(\sigma, a, b) = \pi(a, b)\pi(\sigma). \tag{8.4}$$

There is no recipe how to construct the prior p.d.f. for the signal cross section. A flat prior in σ is assumed:

$$\pi(\sigma) = \begin{cases} \frac{1}{\sigma_{\max}} & 0 \leq \sigma \leq \sigma_{\max} \\ 0 & \text{otherwise} \end{cases}. \tag{8.5}$$

The prior p.d.f. $\pi(a, b)$ encodes the knowledge of the effective signal luminosity and background yields. The parameters a and b are the so-called nuisance parameters. To take systematical uncertainties into account, a multivariate Gaussian p.d.f. centred about the nominal value plus/minus one standard deviation is assumed. The standard deviation is given by the acceptance uncertainty and the shapes of the distributions. The one-sided systematic uncertainties, like jet energy resolution, are symmetrised around the nominal value. In each bin the shift with respect to the nominal yield is sampled from this Gaussian p.d.f.. The new yield is the sum over the shifted yields for each systematic uncertainty plus the nominal yield.

A Bayesian upper limit σ_{up} at a confidence level CL can be obtained by requiring:

$$\int_0^{\sigma_{\text{up}}} p(\sigma|\vec{D}) = CL. \tag{8.6}$$

The integral is solved numerically using Monte Carlo importance sampling. An example of the posterior probability density function is shown in Figure 8.1(a).

To estimate the sensitivity, pseudo-data from the input data distributions has been generated. A count in each bin is sampled from a Poison distribution with mean the same as the nominal distribution and within one standard deviation. For each pseudo-experiment an expected upper limit on the signal cross section is calculated. Figure 8.1(b) is an example of such a distribution. The median defined as the 50% quantile of the upper limit distribution is taken as a final result. The one standard deviation uncertainty on the cross section is defined by 16% and 84% quantiles.

8.2 Sensitivity for Heavy Resonances

To determine the sensitivity of this analysis to discover narrow width $t\bar{t}$ resonances, the statistical analysis has been performed on the $m_{t\bar{t}}$ distributions reconstructed as described in the previous chapter. Using sub-samples as defined in Section 7.3, an upper limit on the signal cross-section at 95% confidence level is extracted assuming that no signal is expected.

The input for the limit calculation is the $m_{t\bar{t}}$ distributions for the signal and for the main sources of background: $t\bar{t}$, W + Jets, Z + Jets, QCD and single top quark. The samples are subdivided in the following channels:

- electron + 3 jets, the jet mass of the jet with the highest jet mass is below 65 GeV/c^2
- muon + 3 jets, the jet mass of the jet with the highest jet mass is below 65 GeV/c^2
- electron + 3 jets, the jet mass of the jet with the highest jet mass is above 65 GeV/c^2
- muon + 3 jets, the jet mass of the jet with the highest jet mass is above 65 GeV/c^2
- electron + 4 jets
- muon + 4 jets
- electron + 5 or more jets
- muon + 5 or more jets

The invariant mass distributions have been shown in Figure 7.8, 7.9, 7.10 and 7.11 for the background processes as well as for the signal with $m_{Z'}$ =500, 700, 1000 and 1300 GeV/c^2.

Figure 8.2 present distributions of upper limits at 95% CL for a Z' resonance at $m_{Z'}$ = 1000 GeV/c^2 for all sub-samples separately and combined. As expected, the "3 jet high m_{jet}" sub-sample is most sensitive to signal. The second-best performance shows the "4 jet" sub-sample, followed by the "3 jet low m_{jet}" and "5 or more jets" sub-sample with a similar performance. These results are in good agreement with the performance estimate presented in Section 7.4. A combination of all sub-samples provides the final result. The expected upper limit is defined as a median of this distribution. It means, that in 50% of cases the measured cross-section will be below the given value.

The expected upper limit on the signal cross-section taking only statistical uncertainty as a function of the resonance mass can be found in Figure 8.3. It shows upper limits for the single sub-samples as well as for the combination of sub-samples. The calculation is prepared only for resonance masses below 2000 GeV/c^2, because it is the most interesting mass range at low integrated luminosity. The "3 jet low m_{jet}" sub-sample looses on sensitivity with the increasing Z' boson mass. In contrast, the "3 jet high m_{jet}" sub-sample is insensitive around $t\bar{t}$ mass threshold, but it has the lowest upper limit on the cross section above 1000 GeV/c^2. The sensitivity of "4 jet" and "5 or more jets" sub-samples is similar at masses above 1300 GeV/c^2, at lower masses we expect less signal events with additional jets.

To estimate the effect of systematic biases and uncertainties on the sensitivity to the signal, the statistical analysis is repeated including several effects, that are expected to lead to significant systematic uncertainties. The following systematic uncertainties have been considered:

- an uncertainty on the jet energy scale of 10%
- the jet energy resolution is degraded by smearing the jet E_T with an additional $\frac{25\%}{\sqrt{E}} +$ 5%
- 10% error on the luminosity
- 30% uncertainty on the amount of the QCD background
- PDF uncertainty
- initial and final state radiation
- top quark mass

These systematics have the largest impact on the sensitivity as discussed in Section 7.5. The upper limits on the signal production cross-section are presented in Figure 8.4 and summarised in Table 8.1. The limits could be set to $3.62^{+1.6}_{-1.1}$ pb ($m_{Z'} = 1000$ GeV/c^2), $2.16^{+0.9}_{-0.7}$ pb ($m_{Z'} = 1300$ GeV/c^2) and $1.01^{+0.5}_{-0.3}$ pb ($m_{Z'} = 2000$ GeV/c^2) assuming $\sqrt{s} = 10$ TeV collisions and 200 pb^{-1} of integrated luminosity. At Z' boson masses below 1000 GeV/c^2, the systematic uncertainties reduces significantly the sensitivity to the signal. At Z' boson masses above 1000 GeV/c^2 prevails the statistical uncertainty. The results obtained here are valid for resonances whose natural width does not contribute significantly to the reconstructed mass distribution of the signal.

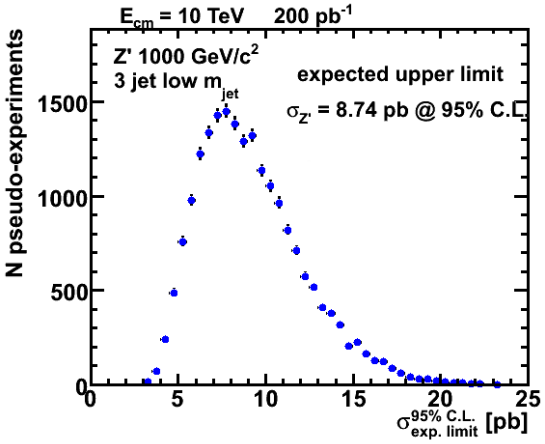

(a) lepton + 3 jets, low m_{jet}

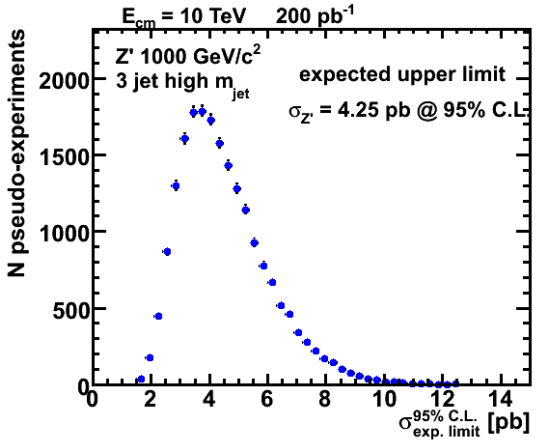

(b) lepton + 3 jets, high m_{jet}

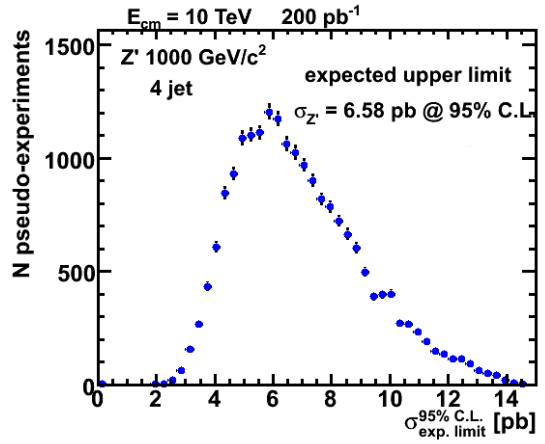

(c) lepton + 4 jets

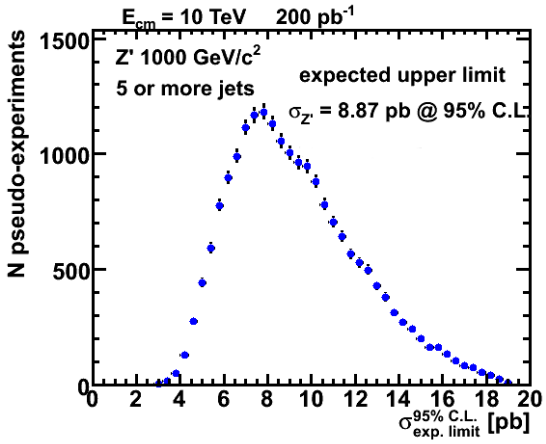

(d) lepton + 5 jets

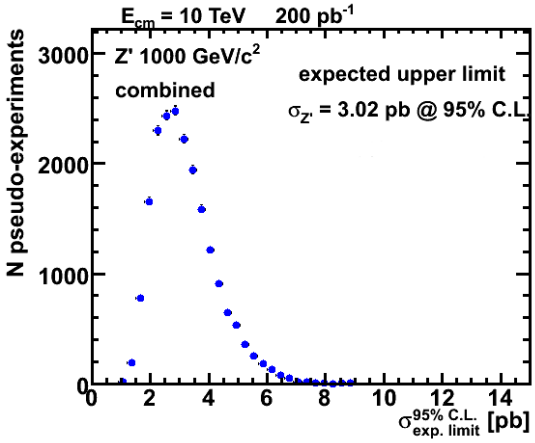

(e) lepton + jets

Figure 8.2: Distributions of the expected upper limits for Z' boson with $m_{Z'} = 1000$ GeV/c^2 for all sub-samples separately and combined. In the plots the electron and muon channels have been combined. The upper limits are calculated under the assumption that no signal is expected.

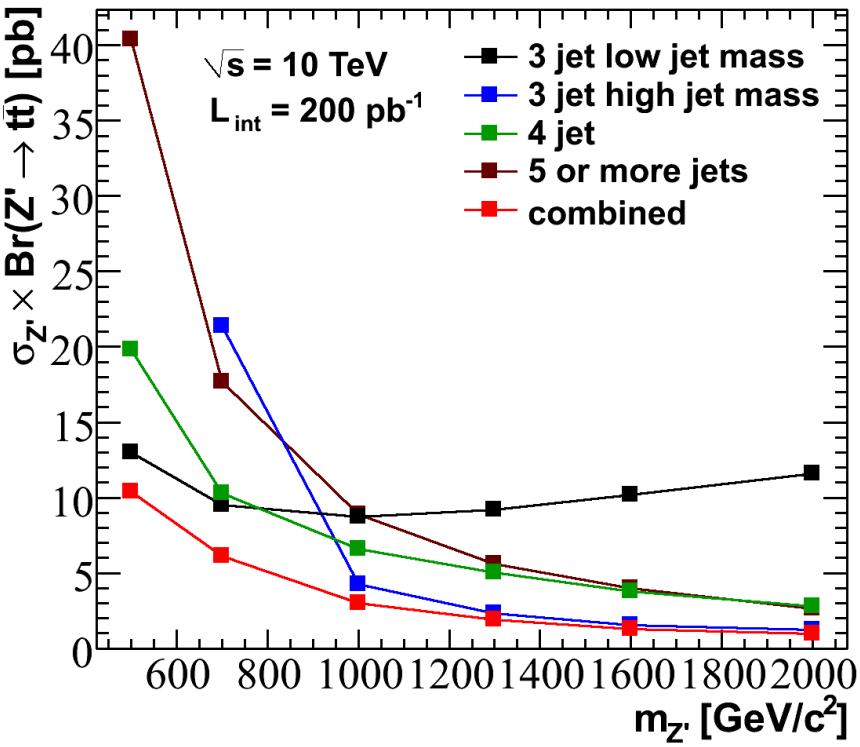

Figure 8.3: Expected upper limits at 95% CL as a function of the Z' boson mass. Only statistical uncertainties have been taken into account.

$m_{Z'}$	stat [pb]			incl. sys [pb]		
	16%	median	84%	16%	median	84%
500 GeV/c^2	7.49	10.4	14.5	12.4	19.1	27.6
700 GeV/c^2	4.41	6.11	8.52	6.27	8.99	13.2
1000 GeV/c^2	2.17	3.02	4.19	2.48	3.62	5.22
1300 GeV/c^2	1.36	1.90	2.64	1.46	2.16	3.09
1600 GeV/c^2	0.94	1.31	1.83	0.96	1.41	2.08
2000 GeV/c^2	0.71	0.99	1.39	0.67	1.01	1.52

Table 8.1: The 95% C.L. exclusion limits on the signal cross-section, taking into account the main sources of systematic uncertainty.

In Figure 8.4 a theoretical cross-section is indicated, corresponding to a narrow leptophobic topcolour Z' with $\Gamma/m_{Z'} = 1.2\%$ listed in Table 4.2. A leptophobic topcolour Z' boson with a mass below 1000 GeV/c^2 can be excluded at 95% confidence level using 200 pb^{-1} of data at $\sqrt{s} = 10$ TeV. Therefore, this analysis is able to constrain this model in a mass range that is not covered by previous experiments.

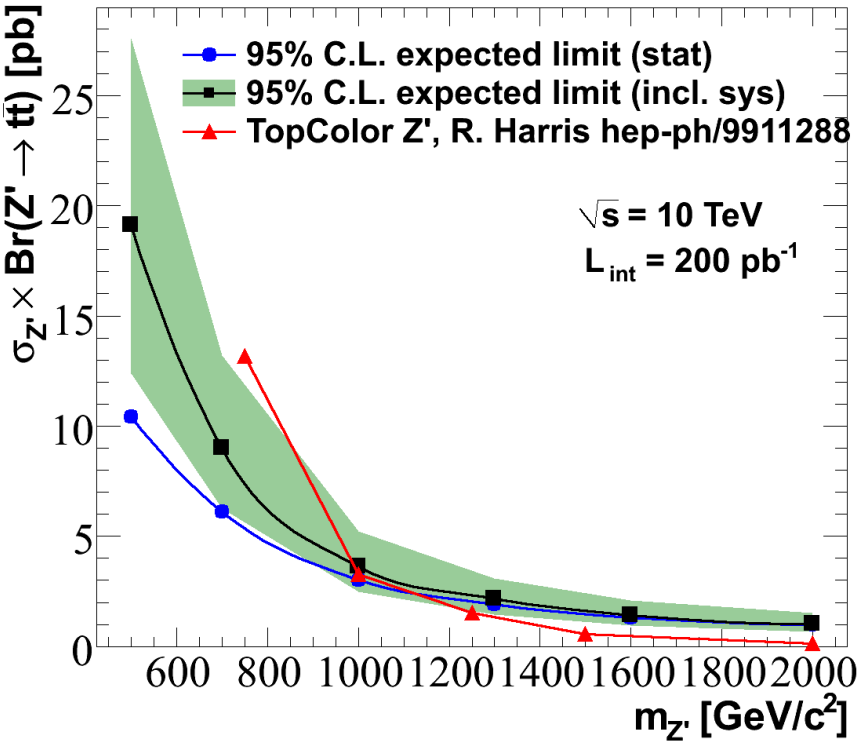

Figure 8.4: The 95% *CL* exclusion limits on the cross section, taking into account the main sources of systematic uncertainty.

8.3 Prospects for Heavy Resonance Searches

The LHC is operating at a centre-of-mass energy of 7 TeV this year instead of the assumed 10 TeV. Lower centre-of-mass energy leads to the reduction of production rates of particles as shown in Figure 8.5. The ratio of the $q\bar{q}$ and gg parton luminosity is plotted versus the mass of the produced particles.

The production cross section of processes initiated through a $q\bar{q}$ annihilation are reduced by a factor of 2.5 and for processes initiated through a gg-fusion the cross section is reduced by a factor of 4. Thus, the Z' boson production cross section is less affected than the predominantly gg-initiated background production cross section. The selection efficiency has been cross-checked for the $t\bar{t}$ and signal samples at 7 TeV and it has been found to be comparable to the values at 10 TeV within 5% [131]. Only the loss in the parton luminosity has to be compensated. Therefore, even at 7 TeV we will be able to extend the current searches for $t\bar{t}$ resonances into the TeV regime collecting a larger data set of order 1 fb^{-1}.

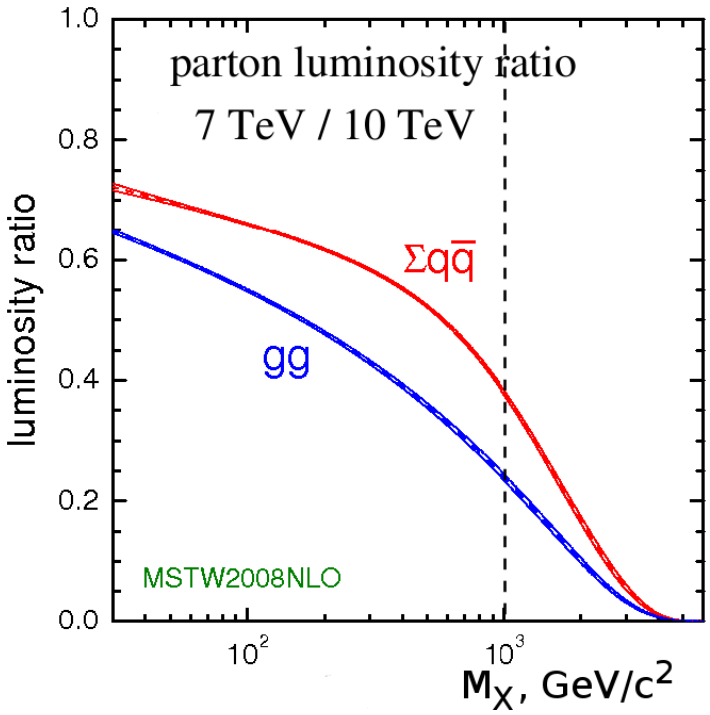

Figure 8.5: Parton luminosity ratio 7 TeV/10 TeV centre-of-mass at the LHC as a function of the mass of produced particles [132].

9 Summary and Conclusions

In this thesis a new inclusive topological multi-vertex finder, ZVTOP, was implemented in the ATLAS software framework. ZVTOP is used for the identification of B to D hadron cascades in b-jets. The main concept is to search for vertices in the three dimensional space in contrast to former algorithms which form vertices from all track combinations. Vertices are found using a vertex probability function which is defined by the trajectories and position resolution of the tracks. Reconstructed vertices are used as input for the b-jet identification. One method is based on a likelihood ratio approach and the second one on an artificial neural network. Using a neural network approach results in the light quark jet rejection rate for $t\bar{t}$ events of 108 (208) with a b-tagging efficiency of 60% (50%). This means only one every 108(280) light-quark jets is mis-identified as a b-jet. The relative improvement compared to the standard algorithm is $\sim$ 8%. Future improvements are expected using collision data collected by the experiment, especially in calibrating and tunnig the ZVTOP tagger.

The main part of the thesis concentrates on the search for heavy narrow width resonances in the $t\bar{t}$ invariant mass spectrum. A new reconstruction scheme has been developed for the efficient selection and reconstruction of $t\bar{t}$ final states at various resonance masses. The topology of events produced at the $t\bar{t}$ mass threshold differs significantly from the event topology at $m_{t\bar{t}} \sim$ 1-2 TeV/c^2. With increasing mass, the decay products of the individual top quarks will become more collimated. The partons from W bosons or even from top quarks may be reconstructed into one jet. Such jets have a high invariant mass comparable to the mass of intrinsic quarks or bosons. The invariant jet mass is used to identify the event topology and the topology dependent reconstruction of the $m_{t\bar{t}}$ distribution can be performed.

The sensitivity of the ATLAS experiment for a discovery of a narrow uncoloured $t\bar{t}$ resonance using the presented method is encouraging: a 95% CL exclusion on the production cross-section including systematical uncertainties could be set to $3.62^{+1.6}_{-1.1}$ pb ($m_{Z'} = 1000$ GeV/c^2), $2.16^{+0.9}_{-0.7}$ pb ($m_{Z'} = 1300$ GeV/c^2) and $1.01^{+0.5}_{-0.3}$ pb ($m_{Z'} = 2000$ GeV/c^2) assuming $\sqrt{s} = 10$ TeV collisions and 200 pb^{-1} of integrated luminosity. So a leptophobic topcolour Z' boson with a mass below 1000 GeV/c^2 can be excluded at 95% confidence level. Therefore, this analysis is able to constrain this model in a mass range that is not covered by the previous experiments.

Two other approaches have been developed at ATLAS to reconstruct heavy $t\bar{t}$ resonances [131]. The first approach performs a full reconstruction of the top and anti-top quarks. Observables like the mass of the reconstructed top quark candidates, in combination with b-tagging, allow for a tight control of the reducible backgrounds. The second approach is designed to reconstruct highly boosted top quarks. This algorithm reconstructs the full top quark decay as a single jet. The sensitivity of all three reconstruction methods is comparable in the mass range around 1000 GeV/c^2. At lower masses, the full reconstruction

approach achieves better results due to a better background suppression. At higher masses, the mono-jet reconstruction approach is more sensitive, because the fraction of fully merged event topology increases with the increasing resonance mass.

The CMS experiment at the LHC has prepared an analysis for a search for narrow width resonances at $\sqrt{s}$ = 10 TeV and an assumed integrated luminosity of 200 pb^{-1} in the muon channel only [133]. They claim the expected cross section exclusion limit at 95% CL of $7.5^{+4.4}_{-2.7}$ pb for a 1000 GeV/c^2 heavy resonance and a limit of $2.9^{+0.5}_{-0.4}$ pb for a 2000 GeV/c^2 heavy resonance. This analysis is more sensitive, because - among other differences - both lepton channels are used.

List of Figures

2.1 Fundamental particles of the Standard Model . . . 6
2.2 Elements of Feynman diagrams in QCD . . . 6
2.3 Higher order corrections to the QCD coupling α_S . . . 7
2.4 Elements of Feynman diagrams in QED . . . 8
2.5 Feynman diagrams associated with the Higgs Lagrangian term $\mathcal{L}_{\text{Higgs}}$ . . . 10
2.6 PDFs for u, $\bar{u}$, d, $\bar{d}$, s quarks and gluons inside the proton at $\mu = m_t$ . . . 12
2.7 $t\bar{t}$ production channels at leading order perturbation theory . . . 13
2.8 PDFs for u, $\bar{u}$, d, $\bar{d}$ quarks and gluons inside the proton at $\mu = 1$ TeV . . . 14
2.9 Feynman diagrams for resonant $t\bar{t}$ production . . . 16
2.10 Z' boson mass distributions in the mass range 500-3000 GeV/c^2 . . . 18

3.1 The LHC injector complex . . . 20
3.2 View of the ATLAS detector . . . 22
3.3 Views of the ATLAS inner detector . . . 24
3.4 Pixel and SCT modules . . . 25
3.5 TRT barrel and endcaps structures and modules . . . 25
3.6 Cut-away view of the calorimeter system . . . 26
3.7 Sketch of the barrel module of electromagnetic calorimeter . . . 28
3.8 The cumulative amounts of material in front of and in the calorimeter . . . 30
3.9 Schematic view of the muon spectrometer . . . 31
3.10 Placement of the forward detectors LUCID, ZDC and ALFA . . . 33
3.11 Expected event rates at luminosity of 10^{34} cm^{-2}s^{-1} and $\sqrt{s} = 14$ TeV . . . 35
3.12 The instantaneous and total luminosity at $\sqrt{s} = 7$ TeV . . . 37

4.1 General structure of a hard proton-proton collision . . . 40
4.2 Z' boson invariant mass distribution, rapidity y and p_T distributions of top and antitop quarks . . . 47

5.1 Track helix in the transverse and in the longitudinal plane. . . . 54
5.2 Electron identification efficiency as a function of E_T and η . . . 58
5.3 Combined muon reconstruction efficiency and resolution . . . 59
5.4 Illustration of infrared and collinear sensitivity . . . 60
5.5 Illustration of signal towers and topological cell clusters . . . 63
5.6 Jet reconstruction flow in ATLAS . . . 64
5.7 Jet mass distributions at hadron colliders . . . 66
5.8 Performance of missing transverse energy reconstruction . . . 68

6.1 Measured e^+e^- fragmentation function of b-quarks into B hadrons at $\sqrt{s} \sim 91$ GeV . . . 72

6.2 Schematic view of a $B \rightarrow D$ hadron decay chain in b-jets . . . 73
6.3 Parameters of tracks associated to jets . . . 76
6.4 Definition of the signed track impact parameter IP in jets . . . 78
6.5 Transverse and longitudinal signed impact parameter significance distributions 78
6.6 Track probability function and angular displacement . . . 82
6.7 Vertex seed finding and clustering of vertex seeds . . . 83
6.8 Reconstructed vertices from K^0_S, Λ decays and material interactions . . . 84
6.9 Ambiguity solving procedure: (a) association of tracks 1 and 2 to vertex 1, removal of these tracks from vertex 2 and 3, vertices 2 and 3 are rejected; (b) association of tracks 3 and 4 to the vertex 4, removal from vertex 5; vertex 5 is rejected; (c) final association. . . . 85
6.10 Secondary Vertex Reconstruction Performance . . . 87
6.11 Distributions of variables used to tag b-jets . . . 89
6.12 B-tagging efficiency versus light quark jet rejection for $t\bar{t}$ events . . . 91

7.1 Missing transverse energy versus transverse W boson mass . . . 96
7.2 Lepton trigger efficiency for signal events after selection cuts . . . 97
7.3 Comparison between the ATLFAST-II and full simulation for a Z' boson with $m_{Z'} = 1000$ GeV/c^2 . . . 98
7.4 Event topology of semi-leptonic $t\bar{t}$ events . . . 100
7.5 Invariant jet mass distributions for different event topologies . . . 102
7.6 The angle between the true lepton and the b-quark ΔR(mc_lep,bquark) for different event topologies . . . 103
7.7 Number reconstructed jets and the highest invariant jet mass for the signal and background . . . 104
7.8 The $t\bar{t}$ invariant mass distributions for signal and main background processes in 3 jet channel . . . 105
7.9 The $t\bar{t}$ invariant mass distributions for signal and main background processes in 4 and 5 or more jets channel . . . 106
7.10 Z' boson mass distribution in 3 jets channel . . . 107
7.11 Z' boson mass distribution in 4 and 5 or more jets channel . . . 108
7.12 Z' boson mass resolution in 3 jets channel . . . 111
7.13 Z' boson mass resolution in 4 and 5 or more jets channels . . . 112
7.14 Jet energy scale systematics for Z' boson events with $m_{Z'} = 1000$ GeV/c^2 . . . 113
7.15 Jet energy scale systematics for $t\bar{t}$ events . . . 114
7.16 Jet energy resolution systematics for Z' boson events with $m_{Z'} = 1000$ GeV/c^2 115
7.17 Parton distribution functions systematics for Z' boson events with $m_{Z'} = 1000$ GeV/c^2 . . . 117
7.18 Initial and final state radiation systematics for Z' boson events with $m_{Z'} = 1000$ GeV/c^2 . . . 118
7.19 Top quark mass systematics for $t\bar{t}$ events . . . 119
7.20 Dependence of the invariant $t\bar{t}$ mass distribution on the width of Z' boson . . . 121

8.1 Bayesian limit calculation techniques . . . 124
8.2 Distribution of the expected upper limits for Z' boson with $m_{Z'} = 1000$ GeV/c^2 127
8.3 Expected upper limits at 95% CL as a function of the Z' boson mass . . . 128

8.4 The 95% CL exclusion limits on the cross section, taking into account the main sources of systematic uncertainty 129
8.5 Parton luminosity ratio 7 TeV/10 TeV at the LHC 130

List of Tables

2.1 The fields of the Standard Model and their quantum numbers 5
2.2 Overview of some $t\bar{t}$ resonance benchmark models 16

3.1 General performance goals of the ATLAS detector 21
3.2 Granularity and number of readout channels of the ATLAS calorimeters . . . 27
3.3 Main parameters of the muon spectrometer 32
3.4 Operational fraction of ATLAS detector components 37

4.1 PYTHIA parameter settings for Z' boson couplings to fermions 46
4.2 Cross section σ and width Γ as a function of the Z' boson mass 46
4.3 Generated single top quark and top quark pairs samples 48
4.4 Generated W + jets samples 49
4.5 Generated Z + jets samples 50
4.6 Generated QCD multijet samples 51

5.1 Expected track parameter resolutions for isolated, single muons 55

6.1 Main decay modes and some properties of B and D hadrons 73
6.2 Jet and track selection criteria for b-tagging 75
6.3 Average track multiplicity in b- and light jets with relative contribution of tracks 77
6.4 The list of tunable parameter of topological vertex finder 86
6.5 Light quark jet rejection for the fixed b-tagging efficiencies of 50%, 60% and 70% for $t\bar{t}$ events 92

7.1 Summary of the semi-leptonic event selection cuts 95
7.2 Number of expected signal and background events after the semi-leptonic selection cuts over the whole $m_{t\bar{t}}$ range 95
7.3 Categorisation of selected signal events in the di-leptonic, semi-leptonic and fully hadronic channels 99
7.4 Signal and background contribution in different event sub-samples 104
7.5 Number of expected signal and background events in the ± 1 RMS range around the signal peak 109
7.6 Z' Mass Resolution 110
7.7 Summary of the relative uncertainty on the overall normalisation 120

8.1 The 95% C.L. exclusion limits on the signal cross-section 128

Bibliography

[1] S. Glashow, Nucl. Phys. 22 , 579 (1961).

[2] S. Weinberg, Phys. Rev. Lett. 19 , 1264 (1967).

[3] A. Salam, *In: Elementary Particle Theory* (8th Nobel Symposium, Almqvist and Wiksell, Stockholm, 1968), p. 367ff.

[4] A. Salam and J. Ward, Phys. Lett. 13 , 168 (1964).

[5] S. Glashow, J. Iliopoulos, and L. Maiani, Phys. Rev. D 2 , 1285 (1970).

[6] H. Georgi and S. L. Glashow, Phys. Rev. Lett. 28 , 1494 (1972).

[7] H. D. Politzer, Phys. Rept. 14 , 129 (1974).

[8] D. J. Gross and F. Wilczek, Phys. Rev. D 8 , 3633 (1973).

[9] G. 't Hooft, Nucl. Phys. B 35 , 167 (1971).

[10] G. 't Hooft and M. Veltman, Nucl. Phys. B 44 , 189 (1972).

[11] P. W. Higgs, Phys. Rev. 145 , 1156 (1966).

[12] J. Goldstone, A. Salam, and S. Weinberg, Phys. Rev. 127 , 965 (1962).

[13] E. Noether, Nachr. v. d. Ges. d. Wiss. zu Goettingen, Math-phys. Klasse, pp. 235-257, 1918.

[14] Particle Data Group, K. Nakamura *et al.*, J. Phys. G 37 , 075021 (2010).

[15] TEVATRON Electroweak Working Group, (2010), arXiv:1007.3178.

[16] T. Degrand and C. DeTar, *Lattice Methods for Quantum Chromodynamics* (World Scientific, 2006).

[17] F. Halzen and A. D. Martin, *Quarks and Leptons: An Introductory Course in Modern Particle Physics.* (John Wiley and Sons Inc., 1984).

[18] C. Wu, E. Ambler, R. Hayward, D. Hoppes, and R. Hudson, Phys. Rev. 105 , 1413 (1957).

[19] G. Abbiendi *et al.*, Phys. Lett. B 565 , 61 (2003).

[20] T. Aaltonen *et al.*, Phys. Rev. Lett. 104 , 061802 (2010).

[21] N. Cabibbo, Phys. Rev. Lett. 10 , 531 (1963).

[22] M. Kobayashi and T. Maskawa, Prog. Theor. Phys. 49 , 652 (1973).

[23] Z. Maki, M. Nakagawa, and S. Sakata, Prog. Theor. Phys. 28 , 870 (1962).

[24] F. Abe *et al.*, Phys. Rev. Lett. 74 , 2626 (1995).

[25] S. Abachi *et al.*, Phys. Rev. Lett. 74 , 2422 (1995).

[26] S. Moch and P. Uwer, Nucl. Phys. Proc. Suppl. 183 (2008), arXiv:0807.2794.

[27] Z. Sullivan, Phys. Rev. D 70 , 114012 (2004), hep-ph/0408049.

[28] W. K. Tung, p. 1369 (1987), FERMILAB-CONF-87-122-T.

[29] J. Pumplin *et al.*, JHEP 07 , 012 (2002), hep-ph/0201195.

[30] M. Beneke *et al.*, (2000), hep-ph/0003033.

[31] S. Catani, D. de Florian, M. Grazzini, and P. Nason, JHEP 07 , 028 (2003), hep-ph/0306211.

[32] N. Andari *et al.*, (2010), ATL-PHYS-INT-2010-030.

[33] K. Gaemers and F. Hoogeveen, Phys. Lett. B 146 , 347 (1984).

[34] D. Dicus, A. Stange, and S. Willenbrock, Phys. Lett. B 333 , 126 (1994), hep-ph/9404359.

[35] W. Bernreuther, M. Flesch, and P. Haberl, Phys. Rev. D 58 , 114031 (1998), hep-ph/9709284.

[36] A. Djouadi, Phys. Rept. 459 , 1 (2008), hep-ph/0503173.

[37] A. Manohar and M. Wise, Phys. Rev. D 74 , 035009 (2006), hep-ph/0606172.

[38] M. Gresham and M. Wise, Phys. Rev. D 76 , 075003 (2007), arXiv:0706.0909.

[39] I. Antoniadis, Phys. Lett. B 246 , 377 (1990).

[40] T. Rizzo and J. Wells, Phys. Rev. D 61 , 0160072 (1999).

[41] A. Leike, Phys. Rept. 317 , 143 (1999), hep-ph/9805494.

[42] J. Hewett and T. Rizzo, Phys. Rept. 183 , 193 (1989).

[43] M. Cvetic and S. Godfrey, (1995), hep-ph/9504216.

[44] T. Rizzo, (1996), hep-ph/9612440.

[45] E. Eichten and K. Lane, Phys. Lett. B 90 , 125 (1980).

[46] C. T. Hill and S. J. Parke, Phys. Rev. D 49 , 4454 (1994), hep-ph/9312324.

[47] C. T. Hill, Phys. Lett. B 345 , 483 (1995), hep-ph/9411426.

[48] L. Randall and R. Sundrum, Phys. Rev. Lett. 83 , 3370 (1999).

[49] H. Davoudiasl, J. L. Hewett, and T. G. Rizzo, Phys. Rev. Lett. 84 , 2080 (2000).

[50] CDF, T. Aaltonen *et al.*, Phys. Rev. Lett. 102 , 091805 (2009), arXiv:0811.0053.

[51] CDF, T. Aaltonen *et al.*, Phys. Rev. Lett. 102 , 031801 (2009), arXiv:0810.2059.

[52] V. Abazov *et al.*, (2009), DØ note 5923-conf.

[53] CDF, T. Aaltonen *et al.*, Phys. Rev. D 79 , 112002 (2009), arXiv:0812.4036.

[54] DØ, V. M. Abazov *et al.*, Phys. Lett. B 668 , 98 (2008), arXiv:0804.3664.

[55] DØ, V. M. Abazov *et al.*, (2009), DØ note 5882-CONF.

[56] CDF, T. Aaltonen *et al.*, Phys. Rev. D 77 , 051102 (2008), arXiv:0710.5335.

[57] V. Abazov *et al.*, (2009), DØ note 5882-conf.

[58] CDF, T. Aaltonen *et al.*, (2008), CDF note 9164.

[59] CDF, C. Ciobanu *et al.*, FERMILAB-FN-0773-E.

[60] S. Godfrey, Phys. Rev. D 51 , 1402 (1995).

[61] A. Leike, Phys. Lett. B 402 , 374 (1997).

[62] A. Scharf, private communication.

[63] ATLAS, G. Aad *et al.*, JINST 3 S08003 (2008).

[64] CMS, S. Chatrchyan *et al.*, JINST 3 S08004 (2008).

[65] LHCb, A. A. Jr *et al.*, JINST 3 S08005 (2008).

[66] TOTEM, G. Antchev *et al.*, Nucl. Inst. Meth. Phys. Res. 617 , 62 (2010).

[67] ALICE, K. Aamondt *et al.*, JINST 3 S08002 (2008).

[68] L. Evans and P. Bryant, JINST 3 S08001 (2008).

[69] J.-L. Caron, The LHC Injection Complex, AC Collection, 1993.

[70] J. Pequenao, Computer Generated Images of the ATLAS Detectors, 2008.

[71] ATLAS, G. Aad *et al.*, (1998), CERN-LHCC-98-14.

[72] ATLAS, G. Aad *et al.*, (2003), CERN/LHCC/03-022.

[73] ATLAS, G. Aad *et al.*, (2009), arXiv:0901.0512v4.

[74] ATLAS, G. Aad *et al.*, (2010), arXiv:1004.5293.

[75] ATLAS, G. Aad *et al.*, (2009), arXiv:0912.2642.

[76] ATLAS, G. Aad *et al.*, (2010), arXiv:1006.4384.

[77] ATLAS, G. Aad *et al.*, (2010), ATLAS-CONF-2010-060.

[78] A. Agostinelli *et al.*, Nucl. Inst. Meth. Phys. Res. 506 , 250 (2003).

[79] ATLAS, G. Aad *et al.*, (05/2010), arXiv:1005.4568, Submitted to Eur. Phys. J. C.

[80] M. Mangano and S. T.J., Annu. Rev. Nucl. Part. Sci. 55 , 555 (2005).

[81] M. Mangano *et al.*, JHEP 07 , 001 (2003), hep-ph/0206293.

[82] F. Krauss, R. Kuhn, and G. Soff, J. Phys. G. 26(1) , L11 (2000), hep-ph/9904274.

[83] S. Catani, F. Krauss, B. R. Webber, and R. Kuhn, JHEP 11 , 063 (2001), hep-ph/0109231.

[84] V. Sudakov, Sov. Phys. JETP 3 , 65 (1956).

[85] S. Frixione, P. Nason, and B. Webber, JHEP 08 , 007 (2003), hep-ph/0305252.

[86] T. Sjöstrand, S. Mrenna, and P. Skands, JHEP 05 , 026 (2006), hep-ph/0603175.

[87] B. Andersson, G. Gustafson, G. Ingelman, and T. Sjöstrand, Phys. Rept. 97 , 31 (1983).

[88] G. Corcella *et al.*, JHEP 01 , 010 (2001), hep-ph/0011363.

[89] G. Corcella *et al.*, (2005), hep-ph/0210213, CERN-TH/2002-270.

[90] UA5, G. Alner *et al.*, Nucl. Phys. B 291 , 445 (1987).

[91] J. Butterworth, J. R. Forshaw, and M. Seymour, Z. Phys. C72 , 637 (1996), hep-ph/9601371.

[92] ATLAS, G. Aad *et al.*, (2010), ATLAS-CONF-2010-058.

[93] ATLAS, G. Aad *et al.*, (2010), ATLAS-CONF-2010-019.

[94] ATLAS, G. Aad *et al.*, (2010), ATLAS-CONF-2010-067.

[95] H. Hakobyan, M. Simonyan, T. Carli, and A. M. Henriques-Correia, (2006), ATL-TILECAL-PUB-2007-008.

[96] ATLAS, G. Aad *et al.*, (2010), ATLAS-CONF-2010-052.

[97] ATLAS, G. Aad *et al.*, (2010), ATLAS-CONF-2010-064.

[98] R. M. Harris, C. T. Hill, and S. J. Parke, (1999), hep-ph/9911288.

[99] A. Shibata *et al.*, (2009), ATL-COM-PHYS-2009-334.

[100] P. Hough, Proc. Int. Conf. High Energy Accelerators and Instrumentation (1959).

[101] R. Kalman, Transaction of the ASME, Journal of Basic Engineering , 35 (1960).

[102] T. Cornelissen *et al.*, (2007), ATL-SOFT-PUB-2007-007.

[103] G. Piacquadio, K. Prokofiev, and A. Wildauer, J. Phys. : Conf. Ser. 119 , 032033 (2008).

[104] M. Cacciari, G. Salam, and G. Soyez, http://www.lpthe.jussieu.fr/~salam/fastjet.

[105] S. Catani, Y. L. Dokshitzer, M. H. Seymour, and B. R. Webber, Nucl. Phys. B406 , 187 (1993).

[106] S. D. Ellis and D. E. Soper, Phys. Rev. D 48 , 3160 (1993).

[107] M. Cacciari, G. P. Salam, and G. Soyez, JHEP 04 , 063 (2008), arXiv:0802.1189.

[108] Y. L. Dokshitzer, G. D. Leder, S. Moretti, and B. R. Webber, JHEP 08 , 001 (1997), hep-ph/9707323.

[109] M. Wobisch and T. Wengler, (1998), hep-ph/9907280.

[110] L. Asquith *et al.*, (2009), ATL-COM-PHYS-2009-630.

[111] I. Abt *et al.*, Nucl. Inst. Meth. A 386 , 348 (1997).

[112] U. Baur and L. H. Orr, Phys. Rev. D 76 , 094012 (2007), arXiv:0707.2066.

[113] J. Thaler and L.-T. Wang, JHEP 07 , 092 (2008), arXiv:0806.0023.

[114] L. G. Almeida *et al.*, Phys. Rev. D 79 , 074017 (2009), arXiv:0807.0234.

[115] S. Ellis, J. Huston, K. Hatakeyama, P. Loch, and M. Tonnesmann, Prog. Part. Nucl. Phys. 60 , 484 (2008), arXiv:0712.2447.

[116] T. Chwalek, *Messung der W-Boson-Helizitätsanteile in Top-Quark-Zerfällen mit dem CDF II Experiment und Studien zu einer frühen Messung des ttbar-Wirkungsquerschnitts mit dem CMS Experiment*, PhD thesis, 2010.

[117] V. Kostyukhin, (2003), ATL-PHYS-2003-031.

[118] V. Kostyukhin, (2003), ATL-PHYS-2003-033.

[119] D. Scott, *Multivariate density estimation theory, practice, and visualization* (NY Wiley, New York, 1992).

[120] G. Piacquadio and K. Jakobs, *Identification of b-jets and investigation of the discovery potential of a Higgs boson in the $WH \to l\nu b\bar{b}$ channel with the ATLAS experiment*, PhD thesis, Freiburg U., Freiburg, 2010.

[121] D. J. Jackson, Nucl. Inst. Meth. A 388 , 247 (1997).

[122] P. Billoir and S.Qian, Nucl. Inst. Meth. A 311 , 139 (1992).

[123] SLD, K. Abe *et al.*, (1999), hep-ex/9907051.

[124] F. Rosenblatt, Psychological Rev. 65 , 386 (1958).

[125] A. Hoecker *et al.*, ArXiv Physics e-prints (2007), arXiv:physics/0703039.

[126] B. Abbott *et al.*, (2009), ATL-COM-PHYS-2009-633.

[127] A. D. Martin, R. G. Roberts, W. J. Stirling, and R. S. Thorne, Phys. Lett. B 531 , 216 (2002), hep-ph/0201127.

[128] S. Jain, H. B. Prosper, and R. Schwienhorst, Statistical Methods Implemented in the Package 'top_statistics', DØ Note 5817, December 8, 2008.

[129] DØ, I. Bertram *et al.*, FERMILAB-TM-2104.

[130] R. Barlow, *A Guide to the Use of Statistical Methods in the Physical Sciences*The Manchester physics series (Wiley, 1989).

[131] ATLAS, G. Aad *et al.*, (2010), ATL-PHYS-PUB-2010-008.

[132] W. Stirling, private communication.

[133] CMS, S. Chatrchyan *et al.*, (2009), CMS-PAS-TOP-09-009.